

Constraining supersymmetric models using Higgs physics, precision observables and direct searches

Dissertation zur Erlangung des Doktorgrades
an der Fakultät für Mathematik, Informatik und Naturwissenschaften
Fachbereich Physik der Universität Hamburg

vorgelegt von

Lisa Zeune

aus Wuppertal, Deutschland

Hamburg
2014

Tag der Disputation: 14. April 2014

Folgende Gutachter empfehlen

die Annahme der Dissertation: Prof. Dr. Georg Weiglein
Prof. Dr. Jochen Bartels
Prof. Dr. Geneviève Bélanger

Zusammenfassung

In dieser Arbeit beschäftigen wir uns mit komplementären Methoden, um supersymmetrische (SUSY) Modelle unter Benutzung von verschiedenen experimentellen Ergebnissen zu testen und den SUSY-Parameterraum einzugrenzen. In der direkten Suche nach SUSY-Teilchen konnte bisher noch kein Signal nachgewiesen werden. Dies führt zu Grenzen an den SUSY-Parameterraum. Durch genaue Messungen der Eigenschaften des Higgs Bosons, das am LHC entdeckt wurde, sowie durch die Messung der Masse des W Bosons (M_W) können weitere Eingrenzungen des Parameterraums bestimmt werden, die die Grenzen von direkten Suchen sinnvoll ergänzen. Diese Arbeit ist in drei Teile gegliedert: Im ersten Teil wird die nach derzeitigem Stand genaueste Vorhersage für M_W im Minimalen Supersymmetrischen Standardmodell (MSSM) mit komplexen Parametern sowie im Nichtminimalen Supersymmetrischen Standardmodell (NMSSM) gegeben. Die Vorhersage beinhaltet das vollständige Ein-Schleifen-Ergebnis und alle relevanten Standardmodell (SM)- und SUSY-artigen Korrekturen höherer Ordnung, die bisher bekannt sind. Anhand eines Scans über den MSSM-Parameterraum, bei dem die experimentellen Einschränkungen insbesondere durch das Higgs-Signal berücksichtigt werden, zeigen wir, dass die aktuellen Messwerte von M_W und der Top-Masse auf einen nicht verschwindenden SUSY Beitrag hindeuten. Anschließend werden die verschiedenen SUSY-Beiträge im Detail analysiert und die Unterschiede zwischen den M_W Vorhersagen im MSSM und im NMSSM diskutiert. Im zweiten Teil der Arbeit diskutieren wir unterschiedliche Interpretationen des Higgs-Signals in SUSY-Modellen. Die Eigenschaften des entdeckten Teilchens sind bisher mit den Vorhersagen des SM Higgs kompatibel, lassen jedoch auch weitere Interpretationen zu. So zeigen Scans über die relevanten Regionen der MSSM- und NMSSM-Parameteräume für den Zerfall eines Higgs Bosons mit einer Masse von 126 GeV in zwei Photonen, dass ein solches Signal in beiden Modellen sowohl als das leichteste als auch das zweitleichteste \mathcal{CP} -gerade Higgs interpretiert werden kann. Wir analysieren mögliche Mechanismen, die zu einer Erhöhung der Zerfallsrate in zwei Photonen im MSSM und im NMSSM führen. Wir untersuchen weiterhin, wie gut das MSSM die experimentellen Daten von Messungen der Higgs-Zerfallsraten, der Higgs-Masse und niederenergetischen Präzisionsobservablen beschreibt. Hierbei nehmen wir an, dass es sich bei dem Higgs-Signal entweder um das leichte oder um das schwere \mathcal{CP} -gerade MSSM Higgs handelt. Es wird deutlich, dass das MSSM eine gute Beschreibung dieser Daten liefert. Die Qualität der Beschreibung ist mit der des SM vergleichbar. Im dritten Teil der Arbeit beschreiben wir das Programm `FastLim` zur Berechnung von Grenzen an SUSY-Modelle, die sich aus direkten SUSY-Suchen am LHC ergeben. Die experimentellen Ergebnisse aus der direkten Suche nach SUSY-Teilchen werden typischerweise als Parameter-Grenzen in sehr vereinfachten Versionen der SUSY-Modelle (“Simplified Models”) präsentiert. Mit `FastLim` kann der Einfluss der experimentellen Ergebnisse auf realistischere SUSY-Modelle analysiert werden, ohne dass dazu Monte-Carlo Simulationen notwendig sind. Hierfür verwendet `FastLim` zuvor berechnete und tabellierte Werte für die experimentellen Effizienzen und die Wirkungsquerschnitte für die “Simplified Models”.

Abstract

We present various complementary possibilities to exploit experimental measurements in order to test and constrain supersymmetric (SUSY) models. Direct searches for SUSY particles have not resulted in any signal so far, and limits on the SUSY parameter space have been set. Measurements of the properties of the observed Higgs boson at ~ 126 GeV as well as of the W boson mass (M_W) can provide valuable indirect constraints, supplementing the ones from direct searches. This thesis is divided into three major parts: In the first part we present the currently most precise prediction for M_W in the Minimal Supersymmetric Standard Model (MSSM) with complex parameters and in the Next-to-Minimal Supersymmetric Standard Model (NMSSM). The evaluation includes the full one-loop result and all relevant available higher order corrections of Standard Model (SM) and SUSY type. We perform a detailed scan over the MSSM parameter space, taking into account the latest experimental results, including the observation of a Higgs signal. We find that the current measurements for M_W and the top quark mass (m_t) slightly favour a non-zero SUSY contribution. The impact of different SUSY sectors on the prediction of M_W as well as the size of the higher-order SUSY corrections are analysed both in the MSSM and the NMSSM. We investigate the genuine NMSSM contribution from the extended Higgs and neutralino sectors and highlight differences between the M_W predictions in the two SUSY models. In the second part of the thesis we discuss possible interpretations of the observed Higgs signal in SUSY models. The properties of the observed Higgs boson are compatible with the SM so far, but many other interpretations are also possible. Performing scans over the relevant parts of the MSSM and the NMSSM parameter spaces and applying relevant constraints from Higgs searches, flavour physics and electroweak measurements, we find that a Higgs boson at ~ 126 GeV, which decays into two photons, can in principle be interpreted as the lightest or the second lightest \mathcal{CP} -even Higgs in both models. We discuss mechanisms to enhance the two photon rate in the MSSM and the NMSSM. Within the framework of the MSSM, we fit the various Higgs decay rates as measured by the Large Hadron Collider (LHC) and the Tevatron experiments, including also low-energy observables, under the hypothesis that either the light or the heavy \mathcal{CP} -even Higgs boson corresponds the observed signal. We find an overall good quality of the fits. For the interpretation of the observed Higgs as the light \mathcal{CP} -even Higgs the fit quality in the MSSM is slightly better than in the SM. In the third part of this thesis we present a tool, called **Fastlim**, to calculate conservative limits on SUSY models from direct SUSY searches at the LHC. Experimentalists present their results from direct SUSY searches in simplified scenarios of more general models. The impact of their results on many other SUSY scenarios has not been investigated, so that the impact of the existing search limits on realistic SUSY scenarios is difficult to assess. Using **Fastlim** the results can be reinterpreted in other (less restricted) models without performing any Monte-Carlo event generation. The program reconstructs the visible cross section from pre-calculated efficiency and cross section tables for simplified event topologies. As an application of our tool we study the constraints from direct LHC searches on the parameter space of “natural” SUSY models.

List of publications

My research during the three years of my PhD resulted in the following publications:

1. R. Benbrik, M. Gomez Bock, S. Heinemeyer, O. Stål, G. Weiglein, and L. Zeune, *Confronting the MSSM and the NMSSM with the Discovery of a Signal in the two Photon Channel at the LHC*, Eur.Phys.J. C72 (2012) 2171, [arXiv:1207.1096].
2. P. Bechtle, S. Heinemeyer, O. Stål, T. Stefaniak, G. Weiglein, and L. Zeune, *MSSM Interpretations of the LHC Discovery: Light or Heavy Higgs?*, Eur.Phys.J. C73 (2013) 2354, [arXiv:1211.1955].
3. S. Heinemeyer, W. Hollik, G. Weiglein, and L. Zeune, *Implications of LHC search results on the W boson mass prediction in the MSSM*, JHEP 1312 (2013) 084, [arXiv:1311.1663].
4. M. Papucci, K. Sakurai, A. Weiler, and L. Zeune, *Fastlim: a fast LHC limit calculator*, [arXiv:1402.0492].

Furthermore, the following work is in preparation:

5. O. Stål, G. Weiglein, and L. Zeune, *Precise prediction for the W boson mass in the NMSSM*

Eidesstattliche Versicherung

Hiermit erkläre ich an Eides statt, dass ich die vorliegende Dissertationsschrift selbst verfasst und keine anderen als die angegebenen Quellen und Hilfsmittel benutzt habe.

Hamburg, den 24.03.2014

Lisa Zeune

Acknowledgements

This dissertation would not have been possible without the people that supported and encouraged me over the last years. I want to take this opportunity to thank the people which made this work possible.

Special thanks goes to my supervisor Georg Weiglein, for his guidance, his support and many valuable advices. I am happy that he encouraged me and gave me the possibility to work on different, interesting projects. I am grateful to Gudrid Moortgat-Pick for her kind support and for refereeing my dissertation. For refereeing my disputation, I want to thank Jörn Kersten. Many thanks go to Sven Heinemeyer for very many helpful discussions and for providing all the different versions of our $M_W - m_t$ plot. It is a pleasure to thank Oscar Stål for his support and understanding and for all he has taught me over the years. I am very grateful to Kazuki Sakurai for helping me understand many new things and patiently answering my questions. For many fruitful discussions and useful suggestions I also want to thank my collaborators Philip Bechtle, Rachid Benbrik, Melina Gomez Bock, Wolfgang Hollik, Michele Papucci, Tim Stefaniak and Andreas Weiler. I am grateful to Florian Domingo, Peter Drechsel, Ayres Freitas, Thomas Hahn, Ashutosh Kotwal, Stefan Prestel, Marco Tonini and Doreen Wackerroth for helpful discussions. At this point I am also happy to thank Arnulf Quadt, Johan Rathsman and Gunnar Ingelman for their support during the time before I started my PhD. Many thanks to Florian Domingo, Oscar Stål, Kazuki Sakurai, Stefan Liebler, Tomas Kasemets and Sophie Zeune for reading parts of the draft of this thesis and providing useful comments.

I want to thank all people in the DESY theory group, especially the people in building 1b (and the former buiding 6) for providing a very open, friendly and inspiring atmosphere. Special thanks to Frank for his support and many good advices. There are many people which I want to thank both for helping me out sometimes and for good times at work and outside — thank you Sara, Aoife, Andreas, Oscar, Moritz, Julia, Peter, Florian, Frank, Jo, Andrew, Max, Stefan, Marco, Shireen and everyone I forgot.

Finally I want to thank my family and my friends that are always there for me, keep my mind off work and cheer me up when needed. Special thanks to Johanna for many great times together and just for being a good friend. Probably I would not have survived the last month without Iris and Robert providing me with food - thank you. For understanding me, cheering me up, making me happy and sometimes angry, for loving me and supporting me, I thank Leo, Sophie and my parents. I also thank the two Stefans for being a good addition to our family. Finally I want to thank Tomas for believing in me, sometimes more than myself, for always encouraging me to do my best and for 31 wonderful letters. But especially for making me happy every day.

Contents

1	Introduction	1
2	The Standard Model and supersymmetric extensions of it	5
2.1	The Standard Model	5
2.1.1	Symmetries	6
2.1.2	Electroweak theory and the BEH mechanism in the SM	7
2.1.3	Fermion sector	8
2.1.4	Gauge fixing, ghost sector	9
2.1.5	Full SM Lagrangian	10
2.1.6	Shortcomings of the SM	10
2.2	The Minimal Supersymmetric Standard Model	12
2.2.1	Concepts of the supersymmetric models	12
2.2.2	The MSSM superpotential	14
2.2.3	R-parity	15
2.2.4	SUSY breaking	16
2.2.5	Constrained models: CMSSM and pMSSM	16
2.2.6	Sfermion sector	18
2.2.7	Chargino sector	19
2.2.8	Neutralino sector	19
2.2.9	Gluino sector	20
2.2.10	Electroweak symmetry breaking and the MSSM Higgs sector	20
2.3	The Next to Minimal Supersymmetric Standard Model	23
2.3.1	Motivation	23
2.3.2	The NMSSM superpotential and soft breaking terms	23
2.3.3	Higgs sector of the NMSSM	24
2.3.4	Neutralino sector of the NMSSM	25
2.3.5	MSSM and decoupling limit	26
3	Perturbative calculations	27
3.1	Introduction	27
3.2	The concepts of regularization and renormalization	27
3.2.1	On-shell renormalization scheme	29
3.2.2	Self-energies	30

3.2.3	$\overline{\text{MS}}$ renormalization scheme, renormalization group equations and implications for QCD	31
4	Experimental status	33
4.1	Collider experiments	33
4.2	Experimental results	36
4.2.1	Discovery of a Higgs boson	36
4.2.2	Searches for SUSY Higgs bosons	38
4.2.3	Direct SUSY searches	40
4.2.4	Precision measurements: M_W and m_t	40
4.2.5	B -physics observables and $(g - 2)_\mu$	42
5	The W boson mass in the SM, the MSSM and the NMSSM	43
5.1	Introduction	43
5.2	Determination of the W boson mass	46
5.3	Calculation of Δr	48
5.3.1	One-loop formula for Δr	48
5.3.2	One-loop Δr in the SM	49
5.3.3	One-loop Δr in the MSSM and the NMSSM	50
5.3.4	Incorporation of higher-order corrections to Δr	53
5.4	Technical aspects	58
5.4.1	Framework for the Δr calculation	58
5.4.2	Framework for the numerical analysis	59
5.4.3	Constraints on the parameter space	60
5.4.4	<code>FeynArts</code> model file for the NMSSM	62
5.5	Theoretical uncertainties in the M_W prediction	64
5.6	Result for M_W in the SM	65
5.7	Result for M_W in the MSSM	66
5.7.1	MSSM parameter scan: Scan ranges and constraints	66
5.7.2	Results of the scan and impact of LHC results on M_W in the MSSM	68
5.7.3	Discussion of future scenarios	76
5.7.4	Dependence of the M_W prediction on complex phases	79
5.8	Results for the M_W prediction in the NMSSM	82
5.8.1	Sfermion sector one-loop contributions	82
5.8.2	Effect of SUSY two-loop corrections	88
5.8.3	NMSSM Higgs sector contributions	90
5.8.4	Neutralino sector contributions	97
5.9	Summary	104
6	The diphoton decay channel in the MSSM and the NMSSM	107
6.1	Introduction	107
6.2	Framework of our analysis	109
6.2.1	General considerations	109
6.2.2	Computational framework	110

6.2.3	Constraints on the parameter space	111
6.3	Numerical analysis	113
6.3.1	Decays of \mathcal{CP} -even Higgs bosons in the MSSM	113
6.3.2	Decays of \mathcal{CP} -even Higgs bosons in the NMSSM	119
6.4	Summary	126
7	Fitting the MSSM to the observed Higgs signal	129
7.1	Motivation	129
7.2	Framework for our analysis	131
7.2.1	pMSSM parameter scans	131
7.2.2	Constraints on the parameter space	133
7.2.3	χ^2 fits	133
7.3	Results	138
7.4	Summary	160
8	Constraining SUSY scenarios using simplified models	163
8.1	Introduction	163
8.2	Methodology	165
8.2.1	The traditional “recasting” approach	165
8.2.2	A new approach to calculate the visible cross section	166
8.3	Functionality of the program <code>Fastlim</code>	168
8.3.1	The calculational procedure	168
8.3.2	Nomenclature of the event topologies	169
8.3.3	Further approximations	170
8.4	<code>Fastlim</code> version 1.0	172
8.4.1	The available analyses	172
8.4.2	The implemented event topologies	172
8.5	Constraints from direct searches on “natural” SUSY models	175
8.6	Summary and future plans	183
9	Conclusions	185

Chapter 1

Introduction

The spectacular discovery of a Higgs boson at the LHC in July 2012 [1,2] marked a milestone of an effort that has been ongoing for several decades. The existence of a Higgs boson as consequence of electroweak symmetry breaking, a mechanism to give mass to the electroweak gauge bosons, was postulated already in 1964 by François Englert and Robert Brout [3] and shortly after by Peter Higgs [4,5]¹. In October 2013, the LHC results had been confirmed by more data, constituting convincing experimental evidence of a Higgs boson with a mass around 126 GeV, and the Swedish Royal Academy of Science awarded the Nobel Prize in Physics to François Englert and Peter Higgs for the theoretical formulation of the BEH (Brout-Englert-Higgs) mechanism. The properties of the discovered particle are so far compatible with the Higgs boson predicted by the Standard Model of particle physics [7–9], a well-tested theory describing the electroweak and strong interactions. Despite its remarkable success, there are several experimental observations and theoretical shortcomings demonstrating that the Standard Model cannot be the complete theory of nature but must be embedded in a more fundamental theory. Among the most promising extensions of the SM are models based on Supersymmetry, a hypothetical symmetry of nature connecting fermions and bosons [10–15]. Supersymmetry is theoretically very appealing, as it is the only possible extension of the spacetime symmetries, which particle physics builds on [16]. Many of the shortcomings of the SM are addressed in supersymmetric models: The new particles predicted in SUSY theories cause a cancellation of the quadratic divergencies in the Higgs sector, solving the hierarchy problem of the SM. Furthermore supersymmetric models predict the unification of the electroweak and the strong force at a high energy scale and provide a candidate which can explain the dark matter in the universe. Well-studied SUSY models are the MSSM (Minimal Supersymmetric Standard Model) and its extension, the NMSSM (Next-to-minimal Supersymmetric Standard Model). There are two complementary methods — direct and indirect ones — to probe physics beyond the SM (also called new physics), such as Supersymmetry, at the LHC and other future collider experiments. Direct methods attempt to observe traces in the detectors arising from

¹This idea was also discussed in an article by Gerald Guralnik, Carl R. Hagen and Tom Kibble [6] later that year, and other activities in this direction were ongoing around that time.

of the production of particles of new physics models, while indirect methods look for the quantum effects induced by those particles. As long as no signs of new physics are seen, both methods can be used to set constraints on the parameter space of new physics models. Extensive direct searches for particles predicted in SUSY models are carried out by the LHC experiments ATLAS and CMS, but so far have not resulted in a signal, and limits on the masses of supersymmetric particles have been set. Even if not yet seen directly, signs of physics beyond the SM may show up indirectly as small deviations between precise measurements and SM predictions. Electroweak precision observables are highly sensitive to quantum corrections of new physics (i.e. to loop contributions involving in principle all the particles of the considered model) and can be measured with high precision. Thus, they provide the possibility to test the SM, to distinguish between different extensions, and to derive indirect constraints on the parameters of a model, such as the masses of the predicted particles. This input can be of great interest regarding the direct searches for those particles. The strength of this method has been demonstrated for instance with the discovery of the top quark with a measured mass in remarkable agreement with the indirect prediction [17, 18]. Even the virtual effects of particles which are too heavy for a direct detection at the LHC may be detected indirectly in this way. In case SUSY particles are found in direct searches at the LHC, electroweak precision observables can provide an important cross-check, can help to understand the nature of the observed particles and may further give valuable indications for the search of additional particles.

The discovered Higgs boson plays a special role in the search for new physics. Contrary to the SM, two Higgs doublets are needed in SUSY models to give mass to up- and down-type fermions. The extended Higgs sector entails the existence of at least five scalar bosons. While being in agreement with the SM so far, the observed Higgs boson can also be interpreted in a variety of models beyond the SM, e.g. as one of the Higgs bosons in the MSSM or the NMSSM, and it is a prime goal of the particle physics community in the upcoming years to reveal the nature of the discovered Higgs boson. In the Higgs sector, new physics may manifest itself indirectly in the form of deviations of the Higgs decay or production rates with respect to the SM prediction. It is therefore particularly important to measure on the one hand the rates of the observed Higgs boson very precisely and on the other hand continue the direct search for additional (non SM-like) Higgs bosons.

The LHC will start running again next year with almost twice its previous energy and increased luminosity. Another major particle physics project, the International Linear Collider (ILC), has been put forward, and Japan has emphasized its interest in hosting it. The ILC is especially suited for precision measurements and could supplement the LHC in order to maximise the gain for exploring the fundamental laws of nature. It is of central importance to exploit the various complementary possibilities provided by direct and indirect methods, to fully exhaust the data and to efficiently test and constrain new physics models. In this thesis we will focus on supersymmetric models (more precisely the MSSM and the NMSSM) and we will study the constraints on the parameter spaces of these models arising from electroweak precision observables, Higgs physics and direct

searches.

The thesis is organized as follows:

Chapter 2 provides the theoretical background and sets the notations needed for our work presented in the later chapters. We start with a theoretical introduction to the SM of particle physics. We outline some shortcomings of the SM, before we turn to the discussion of SUSY models. Supersymmetry is motivated and introduced, followed by a detailed description of the particle sectors of the MSSM. Then we go to NMSSM and show how the Higgs and neutralino sectors are modified compared to the MSSM.

In order to obtain precise theoretical predictions for observables in the SM or its extensions, which can be compared to other models and to experimental data, loop diagrams need to be calculated. **Chapter 3** introduces the basic concepts of regularization and renormalization needed for loop calculations.

Chapter 4 is dedicated to the current status of the results from collider experiments. After going through some general aspects of collider physics, we briefly summarize the up-to-date experimental results that are most relevant in the context of this thesis. The experimental results are of utmost importance for our work, which focuses on confronting the predictions in different models with present and possible future experimental results.

Chapters 5 to 8 constitute the centrepiece of this thesis, describing our research projects. In the context of electroweak precision observables the W boson mass, being highly sensitive to loop corrections of new physics, plays a crucial role. The accuracy of the measurement of M_W has been significantly improved over the last years (particularly by the Tevatron results) and further improvement of the experimental accuracy is expected from future LHC and ILC measurements. In order to fully exploit the precise experimental determination, an accurate theoretical prediction for M_W in models beyond the SM is of central importance. In **Chapter 5** we present the currently most precise prediction of the W boson mass in the MSSM with complex parameters and in the NMSSM, including the full one-loop result and the relevant available higher order corrections of SM and SUSY type. The evaluation of M_W is performed in a very flexible framework, which facilitates the extension to other models beyond the SM. The size of the contribution of the various SUSY sectors in both models is studied in detail. Performing a detailed parameter scan in the MSSM, we investigate the impact of limits from direct SUSY searches as well as from the Higgs discovery on the W boson mass prediction in the MSSM. Assuming hypothetical future scenarios, we discuss the impact of the W boson mass prediction on the MSSM parameter space. A significant part of this chapter concerns the discussion of genuine NMSSM contributions to M_W .

Constraints on the parameter spaces of the MSSM and the NMSSM from experimental Higgs sector results are analysed in Chapters 6 and 7. At the time when the Higgs boson discovery was announced, the two photon decay rate was significantly above the SM expectation [1, 2]². In **Chapter 6** we confront the MSSM and the NMSSM with

²The latest ATLAS result shows still an enhancement of the two photon rate [19], while the value measured by CMS went down when more data was included and is now slightly below the SM rate [20].

the discovery of a Higgs boson decaying into two photons. In particular we discuss the possibilities in both SUSY models to accommodate a Higgs at ~ 126 GeV with a two-photon rate enhanced with respect to the SM — taking into account constraints from direct Higgs searches, flavour physics, electroweak measurements as well as theoretical considerations. We discuss in detail how an enhanced two photon rate can be realised in the MSSM, and which additional mechanisms for an enhancement occur in the NMSSM.

While not being statistically significant at present, the measurements of the Higgs decay rates show some deviations from the SM predictions. In order to investigate whether, and if so how much, the MSSM can improve the theoretical description of the experimental data compared to the SM, we fit the experimentally measured Higgs decay rates, the Higgs mass and low-energy observables under the hypothesis that the light or the heavy \mathcal{CP} -even Higgs of the MSSM is the observed state at ~ 126 GeV. This study is presented in **Chapter 7**. The fit quality in the MSSM, for both Higgs interpretations, is compared to the SM. We determine the regions of the MSSM parameter space which are favoured by the experimental data, and we demonstrate some features of the best-fit point.

The experimental results of direct SUSY searches are typically presented as limits in simplified versions of the full SUSY models, with only a few parameters. The reinterpretation of the results in the context of other models is in principle possible, however time-consuming and computationally very intensive. **Chapter 8** presents a new computer tool, called **Fastlim**, which facilitates and speeds up the calculation of limits on the parameter space of new physics models from direct LHC searches. We explain in detail how the program works. Further we present a first application of **Fastlim**, where we study the constraints from LHC searches for SUSY particles on the parameter space of so called “natural” SUSY models, a class of SUSY models where the particles closely tied to the Higgs boson mass are relatively light, while the rest of the particle spectrum is assumed to be beyond the reach of the LHC.

Finally, in **Chapter 9** we summarize our results and conclude.

The results presented in this thesis are based on several coauthored works, listed in the List of Publications.

Chapter 2

The Standard Model and supersymmetric extensions of it

This chapter provides an introduction to the theoretical models used for my own work described in the later chapters (chapters 5 to 8). The resources I used for this chapter are Refs. [21–33]. Parts of this introductory chapter are based on text which I have written before and that appeared in Refs. [34, 35].

2.1 The Standard Model

The Higgs boson was for a long time the last missing piece predicted by the Standard Model of particle physics. This gap was filled by the spectacular discovery of a particle at the LHC in July 2012 with properties compatible with the SM Higgs boson.

The Standard Model of particle physics [7–9] is a theory formulated (in its current version) in the 1970s, which describes all fundamental particles which make up for the visible matter in the universe and the interactions between them, apart from gravity. It is a quantum field theory (QFT) that exhibits translation invariance and Lorentz invariance, two global symmetries following from special relativity. These global symmetries define the Poincaré group. Further the SM is locally gauge invariant under the gauge group $SU(3)_C \otimes SU(2)_L \otimes U(1)_Y$ ¹. The SM gauge group is split into two parts: Quantum Chromo Dynamics (QCD) and the quantum theory of electroweak interactions. QCD is the theory of strong interactions, described by the $SU(3)_C$ gauge group of colour. The electroweak theory is based on $SU(2)_L \otimes U(1)_Y$. The existence of massive fields implies that the electroweak gauge group must be broken. The breaking is described by the BEH mechanism, which entails the existence of a Higgs boson.

In this section we will outline the symmetries of the SM, the concept of electroweak symmetry breaking and the particle sectors of the SM. The last part of this section discusses the shortcomings of the SM, motivating the study of 'new physics' models.

¹The subscripts refer to colour, left chirality and weak hypercharge.

2.1.1 Symmetries

The kinetic terms of the SM fields are fully determined by the global symmetry assuring translation invariance and invariance under Lorentz transformations. The SM fields are classified into fermionic (spin 1/2) fields, bosonic (spin 1) fields and a scalar boson (spin 0) field. Fermions account for the (visible) matter of the universe, spin 1 bosons carry the forces between them. The special role of the scalar will be discussed in Sect. 2.1.2. The possible kinetic terms for Dirac fermions ψ and vector bosons A_μ^a are

$$\begin{aligned}\mathcal{L}_{\text{kin}} &= \mathcal{L}_{\text{kin}}^{\text{fermion}} + \mathcal{L}_{\text{kin}}^{\text{vector}} \\ &= \bar{\psi} i \not{\partial} \psi - \frac{1}{4} F_{\mu\nu}^a F^{\mu\nu a}\end{aligned}\quad (2.1)$$

with $\bar{\psi} = \psi^\dagger \gamma^0$ and $\not{\partial} = \gamma^\mu \partial_\mu$. The field strength tensor is

$$F_{\mu\nu}^a = \partial_\mu A_\nu^a - \partial_\nu A_\mu^a + g f^{abc} A_\mu^b A_\nu^c. \quad (2.2)$$

Here g denotes the gauge coupling of a gauge group with generators T^a , where $[T^a, T^b] = i f^{abc} T^c$ defines the structure constants f^{abc} .

The interactions of the SM fields are given by the gauge group $SU(3)_C \otimes SU(2)_L \otimes U(1)_Y$. Demanding local gauge invariance, the derivatives in the kinetic terms must be replaced by the covariant derivatives, leading to a coupling of the vector fields to fermions and scalars. For a general gauge theory the covariant derivative is $D_\mu = \partial_\mu - ig T^a A_\mu^a$. For the SM gauge group the derivatives in Eq. (2.1) are replaced by²

$$\partial_\mu \rightarrow D_\mu = \partial_\mu - ig_2 I^a W_\mu^a - ig_1 \frac{Y}{2} B_\mu - ig_s \frac{\lambda^a}{2} g_\mu^a. \quad (2.3)$$

Here g_2 , g_1 and g_s are the coupling constants of $SU(2)_L$, $U(1)_Y$ and $SU(3)_C$. We define $\alpha_s = g_s^2/4\pi$ for the strong $SU(3)_C$ interactions and

$$e = \frac{g_1 g_2}{\sqrt{g_1^2 + g_2^2}}, \quad \alpha = \frac{e^2}{4\pi} \quad (2.4)$$

for the electroweak $SU(2)_L \otimes U(1)_Y$ interactions. The generators of $SU(2)_L$ are $I^a = \sigma^a/2$ (where σ^a are the Pauli matrices), defining the weak isospin I^3 of a field. The generator of $U(1)_Y$ is $Y/2$ defining the hypercharge, and the generators of $SU(3)_C$ are $\lambda^a/2$ (λ^a are the Gell-Mann matrices) defining the colour charge. The gauge bosons of $SU(2)_L$, $U(1)_Y$ and $SU(3)_C$ are W^a ($a = 1, 2, 3$), B and g^a ($a = 1 \dots 8$). The gauge bosons g^a of QCD are called gluons.

²We adopt the sign conventions for the $SU(2)_L$ covariant derivative used in the code `FeynArts` [36–41], where (for historical reasons) the $SU(2)_L$ covariant derivative in the SM is defined by $\partial_\mu - ig_2 I^a W_\mu^a$ (as in Eq. (2.3)), while it is defined by $\partial_\mu + ig_2 I^a W_\mu^a$ in the (N)MSSM, as we will discuss later.

2.1.2 Electroweak theory and the BEH mechanism in the SM

It is impossible to write down gauge-invariant explicit mass terms for vector boson fields. However among the electroweak gauge bosons only the photon is massless³, while the other electroweak gauge bosons are massive, so the $SU(2)_L \otimes U(1)_Y$ gauge symmetry must be broken down to $U(1)_{\text{em}}$. The breaking is accomplished via the BEH mechanism, which, furthermore, is also responsible for the generation of fermion masses. In this framework, gauge boson masses are obtained by adding additional terms

$$\mathcal{L}_{\text{Higgs}} = (D_\mu \phi)^\dagger (D^\mu \phi) - V_H^{\text{SM}} \quad (2.5)$$

to the Lagrangian of the electroweak SM. The scalar Higgs field ϕ is a $SU(2)_L$ doublet with hypercharge $Y = 1$.

Requiring gauge invariance and renormalizability, the potential can be written as

$$V_H^{\text{SM}} = -\mu^2 |\phi|^2 + \frac{\lambda}{4} |\phi|^4, \quad (2.6)$$

where λ must be positive, so that the potential is bounded from below. One chooses $\mu^2 > 0$, such that the potential is minimised at $|\langle \phi \rangle|^2 = 2\mu^2/\lambda \equiv v^2/2$, where v is the (non-zero) vacuum expectation value (vev)⁴. One specific minimum is conventionally chosen as

$$\langle \phi \rangle = \frac{1}{\sqrt{2}} \begin{pmatrix} 0 \\ v \end{pmatrix}. \quad (2.7)$$

This ground state does not reflect the symmetry of the potential anymore. This feature is termed spontaneous symmetry breaking. Expanding around the minimum, the full Higgs field can be written as

$$\phi = \frac{1}{\sqrt{2}} \begin{pmatrix} G^+ \\ v + H + iG^0 \end{pmatrix}. \quad (2.8)$$

From the four degrees of freedom, the three unphysical fields, $G^\pm = G_1^\pm \pm iG_2^\pm$ and G , (called Goldstone bosons) can be absorbed in a suitable gauge transformation. The gauge in which the Goldstone bosons are absent is called unitary gauge.

Expanding the kinetic term $(D_\mu \phi)^\dagger (D^\mu \phi)$ of Eq. (2.5) around the minimum of the Higgs doublet, masses are generated for the fields

$$W^\pm = \frac{1}{\sqrt{2}} (W^1 \mp iW^2), \quad (2.9)$$

called (charged) W bosons and for the neutral Z boson

$$\begin{pmatrix} Z \\ A \end{pmatrix} = \begin{pmatrix} c_W & s_W \\ -s_W & c_W \end{pmatrix} \begin{pmatrix} W^3 \\ B \end{pmatrix}, \quad (2.10)$$

³In the strong sector the gluons of $SU(3)_C$ are also massless.

⁴Note that the vev v of the SM Higgs field differs from the value v which we will define in the MSSM (in Eq. (2.58)) using a different convention. The numerical value here is $v \sim 246$ GeV.

while the photon A remains massless. Here s_W and c_W are the sine and cosine of the weak mixing angle, which at tree level are given by

$$s_W \equiv \sin \Theta_W = \frac{g_1}{\sqrt{g_1^2 + g_2^2}} \quad , \quad c_W \equiv \cos \Theta_W = \frac{g_2}{\sqrt{g_1^2 + g_2^2}}. \quad (2.11)$$

The generated masses are

$$M_W = c_W M_Z = \frac{1}{2} g_2 v \quad , \quad M_A = 0. \quad (2.12)$$

The photon is the mediator of the electromagnetic interaction and remains massless. All charged particles are subject to the electromagnetic interaction. The weak interaction is carried by the charged gauge bosons W^\pm and the neutral gauge boson Z . The neutral interaction involves all (left- and right-handed) fermions, while W^\pm couples only to left-handed fermions.

The remaining real degree of freedom in Eq. (2.8) is the only physical scalar field—the Higgs boson, H . The mass of the Higgs boson can be written as $M_H^2 = 2\mu^2$. However since μ^2 is arbitrary, M_H is a free parameter in the SM that must be determined by experiment. Later we shall call the SM Higgs H^{SM} to avoid confusion when we simultaneously talk about the SM and extensions with several Higgs bosons.

2.1.3 Fermion sector

The fermions in the SM consist of leptons and quarks. Leptons are not charged under $SU(3)_C$ while quarks carry colour. While leptons exist as free particles, quarks are always bound inside hadrons, such as protons and neutrons. The fermions can be ordered into three ($i = 1, 2, 3$) generations or families, which are identical with respect to the quantum numbers of their contents and differ only by the mass of the particles. The fermions building $SU(2)_L$ doublets ($l_{i,L}$ for leptons and $q_{i,L}$ for quarks) are called left-handed, while the fermions building $SU(2)_L$ singlets ($e_{i,R}$ for leptons, $u_{i,R}$ for up-type quarks, $d_{i,R}$ for down-type quarks) are right-handed.

An explicit Dirac-type fermion mass term in the Lagrangian would not preserve gauge invariance. Fermion masses are generated by so called Yukawa couplings of the Higgs field to the fermion fields which can be written as

$$\mathcal{L}_{\text{Yukawa}} = - (\bar{q}_L \mathbf{Y}_u \phi^C u_R + \bar{q}_L \mathbf{Y}_d \phi d_R + \bar{l}_L \mathbf{Y}_l \phi e_R + h.c.) \quad (2.13)$$

where $\phi^C = i\sigma_2 \phi^*$ is the charge conjugated Higgs field (note that the same Higgs doublet is used to give mass to up-type and down-type fermions), q_L , l_L , u_R , d_R , e_R are 3-component vectors in family space, and \mathbf{y}_u , \mathbf{y}_d and \mathbf{y}_l are the 3×3 Yukawa coupling matrices.

There are no right-handed neutrinos in the SM (in its established form) and the neutrinos remain massless in the SM⁵.

⁵The evidence of neutrino oscillation (see e.g. [42]) implies that neutrinos are (against the original assumption) massive. Introducing right handed neutrinos, Dirac mass terms can easily be added. Another possibility is to write down Majorana mass terms. In this thesis neutrinos can be assumed to be massless.

Replacing the Higgs field by its vacuum expectation value, one finds the lepton mass matrix (which can be diagonalised)

$$\mathbf{m}_l = \frac{v}{\sqrt{2}} \mathbf{y}_l . \quad (2.14)$$

The mass eigenstates of the quarks are obtained by unitary transformations on the quark fields; the diagonalised mass matrices for up- and down type fermions read

$$\mathbf{m}_u = \frac{v}{\sqrt{2}} (U_L^U)^\dagger \mathbf{y}_u U_R^U , \quad \mathbf{m}_d = \frac{v}{\sqrt{2}} (U_L^D)^\dagger \mathbf{y}_d U_R^D . \quad (2.15)$$

The product

$$V_{\text{CKM}} = (U_L^U)^\dagger U_L^D \quad (2.16)$$

is referred to as the Cabibbo-Kobayashi-Maskawa (CKM) matrix. A complex phase in the quark mixing matrix provides the only source of \mathcal{CP} -violation in the SM.

2.1.4 Gauge fixing, ghost sector

The quantisation of the SM, requires the insertion of additional, gauge fixing, terms in the Lagrangian. Using a renormalizable 't Hooft gauge the gauge fixing term is

$$\mathcal{L}_{\text{fix}} = -\frac{1}{2} \left[(F^A)^2 + (F^Z)^2 + 2F^{W^+} F^{W^-} \right] , \quad (2.17)$$

with

$$\begin{aligned} F^{W^\pm} &= (\xi_1^W)^{-\frac{1}{2}} \partial^\mu W_\mu^\pm \mp i M_W (\xi_2^W)^{\frac{1}{2}} G^\pm \\ F^Z &= (\xi_1^Z)^{-\frac{1}{2}} \partial^\mu Z_\mu - M_Z (\xi_2^Z)^{\frac{1}{2}} G^0 \\ F^A &= (\xi_1^A)^{-\frac{1}{2}} \partial^\mu A_\mu . \end{aligned} \quad (2.18)$$

Here $\xi_1^W, \xi_2^W, \xi_1^Z, \xi_2^Z$ and ξ_1^A are five gauge parameters. The parameters ξ_i^α can be chosen freely, since in the end the physical observables must be independent of the gauge fixing. In most parts of this work (if not stated otherwise) the particularly simple Feynman-'t Hooft gauge is chosen, where all ξ_i^α are set equal to 1.

In this formulation non-physical contributions appear, which must be canceled. This cancellation is achieved by introducing the so called Faddeev-Popov ghost $u^\alpha(x)$ and antighost $\bar{u}^\alpha(x)$ fields ($\alpha = W^\pm, A, Z$). Ghosts are unphysical mathematical entities, which do not correspond to 'real' external particles and only appear as virtual particles within loops . The additional Faddeev-Popov term in the Lagrangian is

$$\mathcal{L}_{\text{ghost}} = \sum_{\alpha, \beta=W^\pm, A, Z} \bar{u}^\alpha(x) \frac{\delta F^\alpha}{\delta \theta^\beta(x)} u^\beta(x). \quad (2.19)$$

where the θ^α denote infinitesimal gauge transformations and $\delta F^\alpha / \delta \theta^\beta$ are variations of the gauge fixing operators F^α ($\alpha = W^\pm, A, Z$) under θ^α . In the Feynman-'t Hooft gauge each ghost field acquires the same mass parameter as its associated gauge boson field. Also the Goldstone bosons acquire a non-zero mass parameter in this gauge and must be included in our calculations.

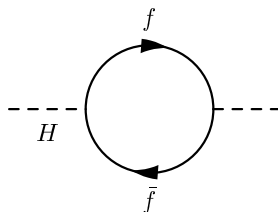


Figure 2.1: Fermion loop diagram which leads to quadratic divergent corrections to the Higgs mass.

2.1.5 Full SM Lagrangian

The full Lagrangian density of the SM is

$$\mathcal{L}_{\text{SM}} = \mathcal{L}_{\text{kin}} + \mathcal{L}_{\text{Higgs}} + \mathcal{L}_{\text{Yukawa}} + \mathcal{L}_{\text{fix}} + \mathcal{L}_{\text{ghost}} \quad (2.20)$$

where in the term \mathcal{L}_{kin} the kinetic term is written down for $\psi = l_{i,L}, e_{i,R}, q_{i,L}, u_{i,R}, d_{i,R}$ ($i = 1, 2, 3$) and $A_\mu^a = W^a$ ($a = 1, 2, 3$), B, g^a ($a = 1 \dots 8$). The derivative in Eq. (2.1) is replaced by the covariant derivative of Eq. (2.3).

2.1.6 Shortcomings of the SM

The Standard Model of particle physics is a very successful theory describing most experimental measurements with high precision. However there are some observations and theoretical shortcomings indicting that the SM cannot be the complete description of elementary particle physics but needs to be embedded in a more complete theory. Some shortcomings of the SM are outlined in the following.

As a start the gravitational force which has profound implications for our everyday lives cannot be described within the SM. Quantum gravitational effects are expected to become relevant only at very high scales ($M_{\text{Planck}} = 10^{19}$ GeV) and therefore are expected to have hardly any impact on particle physics phenomenology. Nevertheless the failure of the SM to include a description of gravity clearly indicates that the SM cannot be an exhaustive theory of nature: It is known to fail (at the latest) at the Planck scale where quantum gravitational effects become important, which implies that the SM must be an effective theory which can be valid only up to a cutoff scale Λ , at which new physics appears.

This has drastic implications for the stability of the Higgs mass. In the SM the Higgs mass is a free parameter, while one might expect that, in a more fundamental theory, the Higgs mass value can be predicted. Quantum level effects affect the Higgs mass and must be included in the calculation of the Higgs mass value giving a correction term ΔM_H^2 , thus

$$M_H^2 = M_{H,0}^2 + \Delta M_H^2. \quad (2.21)$$

Diagrams such as the one depicted in Fig. 2.1 (showing the one-loop correction from a fermion loop) contribute to ΔM_H^2 . Calculating this diagram and cutting off the integral

at the new-physics scale Λ yields a correction term to the Higgs mass

$$\Delta M_H^2 = -\frac{y_f^2}{8\pi^2}\Lambda^2 + \dots . \quad (2.22)$$

The ellipsis denote terms that grow at most logarithmically with Λ . This means that for $\Lambda = M_{\text{Planck}}$ the corrections to the Higgs mass are of the size $\Delta M_H^2 \approx 10^{38} \text{ GeV}^2$. On the other hand we have observed a Higgs boson at 126 GeV. To get $M_H \sim 126 \text{ GeV}$, an immense cancellation between the ΔM_H^2 correction and $M_{H,0}^2$ is necessary (extreme 'fine-tuning'). This seems very unnatural and is known as the Hierarchy Problem.

There is another theoretical unaesthetic feature of the SM: The SM gauge group is not simple, so that the cancellation of gauge anomalies is accidental and the existence of electric charges in fractional amounts is not explained. Another shortcoming (mentioned earlier) is the observation of non-zero neutrino masses, which are not described in the SM in its current form. Further the hierarchy of the fermion masses ($5 \times 10^{-4} \rightarrow 10^2 \text{ GeV}$) remains unexplained in the SM ('Flavour imbalance').

Many astrophysical observations have shown evidence that more gravitationally interacting matter (so called dark matter) than the visible baryonic matter must exist in the universe. Recent results reveal that the largest part ($\sim 68.3\%$) of the total energy in the universe consists of so called dark energy, while dark matter accounts for $\sim 26.8\%$ [43, 44]. Neither dark energy nor dark matter can be explained within the SM. If dark matter consists of elementary particles, these can at most interact weakly with other particles and they have to be stable over cosmological timescales. Another observation is the baryon asymmetry in the universe [43, 45]. This discrepancy cannot be explained by just the \mathcal{CP} -violation from the CKM phase in the SM alone and indicates that further sources of \mathcal{CP} -violation beyond the SM must exist.

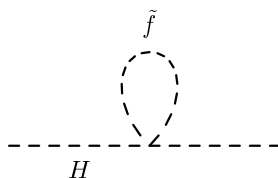


Figure 2.2: Sfermion loop diagram which leads to quadratic divergent corrections to the Higgs mass.

2.2 The Minimal Supersymmetric Standard Model

Supersymmetry (SUSY) is an attractive and popular guideline to extend the SM. Some of the shortcomings of the SM mentioned in the previous section are addressed in supersymmetric models. It is a natural extension of the space-time symmetry of the SM which relates fermionic and bosonic degrees of freedom. In the Minimal Supersymmetric Standard Model (MSSM) the global symmetries of the SM are minimally extended while the local gauge symmetries remain unchanged. In this section we will introduce and motivate weak scale supersymmetry and its minimal realisation, the MSSM. I will discuss how the shortcomings of the SM are addressed in the MSSM. Further I will introduce the particle content of the MSSM and set the notation for later chapters.

2.2.1 Concepts of the supersymmetric models

Possible extensions of the Poincaré group are highly restricted by the Haag-Lopuszański-Sohnius theorem [16] stating that (in 4-dimensional QFT) the Poincaré group can only (non trivially) be extended by (N) fermionic operators. The generator of ($N = 1$) supersymmetry is a fermionic operator Q which converts a bosonic state into a fermionic state and vice versa: $Q|\text{boson}\rangle = |\text{fermion}\rangle$ and $Q|\text{fermion}\rangle = |\text{boson}\rangle$ and has to fulfil the SUSY algebra

$$\begin{aligned} \{Q_\alpha, Q_{\dot{\alpha}}^\dagger\} &= (\sigma^\mu)_{\alpha\dot{\alpha}} P_\mu \\ \{Q_\alpha, Q_\beta\} &= 0, \quad \{Q_{\dot{\alpha}}^\dagger, Q_{\dot{\beta}}^\dagger\} = 0 \\ [Q_\alpha, P_\mu] &= 0, \quad [Q_{\dot{\alpha}}^\dagger, P_\mu] = 0 \end{aligned} \quad (2.23)$$

where P_μ is the four-momentum, α, β and $\dot{\alpha}, \dot{\beta}$ are spinor indices.

In supersymmetric extensions of the Standard Model the SM fermions and gauge bosons get superpartners, with identical quantum numbers except for the spin. This implies that, in an unbroken supersymmetric model, particles and superparticles have degenerate masses.

This already suggests a solution of the hierarchy problem of the SM. In SUSY all fermions have superpartners, \tilde{f} , which give additional corrections to the Higgs mass. Diagrams as the one depicted in Fig. 2.2 lead to a contribution

$$\Delta M_H^2 = \frac{\tilde{y}_f}{8\pi^2} \Lambda^2 + \dots \quad (2.24)$$

Here again the ellipsis denote terms that grow at most logarithmically with the cut off scale. Adding the contributions to the Higgs mass from fermions and their superpartners, we see that (independent on the masses if the superpartners) the quadratic divergent terms cancel if $\tilde{y}_f = y_f^2$. In an unbroken supersymmetric model the fermions and their superpartners have the same mass and the Higgs mass corrections cancel completely. But as we will argue in Sect. 2.2.4, supersymmetry must be broken, which implies that the masses of the superpartners differ from the masses of the SM particles. This will not spoil the cancellation of the quadratic divergencies, long as we require the SUSY breaking to maintain the relation $\tilde{y}_f = y_f^2$. Naively one would think that the remaining corrections (after the cancellation of the quadratically divergent parts) are proportional to squared mass difference $m_{\tilde{f}}^2 - m_f^2$, however calculating the corrections in the MSSM, one finds that in the Higgs mass is only logarithmically sensitive to the mass difference between fermions and their superpartners

$$\Delta M_H^2 \sim \log \left(\frac{m_{\tilde{f}}^2}{m_f^2} \right). \quad (2.25)$$

Therefore the remaining corrections to the Higgs mass stay relatively small and the Higgs mass in the MSSM is protected from large loop corrections. However in the discussion of radiative electroweak symmetry breaking (see below) we will see that also in the context of the MSSM, large corrections sensitive to $m_{\tilde{f}}^2$ appear, indicating that splitting between the masses of the SM and the SUSY particles should not be not too large.

The SM particles and their superpartners are combined within supermultiplets. Quarks and leptons receive scalar superpartners, squarks and sleptons. Supersymmetric extensions of the SM contain several scalar Higgs bosons (as we will discuss below), which get fermionic superpartners, the higgsinos. All these particles are described by so called chiral supermultiplets, each containing a two-component Weyl⁶ fermion ψ , a complex scalar field ϕ and an auxiliary field F . Also the electroweak gauge bosons of the SM and the gluons get fermionic superpartners. These are described by vector multiplets, containing a spin-1 vector boson A_μ^a , a spin-1/2 Majorana fermion λ^a and a scalar auxiliary field D^a , where the index runs over the adjoint representation of the gauge group: $a = 1, \dots, 8$ for $SU(3)_C$, $a = 1, \dots, 3$ for $SU(2)_L$ and $a = 1$ for $U(1)_Y$.

The part of a supersymmetric Lagrangian describing the n free chiral supermultiplets ($i = 1, \dots, n$) is

$$\mathcal{L}_{\text{free}} = \partial_\mu \phi_i^\dagger \partial^\mu \phi_i + \psi_i^\dagger i \bar{\sigma}^\mu \partial_\mu \psi_i + F_i^\dagger F_i. \quad (2.26)$$

The interaction term of the chiral multiplets can be written as (we define W_i and W_{ij} below)

$$\mathcal{L}_{\text{int}} = \left(-\frac{1}{2} W_{ij} \psi_i \psi_j + W_i F_i \right) + c.c. \quad (2.27)$$

⁶In Sect. 2.1 we used Dirac notation to describe the SM fermions. However it turns out to be more convenient to use the two-component Weyl spinor notation for the fermions in the supermultiplets. For the definition of Weyl fermions see Ref. [25].

Using the Euler-Lagrange equation of motion for the auxiliary fields F_i and F_i^\dagger one finds $F_i = -W_i^\dagger$, $F_i^\dagger = -W_i$. Here

$$W_i = \frac{\partial W}{\partial \phi_i} \text{ and } W_{ij} = \frac{\partial^2 W}{\partial \phi_i \partial \phi_j}. \quad (2.28)$$

W is a complex analytic (or holomorphic) function, which determines the allowed interaction terms for chiral multiplets and is called superpotential. The part of the Lagrangian describing chiral multiplets is $\mathcal{L}_{\text{chiral}} = \mathcal{L}_{\text{free}} + \mathcal{L}_{\text{int}}$.

The Lagrangian describing the vectormultiplets is

$$\mathcal{L}_{\text{gauge}} = -\frac{1}{4} F_{\mu\nu}^a F^{\mu\nu a} + i\lambda^{\dagger a} \bar{\sigma}^\mu D_\mu \lambda^a + \frac{1}{2} D^a D^a, \quad (2.29)$$

One proceeds as in the SM and promotes the derivatives in Eq. (2.26) to covariant derivatives, in order to obtain a gauge invariant Lagrangian⁷. This couples the gauge boson in the vectormultiplets to the fermions and scalars of the chiral multiplets. Additional terms must be added to respect supersymmetry.

Including all possible gauge invariant, renormalizable interaction terms, the supersymmetric Lagrangian is

$$\begin{aligned} \mathcal{L}_{\text{susy}} = & \mathcal{L}_{\text{chiral}}(\text{with } \partial_\mu \rightarrow D_\mu) + \mathcal{L}_{\text{gauge}} \\ & - \sqrt{2}g(\phi^* T^a \psi)\lambda^a - \sqrt{2}g\lambda^{\dagger a}(\psi^\dagger T^a \phi) + g(\phi^* T^a \phi)D^a. \end{aligned} \quad (2.30)$$

As introduced earlier T^a are the generators of the gauge group. For the auxiliary fields D^a one finds the equation of motion $D^a = -g(\phi^* T^a \phi)$. The scalar potential part of $\mathcal{L}_{\text{susy}}$ is given by the term $-V(\phi, \phi^*)$ with

$$V(\phi, \phi^*) = F_i^\dagger F_i + \frac{1}{2} D^a D^a = W_i^\dagger W_i + \frac{1}{2} g^2 (\phi^\dagger T^a \phi)^2. \quad (2.31)$$

The first term ('F-term') comes from $\mathcal{L}_{\text{chiral}}$, the second term ('D-term') combines the last term of Eq. (2.30) and the last term in Eq. (2.29). It is a peculiarity of supersymmetric models that the scalar potential is given by the Yukawa (F-term) and gauge (D-term) interactions.

2.2.2 The MSSM superpotential

The chiral multiplets in the MSSM are given in table 2.1. One can see from the table that the MSSM has two Higgs doublets, H_1 and H_2 ⁸. We will explain below why two Higgs doublets are needed. We follow the convention to define chiral multiplets in terms of left-handed Weyl spinors. That means we regard the right-handed fermions and their superpartners as conjugates of the left-handed fields. The vectormultiplets of the MSSM are listed in table 2.2.

⁷As mentioned earlier, we define the $SU(2)_L$ covariant derivative in the SUSY models with opposite sign than in the SM, following the **FeynArts** [36–41] conventions.

⁸In literature the two Higgs doublets are often called $H_u \equiv H_2$ and $H_d \equiv H_1$. For the Higgs doublets we use the same notation for the chiral supermultiplets and for its scalar entry.

	Label	Spin 0	Spin 1/2	$(SU(3)_C, SU(2)_L, U(1)_Y)$
Squarks, quarks	Q	$\tilde{Q} = (\tilde{u}_L, \tilde{d}_L)$	(u_L, d_L)	$(\mathbf{3}, \mathbf{2}, \frac{1}{6})$
	\bar{u}	$\tilde{\bar{u}} = \tilde{\bar{u}}_L$	\bar{u}_L	$(\bar{\mathbf{3}}, \mathbf{1}, -\frac{2}{3})$
	\bar{d}	$\tilde{\bar{d}} = \tilde{\bar{d}}_L$	\bar{d}_L	$(\bar{\mathbf{3}}, \mathbf{1}, \frac{1}{3})$
Sleptons, leptons	L	$\tilde{L} = (\tilde{\nu}, \tilde{e}_L)$	(ν, e_L)	$(\mathbf{1}, \mathbf{2}, -\frac{1}{2})$
	\bar{e}	$\tilde{\bar{e}} = \tilde{\bar{e}}_L$	\bar{e}_L	$(\mathbf{1}, \mathbf{1}, 1)$
Higgs, Higgsinos	H_1	$H_1 = (H_1^0, H_1^-)$	$(\tilde{H}_1^0, \tilde{H}_1^-)$	$(\mathbf{1}, \mathbf{2}, -\frac{1}{2})$
	H_2	$H_2 = (H_2^+, H_2^0)$	$(\tilde{H}_2^+, \tilde{H}_2^0)$	$(\mathbf{1}, \mathbf{2}, \frac{1}{2})$

Table 2.1: Chiral supermultiplets in the MSSM. Family and colour indices are suppressed.

	Spin 1/2	Spin 1	$(SU(3)_C, SU(2)_L, U(1)_Y)$
Gluino, gluon	\tilde{g}	g	$(\mathbf{8}, \mathbf{1}, 0)$
Wino, W -boson	$\tilde{W}^\pm, \tilde{W}^0$	W^\pm, W^0	$(\mathbf{1}, \mathbf{3}, 0)$
Bino, B -boson	\tilde{B}	B	$(\mathbf{1}, \mathbf{1}, 0)$

Table 2.2: Vector supermultiplets in the MSSM.

The superpotential for the MSSM with conserved R-parity (see Sect. 2.2.3) is given by

$$W^{\text{MSSM}} = \bar{u}\mathbf{y}_u Q H_2 - \bar{d}\mathbf{y}_d Q H_1 - \bar{e}\mathbf{y}_l L H_1 + \mu H_2 H_1 \quad (2.32)$$

where $Q, \bar{u}, \bar{d}, L, \bar{e}, H_1, H_2$ are the chiral supermultiplets from table 2.1. The gauge indices and generation indices are suppressed. $\mathbf{y}_u, \mathbf{y}_d$ and \mathbf{y}_l are the dimensionless Yukawa coupling parameters, which are 3×3 matrices in family space. Here one can see that in the MSSM (contrary to the SM) indeed two Higgs doublets are needed to give mass to up- and down-type fermions: In the term $\bar{u}\mathbf{y}_u Q H_2$ one cannot replace H_2 by $H_1^C \propto H_1^*$, since W is a complex analytic (or holomorphic) function and therefore no complex conjugates may appear. Two Higgsinos (and therewith Higgs doublets with opposite hypercharge) are also needed for a successful cancellation of the anomaly that would result from only one Higgsino fermion. To get the supersymmetric Lagrangian of the MSSM, the chiral and vector supermultiplets and the MSSM superpotential must be inserted in Eq. (2.30).

2.2.3 R-parity

Lepton and baryon number conservation have experimentally been probed precisely and searches (e.g. proton decay) have not shown deviations at the present level of sensitivity. Whereas in the SM these symmetries are an accidental consequence of the field content and the gauge symmetry, in supersymmetric models lepton and baryon number can be

violated, which would lead to an unstable proton. One way to prevent a too rapid proton decay is to require that every coupling in the MSSM preserves R parity

$$R = (-1)^{3B+L+2S} = \begin{cases} +1 & \text{for SM particles} \\ -1 & \text{for SUSY particles} \end{cases} \quad (2.33)$$

where B is the Baryon number (quarks have baryon number $+\frac{1}{3}$, the antiquarks have baryon number $-\frac{1}{3}$), L the Lepton number (leptons have lepton number $+1$, the antileptons have lepton number -1) and S is the spin. R parity conservation can also theoretically be motivated, it can e.g. be a remnant of a $U(1)$ gauge symmetry. The conservation of R parity implies that supersymmetric particles can only be produced in pairs and that the lightest supersymmetric particle (LSP) is stable. This has important phenomenological consequences, since the LSP can be a suitable dark matter candidate.

2.2.4 SUSY breaking

SUSY particles have yet to be observed experimentally. Given that SUSY particles would have the same mass as their SM partners in an unbroken supersymmetric theory and that no experimental signal has been seen yet, supersymmetry, if existing, cannot be an exact symmetry but must be broken. Spontaneous breaking of supersymmetry in a hidden sector can be mediated to the visible sector by different mechanisms. The SUSY breaking can generally be parameterised at low scale without being restricted to a particular SUSY breaking mechanism. The breaking is described phenomenologically by explicitly adding terms, called soft breaking terms, to the Lagrangian density. The term 'soft' means that the relations between the dimensionless couplings are not modified and thus no quadratic divergencies are reintroduced. The soft breaking terms in the MSSM are [46]

$$\begin{aligned} -\mathcal{L}_{\text{soft}}^{\text{MSSM}} = & \frac{1}{2} \left(M_1 \tilde{B} \tilde{B} + M_2 \tilde{W}^a \tilde{W}^a + M_3 \tilde{g}^a \tilde{g}^a + c.c \right) \\ & + \left(\tilde{u} \mathbf{a}_u \tilde{Q} H_2 - \tilde{d} \mathbf{a}_d \tilde{Q} H_1 - \tilde{e} \mathbf{a}_e \tilde{L} H_1 + c.c \right) \\ & + \mathbf{m}_Q^2 \tilde{Q}^\dagger \tilde{Q} + \mathbf{m}_L^2 \tilde{L}^\dagger \tilde{L} + \mathbf{m}_U^2 \tilde{u}^\dagger \tilde{u} + \mathbf{m}_D^2 \tilde{d}^\dagger \tilde{d} + \mathbf{m}_E^2 \tilde{e}^\dagger \tilde{e} \\ & + \tilde{m}_2^2 H_2^\dagger H_2 + \tilde{m}_1^2 H_1^\dagger H_1 - (m_{12}^2 H_2 H_1 + c.c) \end{aligned} \quad (2.34)$$

where M_1 , M_2 and M_3 are the bino, wino and gluino mass terms; in the term $M_3 \tilde{g}^a \tilde{g}^a$ the gauge index a runs from 1 to 8 and in the term $M_2 \tilde{W}^a \tilde{W}^a$ from 1 to 3. \mathbf{a}_u , \mathbf{a}_d and \mathbf{a}_e (3×3 matrices in family space) are the trilinear sfermion couplings and \mathbf{m}_Q^2 , \mathbf{m}_U^2 , \mathbf{m}_D^2 , \mathbf{m}_L^2 , \mathbf{m}_E^2 (3×3 matrices in family space) are the sfermion squared mass matrices. The parameters in the last line are the Higgs soft SUSY breaking parameters \tilde{m}_2^2 , \tilde{m}_1^2 , and m_{12}^2 .

2.2.5 Constrained models: CMSSM and pMSSM

A remarkable feature of the MSSM is that it allows for gauge coupling unification (provided that the SUSY particles are at the TeV scale) at a high scale $M_{\text{GUT}} \sim 10^{16}$ GeV,

which is called Grand Unification or GUT scale. The running of gauge couplings is discussed in Sect. 3.2.3. Therefore it is a popular assumption that also the gaugino masses unify at that scale, which leads to the relation

$$M_1 = \frac{3}{5} \frac{s_W^2}{c_W^2} M_2 \approx \frac{1}{2} M_2. \quad (2.35)$$

This assumption is used throughout this work. No relation is assumed for M_3 unless stated otherwise.

Going one step further one can assume that at the GUT scale the theory is described by only a few parameters. The constrained MSSM (CMSSM) is a SUSY model, which contains only five parameters: the universal scalar (soft) mass m_0 , the universal gaugino (soft) mass $m_{1/2}$, the universal trilinear coupling A_0 (all at GUT scale), the ratio of the vacuum expectation values of the two Higgs doublets $\tan \beta$ and the sign of the Higgsino mass parameter. The weak scale parameters are then obtained by renormalization group running (see Sect. 3.2.3).

On the other hand low-scale models, which are not directly derived from some high-scale (GUT) theory, are termed pMSSM models. In this bottom-up approach no assumptions about the mechanism of SUSY breaking are made.

The soft breaking terms introduce plenty of new parameters: in total the MSSM involves 105 new parameters (masses, mixing angles and phases). However many of these new parameters lead to new sources of flavour mixing and \mathcal{CP} -violation, both strongly constrained by experiments (see Ref. [24] and references therein). In phenomenological studies of the MSSM one often makes experimentally motivated and simplifying assumptions, reducing the number of MSSM parameters significantly. In the following we always assume

$$\mathbf{m}_{\tilde{Q}, \tilde{L}}^2 = \begin{pmatrix} M_{\tilde{Q}_1, \tilde{L}_1}^2 & 0 & 0 \\ 0 & M_{\tilde{Q}_2, \tilde{L}_2}^2 & 0 \\ 0 & 0 & M_{\tilde{Q}_3, \tilde{L}_3}^2 \end{pmatrix}, \quad \mathbf{m}_{\tilde{U}, \tilde{D}, \tilde{E}}^2 = \begin{pmatrix} M_{\tilde{U}_1, \tilde{D}_1, \tilde{E}_1}^2 & 0 & 0 \\ 0 & M_{\tilde{U}_2, \tilde{D}_2, \tilde{E}_2}^2 & 0 \\ 0 & 0 & M_{\tilde{U}_3, \tilde{D}_3, \tilde{E}_3}^2 \end{pmatrix} \quad (2.36)$$

and

$$\mathbf{a}_u = \begin{pmatrix} A_u y_u & 0 & 0 \\ 0 & A_c y_c & 0 \\ 0 & 0 & A_t y_t \end{pmatrix}, \quad \mathbf{a}_d = \begin{pmatrix} A_d y_d & 0 & 0 \\ 0 & A_s y_s & 0 \\ 0 & 0 & A_b y_b \end{pmatrix}, \quad \mathbf{a}_e = \begin{pmatrix} A_e y_e & 0 & 0 \\ 0 & A_\mu y_\mu & 0 \\ 0 & 0 & A_\tau y_\tau \end{pmatrix} \quad (2.37)$$

where the y_f are the Yukawa couplings. The Yukawa couplings of the first two generations are small and often neglected. These assumptions already significantly reduce the number of free parameters. In this work (if not stated otherwise) we allow the parameters M_1 , M_2 , M_3 , A_f ($f = u, d, c, s, t, b, e, \mu, \tau$) and μ to be complex. The phase of either M_1 , M_2 or μ (we usually choose M_2) can be rotated away.

2.2.6 Sfermion sector

Putting together the terms of the form $\tilde{f}_L^\dagger \tilde{f}_L$, $\tilde{f}_R^\dagger \tilde{f}_R$ and $\tilde{f}_L^\dagger \tilde{f}_R$, $\tilde{f}_R^\dagger \tilde{f}_L$ ($\tilde{f}_{L/R}$ denoting the superpartner of a left/right-handed fermion f) appearing in the F-term, the D-term and the soft SUSY breaking terms, one can write the sfermion mass part of the MSSM Lagrangian as

$$- \begin{pmatrix} \tilde{f}_L^\dagger & \tilde{f}_R^\dagger \end{pmatrix} \mathbf{M}_{\tilde{f}} \begin{pmatrix} \tilde{f}_L \\ \tilde{f}_R \end{pmatrix} \quad (2.38)$$

Neglecting flavour violation in the sfermion sector (assuming Eq. (2.36)), the 2×2 sfermion mass matrix for each flavour can be written as

$$\mathbf{M}_{\tilde{f}} = \begin{pmatrix} M_{\tilde{f}_L}^2 + m_f^2 + M_Z^2 \cos 2\beta (I_f^3 - Q_f s_w^2) & m_f X_f^* \\ m_f X_f & M_{\tilde{f}_R}^2 + m_f^2 + M_Z^2 \cos 2\beta Q_f s_w^2 \end{pmatrix}, \quad (2.39)$$

where I_f^3 is the third component of the weak isospin, Q_f the electric charge ($Q = I^3 + Y/2$ where Y is the hypercharges), m_f is the corresponding fermion mass and $M_{\tilde{f}_L}^2$ and $M_{\tilde{f}_R}^2$ are defined by

$$M_{\tilde{f}_L}^2 = \begin{cases} M_{\tilde{Q}_i}^2 & \text{for left-handed squarks} \\ M_{\tilde{L}_i}^2 & \text{for left-handed sleptons} \end{cases} \quad (2.40)$$

$$M_{\tilde{f}_R}^2 = \begin{cases} M_{\tilde{U}_i}^2 & \text{for right-handed up-type squarks} \\ M_{\tilde{D}_i}^2 & \text{for right-handed down-type squarks} \\ M_{\tilde{E}_i}^2 & \text{for right-handed sleptons} \end{cases}$$

where i indicates the generation. The mixing parameter X_f is defined by

$$X_f = A_f - \mu^* \{\cot \beta, \tan \beta\}, \quad (2.41)$$

where $\cot \beta$ applies to up-type squarks and $\tan \beta$ for down-type squarks and charged sleptons. In the MSSM with complex parameters, the trilinear couplings $A_f = |A_f| \exp(i\phi_{A_f})$ and the μ parameter $\mu = |\mu| \exp(i\phi_\mu)$ can have non-zero complex phases. Diagonalizing the mass matrix by a complex 2×2 unitary matrix $U_{\tilde{f}}$ (which can be parameterised by an angle $\theta_{\tilde{f}}$ plus a complex phase) gives the sfermion mass eigenstates

$$\begin{pmatrix} \tilde{f}_1 \\ \tilde{f}_2 \end{pmatrix} = U_{\tilde{f}} \begin{pmatrix} \tilde{f}_L \\ \tilde{f}_R \end{pmatrix}, \quad (2.42)$$

In the following we will use the convention $m_{\tilde{f}_1} \leq m_{\tilde{f}_2}$. The explicit mass eigenvalues are then given by

$$m_{\tilde{f}_{1,2}}^2 = m_f^2 + \frac{1}{2} \left[M_{\tilde{f}_L}^2 + M_{\tilde{f}_R}^2 + I_3^f M_Z^2 \cos 2\beta \right. \\ \left. \mp \sqrt{[M_{\tilde{f}_L}^2 - M_{\tilde{f}_R}^2 + M_Z^2 \cos 2\beta (I_3^f - 2Q_f s_w^2)]^2 + 4m_f^2 |X_f|^2} \right]. \quad (2.43)$$

2.2.7 Chargino sector

The electrically charged Higgsinos and gauginos mix into charginos $\tilde{\chi}_{1,2}^\pm$. Defining the gauge-eigenstates as

$$\tilde{g}^+ = \begin{pmatrix} \tilde{W}^+ \\ \tilde{H}_2^+ \end{pmatrix}, \quad \tilde{g}^- = \begin{pmatrix} \tilde{W}^- \\ \tilde{H}_1^- \end{pmatrix} \quad (2.44)$$

the chargino mass terms in the MSSM Lagrangian can be written as

$$\frac{1}{2}[\tilde{g}^{+T} \mathbf{M}_{\tilde{\chi}^\pm} \tilde{g}^- + \tilde{g}^{-T} \mathbf{M}_{\tilde{\chi}^\pm} \tilde{g}^+] + h.c. \quad (2.45)$$

with

$$\mathbf{M}_{\tilde{\chi}^\pm} = \begin{pmatrix} M_2 & \sqrt{2}M_W \sin \beta \\ \sqrt{2}M_W \cos \beta & \mu \end{pmatrix}, \quad (2.46)$$

with the soft breaking parameter M_2 . The mass eigenvalues are obtained by diagonalizing the mass matrix using two unitary matrices U and V

$$U^* \mathbf{M}_{\tilde{\chi}^\pm} V^{-1} = \text{diag}(m_{\tilde{\chi}_1^\pm}, m_{\tilde{\chi}_2^\pm}) \quad (2.47)$$

with the chargino masses $m_{\tilde{\chi}_1^\pm} < m_{\tilde{\chi}_2^\pm}$. The eigenvalues are

$$m_{\tilde{\chi}_{1,2}^\pm}^2 = \frac{M_2^2 + |\mu|^2 + 2M_W^2}{2} \mp \sqrt{\left(\frac{M_2^2 + |\mu|^2 + 2M_W^2}{2}\right)^2 - |\mu M_2 - M_W^2 \sin 2\beta|^2}. \quad (2.48)$$

2.2.8 Neutralino sector

The neutral Higgsinos and gauginos in the MSSM mix (as a result of electroweak symmetry breaking), the resulting mass eigenstates are called neutralinos. Defining the gauge-eigenstate base as

$$\tilde{G}^0 = \begin{pmatrix} \tilde{B} \\ \tilde{W}^0 \\ \tilde{H}_1^0 \\ \tilde{H}_2^0 \end{pmatrix} \quad (2.49)$$

one can rewrite the mass terms of the MSSM Lagrangian containing \tilde{G}^0 as

$$\frac{1}{2} \tilde{G}^{0T} \mathbf{M}_{\tilde{\chi}^0} \tilde{G}^0 + h.c. \quad (2.50)$$

The neutralino mass matrix is given by

$$\mathbf{M}_{\tilde{\chi}^0} = \begin{pmatrix} M_1 & 0 & -M_Z s_W \cos \beta & M_Z s_W \sin \beta \\ 0 & M_2 & M_Z c_W \cos \beta & -M_Z c_W \sin \beta \\ -M_Z s_W \cos \beta & M_Z c_W \cos \beta & 0 & -\mu \\ M_Z s_W \sin \beta & -M_Z c_W \sin \beta & -\mu & 0 \end{pmatrix}. \quad (2.51)$$

The neutralino masses are obtained by a diagonalization of the mass matrix using a single, complex, unitary matrix N

$$\text{diag}(m_{\tilde{\chi}_1^0}, m_{\tilde{\chi}_2^0}, m_{\tilde{\chi}_3^0}, m_{\tilde{\chi}_4^0}) = N^* \mathbf{M}_{\tilde{\chi}^0} N^{-1} \quad (2.52)$$

The neutralinos are ordered in mass such that $m_{\tilde{\chi}_i^0} \leq m_{\tilde{\chi}_j^0}$ for $i < j$. The gaugino masses M_1 and M_2 may (in addition to μ) be complex. However, there are in total only two physically relevant phases. One phase, usually taken to be that for M_2 , can therefore be rotated away (as we already discussed in Sect. 2.2.5).

2.2.9 Gluino sector

The gluino is a colour octet fermion and cannot mix with any other MSSM particle. Its mass

$$m_{\tilde{g}} = |M_3| \quad (2.53)$$

is directly given by the mass term in the soft breaking Lagrangian.

2.2.10 Electroweak symmetry breaking and the MSSM Higgs sector

Writing the components of the two Higgs doublets (with opposite hypercharge $-Y_{H_1} = Y_{H_2} = 1$) as $H_1 = (H_{11}, H_{12}) = (H_1^0, H_1^-)$ and $H_2 = (H_{21}, H_{22}) = (H_2^+, H_2^0)$, the scalar potential of the MSSM can be written as

$$\begin{aligned} V_H^{\text{MSSM}} = & m_1^2 H_{1i}^* H_{1i} + m_2^2 H_{2i}^* H_{2i} - \epsilon^{ij} (m_{12}^2 H_{1i} H_{2j} + m_{12}^{2*} H_{1i}^* H_{2j}^*) \\ & + \frac{1}{8} (g_1^2 + g_2^2) (H_{1i}^* H_{1i} - H_{2i}^* H_{2i})^2 + \frac{1}{2} g_2^2 |H_{1i}^* H_{2i}|^2. \end{aligned}$$

where the indices $\{i, j\} = \{1, 2\}$ refer to the respective Higgs doublet component and $\epsilon^{12} = 1$. Here $m_1^2 \equiv \tilde{m}_1^2 + |\mu|^2$ and $m_2^2 \equiv \tilde{m}_2^2 + |\mu|^2$, where \tilde{m}_1^2 and \tilde{m}_2^2 are the real soft breaking terms. The soft breaking parameter m_{12}^2 can a priori be complex, however its complex phase can be rotated away (see Refs. [29, 47]) and from here on we will treat m_{12}^2 as a real parameter. The terms proportional to $|\mu|^2$ are F-term contributions while the terms proportional to g_1 and g_2 arise from the D-terms. The terms proportional to \tilde{m}_1^2 , \tilde{m}_2^2 and m_{12}^2 are the last three terms of the soft breaking Lagrangian Eq. (2.34).

To get massive gauge bosons, V_H^{MSSM} must have a minimum which breaks the electroweak symmetry. Interestingly, the conditions to find such a minimum cannot be fulfilled for $\tilde{m}_1^2 = \tilde{m}_2^2$. This also means that $\tilde{m}_1^2 = \tilde{m}_2^2 = 0$ is not possible and therefore in the MSSM SUSY breaking is necessary for electroweak symmetry breaking.

GUT models often predict $\tilde{m}_1^2 = \tilde{m}_2^2$ at a high scale. In the evolution of the \tilde{m}_2^2 parameter down to the electroweak scale (RGE running is discussed in Eq. (3.2.3)), radiative corrections occur involving terms proportional to the squared masses of the SUSY particles. In order to fulfill the minimization conditions of the Higgs potential at the electroweak scale, the SUSY particle masses should be at the TeV scale. Otherwise

unnaturally large cancellations (large 'fine tuning') would be necessary to trigger electroweak symmetry breaking. This mechanism to activate electroweak symmetry breaking via quantum corrections is termed 'radiative electroweak symmetry breaking'.

When the electroweak symmetry is broken, the neutral components of the Higgs doublets get vevs

$$\langle H_1^0 \rangle = \frac{v_1}{\sqrt{2}}, \quad \langle H_2^0 \rangle = \frac{v_2}{\sqrt{2}} \quad (2.54)$$

while the charged components can (as in the SM) be chosen zero at the minimum of V_H^{MSSM} . The ratio between the two vevs defines the parameter

$$\tan \beta = \frac{v_2}{v_1}. \quad (2.55)$$

The two complex doublets can be expanded around the minimum as

$$H_1 = \begin{pmatrix} v_1 + \frac{1}{\sqrt{2}}(\phi_1 - i\chi_1) \\ -\phi_1^- \end{pmatrix}, \quad H_2 = e^{i\xi} \begin{pmatrix} \phi_2^+ \\ v_2 + \frac{1}{\sqrt{2}}(\phi_2 + i\chi_2) \end{pmatrix}. \quad (2.56)$$

ξ is a possible phase between the two Higgs doublets (we will see below that this phase must be zero and that the MSSM Higgs sector is \mathcal{CP} -conerving at tree-level). The two MSSM Higgs doublets contain eight degrees of freedom. As in the SM, three degrees of freedom give the unphysical Goldstone bosons, which become the longitudinal polarization modes of the Z and W^\pm bosons. The remaining degrees of freedom give the five physical MSSM Higgs bosons. The generated gauge boson masses are given by

$$M_W^2 = c_W^2 M_Z^2 = \frac{1}{2} g_2^2 (v_1^2 + v_2^2). \quad (2.57)$$

We define

$$v \equiv \sqrt{v_1^2 + v_2^2} \sim 174 \text{ GeV}, \quad (2.58)$$

where the value is given by the measured gauge boson masses.

By rearranging the bilinear terms, the Higgs potential can be written as

$$V_H^{\text{MSSM}} = \frac{1}{2} (\phi_1, \phi_2, \chi_1, \chi_2) \mathbf{M}_{\phi\phi\chi\chi} \begin{pmatrix} \phi_1 \\ \phi_2 \\ \chi_1 \\ \chi_2 \end{pmatrix} + (\phi_1^-, \phi_2^-) \mathbf{M}_{\phi^\pm\phi^\pm} \begin{pmatrix} \phi_1^+ \\ \phi_2^+ \end{pmatrix} + \dots, \quad (2.59)$$

with the mass matrices

$$\mathbf{M}_{\phi\phi\chi\chi} = \begin{pmatrix} M_{\phi\phi} & M_{\phi\chi} \\ M_{\phi\chi}^\dagger & M_{\chi\chi} \end{pmatrix} \quad (2.60)$$

and $\mathbf{M}_{\phi^\pm\phi^\pm}$. Non-zero off diagonal elements $M_{\phi\chi}$ of the mass matrix $\mathbf{M}_{\phi\phi\chi\chi}$, lead to a \mathcal{CP} -violating mixing between the \mathcal{CP} -even and \mathcal{CP} -odd states. The non-vanishing entries of $M_{\phi\chi}$ are proportional to $\sin \xi$.

The (tree-level) mixing of the gauge eigenstates into Higgs mass eigenstates is described by

$$\begin{pmatrix} h \\ H \\ A \\ G \end{pmatrix} = U_{\text{MSSM}}^N \begin{pmatrix} \phi_1 \\ \phi_2 \\ \chi_1 \\ \chi_2 \end{pmatrix}, \quad \begin{pmatrix} G^\pm \\ H^\pm \end{pmatrix} = U_{\text{MSSM}}^C \begin{pmatrix} \phi_1^\pm \\ \phi_2^\pm \end{pmatrix}. \quad (2.61)$$

The condition that v_1 and v_2 are stationary points of the Higgs potential leads to the requirement that the phase ξ between the two Higgs doublets has to be zero. Therefore also $M_{\phi\chi}$ vanishes and there is no \mathcal{CP} violation in the MSSM Higgs sector at tree-level. The mixing matrices can then be parametrised by

$$U_{\text{MSSM}}^N = \begin{pmatrix} -\sin\alpha & \cos\alpha & 0 & 0 \\ \cos\alpha & \sin\alpha & 0 & 0 \\ 0 & 0 & -\sin\beta & \cos\beta \\ 0 & 0 & \cos\beta & \sin\beta \end{pmatrix}, \quad U_{\text{MSSM}}^C = \begin{pmatrix} \cos\beta & \sin\beta \\ -\sin\beta & \cos\beta \end{pmatrix}, \quad (2.62)$$

with

$$\tan 2\alpha = \frac{M_A^2 + M_Z^2}{M_A^2 - M_Z^2} \tan 2\beta, \quad (2.63)$$

and one finds the tree-level mass relations

$$\begin{aligned} M_{H,h}^2 &= \frac{1}{2} \left(M_A^2 + M_Z^2 \pm \sqrt{(M_A^2 + M_Z^2)^2 - 4M_Z^2 M_A^2 \cos^2 2\beta} \right) \\ M_{H^\pm}^2 &= M_A^2 + M_{W^\pm}^2. \end{aligned} \quad (2.64)$$

The mass eigenstates correspond to the neutral Higgs bosons h , H (with $M_h < M_H$) and A , and the charged Higgs pair H^\pm . At tree level, where possible \mathcal{CP} -violating contributions of the soft supersymmetry-breaking terms do not enter, h and H are the light and heavy \mathcal{CP} -even Higgs bosons, and A is \mathcal{CP} -odd. At lowest order the MSSM Higgs sector is fully described by M_Z and two MSSM parameters, often chosen as the \mathcal{CP} -odd Higgs boson mass, M_A , and $\tan\beta$, the ratio of the two vacuum expectation values.

From the above expressions it follows that $M_h < M_Z$ (at tree level). Such a light Higgs boson would be excluded by LEP searches (unless it has strongly suppressed couplings to gauge bosons). But higher order corrections to the Higgs masses are known to be sizeable and must be included; particularly important are the one- and two-loop contributions from top quarks and their scalar top partners.

ATLAS and CMS discovered a Higgs boson at ~ 126 GeV. Within the framework of the MSSM the lighter \mathcal{CP} -even Higgs boson, h , can have a mass of about 126 GeV for sufficiently large M_A and sufficiently large higher-order corrections from the scalar top sector. However, also the interpretation of the discovered particle as the heavy \mathcal{CP} -even Higgs state, H , is, at least in principle, a viable possibility, see Refs. [48–54]⁹. The interpretation of the discovered Higgs in the MSSM will be discussed in detail in chapter 6 and chapter 7.

⁹This scenario is challenged by the recent ATLAS bound on light charged Higgs bosons [55].

2.3 The Next to Minimal Supersymmetric Standard Model

So far there exists no direct evidence for any particular theory beyond the standard model. Therefore it is important to examine also other supersymmetric extensions of the SM besides the MSSM. In the Next-to-Minimal Supersymmetric Standard Model (NMSSM) the Higgs sector of the MSSM is enlarged by an additional Higgs singlet, which entails 7 physical Higgs bosons and leads to a rich phenomenology which can differ significantly from the MSSM. In this section we motivate the NMSSM and discuss the relevant particle sectors. Since the matter content remains the same, the sfermion sector of the NMSSM is unchanged with respect to the MSSM. Also the chargino sector of the NMSSM is identical to that in the MSSM (since no new charged degrees of freedom are introduced), whereas the neutralino sector is extended.

2.3.1 Motivation

The MSSM superpotential Eq. (2.65) contains the bilinear term $\mu H_2 H_1$. Since the dimensionful μ parameter is introduced in the supersymmetric theory it is not connected to the SUSY breaking scale. However a value for μ of the order of that scale is necessary to find an acceptable phenomenology. This issue is called the μ -problem of the MSSM [56]. In the NMSSM the corresponding term in the superpotential is replaced by a coupling of the two Higgs doublets to a new singlet field, and the μ parameter arises dynamically from the vev of the singlet and may therefore be close to the SUSY breaking scale.

The solution of the μ -problem is probably the most compelling motivation to study the NMSSM, however there are further phenomenological motivations. The singlet field modifies the Higgs mass relations compared to the MSSM, such that the tree-level mass of the lightest neutral Higgs boson gets an additional NMSSM contribution, which can increase its value. Consequently the radiative corrections needed to shift the mass of the lightest Higgs mass up to 126 GeV can be smaller. In the MSSM a large splitting in the stop sector is necessary to explain the LHC signal in terms of the lightest Higgs. This requirement is relaxed in NMSSM parameter regions, in which the tree-level Higgs mass is larger than the maximal MSSM value [57]. Another reason to study the NMSSM is the enriched dark matter phenomenology due to a fifth neutralino.

2.3.2 The NMSSM superpotential and soft breaking terms

The NMSSM involves the same supermultiplets as the MSSM listed in table 2.1 and table 2.2, but in addition to the two Higgs doublets of the MSSM it also contains a scalar singlet S which couples only to the Higgs sector. The NMSSM¹⁰ superpotential

¹⁰We consider the Z_3 -symmetric version of the NMSSM, in which no linear or quartic terms in S appear.

has the form

$$W^{\text{NMSSM}} = \bar{u}\mathbf{y}_u QH_2 - \bar{d}\mathbf{y}_d QH_1 - \bar{e}\mathbf{y}_l LH_1 + \lambda SH_2H_1 + \frac{1}{3}\kappa S^3. \quad (2.65)$$

Similar to the Higgs doublets, our notation for S is the same for the supermultiplet as for its scalar component. Obviously the superpotential contains the supermultiplet S , while the scalar component occurs in the soft breaking terms. The new contributions of the Higgs singlet to the soft breaking terms are

$$\mathcal{L}_{\text{soft}}^{\text{NMSSM}} = \mathcal{L}_{\text{soft}}^{\text{MSSM,mod}} - m_S^2 |S|^2 - (\lambda A_\lambda SH_2H_1 + \frac{1}{3}\kappa A_\kappa S^3 + h.c.), \quad (2.66)$$

where $\mathcal{L}_{\text{soft}}^{\text{MSSM,mod}}$ is the soft-breaking Lagrangian $\mathcal{L}_{\text{soft}}^{\text{MSSM}}$ of the MSSM, given in Eq. (2.34), but without the term $m_{12}^2 H_2 H_1$.

2.3.3 Higgs sector of the NMSSM

The additional contributions (and the modified μ term) in the superpotential and in the soft breaking terms lead to a modified Higgs potential in the NMSSM, which contains the additional soft breaking parameters m_S^2 , A_λ , A_κ , as well as the superpotential trilinear couplings λ and κ .

At tree level no \mathcal{CP} violation occurs exclusively within the Higgs doublet sector (as we saw in the discussion of the MSSM Higgs sector). The NMSSM doublet-singlet couplings can violate \mathcal{CP} already at tree-level. However we do not consider this possibility.

The minimum of the NMSSM Higgs potential triggers electroweak symmetry breaking. After electroweak symmetry breaking the Higgs doublets can be expanded around their minima in the same way as in the MSSM (see Eq. (2.56), with $\xi = 0$). The singlet scalar component can be expanded as

$$S = v_s + \frac{1}{\sqrt{2}}(\phi_s + i\chi_s), \quad (2.67)$$

where v_s is the (non-zero) vacuum expectation value of the singlet. The effective μ parameter is dynamically generated by

$$\mu_{\text{eff}} = \lambda v_s, \quad (2.68)$$

and is therefore of the order of the SUSY breaking scale, which solves the μ problem of the MSSM.

The bilinear part of the Higgs potential can be written as

$$\begin{aligned} V_H = & \frac{1}{2}(\phi_1, \phi_2, \phi_S) \mathbf{M}_{\phi\phi\phi} \begin{pmatrix} \phi_1 \\ \phi_2 \\ \phi_S \end{pmatrix} + \frac{1}{2}(\chi_1, \chi_2, \chi_S) \mathbf{M}_{\chi\chi\chi} \begin{pmatrix} \chi_1 \\ \chi_2 \\ \chi_S \end{pmatrix} \\ & + (\phi_1^-, \phi_2^-) \mathbf{M}_{\phi^\pm\phi^\pm} \begin{pmatrix} \phi_1^+ \\ \phi_2^+ \end{pmatrix} + \dots, \end{aligned} \quad (2.69)$$

with the mass matrices $\mathbf{M}_{\phi\phi\phi}$, $\mathbf{M}_{\chi\chi\chi}$ and $\mathbf{M}_{\phi^\pm\phi^\pm}$.

The mixing of the \mathcal{CP} -even, \mathcal{CP} -odd and charged Higgs fields into mass eigenstates is described by unitary matrices U^H , U^A and U^C , where

$$\begin{pmatrix} h_1 \\ h_2 \\ h_3 \end{pmatrix} = U^H \begin{pmatrix} \phi_1 \\ \phi_2 \\ \phi_S \end{pmatrix}, \quad \begin{pmatrix} a_1 \\ a_2 \\ G \end{pmatrix} = U^A \begin{pmatrix} \chi_1 \\ \chi_2 \\ \chi_S \end{pmatrix}, \quad \begin{pmatrix} G^\pm \\ H^\pm \end{pmatrix} = U^C \begin{pmatrix} \phi_1^\pm \\ \phi_2^\pm \end{pmatrix}. \quad (2.70)$$

The matrices U^H , U^A and U^C transform the neutral \mathcal{CP} -even, \mathcal{CP} -odd and charged Higgs fields, respectively, such that the resulting mass matrices

$$\mathbf{M}_{hhh}^{\text{diag}} = U^H \mathbf{M}_{\phi\phi\phi} U^{H\dagger}, \quad \mathbf{M}_{aaG}^{\text{diag}} = U^A \mathbf{M}_{\chi\chi\chi} U^{A\dagger} \quad \text{and} \quad \mathbf{M}_{H^\pm G^\pm}^{\text{diag}} = U^C \mathbf{M}_{\phi^\pm\phi^\pm} U^{C\dagger} \quad (2.71)$$

The mass eigenstates h_1 , h_2 and h_3 (with $m_{h_1} \leq m_{h_2} \leq m_{h_3}$) are the three \mathcal{CP} -even Higgs bosons, a_1 and a_2 (with $m_{a_1} \leq m_{a_2}$) the two \mathcal{CP} -odd Higgs bosons, and H^\pm is (unchanged) the charged Higgs pair. Also unchanged from the MSSM is the presence of the unphysical Goldstone bosons, G and G^\pm . The charged Higgs mass is given by

$$M_{H^\pm}^2 = \hat{m}_A^2 + M_W^2 - \lambda^2 v^2 \quad (2.72)$$

where \hat{m}_A is the effective \mathcal{CP} -odd doublet mass

$$\hat{m}_A^2 = \frac{\lambda v_s}{\sin \beta \cos \beta} (A_\lambda + \kappa v_s). \quad (2.73)$$

It can be seen from Eq. (2.70) that the singlet component of h_i is given by entry U_{i3}^H (accordingly the singlet component of a_i by U_{i3}^A). As singlets do not couple to gauge bosons, a larger singlet component of h_i means a reduced coupling of h_i to gauge bosons (and SM fermions). This will be important later.

2.3.4 Neutralino sector of the NMSSM

In the NMSSM, the singlino \tilde{S} , the superpartner of the additional singlet scalar enlarging the Higgs sector, extends the neutralino sector compared to the MSSM by a fifth mass eigenstate. In the basis $(\tilde{B}, \tilde{W}^0, \tilde{H}_1^0, \tilde{H}_2^0, \tilde{S})$ the neutralino mass matrix at tree-level is now given by

$$\mathbf{M}_{\tilde{\chi}^0} = \begin{pmatrix} M_1 & 0 & -M_Z s_W \cos \beta & M_Z s_W \sin \beta & 0 \\ 0 & M_2 & M_Z c_W \cos \beta & -M_Z c_W \sin \beta & 0 \\ -M_Z s_W \cos \beta & M_Z c_W \cos \beta & 0 & -\mu_{\text{eff}} & -\lambda v_2 \\ M_Z s_W \sin \beta & -M_Z c_W \sin \beta & -\mu_{\text{eff}} & 0 & -\lambda v_1 \\ 0 & 0 & -\lambda v_2 & -\lambda v_1 & 2K \mu_{\text{eff}} \end{pmatrix}. \quad (2.74)$$

where $K \equiv \kappa/\lambda$. As in the MSSM, the mass matrix can be diagonalised by a single unitary matrix N

$$\text{diag}(m_{\tilde{\chi}_1^0}, m_{\tilde{\chi}_2^0}, m_{\tilde{\chi}_3^0}, m_{\tilde{\chi}_4^0}, m_{\tilde{\chi}_5^0}) = N^* \mathbf{M}_{\tilde{\chi}^0} N^\dagger, \quad (2.75)$$

which gives the mass eigenvalues ordered as $m_{\tilde{\chi}_i^0} \leq m_{\tilde{\chi}_j^0}$ for $i < j$.

2.3.5 MSSM and decoupling limit

Since the NMSSM is an extension of the MSSM, the MSSM is recovered for

$$\lambda \rightarrow 0, \quad \kappa \rightarrow 0, \quad K \equiv \kappa/\lambda = \text{constant}, \quad (2.76)$$

with all other parameters (including μ_{eff}) held fixed. This limit is referred to as MSSM limit. In this limit one \mathcal{CP} -even, one \mathcal{CP} -odd Higgs boson (not necessarily the heaviest ones) and one neutralino become completely singlet and decouple from the MSSM sector.

If additionally $M_{H^\pm} \gg M_Z$ is fulfilled and all superpartners are heavy, we are in the decoupling limit, in which the Higgs sector becomes SM-like (decoupled heavy doublet Higgs states, one light Higgs with SM-like couplings).

When the doublet decoupling condition $M_{H^\pm} \gg M_Z$ is fulfilled, but λ and κ have finite non-zero values (i.e. values that differ from the MSSM limit) we call it the SM+singlet limit.

Chapter 3

Perturbative calculations

This chapter introduces regularization and renormalization, two concepts important for the loop calculations as the ones described in the chapter 5. The resources I used for this chapter are Refs. [21–23, 26, 27, 58]. Parts of this introductory chapter are based on text which I have written before and that appeared in Refs. [34].

3.1 Introduction

In quantum field theories an observables O (e.g. a cross section) can be obtained from the S-matrix element \mathcal{M} ($O \propto |\mathcal{M}|^2$) which can be calculated perturbatively

$$\mathcal{M} = c_1 g + c_2 g^2 + c_3 g^3 + \dots . \quad (3.1)$$

If the coupling g is small, the size of the consecutive terms in the power series decreases. In order to improve the prediction for an observable O , theorists calculate, besides the first term, also the leading higher-order corrections. The perturbative series can be illustrated by Feynman diagrams with increasing number of loops and vertices. In an S-matrix element the external particles are on-shell ($p^2 = m^2$) while the virtual particles can be off-shell ($p^2 \neq m^2$).

For the calculation of loop diagrams, an integration over all possible values of the unconstrained momenta of the particles in the loop must be performed, which generally yields a divergent result. In order to deal with the unphysical divergencies, the two concepts of regularization and renormalization are needed, which are introduced in this section.

3.2 The concepts of regularization and renormalization

Regularization makes the divergent expressions mathematically meaningful. It introduces a new parameter δ , in a way that the original theory is retrieved for $\delta \rightarrow \delta_0$. The loop integral is finite for $\delta \neq \delta_0$, but has a pole at $\delta = \delta_0$. Only after renormalization

the limit $\delta \rightarrow \delta_0$ can be taken and finite results in terms of renormalized parameters are obtained. There are several different regularization schemes which do not necessarily yield the same result for a specific loop diagram, but the results for physical observables must always be independent of the regularization scheme. In this work, two different renormalization schemes are used. Calculations within the SM¹ are performed using Dimensional Regularization (DR) [60]. DR is a regularization method which preserves Lorentz- and gauge invariance, and features an elegant and convenient formalism for loop calculations. In DR the definition of momenta and Lorentz covariants $(\gamma_\mu, g_{\mu\nu}, \dots)$ is extended from 4 to $D = 4 - \epsilon$ dimensions. With the extension of space-time dimensions also the integrals have to be calculated in $D = 4 - \epsilon$ instead of 4 dimensions and the crucial point of DR is that the integrals that are UV-divergent in 4 dimensions are convergent for $\epsilon > 0$

$$\int \frac{d^4 q}{(2\pi)^4} \rightarrow \mu^{4-D} \int \frac{d^D q}{(2\pi)^D}. \quad (3.2)$$

An arbitrary energy scale μ is introduced here to keep the couplings dimensionless. At one-loop order² any loop integral can be decomposed (using Passarino-Veltman Reduction [61]) into scalar one-loop integrals that do not contain any Lorentz index in the numerator. Calculating the scalar integrals, one finds terms proportional to $1/\epsilon$, terms independent of ϵ and terms proportional to powers of ϵ . By appropriate renormalization, the terms with $1/\epsilon$ can be canceled and then the limit $\epsilon \rightarrow 0$ can be taken. Dimensional regularization breaks supersymmetry. We perform the calculation of loop diagrams in the MSSM and the NMSSM using Constrained Differential Renormalization (CDR)³, a method for the calculation of loop integrals in 4 dimensions, which preserves supersymmetry and gauge invariance at one-loop level. CDR is equivalent to the more commonly used scheme Dimensional Reduction (DRED)⁴ at one-loop level [62]. More details about CDR can be found in Ref. [62, 63].

Models, like the SM, the MSSM or the NMSSM, involve several free parameters that have to be determined by experiments. At tree level the relations between these parameters and the experimental quantities might be clear, but the inclusion of radiative corrections alters the relations and changes the physical interpretation of the parameters. A redefinition (or renormalization) of the parameters is then required. In a renormalizable theory, this is done in such a way that the divergencies are systematically absorbed into the unphysical (bare) parameters in the Lagrangian. Therefore, the original bare parameters a_0 (e.g. a mass parameter) and fields F_0 in the Lagrangian are replaced by

$$\begin{aligned} a_0 &= a + \delta a \\ F_0 &= \left(1 + \frac{1}{2}\delta Z_F\right) F \end{aligned} \quad (3.3)$$

¹With the exception of one SM diagram, which required a specific treatment and where we use another regularization scheme called Pauli-Villars regularization [59].

²In this work the calculation of diagrams beyond one-loop is not discussed.

³In practise, the loop calculations are done with the programs `FeynArts` (Version 3.5) [36–41] and `FormCalc` (Version 6.2) [62]. In `FormCalc` the user can choose between DR and CDR.

⁴DRED is a regularization scheme, in which the integration momenta are D-dimensional, while the Dirac algebra is kept 4-dimensional.

where a (F) are the renormalized parameters (fields) and δa and δZ_F are the renormalization constants (or counterterms). The physical renormalized parameters are finite while the renormalization constants contain the divergencies. After this redefinition, the bare Lagrangian can be replaced by

$$\mathcal{L}_0(a_0, F_0) = \mathcal{L}(a, F) + \mathcal{L}_{\text{CT}}(a, F, \delta a, \delta Z_F). \quad (3.4)$$

The Lagrangian \mathcal{L} looks like the bare Lagrangian \mathcal{L}_0 but with renormalized parameters, and \mathcal{L}_{CT} contains the counter terms. From this Lagrangian we get an extended set of Feynman rules, consisting of the 'original' Feynman rules with renormalized parameters and additionally new Feynman rules for the counter terms. This procedure has to be done for every order in perturbation theory. At each order the sum of the original Feynman graphs with those involving counterterms is finite (as long as the theory is renormalizable).

The renormalization constants are fixed by a renormalization scheme, which consists of certain renormalization conditions. There are different renormalization schemes, which have in common that the divergencies are absorbed in the counterterms. The treatment of the finite parts determines the relation between the renormalized parameters and measurable quantities. Different finite parts are absorbed in different renormalization schemes. In the minimal subtraction (MS) scheme only the divergence is absorbed. Two common renormalization schemes, the on-shell scheme and the $\overline{\text{MS}}$ scheme, are introduced in the next two sections. In this work we use the on-shell scheme for the one-loop calculation in chapter 5.

3.2.1 On-shell renormalization scheme

In the on-shell scheme the renormalization constants are fixed by the on-shell renormalization conditions, demanding that the renormalized mass parameters are equal to the real parts of the propagator poles, that the residues of the renormalized propagators are equal to 1 and that e is the elementary charge from Thomson-scattering, resulting in vanishing loop contributions to the eeA vertex on-shell and for zero momentum transfer. These conditions imply that the terms containing the scale μ introduced in Eq. (3.2) are absorbed along with the singularities in the counter terms and the renormalized parameters are scale independent.

In our work, we directly use only the renormalization of the electroweak SM parameters and fields at one-loop level. Here we only give the on-shell renormalization constants which we will need later. For a comprehensive review of the renormalization of the electroweak SM at one-loop level including the derivation of the renormalization constants, we refer to Ref. [23]. The renormalization constants of the W/Z boson masses are

$$M_{W/Z,0}^2 = M_{W/Z}^2 + \delta M_{W/Z}^2, \quad \delta M_{W/Z}^2 = \text{Re} \Sigma_T^{WW/ZZ}(M_{W/Z}^2), \quad (3.5)$$

where the self-energy Σ which occurs here is defined in Sect. 3.2.2. The renormalization constant of a (left-handed) lepton field l (neglecting the lepton mass) is

$$l_0^L = (1 + \frac{1}{2} \delta Z^{l,L}) l^L, \quad \delta Z^{l,L} = -\text{Re} \Sigma_L^l(0). \quad (3.6)$$

The renormalization constant of the electric charge is⁵

$$e_0 = (1 + \delta Z_e)e, \quad \delta Z_e = \frac{1}{2}\Pi^{AA}(0) - \frac{s_W}{c_W} \frac{\Sigma_T^{AZ}(0)}{M_Z^2}. \quad (3.7)$$

with

$$\Pi^{AA}(k^2) = \frac{\Sigma_T^{AA}(k^2)}{k^2}, \quad \Pi^{AA}(0) = \left. \frac{\partial \Sigma_T^{AA}(k^2)}{\partial k^2} \right|_{k^2=0}. \quad (3.8)$$

The sine of the weak mixing angle is not an independent parameter in the on-shell renormalization scheme. Its renormalization constant

$$s_{W,0} = s_W + \delta s_W, \quad \frac{\delta s_W}{s_W} = -\frac{1}{2} \frac{c_W^2}{s_W^2} \text{Re} \left(\frac{\Sigma_T^{WW}(M_W^2)}{M_W^2} - \frac{\Sigma_T^{ZZ}(M_Z^2)}{M_Z^2} \right). \quad (3.9)$$

is fixed by renormalization constants of the weak gauge boson masses

3.2.2 Self-energies

In Eq. (3.5) to Eq. (3.9) the quantity Σ denotes the one-loop self-energy. Generally the self-energy contains the loop contributions to the propagator of a field and is given as the sum of all one-particle irreducible⁶ loop diagrams:

$$i\Sigma = \text{[diagram: shaded circle]} = \text{[diagram: fermion loop]} + \text{[diagram: ghost loop]} + \text{[diagram: fermion loop with wavy line]} + \text{[diagram: fermion loop with wavy line]} + \text{[diagram: fermion loop with wavy line]} + \mathcal{O}(e^6) \quad (3.10)$$

The self-energy of a gauge boson can be written as

$$\Sigma_{\mu\nu}(p^2) = \left(-g_{\mu\nu} + \frac{p_\mu p_\nu}{p^2} \right) \Sigma_T(p^2) - \frac{p_\mu p_\nu}{p^2} \Sigma_L(p^2) \quad (3.11)$$

where $\Sigma_T(p^2)$ is the transverse part (which appears in the formulas for the renormalization constants given above) and $\Sigma_L(p^2)$ the longitudinal part of the gauge boson self-energy. The fermion self-energy can be split into a vector, an axial vector, a scalar and a pseudoscalar part

$$\Sigma(p) = \not{p} \Sigma_V(p^2) + \not{p} \gamma^5 \Sigma_A(p^2) + m_f \Sigma_S(p^2) + m_f \gamma^5 \Sigma_P(p^2) \quad (3.12)$$

⁵The sign in front of s_W depends on the choice for the $SU(2)$ covariant derivative. Like δZ_e is given here, it assumes our SM convention. Using our the (N)MSSM convention, the renormalization constant of the electric charge is defined with a + sign between the two terms.

⁶Irreducible means that the diagram cannot be cut into two non-trivial parts by cutting a single line carrying non-zero momentum.

with $\not{p} \equiv \gamma^\mu p_\mu$ or alternatively into left and right handed parts

$$\begin{aligned} \Sigma(p) = & \frac{1}{2} \not{p} (1 - \gamma^5) \Sigma_L(p^2) + \frac{1}{2} \not{p} (1 + \gamma^5) \Sigma_R(p^2) \\ & + \frac{1}{2} m_f (1 - \gamma^5) \Sigma_{L'}(p^2) + \frac{1}{2} m_f (1 + \gamma^5) \Sigma_{R'}(p^2) \end{aligned} \quad (3.13)$$

with

$$\begin{aligned} \Sigma_R(p^2) &= \Sigma_V(p^2) + \Sigma_A(p^2) \\ \Sigma_L(p^2) &= \Sigma_V(p^2) - \Sigma_A(p^2) \end{aligned} \quad (3.14)$$

where Σ_L appears in Eq. (3.6) and

$$\begin{aligned} \Sigma_{R'}(p^2) &= \Sigma_S(p^2) + \Sigma_P(p^2) \\ \Sigma_{L'}(p^2) &= \Sigma_S(p^2) - \Sigma_P(p^2) \end{aligned} \quad (3.15)$$

3.2.3 $\overline{\text{MS}}$ renormalization scheme, renormalization group equations and implications for QCD

The $\overline{\text{MS}}$ renormalization scheme is a modified version of the MS scheme, in which besides the singularity also the constant $\log 4\pi - \gamma_E$ which occurs in the calculation of the scalar integrals together with the $1/\epsilon$ term is absorbed⁷. However the μ dependent term remains in the integral and causes a dependence of the renormalized finite parameters on the scale μ ⁸. The evolution of the renormalized parameters (masses and couplings⁹) with this scale, which is also called renormalization scale, is described by the renormalization group equations (RGEs), which for the strong coupling reads

$$\frac{\partial \alpha_s}{\partial \log \mu^2} = \beta(\alpha_s) \quad (3.16)$$

with

$$\beta(\alpha_s) = -\left(11 - \frac{2n_f}{3}\right) \frac{\alpha_s^2}{4\pi} + \mathcal{O}(\alpha_s^3). \quad (3.17)$$

The negative sign of the beta function (for $n_f \leq 16$, where n_f is the number of active quark flavours) implies that α_s decreases with increasing μ (which is identified with increasing energy or decreasing distance) which has profound implications for QCD. This phenomenon is called asymptotic freedom and assures that the powerful method of perturbative calculations (Eq. (3.1)) can be used at small distances. However at large

⁷A similar renormalization scheme for Dimensional Reduction, which is often used in supersymmetry (e.g. for the renormalization of the parameter $\tan \beta$) is the $\overline{\text{DR}}$ scheme.

⁸This feature is not restricted to the $\overline{\text{MS}}$ renormalization scheme. In the on-shell scheme the equivalent to the scale μ is the scale M where the renormalization condition is fixed. The variation of M plays the same role as the variation of μ in $\overline{\text{MS}}$.

⁹A scale dependent coupling is termed a running coupling.

distances (low energies) α_s gets large and the perturbative expansion fails. The scale which describes the transition to the non-perturbative regime is $\Lambda_{\text{QCD}} \sim 200 \text{ MeV}$. At low energies quarks and gluons (collectively called partons) are bound into colour neutral hadrons (e.g. protons). This phenomenon is termed confinement.

In order to make predictions for high energy hadron collider experiments, the cross sections are factorized into hard scattering cross sections of quarks and gluons at high energies (calculable in perturbative QCD) and functions called parton distribution functions (PDFs) describing the proton structure. The PDFs cannot be calculated perturbatively and are obtained from measurements, however the scale dependence can be calculated perturbatively and is described by the DGLAP [64] evolution equations.

Chapter 4

Experimental status

This is a brief review and does not make any claim to summarise all important aspects/results of collider experiments. The selection is made to introduce and explain in brief the terms related to collider experiments which are used later. The results most relevant for my work presented in the later chapters (chapters 5 to 8) are outlined. Besides the references given in the text below, material used for this chapter has been obtained from [65–70]. Small parts of this chapter are based on text which I have written before and that appeared in Ref. [35].

4.1 Collider experiments

Probing the Standard Model of particle physics and its extensions in collider experiments has a long and successful history. A new era of particle physics begun with the start of the Large Hadron Collider (LHC), which outperforms former collider experiments, such as LEP or the Tevatron, in terms of energy and luminosity, probing new physics up to much higher mass scales. As discussed earlier SUSY particles are expected to be at the TeV scale (in order to solve the hierarchy problem and allow for gauge coupling unification) and there are good prospects that SUSY particles could be in the reach of the LHC, whose design centre-of-mass energy is 14 TeV (more details are given below). However, so far no SUSY particles have been observed.

The Large Electron-Positron Collider (LEP) was a circular electron positron collider, with an energy of initially 45 GeV per beam which was increased in steps to a maximum centre-of-mass energy of 209 GeV, located at CERN. It was running between 1989 and 2000. The four big LEP experiments were ALEPH, Delphi, L3 and OPAL. Many of the LEP results are still very important, the ones most relevant for this work are the lower mass limits on the uncoloured SUSY particles [71–74] and the precise measurement of the W boson mass [75]. The Tevatron was a circular collider at Fermilab which ran from 1983 until 2011 and collided protons with antiprotons at a maximal centre-of-mass energy of 1.96 TeV, with the two large experiments CDF and DØ. The largest success of the Tevatron was the discovery of the top quark in 1995 [17, 18]. An important Tevatron result relevant for this work is the precision measurement of the W boson mass [76].

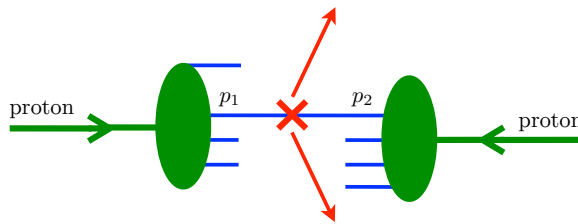


Figure 4.1: Sketch of a proton-proton collision

The LHC is a circular collider (with a ring circumference of 27.6 km) located at CERN. It is built in the former LEP tunnel and collides two proton beams¹ (consisting of ~ 2800 bunches which contain $\sim 10^{11}$ protons at design luminosity). The design centre-of-mass energy is $\sqrt{s} = 14$ TeV. In the first years, 2010-2012, the LHC had extended runtimes at $\sqrt{s} = 7$ TeV and at $\sqrt{s} = 8$ TeV. The LHC will run at close to 14 TeV from 2015 onwards. A proton-proton collision is sketched schematically in Fig. 4.1. Two partons (quarks, antiquarks or gluons) out of the protons collide with momenta $p_1^\mu = x_1\sqrt{s}/2(1, 0, 0, 1)$ and $p_2^\mu = x_2\sqrt{s}/2(1, 0, 0, -1)$, where x_1 and x_2 are the fractions which the colliding partons carry of the proton momenta. The collision events at the LHC can be analysed by 7 experiments, among these the four large detectors are ALICE, LHCb and the two multi-purpose detectors ATLAS and CMS. For a certain process, the number of events recorded in one experiment can be expressed as

$$N_{\text{events}} = \mathcal{L} \times \sigma \times \epsilon, \quad (4.1)$$

where σ is the cross section of that process, \mathcal{L} is the integrated luminosity and ϵ is the detector efficiency \times acceptance. The integrated luminosity is the integral of the instantaneous luminosity, which depends on the beam parameters (e.g. number of protons per bunch, bunch spacing, etc.), over time. In the first three years of running, ATLAS and CMS each collected more than 20fb^{-1} of integrated luminosity. The LHC 'rediscovered' the SM and set stringent mass limits on many particles of new physics models. The largest success of the LHC, so far, is the discovery of a Higgs boson in July 2012.

For the interpretation and understanding of the events detected by the high-energy collider experiments, a precise theoretical modelling of the expected signal and background is necessary, which can be done by Monte-Carlo event generators (e.g. **Herwig++** [77] or **Pythia** [78, 79]) and detector simulators. In reality a particle collision at a hadron collider like the LHC is far more complicated than the sketch in Fig. 4.1. A more realistic picture is given in Fig. 4.2 (figure taken from [65]), which sketches an event ($t\bar{t}h$) as modelled by a Monte-Carlo event generator. The two protons come from the left and the right side. Two partons out of the protons collide in the hard interaction (big red blob). Before the hard interaction, additional colored particles are radiated; this radiation is called initial state radiation (ISR). The particles produced in the hard interaction are unstable and decay (small red blobs). More hard (with energy $\gg \Lambda_{\text{QCD}}$) quarks and

¹The LHC collides also heavy ions. Since the results of heavy ion collisions are not directly relevant for this work this possibility of the LHC is not further discussed here.

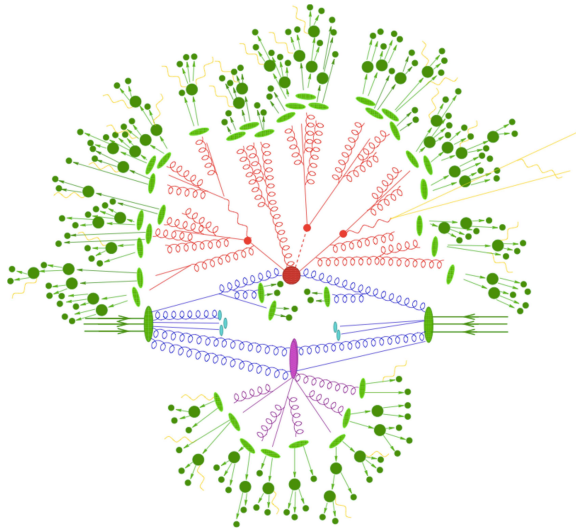


Figure 4.2: Sketch of a proton-proton collision as modelled by a Monte-Carlo event generator. Figure taken from [65].

gluons are radiated (red); this radiation is called final state radiation (FSR). A second interaction takes place (purple blob). The particles lose energy by radiation and hadronise when their energy is down to $\sim \Lambda_{\text{QCD}}$ (light green blobs) and the primary hadrons decay into stable particles (dark green blobs). Additionally photons and leptons can be radiated (yellow). The proton remnants are shown as cyan blobs. The high-energetic stable particles boosted in one direction are grouped into jets by different jet algorithms. To dig out certain signals (e.g. signals from Higgs or SUSY events), the experimentalists define selection cuts, such that the background events get suppressed whilst the signal events get enhanced. Depending on the analyses, these selection cuts define for example the allowed number of leptons/jets and allowed ranges for the p_T (momentum in the plane transverse to the beam pipe) of the objects, the missing transverse energy E_t^{miss} (carried away by undetected objects) or other kinematic variables.

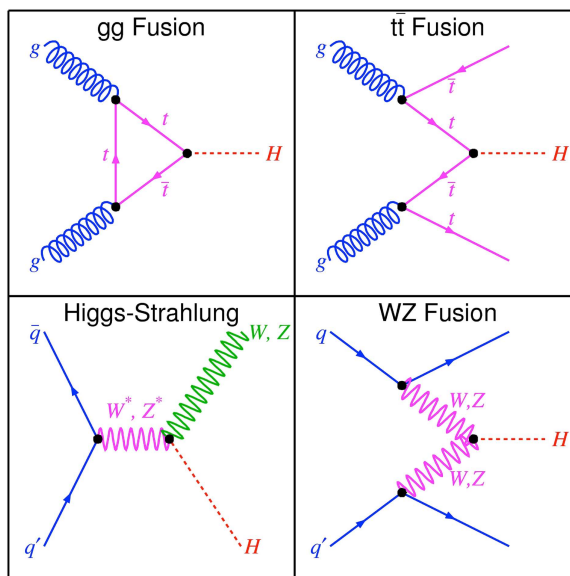


Figure 4.3: Feynman diagrams of the main Standard Model Higgs production processes at the LHC. Figure taken from [80].

4.2 Experimental results

4.2.1 Discovery of a Higgs boson

A new particle with a mass of ~ 126 GeV has been discovered by ATLAS [1] and CMS [2]. This particle is compatible with the Higgs boson postulated by the Standard Model (SM), but can also be interpreted in a variety of models beyond the SM (BSM models). At the LHC a light SM Higgs is produced dominantly in gluon fusion. The other contributing Higgs production modes are vector boson fusion, associated vector boson production (or Higgs-Strahlung) and ttH production, sketched in Fig. 4.3 (figure taken from [80]). The inclusive cross sections for SM Higgs production at 8 TeV are given in the left plot of Fig. 4.4. A SM Higgs with a mass of ~ 126 GeV can decay via many different decay modes; the decay branching ratios ($BR_{xx} = \Gamma_{xx}/\Gamma_{\text{tot}}$, where Γ_{xx} is the decay width of $H \rightarrow xx$ and Γ_{tot} is the total decay width) are given in the right plot of Fig. 4.4 (figure taken from [81]). The decay $H \rightarrow b\bar{b}$ has the largest branching ratio for a SM Higgs at ~ 126 GeV, however this mode suffers from a large hadronic background. Despite the smaller SM branching ratios, the Higgs boson has been discovered first in the cleaner channels $H \rightarrow \gamma\gamma$ (which is a loop-induced process), as well as in $H \rightarrow ZZ^{(*)} \rightarrow 4\ell$. With the full 2011 ($\sim 5 \text{ fb}^{-1}$ at 7 TeV) and 2012 ($\sim 20 \text{ fb}^{-1}$ at 8 TeV) datasets the excess in $H \rightarrow \gamma\gamma$ has a local significance of 7.4σ (ATLAS) [19] and 4.2σ (CMS) [20] and the excess in $H \rightarrow ZZ^{(*)} \rightarrow 4\ell$ has a local significance of 6.6σ (ATLAS) [82] and 6.8σ (CMS) [83]. The discovery is further corroborated, though with lower significance, by the $WW^{(*)}$ channel [84,85] and by the excess seen in $b\bar{b}$ by the Tevatron [86]. Recently also an excess in $H \rightarrow \tau\tau$ has been observed [87,88]. ATLAS and CMS measure the

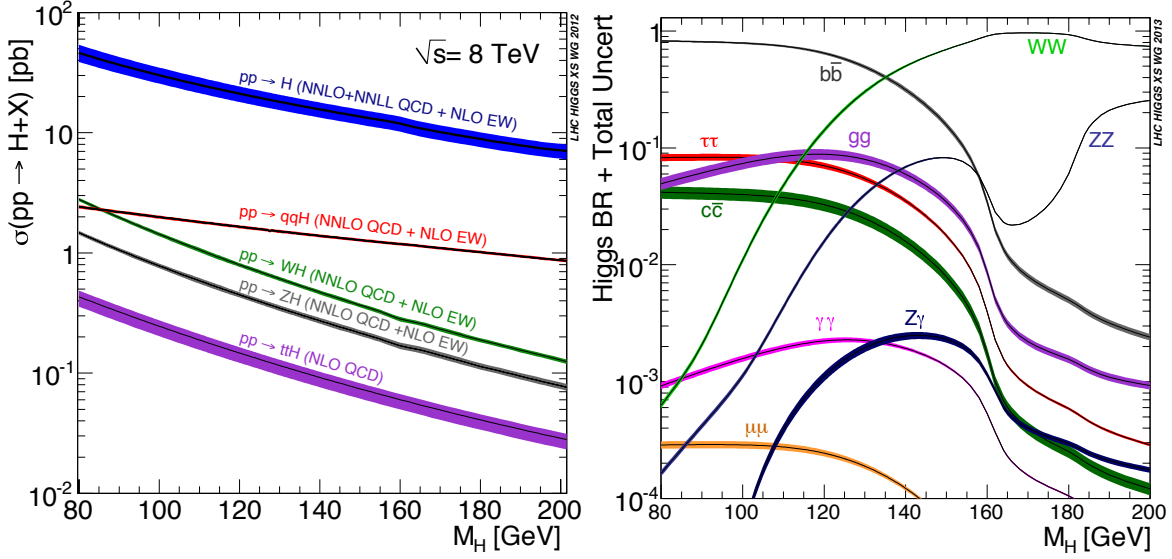


Figure 4.4: Left: Inclusive Standard Model Higgs boson production cross sections at 8 TeV. Right: Standard Model Higgs boson decay branching ratios. Figures taken from [81].

signal strength in the different decay channels, defined as the production cross section times the branching ratio normalized to the SM prediction

$$\mu_i = \frac{\sigma(pp \rightarrow H) \times BR(H \rightarrow i)}{\sigma^{\text{SM}}(pp \rightarrow H) \times BR^{\text{SM}}(H \rightarrow i)} \quad (4.2)$$

The results are summarised in Fig. 4.5 (left: ATLAS [89], right: CMS [70]). In the first data analysed by autumn 2012 ($\sim 5 \text{ fb}^{-1}$ at 7 TeV and $\sim 5 \text{ fb}^{-1}$ at 8 TeV) both experiments saw an enhancement of the di-photon channel compared to the SM. Including more data, the signal strength in the $\gamma\gamma$ channel observed by ATLAS [19] remains above the value expected in the SM (but is still compatible with the SM at the 2σ level), while the signal strength observed by CMS [20] is currently slightly below the SM level.

While not statistically significant at present, the deviations from the SM could be signs of new physics. Extensions of the SM predict Higgs bosons with modified couplings to gauge bosons and fermions. Furthermore BSM particles can occur inside loops and thus modify in particular the prediction for the decay process $H \rightarrow \gamma\gamma$ and the production process $gg \rightarrow H$. Since here the loop contributions of BSM particles do not have to compete with a SM-type tree-level contribution, these loop-induced quantities are of particular relevance for investigating possible deviations from the SM predictions.

The mass of the discovered signal in the Higgs boson searches is measured mainly in the $\gamma\gamma$ and the $ZZ^{(*)}$ channels. Currently, the combined mass measurement from ATLAS is $M_H = 125.5 \pm 0.2 \pm 0.6 \text{ GeV}$ [90] and from CMS $M_H = 125.7 \pm 0.3 \pm 0.3 \text{ GeV}$ [91]. Adding systematic and statistical errors in quadrature and determining the weighted average between the ATLAS and CMS measurements one gets $m_h^{\text{exp}} = 125.64 \pm 0.35 \text{ GeV}$.

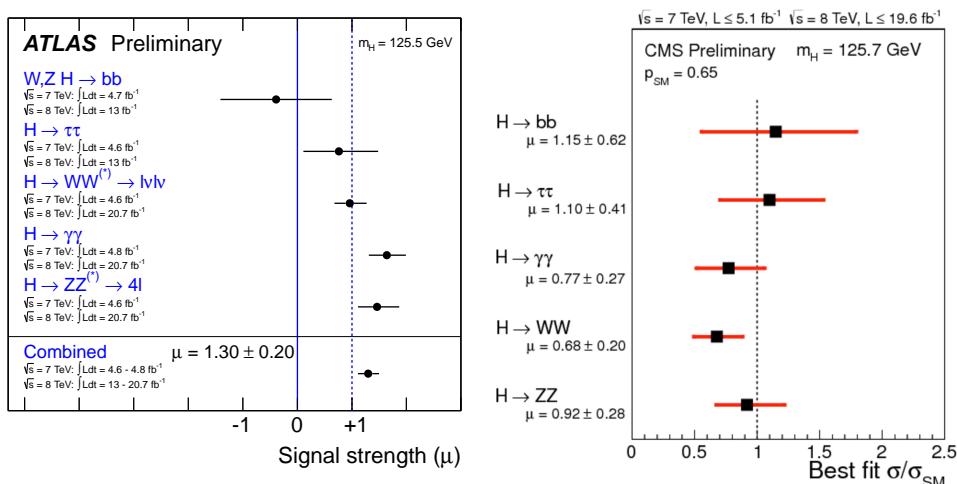


Figure 4.5: Measurements of the signal strength parameter μ in the individual channels by ATLAS (left) and CMS (right). Figures taken from [70, 89].

The experiments also provide evidence for the spin-0 nature of the discovered Higgs boson [92, 93]. The measurements of the \mathcal{CP} properties of the discovered boson are experimentally difficult. While the detected signal in processes involving the Higgs coupling to gauge bosons disfavors a pure \mathcal{CP} -odd state, the ATLAS and CMS measurements have a limited sensitivity to the possible effects of a \mathcal{CP} -odd admixture, as it could occur for example in the MSSM with complex parameters.

In order to investigate whether the observed Higgs boson is compatible with the one predicted in the SM or a Higgs boson of a new physics model, high-precision measurements of the properties of the signal are necessary.

4.2.2 Searches for SUSY Higgs bosons

As discussed earlier, the discovered Higgs boson can also be interpreted as one of the Higgs bosons of the MSSM or the NMSSM. Both SUSY models permit in principle the interpretation of the discovered state as the lightest or the second lightest \mathcal{CP} -even Higgs. While the interpretation of the signal as the second lightest \mathcal{CP} -even Higgs state is very constrained in the MSSM (as discussed below), it remains a viable option in models with extended Higgs sectors, such as the NMSSM. Besides the state that is identified with the signal at 125.6 GeV, both SUSY models predict the existence of several additional Higgs bosons (in total 5 Higgs bosons in the MSSM and 7 Higgs bosons in the NMSSM, as explained in Sect. 2.2 and Sect. 2.3), which are searched for at the LHC.

Within the MSSM, it is interesting to note that a mass value as high as 125.6 GeV for the lighter \mathcal{CP} -even Higgs boson implies that M_A has to be in the decoupling region, $M_A \gtrsim 200$ GeV, which in turn has the consequence that the state at about 125.6 GeV has SM-like couplings [48, 54]. This implies that no large deviations from the SM prediction are expected in this interpretation. If the light \mathcal{CP} -even Higgs boson is at ~ 125.6 GeV, the heavier MSSM Higgs bosons could be within but also outside of the LHC reach.

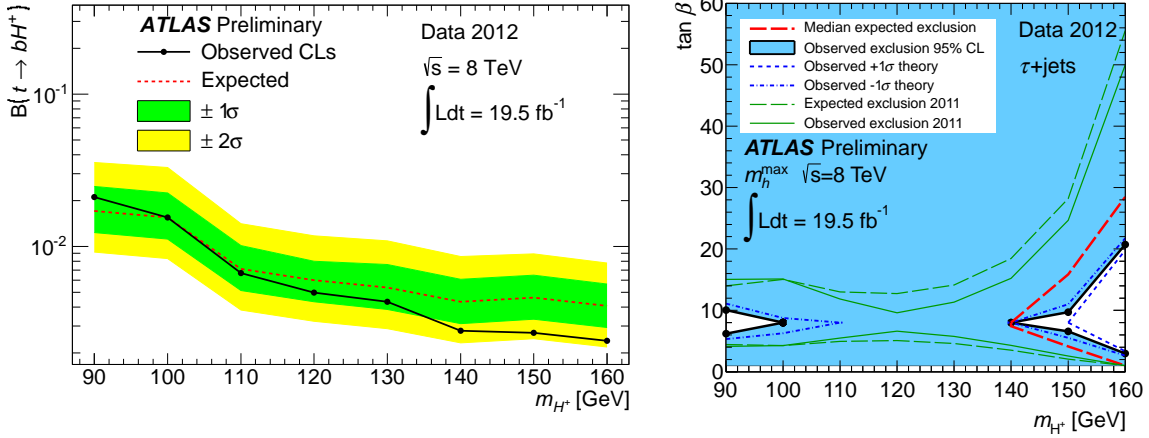


Figure 4.6: Left: Upper limit on $BR(t \rightarrow bH^+)$ from the light charged Higgs boson search at ATLAS (with the assumption that $BR(H^+ \rightarrow \tau\nu) = 1$). Right: Interpretation of the limits in the context of the MSSM m_h^{\max} scenario with $\mu = 200$ GeV. Figures taken from [55].

If the discovered state would be the heavy \mathcal{CP} -even Higgs state of the MSSM², the MSSM would be in the non-decoupling region which implies that all other Higgs bosons would be relatively light: the \mathcal{CP} -odd and the charged Higgs bosons would be of similar mass as the heavy \mathcal{CP} -even Higgs, while the mass of the light \mathcal{CP} -even Higgs would be below 125.6 GeV. The mass of the light \mathcal{CP} -even state could even be below the LEP limit for a SM-like Higgs of ~ 114 GeV, avoiding this limit due to reduced couplings of h to vector bosons.

ATLAS and CMS search for additional SUSY Higgs bosons. The ATLAS searches for the charged Higgs set stringent limits on the MSSM parameter space [55]. A light charged Higgs in the MSSM is mainly produced at the LHC via the decay $t \rightarrow H^+b$ and decays (for $\tan \beta > 3$) mainly through $H^+ \rightarrow \tau\nu$. Assuming $BR(H^+ \rightarrow \tau\nu) = 1$, ATLAS set strong limits on $BR(t \rightarrow bH^+)$, as shown in the left plot of Fig. 4.6. This limit can be interpreted in the context of the ' m_h^{\max} scenario' [54] (a benchmark scenario in which the radiative corrections are such that M_h are maximised for fixed values of m_t , $\tan \beta$ and M_{SUSY}) and leads to the exclusion as shown in the right plot of Fig. 4.6. This limit strongly constrains the interpretation of the observed Higgs signal as the heavy \mathcal{CP} -even MSSM Higgs.

In the NMSSM the mass relations between the Higgs bosons are altered compared to the MSSM by the additional singlet, and it is possible to have a SM-like second-lightest Higgs, while the charged Higgs boson can be much heavier in this case. In addition the charged Higgs decay modes are modified, e.g. the decay $H^\pm \rightarrow A_1 W^\pm$ can have a large branching ratio. Therefore the interpretation of the signal as the second lightest \mathcal{CP} -even Higgs is less constrained in the NMSSM.

²This scenario is challenged by the recent ATLAS bound on light charged Higgs bosons [55] as we will discuss below.

4.2.3 Direct SUSY searches

Extensive direct searches for SUSY particles are performed by ATLAS and CMS. No indication of physics beyond the SM has been seen so far and limits are set on the masses of SUSY particles. However, the reported limits imply strong assumptions on the model parameters, e.g. relations between the masses of the SUSY particles, and caution is required when using these limits in different MSSM (or NMSSM) realisations.

The general MSSM has more than 100 parameters, and it is therefore extremely difficult for the experiments to present their results in a generic way. Therefore limits are typically presented in constrained models where the parameter space is reduced (by several motivated model assumptions) to only a few free parameters. One example often used to present the experimental limits is the CMSSM, introduced in Sect. 2.2.5. As an example, the exclusion limits from the 8 TeV ATLAS searches in the m_0 - $m_{1/2}$ plane of the CMSSM³ are shown in the left plot of Fig. 4.7 (figure taken from [67]).

Another approach employed by the experiments is to present limits in so called simplified models [94–96], which restrict the particle content to the particles appearing in the particular topologies considered in a specific search. In the right plot of Fig. 4.7, we show again as an example the results from the 8 TeV ATLAS searches, here on the $m_{\tilde{g}}-m_{\tilde{\chi}_1^0}$ plane of a simplified model, in which a pair of gluinos decay (with 100% branching ratio) via off-shell stops to four top quarks and two of the lightest neutralinos. In general it is difficult to map the search results in simplified models to the situation in a more realistic model. A method to use simplified model limits to constrain general SUSY models is discussed in chapter 8.

The most stringent limits are set on the masses of the first and second generation squarks and the gluino, which go beyond ~ 1 TeV⁴. Substantially weaker limits have been reported for the particles of the other MSSM sectors, so that third-generation squarks, stops and sbottoms, as well as the uncoloured SUSY particles, are significantly less constrained by LHC searches, and LEP limits still give relevant constraints.

4.2.4 Precision measurements: M_W and m_t

Electroweak precision observables, such as the W boson mass, are highly sensitive to quantum corrections of physics beyond the SM as they are measurable with high precision. They are therefore a powerful tool to test the SM and to derive strong indirect constraints on the parameter space of possible extensions, complementary to the direct searches for BSM particles carried out at the LHC (see Sect. 4.2.3). In order to make use of the strength of electroweak precision tests, both a precise theoretical prediction as well as a precise experimental measurement of M_W are of central importance.

The accuracy of the measurement of the W boson mass has been significantly improved with the latest results presented by CDF [98] and DØ [99]. Together with the

³Note that not the full plane can accommodate for a Higgs at 125.6 GeV and one can impose additional constraints by requiring the light Higgs to be in the experimentally allowed region.

⁴However these limits depend on the model assumptions. Relaxing these assumptions, squarks can still be significantly lighter [97].

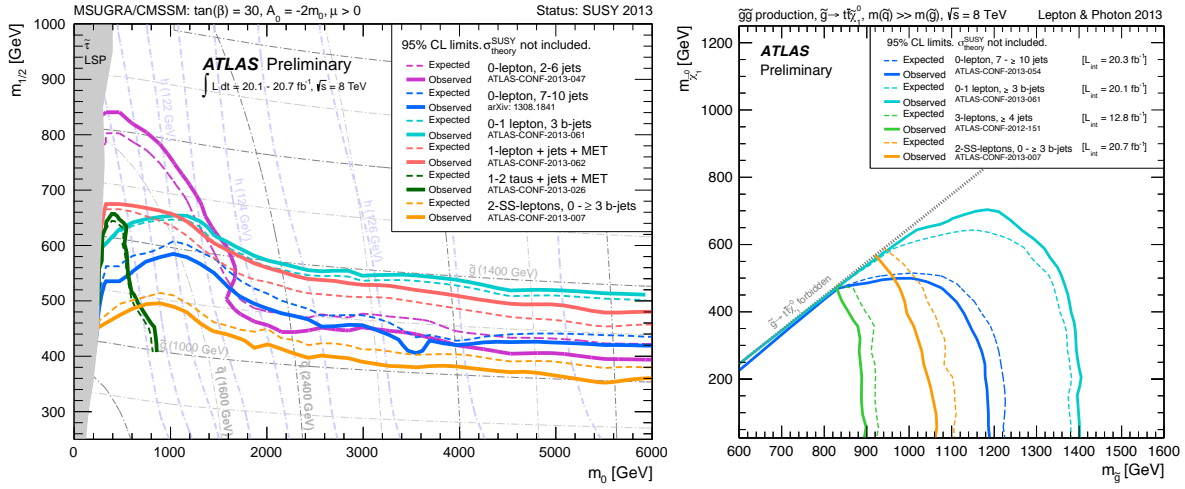


Figure 4.7: Left: Exclusion limits from the 8 TeV ATLAS searches on the m_0 - $m_{1/2}$ plane of the CMSSM (with $\tan\beta = 30$, $A_0 = -2m_0$, $\mu > 0$). Right: Exclusion limits from the 8 TeV ATLAS searches on the $m_{\tilde{g}}$ - $m_{\tilde{\chi}_1^0}$ plane of a simplified model, in which a pair of gluinos decay (with 100% branching ratio) via off-shell stops to four top quarks and two lightest neutralinos. The figures are taken from [67].

results obtained at LEP [75] this gives rise to the latest world average of [76, 100]

$$M_W^{\text{exp}} = 80.385 \pm 0.015 \text{ GeV}, \quad (4.3)$$

i.e. to a relative experimental accuracy of better than 2×10^{-4} . The measurement is expected to be further improved by including the full dataset from the Tevatron and by future LHC measurements.

The improved measurement of the top-quark mass,

$$m_t^{\text{exp}} = 173.2 \pm 0.9 \text{ GeV}, \quad (4.4)$$

at the Tevatron [101] and the LHC [102–109]⁵ has improved the accuracy of the theoretical prediction for M_W , since the experimental error of the input parameter m_t constitutes a dominant source of (parametric) uncertainty in the theoretical prediction, see e.g. Ref. [111]. Unfortunately, a considerable further improvement of the m_t^{exp} value at the LHC is unlikely.

As discussed in Sect. 3.2.3, mass parameters such as m_t can be defined in different renormalization schemes, examples are the $\overline{\text{MS}}$ mass or the pole mass. It is not straightforward to relate the mass parameter m_t measured at hadron colliders (by using information about the decay products) to a theoretically well-defined parameter, such as the $\overline{\text{MS}}$ mass. The parameter measured with high precision at the Tevatron and the LHC is expected to be close to the top pole mass Refs. [112, 113]. In the calculation of

⁵While finalizing this thesis a combination of Tevatron and LHC measurements of m_t became available [110]. The combined value is $173.34 \pm 0.27 \pm 0.71 \text{ GeV}$.

M_W (discussed in chapter 5) the input parameter m_t corresponds to the pole mass, and we adopt the interpretation of the measured value as the pole mass.

The project to build a linear e^+e^- collider, called International Linear Collider (ILC), has been discussed and developed for many years. Although no final decision has been made yet, there is a strong interest by the Japanese community to host the ILC. The ILC would be an excellent machine for high precision measurements; the reasons are (among other things) its clean experimental environment, the tunable energy and the possibility to produce polarised electron and positron beams. At the ILC, the top mass could be obtained from scanning the top-antitop threshold. This would give a significantly improved m_t^{exp} value, which can be translated to the $\overline{\text{MS}}$ mass by a well-defined procedure. Besides other important electroweak precision observables (which are not directly relevant for this work and therefore not further discussed), also M_W can be determined very precisely at the ILC using different methods, running either at the WW threshold or at higher energies (using kinematic reconstruction of the decay products). The ILC estimates for the achievable precision are: $\Delta m_t^{\text{ILC}} = 0.1 \text{ GeV}$ and $\Delta M_W^{\text{ILC}} \sim 2.5 - 5 \text{ MeV}$ [114].

4.2.5 B -physics observables and $(g - 2)_\mu$

A powerful method to constrain the parameter space of BSM models is provided by flavour-physics observables, in particular these from B -physics. Low-energy experiments measure, for example, the rates of rare decays of B mesons; these processes have a small branching ratio in the SM, and new physics contributions can be sizeable. By comparing the measurement of the decay rates with the predictions of the SM, and of its extensions, models can be tested, and the parameter space can be constrained. The specific processes which are most important for our work later are: $B \rightarrow X_s \gamma$, $B_s \rightarrow \mu^- \mu^+$ and $B_u \rightarrow \tau \nu_\tau$. The rare process $B \rightarrow X_s \gamma$ occurs at one-loop level in the SM and the SUSY contributions from charged Higgs bosons, charginos and squarks can be of comparable size as the SM prediction. $B_u \rightarrow \tau \nu_\tau$ is a helicity suppressed process in the SM. In the (N)MSSM (for high $\tan \beta$) charged Higgs exchange at tree-level can give large contributions. The process $B_s \rightarrow \mu^- \mu^+$, which occurs at the one-loop level in the SM, was observed for the first time by LHCb and CMS last year [115, 116]. The SUSY contributions (e.g. by neutral Higgs boson exchange) to $B_s \rightarrow \mu^- \mu^+$ can be sizeable. The measured values used for the B -physics observables which we include are given in chapter 6 and chapter 7. Among the low-energy observables we also include the anomalous magnetic moment of the muon, $a_\mu = 1/2 (g - 2)_\mu$, which shows a deviation of more than 3σ between the experimental measurement and the SM prediction [117, 118]. Possible SUSY contributions here include loop diagrams with neutralino-smuon and chargino-sneutrino exchange.

Chapter 5

The W boson mass in the SM, the MSSM and the NMSSM

Parts of this chapter (in particularly Sect. 5.7) are based on Ref. [35], and in these parts we largely follow this article. Another publication, Ref. [119], is in preparation. I have been heavily involved in obtaining all results presented in this chapter: I have performed the described calculation of M_W in the SM, the MSSM and the NMSSM and I have set up the computational framework (written in Mathematica and Fortran) for the numerical evaluation. I studied the prediction for M_W in the SM, analysed the size of the MSSM contributions and the genuine NMSSM effects. I performed the scans in the MSSM case. Further I studied the effect of constraints from Higgs and SUSY searches on the M_W prediction in the MSSM as well as the impact of possible future experimental results. I have done all the plots in this chapter apart from the ones in Fig. 5.11, Fig. 5.14, Fig. 5.16 and Fig. 5.17, for which I provided the data but did not produce the final plots. For loop calculations within the NMSSM, a model file was developed (see Ref. [32]) which was used for the work in this chapter and is therefore described here. I have not been part of implementing the model file, but participated in some of the validation checks. The description of the computational framework is partially based on Ref. [32]. The description of the M_W calculation in the SM and the MSSM are partially based on text which I have written before and that appeared in Ref. [34].

5.1 Introduction

Electroweak precision observables are highly sensitive to quantum corrections of physics beyond the SM. They are therefore a powerful tool to test the SM and to derive strong indirect constraints on the parameter space of possible extensions. In this context, the relation between the W boson mass, M_W , and the Z boson mass, M_Z , in terms of the fine-structure constant, α , the Fermi constant, G_μ , and the parameters entering via loop contributions plays a crucial role. As already discussed in Sect. 4.2.4, the accuracy of the measurement of the W boson mass ($M_W^{\text{exp}} = 80.385 \pm 0.015$ GeV) has been significantly improved with the latest results presented by CDF [98] and DØ [99]. Since the largest

parametric uncertainty in the theoretical M_W prediction arises from the top mass, also the accuracy of the theoretical M_W prediction improved with the latest m_t measurements at the Tevatron [101] and the LHC [102–109]. The top quark mass used in our evaluation corresponds to the pole mass. In our results it could easily be re-expressed in terms of a properly defined short distance mass such as the $\overline{\text{MS}}$ or $\overline{\text{DR}}$ mass. The parameter measured via direct reconstruction at the Tevatron and the LHC is expected to be close to the top pole mass, and we adopt this interpretation in the following. For a discussion of the systematic uncertainties arising from the difficulties to relate the measured mass parameter to the pole mass see e.g. Refs. [112, 113].

Particularly with regard to the very precise experimental measurements of M_W and m_t and the prospect of further improvement in the next years (see Sect. 4.2.4), a precise theoretical determination of M_W is of central importance for electroweak precision tests. Within the SM, the interpretation of the discovered new state as the SM Higgs boson implies that there is no unknown parameter anymore in the prediction for M_W . This fact considerably sharpens the comparison both with the experimental result for M_W and with predictions in extensions of the SM.

For the theoretical prediction of M_W the quantity Δr is calculated, which summarizes all (non-QED) quantum correction to the muon decay amplitude. Besides its importance as for electroweak precision tests, Δr is needed whenever a theoretical prediction is parametrized in terms of the Fermi constant G_μ , instead of M_W or $\alpha_{\text{em}}(M_Z)$.

In this chapter we present the calculation of the prediction for M_W in the SM, the MSSM (with complex parameters) and the NMSSM. The calculation within the NMSSM is described in detail, which contains also the SM and MSSM contributions.

Within the SM the full one-loop [120,121] and two-loop [122–133], as well as the leading higher-order corrections [134–142] are known. In addition a convenient fitting formula for M_W containing all numerically relevant contributions has been developed [143], and in Ref. [144] a corresponding formula has been given, approximating the two-loop electroweak contributions on their own. In the MSSM the one-loop result [145–156] and leading two-loop corrections have been obtained [157–160]. In the MSSM also the effects of non-minimal flavour violation [161] and \mathcal{CP} -violating phases [156, 162] on M_W have been studied. Within the NMSSM, the one-loop calculation has been performed in Ref. [163].

Our evaluation of M_W in the MSSM and the NMSSM gives the currently most precise predictions, consisting of complete one-loop calculations (without flavour violation in the sfermion sector [161]), combined with all known higher-order corrections of SM and SUSY type. In the MSSM we work in the general case of complex parameters. Complex phases in the NMSSM are not included in this work. Compared to earlier results, the (N)MSSM prediction used in the present analysis has been improved in several respects: the one-loop results have been reevaluated and coded in a more flexible way, which permits an improved treatment of regions of parameter space that can lead to numerical instabilities and furthermore provides the functionality to easily implement results in other SUSY models. The incorporation of the state-of-the-art SM result has been improved using the expressions given in Ref. [144]. Furthermore all known SUSY corrections are used,

in particular also the Higgsino corrections calculated in Refs. [159,160] (the treatment of these corrections within the NMSSM prediction is discussed in Sect. 5.3.3). Our `Mathematica` code for the M_W prediction in the SM, the MSSM and the NMSSM, provides the flexibility that allows us to analyse the functions at an analytic level. For a faster evaluation we implemented our SM and MSSM results additionally into a `Fortran` code, which is particularly useful for parameter scans.

In the numerical evaluation at the end of this chapter, we compare the prediction of the SM with that in the MSSM and the NMSSM, taking into account the latest experimental results. Our analysis within the MSSM updates previous studies, see in particular Refs. [156,164]. In the MSSM we perform scans over the relevant SUSY parameters and we analyse in detail the impact of different SUSY sectors on the prediction for M_W . Further we discuss the prediction for M_W in view of the discovery of the signal in the Higgs searches at ATLAS and CMS. We also investigate possible effects of either future limits from SUSY searches at the LHC or of the detection of a scalar partner of the top quark. The effect of complex phases in the MSSM is analysed. The size of the higher-order corrections, both of SM and SUSY type, is studied. In the NMSSM we discuss possible genuine NMSSM contributions to the W -boson mass and differences to the MSSM prediction.

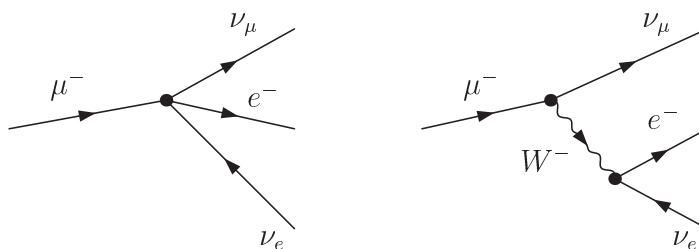


Figure 5.1: Left: Muon decay in the Fermi model, tree level diagram with four-fermion vertex. Right: Muon decay in the electroweak SM, tree level diagram with W boson exchange.

5.2 Determination of the W boson mass

Muons decay via the weak interaction almost exclusively into $e\bar{\nu}_e\nu_\mu$ [165]. The decay was originally described within the Fermi model, which is a low-energy effective theory that emerges from the SM in the limit of vanishing momentum transfer (left diagram in Fig. 5.1). The Fermi constant, G_μ , is determined with high accuracy from precise measurements of the muon life time [166] and the corresponding Fermi-model prediction including QED corrections up to $O(\alpha^2)$ for the point-like interaction [167–171]. Comparison of the muon-decay amplitude in the Fermi model and in the SM or extensions of it (tree-level diagram at the right side of Fig. 5.1) yields the relation

$$\frac{G_\mu}{\sqrt{2}} = \frac{e^2}{8s_W^2 M_W^2} (1 + \Delta r). \quad (5.1)$$

Here Δr represents the sum of all loop diagrams contributing to the muon-decay amplitude after splitting off the Fermi-model type virtual QED corrections,

$$\Delta r = \sum_i \Delta r_i, \quad (5.2)$$

with

$$\mathcal{M}_{\text{Loop},i} = \Delta r_i \mathcal{M}_{\text{Born}}. \quad (5.3)$$

This decomposition is possible since after subtracting the Fermi-model QED corrections, masses and momenta of the external fermions can be neglected, which allows the reduction of all loop contributions to a term proportional to the Born matrix element, see Refs. [120, 129]. By rearranging Eq. (5.1), the W boson mass can be calculated via

$$M_W^2 = M_Z^2 \left(\frac{1}{2} + \sqrt{\frac{1}{4} - \frac{\alpha\pi}{\sqrt{2}G_\mu M_Z^2} (1 + \Delta r)} \right). \quad (5.4)$$

In different models, different particles can contribute as virtual particles in the loop diagrams to the muon-decay amplitude. Therefore, the quantity Δr depends on the specific model parameters, and Eq. (5.4) provides a model-dependent prediction for the

W boson mass. The quantity Δr itself does depend on M_W as well; hence Eq. (5.4) cannot be solved directly. In practice the value M_W as a solution of Eq. (5.4) is obtained by iteration. In most cases this procedure converges quickly and only a few iterations are necessary.

5.3 Calculation of Δr

In order to exploit M_W as a precision observable providing sensitivity to quantum effects it is crucial that the theoretical predictions for Δr are sufficiently precise with respect to the present and expected future experimental accuracies of M_W . In this section we describe the calculation of Δr . The one-loop calculation is discussed simultaneously for the MSSM and the NMSSM. When describing the incorporation of higher-order corrections we focus on the NMSSM, but comment also on the MSSM case. More details about the SM and MSSM calculations can be found in Refs. [34,156] and references therein.

5.3.1 One-loop formula for Δr

The one-loop contributions to Δr consist of the W boson self-energy, vertex and box diagrams, and the related counter terms (CT),

$$\begin{aligned} \Delta r^{(\alpha)} &= W \text{ Self-energy} + W \text{ Self-energy CT} + \text{Vertex} + \text{Vertex CT} + \text{Box} \\ &= \frac{\Sigma_T^{WW}(0)}{M_W^2} + \left(-\delta Z_W - \frac{\delta M_W^2}{M_W^2} \right) + \text{Vertex} \\ &\quad + \left(2\delta Z_e - 2\frac{\delta s_w}{s_w} + \delta Z_W + \frac{1}{2}(\delta Z^\mu + \delta Z^e + \delta Z^{\nu\mu} + \delta Z^{\nu e}) \right) + \text{Box}. \end{aligned} \quad (5.5)$$

Here Σ_T denotes the transverse part of a gauge boson self-energy, δM_W is the counterterm for the W boson mass, δZ_e and δs_w are the renormalization constants for the electric charge and the (sine of the) weak mixing angle, respectively, while the other δZ denote field renormalization constants. Since the W boson appears only as a virtual particle, its field renormalization constant δZ_W drops out in the Δr formula. The box diagrams are themselves UV-finite in a renormalizable gauge.

Inserting the on-shell renormalization conditions ensures that Eq. (5.1) corresponds to the relation between the physical masses of the W and Z bosons and we find (neglecting the masses of the external fermions)

$$\begin{aligned} \Delta r^{(\alpha)} &= \frac{\Sigma_T^{WW}(0) - \text{Re}(\Sigma_T^{WW}(M_W^2))}{M_W^2} + \Pi^{AA}(0) - \frac{c_w^2}{s_w^2} \text{Re} \left[\frac{\Sigma_T^{ZZ}(M_Z^2)}{M_Z^2} - \frac{\Sigma_T^{WW}(M_W^2)}{M_W^2} \right] \\ &\quad + 2 \frac{\text{sgn } s_w}{c_w} \frac{\Sigma_T^{AZ}(0)}{M_Z^2} + \text{Vertex} + \text{Box} - \frac{1}{2} \text{Re}(\Sigma_L^e(0) + \Sigma_L^\mu(0) + \Sigma_L^{\nu e}(0) + \Sigma_L^{\nu\mu}(0)). \end{aligned} \quad (5.6)$$

We adopt here the sign conventions for the covariant derivative used in `FeynArts` [36–41], which are different for the SM and the MSSM/NMSSM. Accordingly, sgn (the sign of the term involving the $SU(2)$ coupling in the covariant derivative) in Eq. (5.6) is $\text{sgn} = -1$ in the SM and $\text{sgn} = +1$ in the MSSM and NMSSM. The one-loop contributions to Δr in the SM, the MSSM and the NMSSM are discussed in detail in Sects. 5.3.2 and 5.3.3.

At the one-loop level, the quantity Δr can be split into three parts

$$\Delta r^{(\alpha)} = \Delta\alpha - \frac{c_w^2}{s_w^2} \Delta\rho + \Delta r_{\text{rem}}. \quad (5.7)$$

The shift of the fine structure constant $\Delta\alpha$ arises from the charge renormalization which contains the contributions from light fermions (see discussion below in Sect. 5.3.2). The quantity $\Delta\rho$ contains loop corrections to the ρ parameter [172], which describes the ratio between neutral and charged weak currents, and can be written as

$$\Delta\rho = \frac{\Sigma_T^{ZZ}(0)}{M_Z^2} - \frac{\Sigma_T^{WW}(0)}{M_W^2}. \quad (5.8)$$

This quantity is sensitive to the mass splitting between the isospin partners in a doublet [172], which leads to a sizeable effect in the SM in particular from the heavy fermion doublet. While $\Delta\alpha$ is a pure SM contribution, $\Delta\rho$ can get large contributions also from SUSY particles, in particular the superpartners of the heavy quarks. All other terms, both of SM and SUSY type, are contained in the remainder term Δr_{rem} .

5.3.2 One-loop Δr in the SM

To obtain the one-loop result in the SM, self-energy, vertex and box diagrams need to be calculated. The SM one-loop calculation has been discussed in literature already many years ago [120,121]. For the details of the calculation in the SM, we refer to Refs. [34,129] where the occurring diagrams and their calculation is discussed in detail.

Here we only want to point out two peculiarities about the SM calculation. As mentioned above the QED corrections to the Fermi model are already included in the definition of G_μ and have to be subtracted, therefore the QED SM box diagram minus the QED 'box' diagram in the Fermi model is needed to obtain Δr . While the SM box diagram is IR-divergent but UV-finite, the 'box' diagram of the Fermi model is both IR- and UV-divergent, which makes the calculation tricky. For all other SM one-loop diagrams Dimensional Regularization is used. However, if one uses Dimensional Regularization, the Chisholm identity (used to reduce the spinor structure of the box diagrams to one of the Born matrix element), which holds only in four dimensions, cannot be applied. The original analysis of this calculation is given in Refs. [120,121]. We follow Ref. [129] and calculate the diagram of the effective theory using Pauli-Villars Regularization.

Another difficulty in the SM one-loop calculation arises from the contributions of light fermions to the term $\Pi^{AA}(0)$ in the charge renormalization, see Eq. (3.7), since the calculation of

$$\Pi_{\text{light fermions}}^{AA}(0) = \left. \frac{\partial \Sigma_T^{AA}(k^2)}{\partial k^2} \right|_{k^2=0, m_f \rightarrow 0} \quad (5.9)$$

yields terms proportional to $\log(\mu^2/m_f^2)$ (μ is the renormalization scale, see Sect. 3.2), that diverge for vanishing fermion masses. This term can be rewritten as

$$\Pi_{\text{light fermions}}^{AA}(0) = \Delta\alpha + \text{Re} \Pi_{\text{light fermions}}^{AA}(M_Z^2), \quad (5.10)$$

where the term $\text{Re } \Pi_{\text{light fermions}}^{AA}(M_Z^2)$ can be calculated straightforward by neglecting the light fermion masses and $\Delta\alpha$ is given by

$$\Delta\alpha = \Pi_{\text{light fermions}}^{AA}(0) - \text{Re } \Pi_{\text{light fermions}}^{AA}(M_Z^2). \quad (5.11)$$

This UV-finite quantity gives the corrections to the fine-structure constant $\alpha = e^2/4\pi$ (from Eq. (2.4)) and describes the running of the electromagnetic coupling from $q^2 = 0$, where light fermion masses set the scale, to the electroweak scale $q^2 = M_Z^2$.

The hadronic contribution can not be theoretically determined, since the masses of the light quarks are not known with sufficient accuracy, but $\Delta\alpha_{\text{had}}$ can be extracted from experimental data. $\Delta\alpha_{\text{had}}$ is related to the measurable quantity

$$R(s) = \frac{\sigma(e^+e^- \rightarrow A \rightarrow \text{hadrons})}{\sigma(e^+e^- \rightarrow A \rightarrow \mu^+\mu^-)} \quad (5.12)$$

via the dispersion relation [173]

$$\Delta\alpha_{\text{had}} = -\frac{\alpha}{3\pi} M_Z^2 \text{Re} \left[\int_{4m_\pi^2}^{\infty} ds \frac{R(s)}{s(s - M_Z^2 - i\epsilon)} \right]. \quad (5.13)$$

Various recent evaluations of $\Delta\alpha_{\text{had}}$ are summarised in [165].

The calculation of the leptonic contributions to $\Delta\alpha$ has been done up to three-loop order [174]. The value for $\Delta\alpha$ used in our evaluation is $\Delta\alpha = \Delta\alpha_{\text{lep}} + \Delta\alpha_{\text{had}}$ with $\Delta\alpha_{\text{lep}} = 0.031497686$ [174] and $\Delta\alpha_{\text{had}}(M_Z) = 0.02757$ [117].

5.3.3 One-loop Δr in the MSSM and the NMSSM

The contributions to Δr in the MSSM and the NMSSM consist, besides the ones with SM fermions and gauge-bosons in the loop (which are not discussed here, see Sect. 5.3.2 and [34, 129]), of a large number of additional self-energy, vertex and box diagrams containing sfermions, (SUSY) Higgs bosons, charginos and neutralinos in the loop. The one-loop calculation of Δr in the (complex) MSSM has been discussed in detail in the literature, see e.g. [156]. The calculation in the NMSSM and in the MSSM are very similar, however the results get modified from differences in the Higgs and the neutralino sectors.

The gauge-boson self-energy diagrams containing sfermions (depicted in Fig. 5.2) are identical in the MSSM and the NMSSM. Their contribution to Δr is finite by itself.

The contributions from the Higgs sector differ in the MSSM and the NMSSM. The SUSY Higgs bosons enter only in gauge boson self-energy diagrams, since we neglected the masses of the external fermions. The contributing diagrams are sketched in Fig. 5.3¹. These contributions are not finite by themselves. Only if one considers all gauge boson and Higgs contributions to the gauge boson self-energy diagrams, the vertex diagrams and vertex counterterm diagrams, the divergencies cancel and one finds a finite result.

¹Note that in our convention A is used to denote both the photon and the \mathcal{CP} -odd Higgs in the MSSM. In the context of Higgs decays we denote the photon γ .

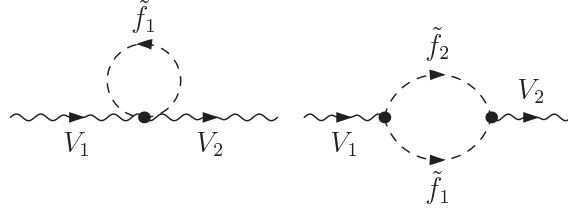


Figure 5.2: Generic (N)MSSM gauge boson self-energy diagrams with a sfermion loop with $V_1, V_2 = A, Z, W^\pm$ and $\tilde{f}_1, \tilde{f}_2 = \tilde{\nu}, \tilde{l}, \tilde{u}, \tilde{d}$.

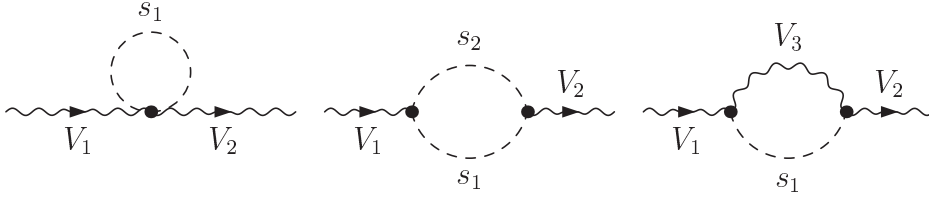


Figure 5.3: Generic (N)MSSM one-loop gauge boson self-energy diagrams with gauge bosons, Higgs and Goldstone bosons in the loop with $V_1, V_2, V_3 = A, Z, W^\pm$. In the MSSM $s_1, s_2 = h, H, A, H^\pm, G, G^\pm$ and in the NMSSM $s_1, s_2 = h_1, h_2, h_3, a_1, a_2, H^\pm, G, G^\pm$.

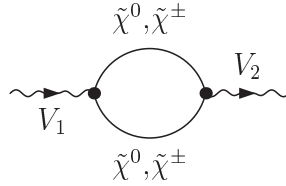


Figure 5.4: Generic (N)MSSM gauge boson self-energy diagram with a chargino/neutralino loop with $V_1, V_2 = A, Z, W^\pm$, and $\tilde{\chi}^\pm = \tilde{\chi}_{1,2}^\pm$. In the MSSM $\tilde{\chi}^0 = \tilde{\chi}_{1,2,3,4}^0$, in the NMSSM $\tilde{\chi}^0 = \tilde{\chi}_{1,2,3,4,5}^0$.

Charginos and neutralinos enter in gauge boson self-energy diagrams (depicted in Fig. 5.4), fermion self-energy diagrams (depicted in Fig. 5.5), vertex diagrams (depicted in Fig. 5.6, the analogous vertex corrections exist also for the other vertex) and box diagrams (depicted in Fig. 5.7). The contributions from the chargino/neutralino sector are modified in the NMSSM compared to the MSSM, due to the existence of a fifth neutralino. In both models the vertex contribution from the chargino and neutralino sector, together with the chargino/neutralino contributions to the vertex counter term, containing gauge boson and fermion self-energies, is finite. Each box-diagram is UV-finite by itself.

In order to determine the contribution to Δr from a particular loop diagram, the Born amplitude has to be factored out of the one-loop muon decay amplitude, as shown in Eq. (5.3). While most loop diagrams directly give a result proportional to the Born amplitude, more complicated spinor structures that do not occur in the SM case arise from box diagrams containing neutralinos and charginos. The spinor chains that occur

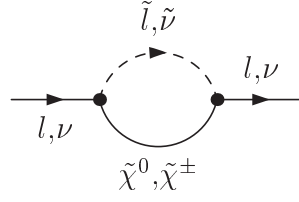


Figure 5.5: Generic (N)MSSM fermion self-energy diagram with a chargino/neutralino contribution. \tilde{l} and $\tilde{\nu}$ are the superpartners of the lepton l and the neutrino ν and $\tilde{\chi}^\pm = \tilde{\chi}_{1,2}^\pm$. In the MSSM $\tilde{\chi}^0 = \tilde{\chi}_{1,2,3,4}^0$, in the NMSSM $\tilde{\chi}^0 = \tilde{\chi}_{1,2,3,4,5}^0$.

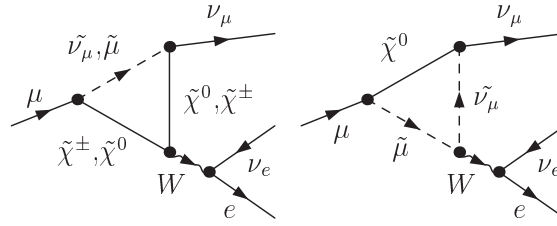


Figure 5.6: Generic vertex diagrams in the (N)MSSM with $\tilde{\chi}^\pm = \tilde{\chi}_{1,2}^\pm$. In the MSSM $\tilde{\chi}^0 = \tilde{\chi}_{1,2,3,4}^0$, in the NMSSM $\tilde{\chi}^0 = \tilde{\chi}_{1,2,3,4,5}^0$.

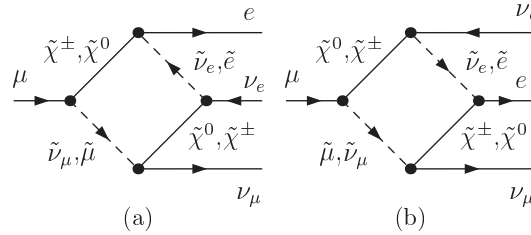


Figure 5.7: Generic box diagram in the (N)MSSM with $\tilde{\chi}^\pm = \tilde{\chi}_{1,2}^\pm$. In the MSSM $\tilde{\chi}^0 = \tilde{\chi}_{1,2,3,4}^0$, in the NMSSM $\tilde{\chi}^0 = \tilde{\chi}_{1,2,3,4,5}^0$.

are the same in the MSSM and the NMSSM. Performing the calculation of the box diagrams in Fig. 5.7 in `FormCalc`, the results for the diagrams in (a) and (b) are returned in the form

$$\begin{aligned} \mathcal{M}_{\text{SUSY Box}(a)} &= (\bar{u}_e \gamma_\lambda \omega_- u_\mu) (\bar{u}_{\nu_\mu} \gamma^\lambda \omega_- v_{\nu_e}) b_{(a)} \\ \mathcal{M}_{\text{SUSY Box}(b)} &= (\bar{u}_{\nu_e} \omega_- u_\mu) (\bar{u}_{\nu_\mu} \omega_+ v_e) b_{(b)}. \end{aligned} \quad (5.14)$$

The expressions for $b_{(a)}$ and $b_{(b)}$, which differ between the MSSM and the NMSSM, are lengthy and not given here explicitly. To factor out the Born amplitude

$$\mathcal{M}_{\text{Born}} = \frac{2\pi\alpha}{s_W^2 M_W^2} (\bar{u}_{\nu_\mu} \gamma_\lambda \omega_- u_\mu) (\bar{u}_e \gamma^\lambda \omega_- v_{\nu_e}), \quad (5.15)$$

the spinor chains in Eq. (5.14) have to be transformed into the same structure as the ones appearing in $\mathcal{M}_{\text{Born}}$. In order to carry out these transformations, in a first step

the Fierz identities (see for example Ref. [175]) are used. The spinor structure of the diagrams in (a) can be rewritten as

$$(\bar{u}_e \gamma_\lambda \omega_- u_\mu)(\bar{u}_{\nu_\mu} \gamma^\lambda \omega_- v_{\nu_e}) = - (\bar{u}_{\nu_\mu} \gamma_\lambda \omega_- u_\mu) (\bar{u}_e \gamma^\lambda \omega_- v_{\nu_e}) . \quad (5.16)$$

For the spinor chain in diagram (b) we get

$$\begin{aligned} (\bar{u}_{\nu_e} \omega_- u_\mu)(\bar{u}_{\nu_\mu} \omega_+ v_e) &= \frac{1}{2} (\bar{u}_{\nu_\mu} \gamma_\lambda \omega_- u_\mu) (\bar{u}_{\nu_e} \gamma^\lambda \omega_+ v_e) \\ &= \frac{1}{2} (\bar{u}_{\nu_\mu} \gamma_\lambda \omega_- u_\mu) (\bar{u}_e \gamma^\lambda \omega_- v_{\nu_e}) . \end{aligned} \quad (5.17)$$

where for the last transformation we made use of charge conjugation relations. Using the relations Eq. (5.16) and Eq. (5.17), the box matrix elements can be rewritten as

$$\begin{aligned} \mathcal{M}_{\text{SUSY Box}(a)} &= -\frac{s_W^2 M_W^2}{2\pi\alpha} b_{(a)} \mathcal{M}_{\text{Born}} \\ \mathcal{M}_{\text{SUSY Box}(b)} &= \frac{s_W^2 M_W^2}{4\pi\alpha} b_{(b)} \mathcal{M}_{\text{Born}} . \end{aligned} \quad (5.18)$$

For more details see [34, 156]².

The result of the box diagrams, containing a selectron and a smuon or an electron and a muon sneutrino, contain coefficients with the mass-squared difference of the two particles in the denominator. But in the case of degenerate slepton/sneutrino masses also the numerators of the potentially divergent terms become zero. There is thus no physical problem but zero valued denominators may cause problems in the numerical evaluation. This technical issue is solved by adding a distinction of cases, such that the result is expanded if the two masses are identical, making use of the analytic result that has been obtained in computer-algebra form. Thus we obtain a valid result for all possible input parameters and avoid the restriction to a special set of scenarios.

5.3.4 Incorporation of higher-order corrections to Δr

The on-shell renormalization conditions correspond to the definition of the W and Z boson masses as the real part of the complex pole of the propagator (which is from two-loop order on, the only gauge invariant way to define the mass of unstable particles [129]). This leads to the fact that we internally use the definition of the gauge boson masses in terms of a BreitWigner shape with a fixed width, while the experimental values are obtained using a definition of the gauge boson masses in terms of a BreitWigner shape with a running width. For a comparison with the measurements, the W boson mass value is, in a last step of our calculation, transformed to the running width definition, such that our code returns M_W^{rw} (= running width definition). The difference between the two definitions is [176]

$$M_W^{\text{rw}} = M_W^{\text{fw}} + \frac{\Gamma_W^2}{2M_W^{\text{rw}}} . \quad (5.19)$$

²The results given in Ref. [156] are correct, while there is a sign error in Eq. (7.9) of Ref. [34].

where M_W^{fw} corresponds to the fixed width description. We use the prediction of the W decay with

$$\Gamma_W = \frac{3G_\mu M_W^{\text{rw}3}}{2\sqrt{2}\pi} \left(1 + \frac{2\alpha_s}{3\pi} \right), \quad (5.20)$$

parameterized by G_μ and including first order QCD correction. This difference is numerically relevant and a clear distinction of the two mass definitions will be needed for the discussion of the higher-order contributions. In the rest of this work we will not use the labels (rw, fw) explicitly. If not stated explicitly that we talk about an internal variable, M_W will always mean the W-boson mass according to the running width definition. See e.g. Ref. [129] for further details.

To obtain the most precise result for M_W^{SM} , we combine our SM one-loop result with the relevant available higher order corrections. The SM higher-order corrections will also be used in the full Δr expressions in the MSSM and the NMSSM, as we will discuss below. The SM part of Δr including contributions up to four-loop order is given by

$$\begin{aligned} \Delta r^{\text{SM}} = & \Delta r^{(\alpha)} + \Delta r^{(\alpha\alpha_s)} + \Delta r^{(\alpha\alpha_s^2)} + \Delta r_{\text{ferm}}^{(\alpha^2)} + \Delta r_{\text{bos}}^{(\alpha^2)} \\ & + \Delta r^{(G_\mu^2\alpha_s m_t^4)} + \Delta r^{(G_\mu^3 m_t^6)} + \Delta r^{(G_\mu m_t^2 \alpha_s^3)}. \end{aligned} \quad (5.21)$$

It contains, besides the one-loop contribution $\Delta r^{(\alpha)}$,

- the two-loop QCD corrections $\Delta r^{(\alpha\alpha_s)}$ [122–127],
- the three-loop QCD corrections $\Delta r^{(\alpha\alpha_s^2)}$ [134–137],
- the fermionic electroweak two-loop corrections $\Delta r_{\text{ferm}}^{(\alpha^2)}$ [128–130],
- the purely bosonic electroweak two-loop corrections $\Delta r_{\text{bos}}^{(\alpha^2)}$ [131–133],
- the mixed QCD and electroweak three-loop contributions $\Delta r^{(G_\mu^2\alpha_s m_t^4)}$ [138, 141],
- the purely electroweak three-loop contribution $\Delta r^{(G_\mu^3 m_t^6)}$ [138, 141],
- and the four-loop QCD correction $\Delta r^{(G_\mu m_t^2 \alpha_s^3)}$ [140].

The full result for the electroweak two-loop contributions in the SM involves numerical integrations of the two-loop scalar integrals, which make the corresponding code rather unwieldy and slow. Thus, we make use of the simple parametrisation that has been given in Ref. [144] for the combined result of the fermionic and bosonic electroweak two-loop corrections in the SM:

$$\Delta r_{\text{ferm}}^{(\alpha^2)} + \Delta r_{\text{bos}}^{(\alpha^2)} = (\Delta\alpha)^2 + 2\Delta\alpha \Delta r^{(\alpha, \text{sub})} + \Delta r_{\text{rem}}^{(\alpha^2)} \quad (5.22)$$

with

$$\begin{aligned} \Delta r_{\text{rem}}^{(\alpha^2)} = & r_0 + r_1 L_H + r_2 L_H^2 + r_3 L_H^4 + r_4 (\Delta_H^2 - 1) + r_5 \Delta_t + r_6 \Delta_t^2 + r_7 \Delta_t L_H \\ & + r_8 \Delta_W + r_9 \Delta_W \Delta_t + r_{10} \Delta_Z, \end{aligned} \quad (5.23)$$

and

$$\begin{aligned}
r_0 &= 0.003354, & r_1 &= -2.09 \times 10^{-4}, & r_2 &= 2.54 \times 10^{-5}, & r_3 &= -7.85 \times 10^{-6}, \\
r_4 &= -2.33 \times 10^{-6}, & r_5 &= 7.83 \times 10^{-3}, & r_6 &= 3.38 \times 10^{-3}, & r_7 &= -9.89 \times 10^{-6}, \\
r_8 &= 0.0939, & r_9 &= 0.204, & r_{10} &= -0.103.
\end{aligned}
\tag{5.24}$$

Note that $\Delta r^{(\alpha, \text{sub})}$ in Eq. (5.22) is the full one-loop result $\Delta r^{(\alpha)}$ without the $\Delta\alpha$ term. This approximates the exact result for $\Delta r_{\text{ferm}}^{(\alpha^2)} + \Delta r_{\text{bos}}^{(\alpha^2)}$ to better than 2.7×10^{-5} for $10 \text{ GeV} \leq M_{H\text{SM}} \leq 1 \text{ TeV}$ (and the other input parameters in their 2σ ranges), corresponding to an uncertainty of 0.4 MeV for M_W . The use of a parametrisation directly for the SM prediction of $\Delta r_{\text{ferm}}^{(\alpha^2)} + \Delta r_{\text{bos}}^{(\alpha^2)}$ rather than for the full SM prediction of M_W leads to an improved accuracy in the combination with the SUSY contributions as compared to Ref. [156]³. Note that the gauge boson masses with running width definition are needed as input for the formula given in Ref. [144] (this is the only part of our calculation where the running width definition is used internally). The output of this formula approximates the full result of $\Delta r_{\text{ferm}}^{(\alpha^2)} + \Delta r_{\text{bos}}^{(\alpha^2)}$ using the fixed-width definition, such that it can directly be combined with other terms of our calculation, using also the fixed-width definition of the gauge boson masses.

Concerning the QCD corrections, which enter from the two-loop level onwards, it should be noted that they result in a rather large downward shift of the W boson mass prediction (as will be discussed later). It is obvious that this kind of corrections needs to be theoretically well under control in order to gain sensitivity to effects of physics beyond the SM. In the current implementation, we use the $\Delta r^{\alpha\alpha_s} + \Delta r^{\alpha\alpha_s^2}$ contributions from Ref. [136]. In a future update of our code, we plan to replace the $\mathcal{O}(\alpha\alpha_s)$ corrections by the more complete result given in Refs. [124, 177] which contains also contributions from fermions of the first two generations. The latter result agrees with the result calculated in Ref. [178].

Now we turn to the discussion of the full result for M_W in the MSSM and the NMSSM, including all available higher order corrections. This discussion focuses on the NMSSM, however it can be applied in the same way also to the MSSM, unless a difference between the MSSM and the NMSSM is pointed out explicitly. For a discussion of the incorporation of higher order contributions in the MSSM see also Refs. [35, 156].

Since the calculation of Δr in the SM is more advanced than in the SUSY models we have organised our result such that the full SM result for Δr can be used also for the NMSSM prediction of M_W . Therefore the NMSSM results are split into a SM part and a SUSY part⁴

$$\Delta r^{\text{NMSSM}} = \Delta r^{\text{SM}} + \Delta r^{\text{SUSY}}.
\tag{5.25}$$

³In the procedure that was applied in Ref. [156], $\Delta r_{\text{ferm}}^{(\alpha^2)} + \Delta r_{\text{bos}}^{(\alpha^2)}$ could only be evaluated at M_W^{SM} . As mentioned already before, we will include the SM higher order corrections also in the (N)MSSM M_W prediction. Using the fit formula for $\Delta r_{\text{ferm}}^{(\alpha^2)} + \Delta r_{\text{bos}}^{(\alpha^2)}$ allows us to evaluate these contributions (in each iteration step) at the particular (N)MSSM value for M_W .

⁴Since the complete one-loop results for Δr in the SM and in the NMSSM are used in Eq. (5.25), this splitting has an impact only from the two-loop level onwards.

Writing the NMSSM result in terms of Eq. (5.25) ensures in particular that the full SM result is recovered in the decoupling limit, where all superpartners are heavy, the singlet decouples and the Higgs sector becomes SM-like. The term Δr^{SM} is given in Eq. (5.21).

The quantity Δr^{SUSY} in Eq. (5.25) denotes the difference between Δr in the NMSSM and the SM, i.e. it only involves the contributions from the additional SUSY particles and the extended Higgs sector. All SUSY corrections beyond one-loop order that are known to date are implemented. The leading reducible $\mathcal{O}(\alpha^2)$ two-loop corrections (that can be obtained via the resummation formula given in Ref. [179]) and the leading SUSY two-loop QCD corrections of $\mathcal{O}(\alpha\alpha_s)$ to $\Delta\rho$ as given in Refs. [157, 158] are identical for the MSSM and the NMSSM and can directly be included in our NMSSM calculation.

The leading reducible $\mathcal{O}(\alpha^2)$ two-loop corrections are obtained by expanding the resummation formula [179]

$$1 + \Delta r = \frac{1}{(1 - \Delta\alpha)(1 + \frac{c_W^2}{s_W^2}\Delta\rho) - \Delta r_{\text{rem}}}, \quad (5.26)$$

which takes the terms of the type $(\Delta\alpha)^2$, $(\Delta\rho)^2$ and $\Delta\alpha\Delta\rho$ correctly into account⁵, if $\Delta\rho$ is parametrized by G_μ . The pure SM terms are already included in Δr^{SM} . Thus, only the leading two-loop terms with SUSY contributions,

$$\Delta r_{\text{red}}^{\text{SUSY}(\alpha^2)} = -\frac{c_W^2}{s_W^2}\Delta\alpha\Delta\rho^{\text{SUSY}} + \frac{c_W^4}{s_W^4}\Delta\rho^{\text{SUSY}2} + 2\frac{c_W^4}{s_W^4}\Delta\rho^{\text{SUSY}}\Delta\rho^{\text{SM}}, \quad (5.27)$$

are additionally needed and inserted into our calculation.

The two-loop $\mathcal{O}(\alpha\alpha_s)$ contributions contain squark loops with gluon exchange and quark/squark loops with gluino exchange (both depicted in Fig. 5.8). While the formula for the gluino contributions is very lengthy, a compact result for the gluon contributions to $\Delta\rho$ was derived in Ref. [158]. The formula for the SUSY contributions to M_W require the on-shell (physical) values for the squark masses as input. The $SU(2)$ relation $M_{\tilde{t}_L} = M_{\tilde{b}_L}$ implies that one of the stop/sbottom masses is not independent but can be expressed in terms of the other parameters. Therefore, when including higher orders, one cannot choose independent renormalization conditions for all four (stop and sbottom) masses. Loop corrections to the relation between the squark masses must be taken into account to be able to insert the proper on-shell values for the squark masses into our calculation. The difference of using the tree-level mass relation instead to the one-loop corrected one for the two-loop SUSY contributions to M_W is of three-loop order and therefore not considered here. However for the evaluation of the one-loop SUSY contributions to M_W the loop corrected mass relation must be used. In our evaluation of M_W this is taken into account by a “mass-shift” correction term. For more details see Ref. [158].

The dominant Yukawa-enhanced electroweak corrections of $\mathcal{O}(\alpha_t^2)$, $\mathcal{O}(\alpha_t\alpha_b)$, $\mathcal{O}(\alpha_b^2)$ to $\Delta\rho$ [159, 160] are two-loop corrections containing quarks (t/b) loops with Higgs exchange, squark (\tilde{t}/\tilde{b}) loops with Higgs exchange and mixed quark-squark loops with Higgsino exchange. The generic diagrams are shown in Fig. 5.9. These contribution were calculated

⁵One could also include the term $\Delta\alpha\Delta r_{\text{rem}}$, which is however numerically small and not included.

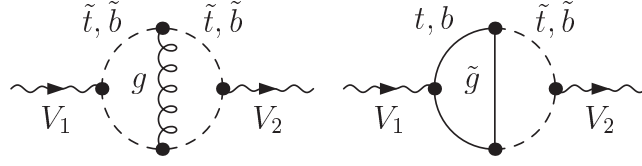


Figure 5.8: Generic $\mathcal{O}(\alpha\alpha_s)$ two-loop diagrams in the NMSSM. g denotes a gluon and \tilde{g} a gluino; $V_1, V_2 = A, Z, W^\pm$.

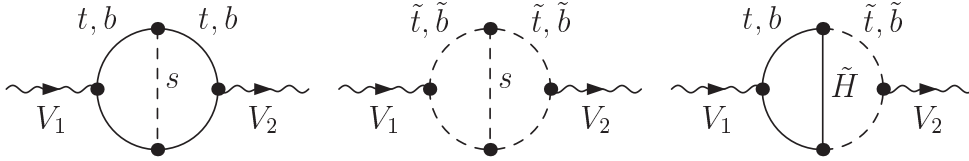


Figure 5.9: Generic $\mathcal{O}(\alpha_t^2)$, $\mathcal{O}(\alpha_t\alpha_b)$, $\mathcal{O}(\alpha_b^2)$ two-loop diagrams. \tilde{H} denotes a Higgsino and s a Higgs or Goldstone boson; $V_1, V_2 = A, Z, W^\pm$.

for the MSSM, and the incorporation into the NMSSM result is not straightforward. In order to be able to include these contributions we assign a MSSM parameter point, which has the same values for $\tan\beta$, the sfermion mixing parameters A_f , and all the soft mass parameters as the considered NMSSM point. Further we set the MSSM μ parameter equal to μ_{eff} . The charged Higgs mass (calculated in the NMSSM beforehand) is then used as input for the calculation of the MSSM Higgs masses. This ensures that the mass of the charged Higgs boson (which is the only Higgs boson which appears the same way in both SUSY models) is the identical in the NMSSM and the MSSM, since we calculate the MSSM Higgs masses in `FeynHiggs` where the input parameter M_{H^\pm} is interpreted as on-shell mass parameter. The MSSM Higgs masses which are determined this way and the Higgsino parameter μ are then used as input for the $\Delta\rho$ ($\mathcal{O}(\alpha_t^2)$, $\mathcal{O}(\alpha_t\alpha_b)$, $\mathcal{O}(\alpha_b^2)$) formula. The dominant Yukawa-enhanced electroweak corrections in the SM [180, 181] have been subtracted according to Eq. (5.25). For this purpose we have identified the SM Higgs mass entering the result of Refs. [180, 181] with the mass of the MSSM Higgs boson, that has the largest coupling to gauge bosons. The size of Yukawa-enhanced electroweak corrections is typically small ($\lesssim 5$ MeV) while the calculation is rather time-consuming. In the M_W codes for the MSSM and in the NMSSM, the user can choose whether these contributions should be included or not. The numerical results in the MSSM (presented in Sect. 5.7) embody the Yukawa-enhanced electroweak two-loop corrections, while in the NMSSM results (presented in Sect. 5.8) they are not included, unless stated otherwise.

It should be emphasised at this point that the approach followed in (5.25), i.e. combining the most up-to-date SM prediction with the 'new physics' contributions from supersymmetry, is well suited for extending it further to other scenarios of physics beyond the SM. This provides an appropriate framework for comparing the M_W prediction of different models in a consistent way.

5.4 Technical aspects

5.4.1 Framework for the Δr calculation

The one-loop calculation of Δr in the SM, the MSSM with complex parameters and the NMSSM has been carried out using the `Mathematica` [182] based programs `FeynArts` (Version 3.5) [36–41] and `FormCalc` (Version 6.2) [62], with which one-loop calculations can be carried out with a high degree of automation. The program `FeynArts` can be used to generate and draw the Feynman diagrams to a given order for the process under study, based on a so-called model file, which provides the information about the particle content and interactions in a certain model. For the SM and the MSSM we used the model files which are included in the `FeynArts` standard distribution. For the NMSSM we used a new model file, which we developed in Ref. [32] and which is discussed in more detail in Sect. 5.4.4. From the Feynman rules a mathematical expression for the amplitudes is generated. For one-loop amplitudes, the analytic simplifications, trace evaluation, tensor decomposition, etc. can be carried out by `FormCalc`, which combines the speed of `FORM` [183] with the more user-friendly interface of `Mathematica`.

The one-loop results are combined with all known higher-order corrections of SM and SUSY type as specified in Sect. 5.3.4. Therefore we have transcribed the higher-order corrections taken from the literature into `Mathematica` format. `Mathematica` provides the flexibility that allows us to analyse the functions at an analytic level and treat possible threshold effects or numerical instabilities analytically by adding appropriate expansions. We took special care of parameter regions with mass degeneracies, so that a numerically stable evaluation is ensured (for details see also Sect. 5.3.3). For the MSSM we have done a second implementation of our results in `Fortran`⁶. The `Fortran` code runs significantly faster and is therefore especially suitable for scans. Our numerical results in the MSSM (see Sect. 5.7) are generated using the `Fortran` code, while the NMSSM results (see Sect. 5.8) are produced using the `Mathematica` setup.

We cross-checked our evaluations in the MSSM and in the NMSSM with the earlier results given in Ref. [156] and Ref. [163] and found in both cases good agreement at the level of 1–2 MeV. In the MSSM, deviations can arise from the different treatment of the $\mathcal{O}(\alpha^2)$ SM-type corrections as we discussed in Sect. 5.3.4. In our result, the incorporation of the state-of-the-art SM result has been improved by using the expressions for $\Delta r_{\text{ferm}}^{(\alpha^2)} + \Delta r_{\text{bos}}^{(\alpha^2)}$ given in Ref. [144], while in Ref. [156] the fit formula for M_W^{SM} [143] was employed. In the NMSSM results presented in Ref. [163] the SUSY two-loop contributions, apart from the gluon contributions, are not included. Taking these contributions into account, we get an improved prediction for M_W^{NMSSM} . The comparison was done, by “switching off” the SUSY two-loop contributions (apart from the gluon contributions) in our result. One difference between the two NMSSM evaluations stems from the fact that we use the on-shell masses for sfermions, charginos and neutralinos, while in Ref. [163] the `NMSSMTools` masses are used (see below).

⁶We plan to provide a `Fortran` code also for the NMSSM.

5.4.2 Framework for the numerical analysis

For the numerical evaluation in the complex MSSM, all values for the masses and mixing matrices are calculated using `FeynHiggs` (version 2.9.4) [29, 184–187]. In `FeynHiggs` the sfermion, chargino and neutralino masses are derived using the relations for the on-shell masses, as given in Sect. 2.2. For the M_W prediction, we use (if not stated otherwise) the numerical values for the masses and effective couplings of the MSSM Higgs bosons including the full one-loop and the dominant two-loop corrections. The W boson mass enters in the evaluation of the Higgs masses. So far `FeynHiggs` uses the experimental value for M_W as input. We plan to include our M_W prediction in `FeynHiggs`, such that the predicted value for M_W can be used as input for the Higgs mass calculation.

In the setup for the NMSSM the sfermion, chargino and neutralino masses are derived using the on-shell relations given in Sect. 2.2 and Sect. 2.3. Our setup allows the user to choose whether the Higgs masses should be calculated using the tree-level relations (given Sect. 2.3) or using `NMSSMTools` (version 4.1.1) [188–191]. In `NMSSMTools` the input parameters are assumed to be $\overline{\text{DR}}$ parameters at the SUSY breaking scale, which is by default set to the average of the squark masses. The pole masses are computed, taking one-loop corrections into account. In order to use the `NMSSMTools` Higgs masses in our result, a transformation from the on-shell parameters, needed for our evaluation, to the $\overline{\text{DR}}$ parameters, needed as `NMSSMTools` input, is necessary. This effect is approximately taken into account, by transforming the on-shell X_t parameter into its $\overline{\text{DR}}$ value by the relation given in [192]. The shift in the other parameters is significantly smaller and therefore neglected here.

In our setup, the MSSM and NMSSM parameter spaces can be tested against a broad set of experimental and theoretical constraints. Besides the constraints already implemented in the two codes `FeynHiggs` and `NMSSMTools`⁷, further direct constraints on the Higgs sectors can be evaluated with help of the code `HiggsBounds` (version 4.0.0) [194–196]. The constraints most relevant for this chapter are outlined in the next section, Sect. 5.4.3.

All programs used for the numerical evaluation are linked through an interface to our two codes for the W -boson mass prediction: our general `Mathematica` code⁸ as well as to the MSSM `Fortran` code. Inserting the mass eigenvalues, we use `LoopTools` (Version 2.7) [62] (which can be called both from `Fortran` and from `Mathematica`) for the numerical evaluation of the one-loop scalar and tensor integrals.

⁷The code `FeynHiggs` includes (amongst others) predictions for the anomalous magnetic moment of the muon and electric dipole moments of electron, neutron and mercury. Additionally it provides the information whether a parameter point corresponds to a colour-breaking minimum. `NMSSMTools` contains a list of theoretical and experimental constraints, e.g. constraints from collider experiments (such as LEP mass limits on SUSY particles), B -physics and astrophysics. More details on the constraints included in `NMSSMTools` can be found in Refs. [188, 193].

⁸The `Mathematica` code is linked to a `Fortran` driver program, calling the other programs (`FeynHiggs` for the MSSM, `NMSSMTools` for the NMSSM and `HiggsBounds` for both models). In the NMSSM case the calculation of the SUSY particle masses and the tree-level Higgs masses is also included in the `Fortran` driver.

5.4.3 Constraints on the parameter space

We briefly discuss the phenomenological constraints on the MSSM and NMSSM parameter space, which are applied in the numerical analysis presented in this chapter. The same constraints will also be relevant in later chapters (in particular in chapter 6 and chapter 7), where we will refer back to the description of the constraints here.

Bounds from direct Higgs searches

Limits from Higgs searches at LEP, the Tevatron and the LHC set stringent bounds on the Higgs masses and couplings in SUSY models.

In order to test whether a given point in the MSSM or the NMSSM parameter space is allowed or ruled out by the Higgs searches one needs to confront the predictions of the model with the available cross section limits in the various search channels at each collider. For this purpose we make use of the code `HiggsBounds` [194–196], which includes limits from searches for neutral and charged MSSM Higgs bosons, as well as the limits on Higgs bosons with SM-like couplings.

`HiggsBounds` uses the input provided for the model under consideration (in the case of our analysis the masses, effective couplings and partial widths of the Higgs bosons of the MSSM and the NMSSM) to determine, separately for each Higgs boson in the model, the channel that has the highest expected sensitivity for an exclusion. For this particular channel the theory prediction is then compared to the observed experimental limit, which determines whether the parameter point is allowed or excluded. The exclusion obtained this way corresponds to a limit at somewhat lower statistical confidence level than 95% [197]. A theoretical uncertainty on the Higgs mass calculation is included when determining the exclusion.

For the numerical evaluation of the W boson mass prediction, which is presented in this chapter, we use `HiggsBounds` version 4.0.0, which includes the LHC limits presented until Moriond 2013. The latest ATLAS result on light charged Higgs boson searches [55] (important in particular for the interpretation of the Higgs signal as the heavy \mathcal{CP} -even MSSM Higgs) is not included in this `HiggsBounds` version. A new `HiggsBounds` version including this result is meanwhile available.

Bounds from direct searches for SUSY particles

As mentioned already in Sect. 4.2.3, the limits from direct searches for SUSY particles at LEP, the Tevatron and the LHC restrict the allowed parameter space of SUSY models. The least model-dependent limits are the ones from LEP. In particular the limit on the lightest chargino mass, $m_{\chi_1^\pm} > 94$ GeV [165], applies to both the MSSM and the NMSSM and restricts the parameter μ (μ_{eff}) of the (N)MSSM to values above about 100 GeV. The LEP limits on sfermion and chargino masses are applied throughout this chapter (as well as in chapter 6 and chapter 7). For the squarks of the first two generations and the gluino the LHC mass limits are most stringent [67, 68], but have a certain model dependence (see Sect. 4.2.3). In the numerical analysis we will often choose our

parameters such that the squarks of the first two generations and the gluino are heavy (> 1 TeV)⁹. The LHC limits on third-generation squarks, stops and sbottoms, and on uncolored particles are substantially weaker. They also depend strongly on the assumed model, therefore it is not straightforward to apply these limits to the parameter space of the general MSSM or NMSSM. For third generation squarks and uncolored SUSY particles we apply only the LEP limits in our analysis. In Sect. 5.7.3 we will comment on the effect that stronger mass limits on stops and sbottoms (as expected from the LHC if no SUSY particle will be discovered) would have on our analysis of the M_W prediction in the (N)MSSM. In chapter 8 we will present a new tool (**FastLim**), which can test any MSSM parameter point against the limits from direct SUSY searches at the LHC. However this tool was not yet available when we performed the analysis presented in this chapter (and chapters 6 and 7).

Neutralino LSP

In the numerical analyses (throughout this thesis) we consider only parameter points for which the lightest neutralino $\tilde{\chi}_1^0$ is the LSP. It is then automatically stable (in R-parity conserving models¹⁰) and can provide a viable dark matter candidate. Even though not studied in this thesis, scenarios in which $\tilde{\chi}_1^0$ is not the LSP can be phenomenologically viable and interesting. In such cases one needs another dark matter candidate, e.g. the gravitino [198, 199].

Theoretical constraints

In the analyses within the NMSSM, additional theoretical constraints are applied. Constraints originate from the requirement of a viable physical minimum of the Higgs potential. The physical minimum, with non-vanishing vacuum expectation values for the two Higgs doublets H_1 and H_2 , should be deeper than minima with vanishing vevs. Furthermore the physical vacuum should have a non-zero singlet vev to be able to generate the μ_{eff} parameter. In the NMSSM, a stable symmetry breaking minimum of the potential is ensured approximately by the condition $A_\kappa^2 \geq 9 m_S^2$ [200]. For each point considered in the NMSSM parameter space, we verified numerically (using **NMSSMTools**) that the Higgs potential is bounded from below and stable.

Another requirement is that there be no Landau pole for any of the running couplings λ , κ , y_t and y_b below the GUT scale. The renormalisation group equations for the NMSSM are known to two-loop order [201]. The constraint of perturbativity up to a very high scale restricts the range of λ and κ . Values of these parameters in the perturbative regime at the GUT scale lead to comparably small values at the weak scale, which may be combined to give the approximate upper bound [202]

$$\lambda^2 + \kappa^2 \leq 0.5. \quad (5.28)$$

⁹Since this limit is not applied everywhere we will comment on whether a LHC mass limit on squarks and gluinos is considered, when discussing a specific analysis.

¹⁰R-parity violation is not discussed in this thesis.

We choose λ and κ to respect this limit.

5.4.4 FeynArts model file for the NMSSM

The NMSSM prediction for M_W (as well as the results presented in chapter 6) have been obtained using a new NMSSM model file for **FeynArts**, which was presented first in Ref. [32]. In this section we discuss the development of the NMSSM model file and give details on how it was derived and tested.

In order to get precise theoretical predictions for observables in the NMSSM that can be compared with the ones in other scenarios of physics beyond the SM and be confronted with the available data, it is often necessary to include radiative corrections.

The calculation of loop diagrams, often involving a large number of fields, is a tedious and error-prone task if done by hand. This is true in particular for theories beyond the SM where the number of fields is significantly increased. For one-loop calculations, as will be the focus in the following, computer methods with a high degree of automation have been devised to simplify the work. However, most of the available tools so far have focused on calculations either in the SM or the MSSM. In order to facilitate loop calculations in the NMSSM, it is useful to employ the well-established public tools **FeynArts**, **FormCalc** and **LoopTools**. As a first step towards the goal of treating the NMSSM at the same level of accuracy as the MSSM, we have compiled a new **FeynArts** model file for the NMSSM. The basis for the model file itself — defining the particle content and interactions of the NMSSM — was generated with the help of the program **SARAH** [203, 204]. This program can be used to generate **FeynArts** model files, as well as output for many other programs, for any supersymmetric theory starting from its superpotential. For consistency checks, we also use an independent NMSSM model file generated with **FeynRules** [205]. Starting from the output of **SARAH** we have introduced the standard nomenclature of **FormCalc** to activate its internal MSSM simplifications and we have applied unitarity relations to mixing matrices and couplings. These modifications, besides greatly improving the speed at which **FormCalc** performs one-loop calculations of NMSSM amplitudes, are essential for instance for verifying the cancellation of UV divergences at the algebraic level.

We have performed several tests on the model file to verify the NMSSM implementation. The analytical expressions for the Feynman rules for the interaction vertices of the NMSSM obtained from **SARAH** have been compared to the independent **FeynRules** output. They have also been compared (analytically) in the MSSM limit to the corresponding vertices in the default MSSM implementation distributed with **FeynArts**. A number of tree-level processes have been analysed numerically, including the decays of Higgs bosons and neutralinos, to test the mixing properties of the singlet state in the NMSSM. Comparing these to the results of **NMSSMTools** and **NMSDECAY** [206], we find overall good agreement with those previously obtained results after correcting for differences due to QCD corrections and the running of gauge couplings. A further, extensive, and non-trivial test of the working NMSSM implementation is provided by the results for the processes that are induced at the one-loop level in the NMSSM. We have evaluated $\mathcal{O}(50)$ $1 \rightarrow 2$ processes and $\mathcal{O}(100)$ $2 \rightarrow 2$ processes of this type and checked them

successfully for their UV- and IR-finiteness.

5.5 Theoretical uncertainties in the M_W prediction

Before moving on to our numerical results for the W boson mass prediction in the SM, the MSSM and the NMSSM, we discuss the theoretical uncertainty in the M_W calculation.

The dominant theoretical uncertainty of the prediction for M_W arises from the parametric uncertainty induced by the experimental error in the measurement of the top-quark mass. An experimental error of 1 GeV on m_t causes a parametric uncertainty on M_W of about 6 MeV, while the parametric uncertainties induced by the current experimental error of the hadronic contribution to the shift in the fine-structure constant, $\Delta\alpha_{\text{had}}$, and by the experimental error of M_Z amount to about 2 MeV and 2.5 MeV, respectively. The uncertainty of the SM M_W prediction caused by the experimental error of the Higgs mass $\delta M_H^{\text{exp}} = 0.35$ GeV is significantly smaller (~ 0.2 MeV). In [114] the impact of improved accuracies of m_t and $\Delta\alpha_{\text{had}}$ has been discussed. With a precise top mass measurement of $\Delta m_t = 0.1$ GeV (anticipated ILC precision) the parametric uncertainty in M_W is 0.6 MeV.

The uncertainties from unknown higher-order corrections have been estimated to be around 4 MeV in the SM for a light Higgs boson ($M_{H^{\text{SM}}} < 300$ GeV) [143]. The prediction for M_W in the MSSM and the NMSSM are affected by additional theoretical uncertainties from unknown higher-order corrections of SUSY type. While in the decoupling limit those additional uncertainties vanish, they can be important if some SUSY particles, in particular in the scalar top and bottom sectors, are relatively light. The combined theoretical uncertainty from unknown higher-order corrections of SM- and SUSY-type has been estimated (for the MSSM with real parameters) in Refs. [156, 160] as $\delta M_W \sim (4-9)$ MeV, depending on the SUSY mass scale¹¹. Since we include the same higher-order corrections in the NMSSM as in the MSSM, the uncertainty from unknown higher-order corrections is estimated to be of similar size.

¹¹The lower limit of 4 MeV corresponds to the SM uncertainty, which one gets in the decoupling limit of the MSSM. For the upper limit of 9 MeV very light SUSY particles were considered, which are not in agreement with the current limits anymore. Taking the experimental bounds into account the (maximal) uncertainty from missing higher orders should be considerably reduced.

5.6 Result for M_W in the SM

As mentioned already in Sect. 5.3.2 the SM prediction for the W boson mass is affected by large radiative corrections beyond one-loop level. The size of the corrections beyond one-loop order is shown in Fig. 5.10 where we plot the SM M_W predictions against the SM Higgs mass. The orange curve shows the result we find using the full one-loop result for Δr but no further corrections beyond one-loop. The red curve is the SM M_W result using the full Δr result as given in Eq. (5.21). Comparing the two predictions one finds that the corrections beyond one-loop order lead to a large downward shift in M_W by more than 100 MeV. The largest shift (beyond one-loop) is caused by the two-loop QCD corrections [122–127] followed by the three-loop QCD corrections $\Delta r^{(\alpha_s^2)}$ [134–137]. The gray band indicates the current M_W measurement with the 1σ experimental uncertainty. Comparing only the one-loop result with the measurement, one would conclude that a SM Higgs mass of around 500 GeV would be favored by the M_W measurement while a light Higgs would clearly be disfavored. Taking the full result one finds the important result that the SM M_W prediction favors a light Higgs boson. Therefore it is crucial to include all known higher-order corrections to obtain a reliable prediction for the W boson mass.

Interpreting the observed Higgs as the SM Higgs boson, the SM prediction for W boson mass reads (the other relevant SM parameters are: $M_Z = 91.1876$ GeV, $G_\mu = 1.1663787 \times 10^{-5}$ GeV $^{-2}$, $\alpha_s(M_Z) = 0.1184$, $\Delta\alpha_{\text{had}}(M_Z) = 0.02757$, $m_b = 4.7$ GeV)

$$M_W^{\text{SM}}(m_t = 173.2 \text{ GeV}, M_{H^{\text{SM}}} = 125.64 \text{ GeV}) = 80.361 \text{ GeV}. \quad (5.29)$$

Accordingly, the SM prediction for M_W turns out to be below the current experimental value, $M_W^{\text{exp}} = 80.385 \pm 0.015$ GeV, by about 1.5σ . We have investigated the possible effects of CKM mixing. We checked analytically that the contributions from CKM mixing are non-zero, but the numerical impact turns out to be negligible (below 0.01 MeV in M_W).

We compared our evaluation of M_W^{SM} to the result one gets from the fit formula for M_W^{SM} , given in Ref. [143]. The effect of using the simple parametrisation for $\Delta r_{\text{ferm}}^{(\alpha^2)} + \Delta r_{\text{bos}}^{(\alpha^2)}$ of Ref. [144] instead of the full result is small (< 0.1 MeV)¹². The four-loop QCD corrections given in Ref. [140] are not included in the simple M_W^{SM} parametrisation. It accounts for a shift of ~ -2 MeV in M_W^{SM} . The difference between the $\mathcal{O}(\alpha\alpha_s)$ corrections given in Ref. [136], which we implemented, and the corresponding contributions of Ref. [178], which are used for the M_W^{SM} fit formula, is $\sim 1 - 2$ MeV (depending on the $\alpha_s(m_t)$ value)¹³. The effect of these two differences accidentally cancels, so that the difference between our full M_W^{SM} result and the fit formula of Ref. [143] is $\lesssim 1$ MeV.

¹²For the parameters given in Eq. (5) in Ref. [143] and $M_{H^{\text{SM}}} = 100$ GeV.

¹³As discussed in Sect. 5.3.4, we plan to use the more complete $\Delta r^{\alpha\alpha_s}$ contributions of Refs. [124, 177], which agree with the ones of Ref. [178], in a future update of our code.

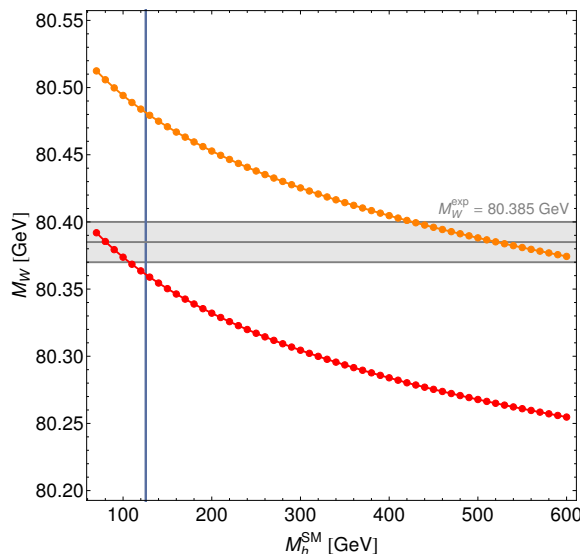


Figure 5.10: Prediction for M_W in the SM. The orange line is the SM M_W result using only the one-loop Δr result, the red line is the SM M_W result using the full Δr expression as given in Eq. (5.21). The gray band indicated the current M_W measurement with the 1σ experimental uncertainty. The thin blue vertical band indicates the mass M_h^{exp} of the discovered Higgs boson.

5.7 Result for M_W in the MSSM

In this section we discuss the results for M_W in the MSSM, based on a parameter scan. While the numerical analysis has been done for the MSSM, the results can also be of interest in the context of the NMSSM. Obviously in the MSSM-limit the NMSSM results are identical with the MSSM ones. Furthermore, the effect of the M_W contributions from the sfermion sector, in particular from stops and sbottoms, which are discussed in detail in this section, are identical in the NMSSM (also away from the MSSM-limit).

5.7.1 MSSM parameter scan: Scan ranges and constraints

Our numerical results are based on the contributions to Δr described in Sect. 5.3.3 and Sect. 5.3.4, where the `Fortran` implementation has been used to generate the MSSM results presented below.

In the following we will investigate the prediction for M_W in the MSSM based on scans of the MSSM parameters over a wide range (using flat distributions). We have performed two versions of the random scan, one where the top-quark mass is kept fixed at $m_t = 173.2$ GeV and one where m_t is allowed to vary in the scan. Both scans use initially $\sim 5 \times 10^6$ points, and dedicated smaller scans have been performed in parameter regions where the SUSY contributions to M_W are relatively large. The scan ranges are given in table 5.1. We restrict our numerical analysis based on the parameter scan to the case of real parameters, for the effects of complex phases see Sect. 5.7.4. Possible

flavor violation in the SUSY sector [161] is neglected here. In order to avoid unphysical parameter regions and regions of numerical instabilities we disregard parameter points for which `FeynHiggs` indicates a large theoretical uncertainty in the evaluation of the Higgs mass predictions (larger than 20% of the Higgs mass value). We also exclude points where stop and sbottom masses are mass-degenerate within less than 0.1 GeV causing numerical instabilities in the gluino corrections of $\mathcal{O}(\alpha\alpha_s)$ to $\Delta\rho$. Furthermore we apply a stability criterion on the $\mathcal{O}(\alpha_t^2)$, $\mathcal{O}(\alpha_t\alpha_b)$, $\mathcal{O}(\alpha_b^2)$ corrections ('Higgsino corrections'). For that we vary input parameters (one by one) by $\pm 1\%$ and look at the change in the Higgsino corrections. If the Higgsino corrections 'jump' by more than 10% we disregard that parameter point.

Parameter	Minimum	Maximum
μ	-2000	2000
$M_{\tilde{E}_{1,2,3}} = M_{\tilde{L}_{1,2,3}}$	100	2000
$M_{\tilde{Q}_{1,2}} = M_{\tilde{U}_{1,2}} = M_{\tilde{D}_{1,2}}$	500	2000
$M_{\tilde{Q}_3}$	100	2000
$M_{\tilde{U}_3}$	100	2000
$M_{\tilde{D}_3}$	100	2000
$A_e = A_\mu = A_\tau$	$-3 M_{\tilde{E}}$	$3 M_{\tilde{E}}$
$A_u = A_d = A_c = A_s$	$-3 M_{\tilde{Q}_{12}}$	$3 M_{\tilde{Q}_{12}}$
A_b	$-3 \max(M_{\tilde{Q}_3}, M_{\tilde{D}_3})$	$3 \max(M_{\tilde{Q}_3}, M_{\tilde{D}_3})$
A_t	$-3 \max(M_{\tilde{Q}_3}, M_{\tilde{U}_3})$	$3 \max(M_{\tilde{Q}_3}, M_{\tilde{U}_3})$
$\tan\beta$	1	60
M_3	500	2000
M_A	90	1000
M_2	100	1000

Table 5.1: Parameter ranges considered in the scans. All parameters with mass dimension (all except $\tan\beta$) are given in GeV.

In the SM and SUSY higher-order corrections, as listed in Sect. 5.3.4, the bottom-quark mass has been renormalized in the on-shell scheme. Accordingly, in our evaluation of M_W the bottom-quark pole mass, m_b^{pole} , is used everywhere. This also applies to the calculation of the sbottom masses from the MSSM input parameters, and we have modified the corresponding routine in `FeynHiggs` accordingly. For every parameter point we test whether it is allowed by direct Higgs searches using the code `HiggsBounds` (version

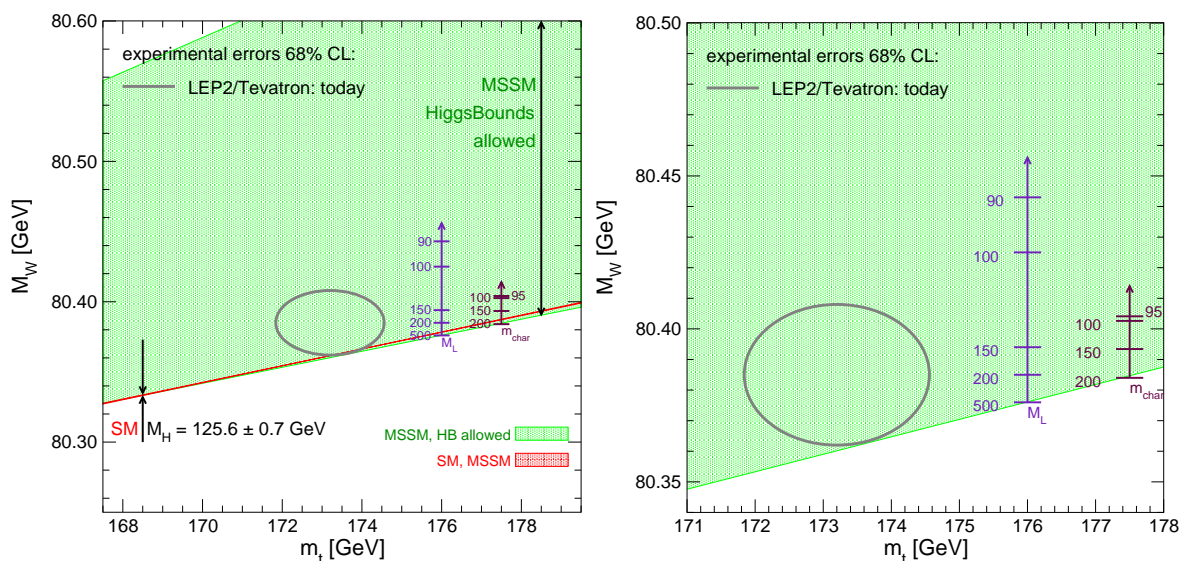


Figure 5.11: Prediction for M_W as a function of m_t . Left: The green region shows the **HiggsBounds** allowed region for the MSSM M_W prediction. It has been obtained by scanning over the MSSM parameters as described in the text. The cuts $m_{\tilde{t}_2}/m_{\tilde{t}_1} < 2.5$ and $m_{\tilde{b}_2}/m_{\tilde{b}_1} < 2.5$ are applied. The red strip indicates the overlap region of the SM and the MSSM, with $M_{HSM} = 125.6 \pm 0.7$ GeV. The two arrows indicate the possible size of the slepton and the chargino (and neutralino) contributions. Right: zoom into the most relevant region, with the SM area omitted.

4.0.0) [194–196]. Running **HiggsBounds**, we take into account the theoretical uncertainties on the Higgs masses using the estimate provided by **FeynHiggs**. All MSSM points included in our results have the lightest neutralino as LSP and have SUSY particle masses that pass the lower mass limits from direct searches at LEP.

Our MSSM results presented below improve on earlier results given in Ref. [156] in several respects. We study here the impact of both the limits from the Higgs boson searches as well as from the signal observed at about 125.6 GeV. Furthermore we investigate constraints from present and possible future limits from searches for SUSY particles. On a more technical level, our analysis incorporates the SUSY two-loop corrections of $\mathcal{O}(\alpha_t^2)$, $\mathcal{O}(\alpha_t\alpha_b)$, $\mathcal{O}(\alpha_b^2)$, which were not included in the scan results presented previously, and we perform a more detailed scan involving a larger number of sampling points.

5.7.2 Results of the scan and impact of LHC results on M_W in the MSSM

In this section we study the MSSM prediction for M_W , starting in Fig. 5.11 where M_W is displayed as a function of the top-quark mass, m_t , in the SM and the MSSM. The green area shows the MSSM parameter space that is allowed by **HiggsBounds** and the various other constraints described in the previous subsection. It should be noted that

in this plot only the limits from the Higgs searches are considered as constraints on the MSSM parameter space, not the observed signal at about 125.6 GeV (the latter will be discussed below). The region where the MSSM prediction for M_W overlaps with the one in the SM is indicated by the red strip, where $M_{H^{\text{SM}}} = 125.6 \pm 0.7$ GeV (corresponding roughly to the 2σ experimental error on M_H) has been used for the SM prediction. The left plot shows the results on a larger scale, in order to indicate the possible range of the MSSM prediction, while the right plot is a zoom into the parameter region of the MSSM near the experimental central values of M_W and m_t . In order to obtain the MSSM prediction shown as the green band in Fig. 5.11 we have imposed as an additional restriction a limit on the mass splittings in the stop and sbottom sector, which has been implemented via the conditions $m_{\tilde{t}_2}/m_{\tilde{t}_1} < 2.5$ and $m_{\tilde{b}_2}/m_{\tilde{b}_1} < 2.5$. If no such condition on the mass splittings in the stop and sbottom sector were imposed, even larger values of M_W (up to ~ 80.8 GeV) would be possible in the MSSM, see also the discussion in Ref. [156]. Since this parameter region far above the experimental value of M_W is of little phenomenological interest, we will not consider it further here. While it is well-known that a non-zero SUSY contribution tends to increase the prediction for M_W as compared to the SM case, close inspection of Fig. 5.11 reveals that there exists a small MSSM (green) region below the overlap region (red), which is most clearly visible for the largest m_t values. The reason for this feature lies in the fact that, as explained above, the SM prediction is shown for the range $M_{H^{\text{SM}}} = 125.6 \pm 0.7$ GeV, while no restriction from the signal observed in the Higgs searches has been applied to the MSSM parameter space. As a consequence, the MSSM region (green) contains parameter points where the lightest \mathcal{CP} -even Higgs boson of the MSSM has a mass above the range allowed for $M_{H^{\text{SM}}}$ (and below the upper bound on M_h in the MSSM, which increases with increasing m_t). In the decoupling region, where all superpartners are heavy, the MSSM prediction for M_W in this case corresponds to the prediction in the SM with a higher value of $M_{H^{\text{SM}}}$, which yields a lower value of M_W ¹⁴.

The predictions for M_W in the SM and the MSSM are compared with the current experimental results for M_W and m_t [76] which are displayed by the corresponding 68% C.L. ellipse shown in gray. One can see that the SM prediction barely touches the 68% C.L. ellipse, whereas the ellipse is fully contained in the MSSM area. It is obvious that the MSSM contains parameter regions where the MSSM prediction for M_W is in very good agreement with the data. On the other hand, also M_W values significantly above the experimental value are possible in the MSSM. The latter arise mainly from very light states and a large mass splitting in the stop and sbottom sector (see the discussion below).

Fig. 5.11 shows that confronting the prediction for M_W in the MSSM with the experimental result is of interest both for putting constraints on parameter regions that would give rise to a too high value of M_W and for investigating the parameter region where the agreement between the MSSM prediction and the data is in fact better than

¹⁴It should be noted that a similar kind of feature would occur even if one restricted the predicted value for M_h in the MSSM to the same region as the range adopted for $M_{H^{\text{SM}}}$. This is caused by the fact that the additional theoretical uncertainties from unknown higher-order corrections affecting the prediction for M_h in the MSSM, which are not present in the SM where $M_{H^{\text{SM}}}$ is a free input parameter, essentially lead to a broadening of the allowed range of M_h in the MSSM as compared to $M_{H^{\text{SM}}}$.

for the SM case. While the deviation between the SM prediction and the experimental result for M_W is statistically not very significant (the SM prediction is well compatible with the experimental result at the 95% C.L.), the pattern that the SM prediction is somewhat low as compared to the data has been robust for many years in spite of numerous updates of the experimental results. Focussing now on the region where we find the best agreement between the MSSM prediction for M_W and the experimental result, it is interesting to note that in this region some of the superpartner masses are expected to be relatively light. In order to illustrate this feature we furthermore show in Fig. 5.11 the impact of the slepton sector (left arrow) and the chargino sector (right arrow), where the mass values indicated at the arrows (approximately) show the effect in M_W arising from the contribution of a slepton and a chargino of such mass, respectively. We have chosen to display those arrows such that they start at the lower border, corresponding to the situation where all other superpartners are heavy and decoupled. For the sleptons we show the corrections to M_W as a function of $M_L \equiv M_{\tilde{E}_{1,2,3}} = M_{\tilde{L}_{1,2,3}}$, where the lower limit of ~ 90 GeV roughly corresponds to the (fairly model-independent) limit obtained at LEP. One can see that very light sleptons, just above the LEP limit, could induce a shift in M_W of about 60 MeV. We have checked that each generation contributes roughly the same to this effect. The major contributions to M_W from the sleptons arise from the $\Delta\rho$ term in Eq. (5.7), which is sensitive to the mass splitting between $\tilde{l}_{1,2}$ and $\tilde{\nu}_l$. The splitting between the sneutrinos and the sleptons becomes significant if $M_{\tilde{E}} = M_{\tilde{L}}$ and M_W are of comparable size. The contributions to M_W from light charginos and neutralinos are substantially smaller, but clearly not negligible in this context. They reach about 20 MeV for $m_{\tilde{\chi}_1^\pm} \sim 95$ GeV, close to its lower mass limit from LEP. In that case, due to the assumed GUT relation between M_1 and M_2 , the mass of $\tilde{\chi}_1^0$ is ~ 50 GeV. Our analysis of the contributions in the slepton and the chargino/neutralino sector shows that even if all squarks were so heavy that their contribution to the M_W prediction were negligible, contributions from the slepton sector or the chargino/neutralino sector could nevertheless be sufficient to bring the MSSM prediction in perfect agreement with the data. This could be the case for slepton masses of about 150–200 GeV or for a chargino mass of about 100–150 GeV. If the squark sector gives rise to a non-zero contribution to M_W the same predicted value for M_W could be reached with heavier sleptons and charginos/neutralinos.

In Fig. 5.12 and Fig. 5.13 we analyze in detail the dependence of M_W on the scalar quark masses, in particular on $m_{\tilde{t}_1}$ and $m_{\tilde{b}_1}$, with m_t fixed to 173.2 GeV. The upper left plot of Fig. 5.12 shows the prediction for M_W (green dots) as a function of $m_{\tilde{t}_1}$. All points are allowed by the constraints discussed in Sect. 5.4.3 and fulfill the additional constraint $m_{\tilde{t}_2, \tilde{b}_2}/m_{\tilde{t}_1, \tilde{b}_1} < 2.5$. The SM prediction is shown as a red strip for $M_{H^{\text{SM}}} = 125.6 \pm 0.7$ GeV, and the 1σ experimental result is indicated as a gray band. We checked that without the cut $m_{\tilde{t}_2, \tilde{b}_2}/m_{\tilde{t}_1, \tilde{b}_1} < 2.5$ the largest M_W values are reached for very light stop masses with a very large (> 2.5) splitting in the stop sector. Applying this cut, the maximum of ~ 80.6 GeV is reached for $m_{\tilde{t}_1}$ around 800 GeV. The position where the maximum is reached depends strongly on the splitting between stops and sbottoms and will be further explained below (in the discussion of Fig. 5.13). In the upper right

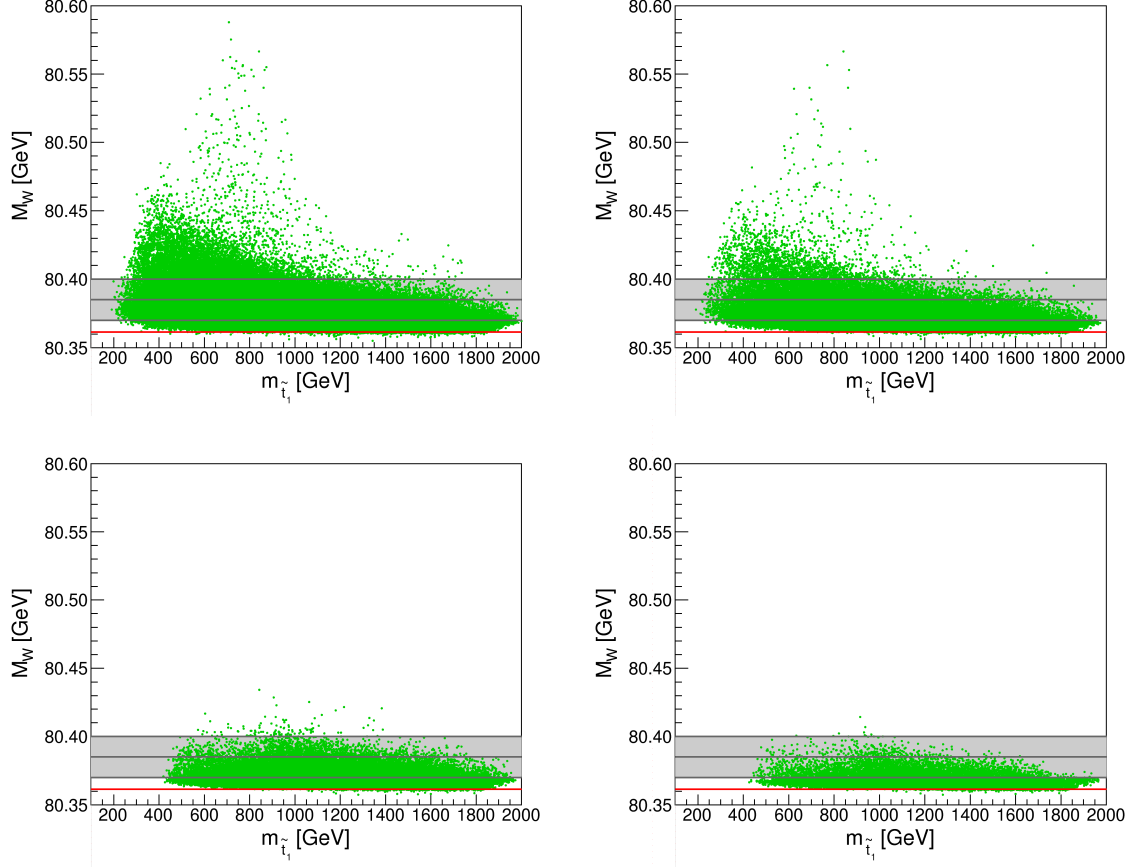


Figure 5.12: Prediction for M_W as a function of the lightest stop mass $m_{\tilde{t}_1}$. In all plots the cuts $m_{\tilde{t}_2}/m_{\tilde{t}_1} < 2.5$ and $m_{\tilde{b}_2}/m_{\tilde{b}_1} < 2.5$ are applied. In the upper left plot all HiggsBounds allowed points are shown, in the upper right plot only the points are shown for which additionally the squarks of the first two generations and the gluino are heavier than 1200 GeV, in the lower left plot only the points are shown for which additionally the sbottoms are heavier than 1000 GeV, and in the lower right plot only the points are shown for which additionally also the sleptons and charginos are heavier than 500 GeV. The red line indicates the SM prediction for M_W .

plot we only show points which have first and second generation squark masses and the gluino mass above 1.2 TeV, i.e. roughly at the limit obtained at the LHC for simplified spectra [67, 68]. It can be observed that the effects on M_W of the first and second generation squarks as well as of the gluino are rather mild. Next, in the lower left plot we only show points which in addition have \tilde{b} masses above 1000 GeV (this is a hypothetical cut that is applied for illustration purposes only; it does not reflect the current experimental situation). The fact that all MSSM points in the lower left and lower right plots have stop masses larger than 400 GeV results from the restrictions that we have imposed, constraining the sbottom masses (> 1000 GeV) and the maximal

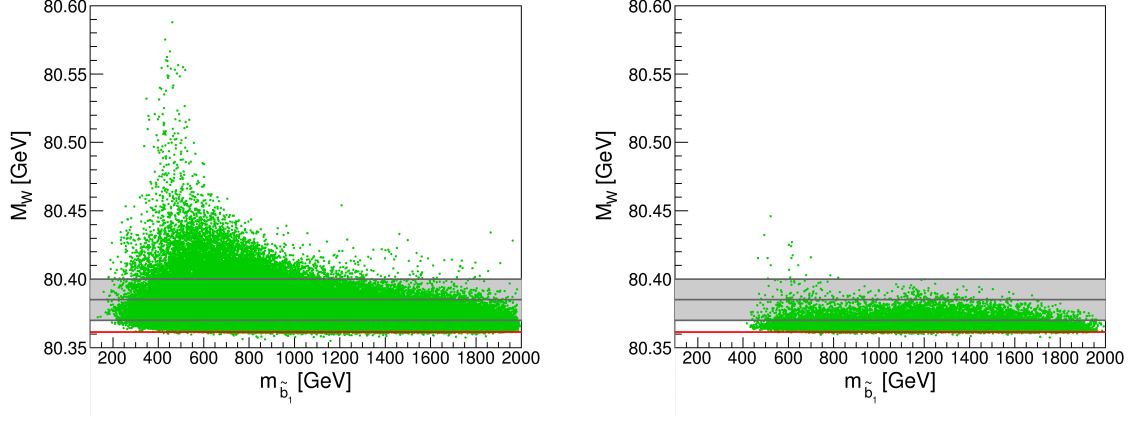


Figure 5.13: Prediction for M_W as a function of the lightest sbottom mass. The cuts $m_{\tilde{t}_2}/m_{\tilde{t}_1} < 2.5$ and $m_{\tilde{b}_2}/m_{\tilde{b}_1} < 2.5$ are applied. In the left plot all HiggsBounds allowed points are shown, in the right plot only the points are shown for which additionally the squarks of the first two generations and the gluino are heavier than 1200 GeV, stops are heavier than 1000 GeV and also the sleptons and charginos are heavier than 500 GeV. As above, the red line indicates the SM prediction for M_W .

splitting in the stop and sbottom sector ($m_{\tilde{t}_2, \tilde{b}_2}/m_{\tilde{t}_1, \tilde{b}_1} < 2.5$) at the same time. Clearly the sbottoms have a large impact on the M_W prediction. After applying (for illustration) the sbottom mass cut the maximal M_W values obtained in the scan are ~ 80.43 GeV, i.e. the SUSY contributions can still be so large in this case that they can yield not only predicted M_W values that are in good agreement with the experimental result but also ones that are significantly higher. The SUSY shift in this case is caused by the remaining contribution from the stop–sbottom sector, as well as by the contributions from charginos, neutralinos and sleptons. In order to disentangle these effects, in the lower right plot we also require (again, for illustrative purposes only) the electroweak SUSY particles to be heavy and show only points with slepton and chargino masses above 500 GeV. A direct mass limit on neutralinos is not applied. Since we fixed $M_1 \approx \frac{1}{2}M_2$, all points have neutralino masses above ~ 240 GeV. In this plot the shift in the M_W prediction as compared to the SM case arises solely from the stop–sbottom sector with $m_{\tilde{b}_1} > 1000$ GeV (neglecting the numerically insignificant contributions from the other sectors for large SUSY particle masses). One can observe that M_W values up to the upper edge of the experimental 1σ band (~ 80.400 GeV) can still be reached for $m_{\tilde{t}_1}$ values as high as $m_{\tilde{t}_1} \sim 1100$ GeV in this case. For larger stop masses, $m_{\tilde{t}_1} \gtrsim 1100$ GeV, the contributions from the stop–sbottom sector decrease as expected in the decoupling limit.¹⁵

¹⁵In all plots in Fig. 5.12 one can see a small gap between the MSSM points for $m_{\tilde{t}_1} > 1900$ GeV and the SM line. This is an artefact of the chosen scan ranges: in this region the mass-splitting between \tilde{t}_1 and \tilde{t}_2 is small, and m_h does not reach values up to ~ 126 GeV. The M_W value approached in the decoupling limit therefore corresponds to the SM prediction for a lower Higgs mass value.

Now we turn to Fig. 5.13 showing the M_W prediction plotted against $m_{\tilde{b}_1}$. In the left plot we show all points that are allowed by `HiggsBounds` and the other constraints described above (in particular, $m_{\tilde{t}_2}/m_{\tilde{t}_1} < 2.5$ and $m_{\tilde{b}_2}/m_{\tilde{b}_1} < 2.5$ is required). In the right plot only those points are displayed for which the stops are heavier than 1000 GeV, the first and second generation squark masses as well as the gluino mass are above 1200 GeV, and the sleptons and charginos are heavier than 500 GeV. Focusing first on the left plot, one can see that it displays the same qualitative features as the upper left plot of Fig. 5.12. While one would normally expect that the highest values for M_W are obtained for the smallest values of $m_{\tilde{t}_1}$ and $m_{\tilde{b}_1}$, in the corresponding plots of Fig. 5.12 and Fig. 5.13 the highest M_W values are found for $m_{\tilde{t}_1} \sim 800$ GeV and $m_{\tilde{b}_1} \sim 400$ GeV. This feature is related to the imposed restriction that the maximal mass splitting for stop and sbottom masses is limited to be smaller than 2.5. The largest correction to M_W originates from the stop–sbottom contributions to $\Delta\rho$, which depend sensitively on the mass splittings between the four squarks of the third generation. After imposing the limit on the maximal mass splittings of stops and sbottoms, these contributions become largest if the relative size of the sbottom mixing, $|X_b/\max(M_{\tilde{Q}_3}, M_{\tilde{D}_3})|$, reaches its maximum. This is realized in this case for $m_{\tilde{b}_1} \sim 400$ GeV and $m_{\tilde{b}_2}/m_{\tilde{b}_1} \sim 2.5$, $m_{\tilde{t}_1}/m_{\tilde{b}_1} \sim 2$, giving rise to the maximum around $m_{\tilde{t}_1} \sim 800$ GeV and $m_{\tilde{b}_1} \sim 400$ GeV in the upper left plot of Fig. 5.12 and the left plot of Fig. 5.13, respectively. As expected, for higher values of $m_{\tilde{b}_1}$ the maximum value reached for M_W in Fig. 5.13 decreases, but M_W values as high as the experimental central value are seen to be possible all the way up to $m_{\tilde{b}_1} \sim 2$ TeV. In the right plot the other SUSY particles are required to be rather heavy (in particular, the stop masses are assumed to be above 1000 GeV; the other masses are restricted as described above), so that the impact of the contributions from the sbottom sector becomes apparent. While rather large contributions are possible for sbottom masses below about 800 GeV, for the highest values of $m_{\tilde{b}_1}$ shown in the figure the MSSM prediction for M_W approaches the one in the SM.

So far we have only taken into account the existing *limits* from the Higgs searches at the LHC and other colliders (via the program `HiggsBounds`), but we have not explicitly imposed a constraint in view of the observed *signal* at ~ 125.6 GeV. Within the MSSM (referring to the \mathcal{CP} -conserving case for simplicity), the signal can, at least in principle, be identified either with the light \mathcal{CP} -even Higgs boson h or the heavy \mathcal{CP} -even Higgs boson H . In Fig. 5.14 we show the SM and MSSM prediction of M_W as a function of m_t as obtained from our scan according to table 5.1, where in the left plot the green MSSM area fulfills $M_h = 125.6 \pm 3.1$ GeV, while in the right plot the green MSSM area fulfills $M_H = 125.6 \pm 3.1$ GeV. The substantially larger uncertainty with respect to the SM experimental uncertainty of 0.7 GeV (at the 2σ level) arises as a consequence of the theoretical uncertainties from unknown higher-order corrections in the MSSM prediction for the Higgs boson mass. We have added a global uncertainty of 3 GeV [185] in quadrature, yielding a total uncertainty of 3.1 GeV.

Starting with the left plot, where the light \mathcal{CP} -even Higgs boson has a mass that is compatible with the observed signal, we find a similar result as in Fig. 5.11. In particular, the comparison with the experimental results for M_W and m_t , indicated by the gray

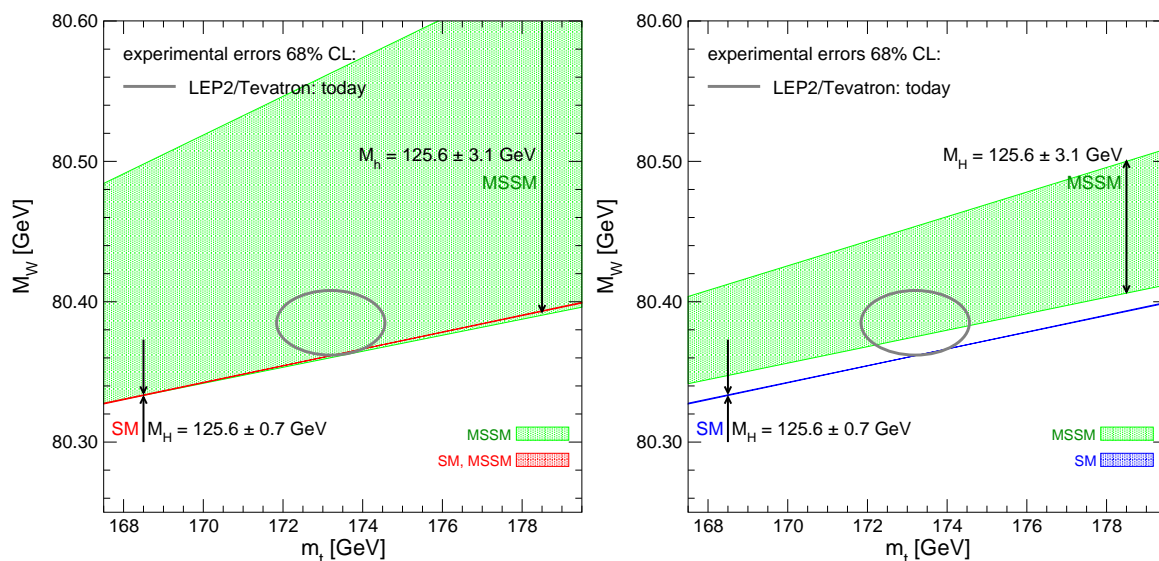


Figure 5.14: Prediction for M_W as a function of m_t . The left plot shows the M_W prediction assuming the *light* \mathcal{CP} -even Higgs boson h in the mass region 125.6 ± 3.1 GeV. The red band indicates the overlap region of the SM and the MSSM with $M_{HSM} = 125.6 \pm 0.7$ GeV. The right plot shows the M_W prediction assuming the *heavy* \mathcal{CP} -even Higgs boson H in the mass region 125.6 ± 3.1 GeV. The blue band indicates the SM region with $M_{HSM} = 125.6 \pm 0.7$ GeV. All points are allowed by HiggsBounds.

ellipse, shows a slight preference for a non-zero SUSY contribution to M_W . While the width of the MSSM area shown in green is somewhat reduced compared to Fig. 5.11 because of the additional constraint applied here (requiring M_h to be in the range $M_h = 125.6 \pm 3.1$ GeV leads to a constraint on the stop sector parameters, see, e.g., Ref. [48], which in turn limits the maximal contribution to M_W), the qualitative features are the same as in Fig. 5.11. This is not surprising, since the limits from the Higgs searches implemented in Fig. 5.11 have already led to a restriction of the allowed mass range to the unexcluded region near the observed signal. As in Fig. 5.11 the plot shows a small MSSM region (green) below the overlap region between the MSSM and the SM (red), which is a consequence of the broadening of the allowed range of M_h caused by the theoretical uncertainties from unknown higher-order corrections, as explained above.

In the right plot of Fig. 5.14 we show the result for the case where instead the mass of the heavy \mathcal{CP} -even Higgs boson is assumed to be compatible with the observed signal, i.e. $M_H = 125.6 \pm 3.1$ GeV. While as mentioned above the interpretation of the discovered signal in terms of the heavy \mathcal{CP} -even Higgs boson within the MSSM is challenged in particular by the recent ATLAS bound on light charged Higgs bosons [55] (which is not yet included in the version of HiggsBounds used for our analysis),¹⁶ it is nevertheless interesting to investigate to what extent the precision observable M_W is sensitive to such

¹⁶If the Higgs sector contains an additional singlet, as in the NMSSM, it is possible to have a SM-like second-lightest Higgs, while the charged Higgs boson can be much heavier in this case, see e.g. Ref. [207].

a rather exotic scenario where all five states of the MSSM Higgs sector are light. The lightest \mathcal{CP} -even Higgs in this scenario has a heavily suppressed coupling to gauge bosons and a mass that can be significantly below the LEP limit for a SM-like Higgs, see e.g. Ref. [54]. As shown in the right plot of Fig. 5.14, the constraint $M_H = 125.6 \pm 3.1$ GeV gives rise to a situation where the MSSM region (green) does not overlap with the SM prediction (blue). This gap between the predictions of the two models is caused by the fact that $M_H = 125.6 \pm 3.1$ GeV implies light states in the Higgs sector (in particular a light charged Higgs), which lead to a non-zero SUSY contribution to M_W in this case, whereas for the light \mathcal{CP} -even Higgs boson the constraint $M_h = 125.6 \pm 3.1$ GeV can be fulfilled in the decoupling region of the MSSM. The plot furthermore shows that the constraint $M_H = 125.6 \pm 3.1$ GeV implies not only a lower bound on the SUSY contribution to M_W but also a more restrictive upper bound, as can be seen from comparing the two plots in Fig. 5.14. It is interesting to note that also in the case where the heavy \mathcal{CP} -even Higgs is in the mass range compatible with the observed signal, the MSSM turns out to be better compatible with the experimental results for M_W and m_t (indicated by the gray ellipse) than the SM.

In Fig. 5.15 we analyze the dependence of the M_W prediction on light scalar taus. In Refs. [208, 209] it was shown that light scalar taus can enhance the decay rate of the light \mathcal{CP} -even Higgs boson into photons. This is of interest in view of the current experimental situation, where the signal strength in the $\gamma\gamma$ channel observed by ATLAS [19] lies significantly above the value expected in the SM (but is still compatible at the 2σ level), while the signal strength observed in CMS [20] is currently slightly below the SM level. Since loop contributions of BSM particles to the decay width $\Gamma(h \rightarrow \gamma\gamma)$ do not have to compete with a SM-type tree-level contribution, this loop-induced quantity is of particular relevance for investigating possible deviations from the SM prediction. Fig. 5.15 shows the prediction for M_W as a function of $\Gamma(h \rightarrow \gamma\gamma)/\Gamma(H \rightarrow \gamma\gamma)_{\text{SM}}$, where the latter has been evaluated with `FeynHiggs`. As a starting point we use the best-fit point of the analysis presented in chapter 7 and Ref. [49] obtained from a pMSSM-7 fit to all Higgs data (available at that time), which indeed exhibited an enhancement of $\Gamma(h \rightarrow \gamma\gamma)$ due to scalar taus with a mass close to 100 GeV. The parameters of the best fit point are $M_A = 669$ GeV, $\tan\beta = 16.5$, $\mu = 2640$ GeV, $M_{\tilde{Q}_3} = M_{\tilde{U}_3} = M_{\tilde{D}_3} = 1100$ GeV, $M_{\tilde{Q}_{1,2}} = M_{\tilde{U}_{1,2}} = M_{\tilde{D}_{1,2}} = 1000$ GeV, $M_{\tilde{L}_3} = M_{\tilde{E}_3} = 285$ GeV, $M_{\tilde{L}_{1,2}} = M_{\tilde{E}_{1,2}} = 300$ GeV, $A_f = 2569$ GeV, $M_2 = 201$ GeV and $M_3 = 1000$ GeV. In Fig. 5.15 the best-fit point is indicated as a black star. We vary the stau mass scale $M_{\tilde{E}_3} = M_{\tilde{L}_3}$ in the range of 280 GeV to 500 GeV, giving rise to a corresponding variation of the lighter stau mass. The results are shown as the green line in Fig. 5.15, where the current experimental 1σ region for M_W is indicated as a gray band. One can observe that for light scalar taus, corresponding to larger $\Gamma(h \rightarrow \gamma\gamma)$, the agreement of the prediction for M_W with the experimental value is improved. A certain level of enhancement of $\Gamma(h \rightarrow \gamma\gamma)$ is also compatible with the current experimental results on the signal strength in the $\gamma\gamma$ channel. For heavy scalar taus, as obtained for $M_{\tilde{E}_3} = M_{\tilde{L}_3} = 500$ GeV (and keeping the other parameters as defined above), the M_W prediction still remains within the experimental 1σ band, while nearly SM values for $\Gamma(h \rightarrow \gamma\gamma)$ are reached.

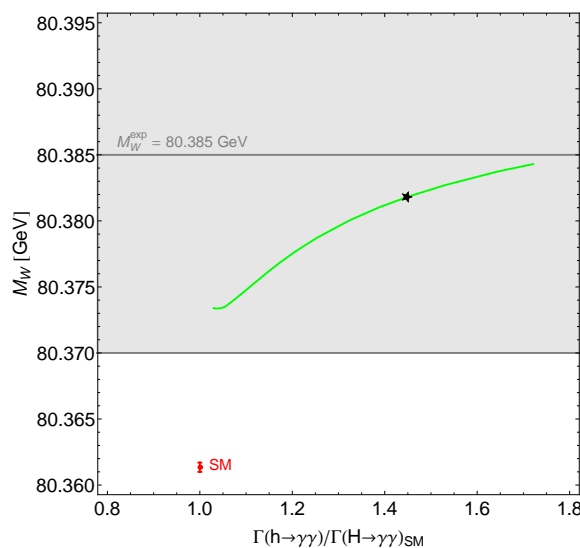


Figure 5.15: M_W prediction in the MSSM as a function of $\Gamma(h \rightarrow \gamma\gamma)$, normalized to the SM value. The black star indicates the best fit point from a pMSSM-7 fit to all Higgs data (available at that time) [49]. The green line is obtained by varying $M_{\tilde{E}_3} = M_{\tilde{L}_3}$ from 280 GeV to 500 GeV.

5.7.3 Discussion of future scenarios

In the final step of our investigation of parameter scans in the MSSM we discuss the precision observable M_W in the context of possible *future* scenarios. We first investigate the impact of an assumed limit of 500 GeV on stops and sbottoms (and assume that no other colored particles are observed below 1200 GeV).

In Fig. 5.16 we show again the M_W – m_t planes as presented in Fig. 5.11 (where the parameter region allowed by `HiggsBounds` is displayed) and in Fig. 5.14 (M_h or M_H in the range of 125.6 ± 3.1 GeV), but now in addition the light blue points obey the (hypothetical) mass limits for stops and sbottoms (500 GeV) and for other colored particles (1200 GeV). The left plot shows the `HiggsBounds` allowed points, whereas in the middle (right) plot $M_h(M_H) = 125.6 \pm 3.1$ GeV is required. It can be observed that the light blue points corresponding to a relatively heavy colored spectrum are found at the lower end of the predicted M_W range, i.e. in the decoupling region of the MSSM. As discussed above the largest SUSY contributions arise from the stop–sbottom sector. If lower mass limits on stops and sbottoms of 500 GeV are assumed, it can be seen that the band corresponding to the possible range of predictions for M_W in the MSSM would shrink significantly, to the region populated by the blue points. It should be noted that the prediction for M_W in this region is in perfect agreement with the experimental measurements of M_W and m_t . Besides the contributions of stops and sbottoms, which can still be significant even if the stops and sbottoms are heavier than 500 GeV, the main SUSY corrections arise from relatively light sleptons, charginos and neutralinos, as analyzed above.

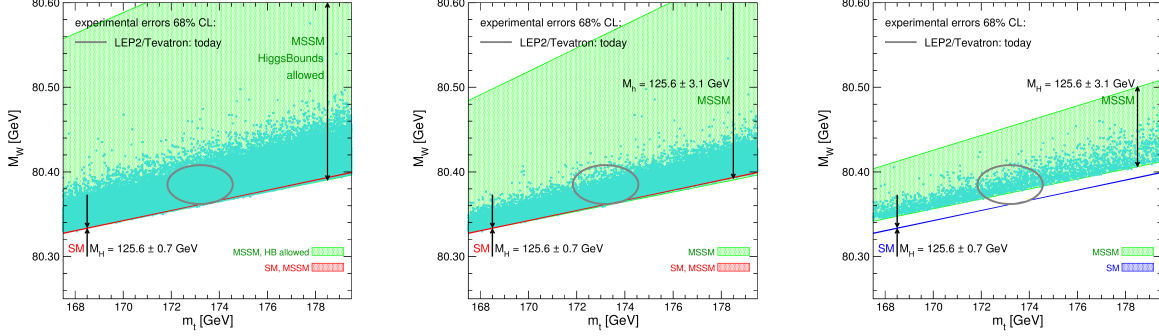


Figure 5.16: Prediction for M_W as a function of m_t . The left plot shows all points allowed by HiggsBounds, the middle one requires M_h to be in the mass region 125.6 ± 3.1 GeV, while in the right plot M_H is required to be in the mass region 125.6 ± 3.1 GeV. The color coding is as in Figs. 5.11 and 5.14. In addition, the blue points are the parameter points for which the stops and sbottoms are heavier than 500 GeV and squarks of the first two generations and the gluino are heavier than 1200 GeV.

While so far we have compared the various predictions with the current experimental results for M_W and m_t , we now discuss the impact of future improvements of these measurements. For the W boson mass we assume, based on a recent study [114], an improvement of a factor three compared to the present case down to $\Delta M_W = 5$ MeV from future measurements at the LHC and a prospective Linear Collider (ILC), while for m_t we adopt the anticipated ILC accuracy of $\Delta m_t = 100$ MeV [210]. For illustration we show in Fig. 5.17 again the left plot of Fig. 5.14, assuming the mass of the light \mathcal{CP} -even Higgs boson h in the region 125.6 ± 3.1 GeV, but supplement the gray ellipse indicating the present experimental results for M_W and m_t with the future projection indicated by the red ellipse (assuming the same experimental central values). While currently the experimental results for M_W and m_t are compatible with the predictions of both models (with a slight preference for a non-zero SUSY contribution), the anticipated future accuracies indicated by the red ellipse would clearly provide a high sensitivity for discriminating between the models and for constraining the parameter space of BSM scenarios.

As a further hypothetical future scenario we assume that a light scalar top quark has been discovered at the LHC with a mass of $m_{\tilde{t}_1} = 400 \pm 40$ GeV, while no other new particle has been observed. As before, for this analysis we use an anticipated experimental precision of $\Delta M_W = 5$ MeV (other uncertainties have been neglected in this analysis). Concerning the masses of the other SUSY particles, we assume lower limits of 300 GeV on both sleptons and charginos, 500 GeV on other scalar quarks of the third generation and

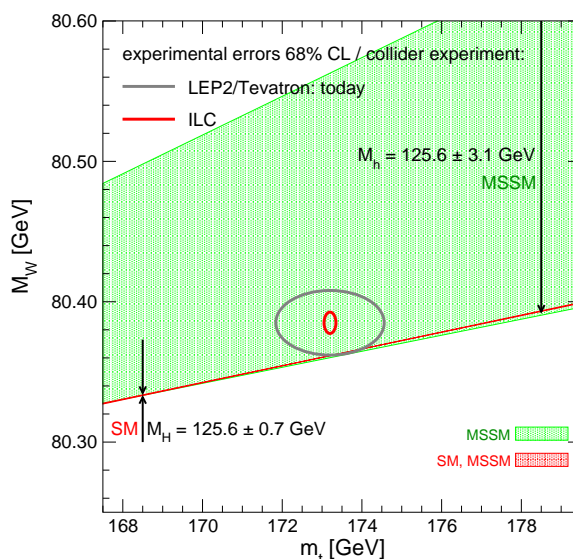


Figure 5.17: Prediction for M_W as a function of m_t , as given in the left plot of Fig. 5.14 (the mass M_h of the light \mathcal{CP} -even Higgs boson is assumed to be in the region 125.6 ± 3.1 GeV). In addition to the current experimental results for M_W and m_t that are displayed by the gray 68% C.L. ellipse the anticipated future precision at the ILC is indicated by the red ellipse (assuming the same experimental central values).

of 1200 GeV on the remaining colored particles. We have selected the points from our scan accordingly. Any additional particle observation would impose a further constraint and would thus enhance the sensitivity of the parameter determination. In Fig. 5.18 we show the parameter points from our scan that are compatible with the above constraints. All points fulfill $M_h = 125.6 \pm 3.1$ GeV and $m_{\tilde{t}_1} = 400 \pm 40$ GeV. Yellow, red and blue points have furthermore a W boson mass of $M_W = 80.375, 80.385, 80.395 \pm 0.005$ GeV, respectively, corresponding to three hypothetical future central experimental values for M_W . The left plot in Fig. 5.18 shows the M_W prediction as a function of the lighter sbottom mass. Assuming that the experimental central value for M_W stays at its current value of 80.385 GeV (red points) or goes up by 10 MeV (blue points), the precise measurement of M_W would set stringent upper limits of ~ 800 GeV (blue) or ~ 1000 GeV (red) on the possible mass range of the lighter sbottom. As expected, this sensitivity degrades if the experimental central value for M_W goes down by 10 MeV (yellow points), which would bring it closer to the SM value given in Eq. (5.29). The right plot shows the results in the $m_{\tilde{b}_1} - m_{\tilde{t}_2}$ plane. It can be observed that sensitive upper bounds on those unknown particle masses could be set¹⁷ based on an experimental value of M_W of 80.385 ± 0.005 GeV or 80.395 ± 0.005 GeV (i.e. for central values sufficiently different from the SM prediction). In this situation the precise M_W measurement could give interesting indications regarding the search for the heavy stop and the light sbottom (or put the interpretation within the MSSM under tension).

¹⁷See also Ref. [211] for a recent analysis investigating constraints on the scalar top sector.

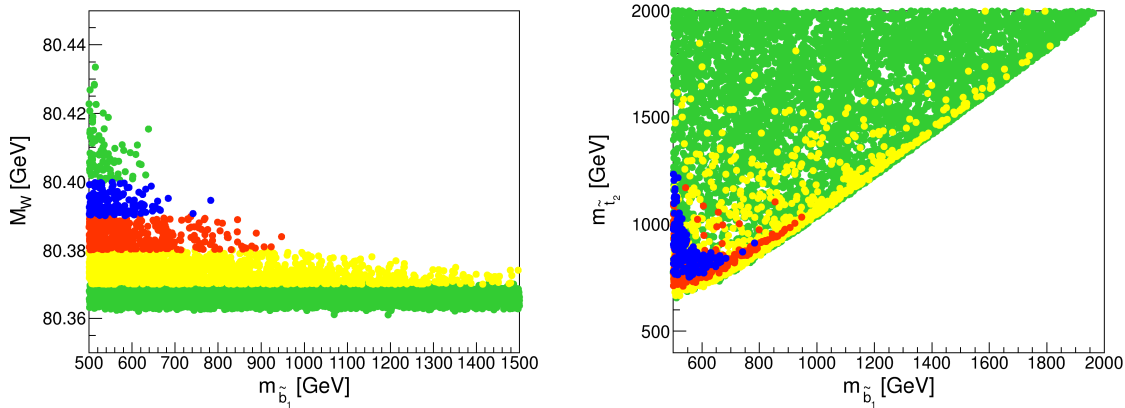


Figure 5.18: Results of an MSSM parameter scan illustrating the prediction for M_W in a hypothetical future scenario assuming a measurement of $m_{\tilde{t}_1} = 400 \pm 40$ GeV at the LHC as well as lower limits on all other SUSY particles: the assumed lower limits are 500 GeV for the other third generation squarks, 1200 GeV for all other colored particles, and 300 GeV for sleptons and charginos. All displayed points fulfill $M_h = 125.6 \pm 3.1$ GeV. The yellow, red and blue points correspond to $M_W = 80.375 \pm 0.005$ GeV (yellow), $M_W = 80.385 \pm 0.005$ GeV (red), and $M_W = 80.395 \pm 0.005$ GeV (blue). The left plot shows the prediction for M_W as a function of the lighter sbottom mass, $m_{\tilde{b}_1}$, while the right plot shows the M_W prediction in the $m_{\tilde{b}_1} - m_{\tilde{t}_2}$ plane.

5.7.4 Dependence of the M_W prediction on complex phases

Before turning to the M_W prediction in the NMSSM, we want to discuss the impact of complex phases on the M_W prediction in the MSSM. The effect of complex phases on the M_W^{MSSM} prediction has been discussed in detail in Ref. [156]. It was shown in Ref. [156] that the phase dependence of the sfermion one-loop contributions can be sizable, while the phase dependence of the chargino/neutralino one-loop contributions is smaller ($\mathcal{O}(1 \text{ MeV})$).

As discussed in the previous subsection, the leading sfermion contributions stem from the stop/sbottom sector, where the dominant effect comes from $\Delta\rho$ which is highly sensitive to the mass splitting between the sfermions. The size of the sfermion contributions will be discussed in more detail in the context of the NMSSM (in the next section). The results we derive in the NMSSM hold also for the MSSM, since the sfermion sector is identical in these two models. Here we focus on the dependence of the M_W^{MSSM} prediction on complex phases in the stop/sbottom sector.

The complex parameters in the stop/sbottom sector are $A_{t/b}$ and μ , which do not appear separately in the one-loop contributions but only in the combinations $X_{t/b}$. It has been shown in Ref. [156] that the complex phase of $X_{t/b}$ drops out in the one-loop Δr result and that therefore the phases only occur in the combination $(\phi_{A_{t/b}} + \phi_\mu)$ in the one-loop sfermion contributions. We illustrate the phase dependence in Fig. 5.19. Here

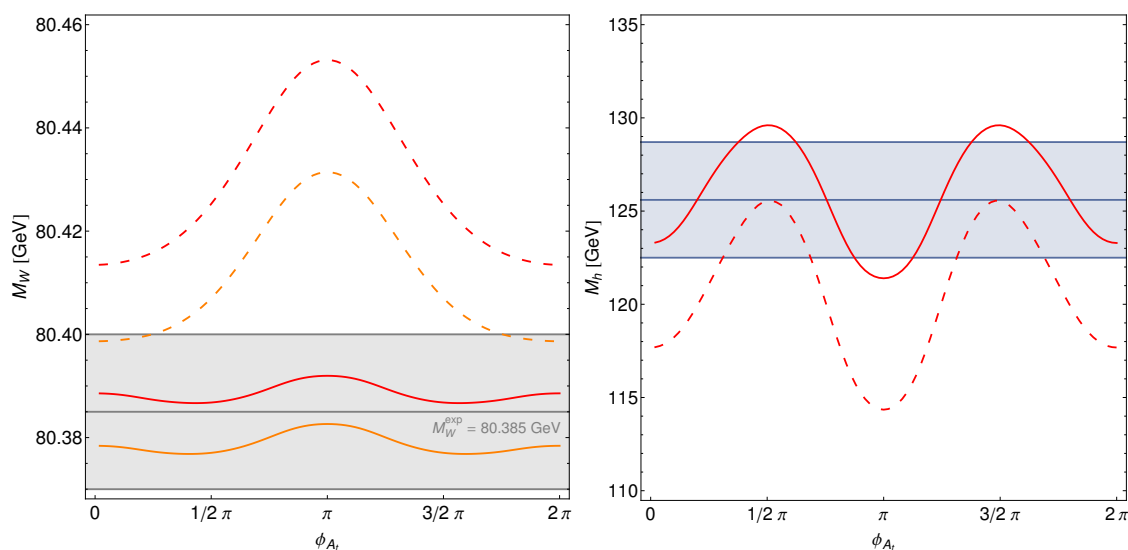


Figure 5.19: Dependence of the M_W prediction and the M_h prediction on the complex phase ϕ_{A_t} . As a starting point we take the *light stop* benchmark scenario of Ref. [54] with $\tan\beta = 15$ and $M_A = 800$ GeV. For the solid lines $M_{\text{SUSY}} = 500$ GeV is chosen (as in the original benchmark scenario), and for the dashed lines $M_{\text{SUSY}} = 300$ GeV. We set $A_t = |A_t| \exp(i\phi_{A_t})$ with $|A_t| = 2 M_{\text{SUSY}} + \mu/\tan\beta$ and vary ϕ_{A_t} from 0 to 2π , while ϕ_μ is set to zero. The left plot shows the MSSM prediction for M_W . The orange curves show the prediction based on the full SM result but including only the one-loop MSSM contributions, while the red curves show the full MSSM result obtained as in Eq. (5.30). The right plot shows the M_h prediction.

we set $\phi_\mu = 0$ for simplicity, so that the phase $(\phi_{A_{t/b}} + \phi_\mu)$ reduces to $\phi_{A_{t/b}}$. Further we set $\phi_{A_b} = \phi_{A_t}$ and we show the M_W prediction as a function of ϕ_{A_t} .

As a starting point, we choose the *light stop* benchmark scenario of Ref. [54]¹⁸. In this scenario the mixing parameter X_t is chosen close to the value which maximises the lightest \mathcal{CP} -even Higgs mass ($X_t = 2 M_{\text{SUSY}}$). For this choice of X_t , M_h predictions in accordance with the experimental value are obtained for stop masses significantly below 1 TeV (for this benchmark point $m_{\tilde{t}_1} \sim 325$ GeV and $m_{\tilde{t}_2} \sim 670$ GeV). We set $A_t = |A_t| \exp(i\phi_{A_t})$ with $|A_t| = 2 M_{\text{SUSY}} + \mu/\tan\beta$ and vary ϕ_{A_t} from 0 to 2π (setting the phase of μ to zero). We choose $A_b = A_t$ and for all other sfermions $A_f = 0$. The results choosing $M_{\text{SUSY}} = 500$ GeV (as in the original benchmark point) are shown as solid lines, whereas the dashed lines are obtained by setting $M_{\text{SUSY}} = 300$ GeV (in the latter case the stops are lighter, $m_{\tilde{t}_1} \sim 118$ GeV for $\phi_{A_t} = 0$).

The left plot shows the MSSM prediction for M_W . For the orange lines we use the full result for the SM-type contributions but only the one-loop MSSM contributions. For

¹⁸The exact parameters we use are $m_t = 173.2$, $\tan\beta = 15$, $\mu = 350$ GeV, $M_{\tilde{L}/\tilde{E}_{1,2}} = 500$ GeV, $M_{\tilde{L}/\tilde{E}_3} = 1000$ GeV, $M_{\tilde{Q}/\tilde{U}/\tilde{D}_{1,2}} = 1500$ GeV, $M_{\tilde{Q}_3} = M_{\tilde{U}_3} = M_{\tilde{D}_3} = 500/300$ GeV (see description in text), $A_t = |A_t| \exp(i\phi_{A_t})$ with $|A_t| = 2 M_{\text{SUSY}} + \mu/\tan\beta$, $A_b = A_t$, $A_\tau = 0$, $M_2 = 350$ GeV, $M_3 = 1500$ GeV and $M_A = 800$ GeV. All parameters apart from $A_{t/b}$ are chosen real.

the red lines we include also the SUSY higher order corrections, which have so far only been calculated for real parameters. Therefore the full $M_W(\phi)$ is approximated by

$$M_W(\phi) = M_W^{\text{1L}}(\phi) + [M_W(0) - M_W^{\text{1L}}(0)] \times \frac{1 + \cos \phi}{2} + [M_W(\pi) - M_W^{\text{1L}}(\pi)] \times \frac{1 - \cos \phi}{2}, \quad (5.30)$$

following the procedure of Ref. [156], where a simple interpolation has been performed such that the full result is recovered for $M_W(\phi = 0)$ and $M_W(\phi = \pi)$.

To get a feeling for the size of the discussed SUSY contributions (here the effect of varying ϕ_{A_t}), the experimental value $M_W^{\text{exp}} = 80.385 \pm 0.015$ GeV is shown as a grey band for comparison. However it should be noted here that the relative position of the curve compared to the M_W^{exp} band should not be overinterpreted, since the position of the M_W curve depends on other parameters unrelated to the complex phase discussed here (e.g. making the charginos lighter/heavier will shift the entire curve upwards/downwards.) This should be kept in mind also for plots in the next section displaying the M_W^{exp} band for comparison.

Starting with the solid curves ($M_{\text{SUSY}} = 500$ GeV) we see that both curves have a maximum at $\phi_{A_t} = \pi$ and minima close to $\pi/2$ and $3\pi/2$. The effect in the SUSY one-loop contributions (orange curve) from varying the complex phase ϕ_{A_t} from 0 to 2π is around 6 MeV. Looking at the full M_W prediction (red curve), we find that the SUSY two-loop corrections shift the M_W prediction upwards by ~ 10 MeV. Their size depends only very little on the complex phase, evaluated as in Eq. (5.30). Turning to the dashed curved ($M_{\text{SUSY}} = 300$ GeV) we see that the phase dependence here is significantly larger. The effect in the M_W predictions including only the SUSY one-loop contributions (orange curve) from varying ϕ_{A_t} from 0 to 2π is ~ 30 MeV. Turning to the red, dashed curve, we find that the SUSY 2-loop corrections are smallest at $\phi = 0$ where they account for ~ 14 MeV and get largest at $\phi = \pi$, where they reach ~ 21 MeV. At $\phi = 0$ the gluon, gluino and mass-shift two-loop corrections are of similar size (4 – 5 MeV), while for $\phi = \pi$ the mass-shift corrections dominate with ~ 11 MeV. The SUSY two-loop contributions are defined in Sect. 5.3.4 and their size will be analysed in more detail in Sect. 5.8.

The right plot shows the M_h prediction. We see that for $M_{\text{SUSY}} = 500$ GeV the predicted value for M_h (calculated with `FeynHiggs`) lies in the mass range of the observed signal 125.6 ± 3.1 GeV (we include a 3 GeV theoretical uncertainty added quadratically to the experimental error from unknown higher order corrections, see above), indicated by the blue band, for most values of the complex phase ϕ_{A_t} , just for $\phi_{A_t} \sim \pi/2, 3\pi/2$ ($\phi_{A_t} = \pi$) the Higgs mass value is slightly too high (low) for the parameters in this scenario. For $M_{\text{SUSY}} = 300$ GeV the value for M_h is too low for most values of ϕ_{A_t} , only in the regions around $\phi_{A_t} \sim \pi/2, 3\pi/2$ a Higgs mass value large enough to explain the LHC signal is reached. The value $M_{\text{SUSY}} = 300$ GeV has been chosen to demonstrate the possible size of the complex phases on the M_W prediction, even though a large range of ϕ_{A_t} values is phenomenologically disfavoured by the low M_h value in this scenario.

5.8 Results for the M_W prediction in the NMSSM

We now turn to the discussion of the prediction for M_W in the NMSSM. Our numerical results are based on the contributions to Δr described in Sect. 5.3.3 and Sect. 5.3.4 and we use the computational framework for the NMSSM presented in Sect. 5.4. Complex phases are not included in the NMSSM evaluation, consequently for all parameters given in this section the phases are set to zero and will not be listed as separate input parameters. Throughout this section, all points are allowed by the LEP limits on SUSY particle masses, all theoretical constraints in `NMSSMTools`, and have the neutralino as LSP. Unless stated otherwise, we choose the masses of the first and second generation squarks and the gluino to be large enough to not be in conflict with the negative search results for these particles at the LHC. In (some) parts of this section we want to demonstrate the size and the behaviour of the SUSY contributions also for parameter points which may not be in agreement with the Higgs search results. Therefore we discuss for each of the scenarios discussed here separately whether they are allowed by `HiggsBounds` and can explain the observed signal at 125.6 GeV. In order to study the W boson mass prediction in the NMSSM, we discuss the one-loop contributions from the sfermion sector (which are identical to the ones in the MSSM), the SUSY two-loop contributions, and then turn to the Higgs and the neutralino sectors investigating the genuine NMSSM effects.

5.8.1 Sfermion sector one-loop contributions

We start the discussion of the M_W prediction in the NMSSM by showing the contributions from the sfermion sector. The predictions for M_W which we show in this section include (unless stated otherwise) all higher-order corrections, besides the Higgsino two-loop corrections (which are numerically small, as we will discuss below). This means that the sfermion sector contributions discussed in this subsection include both one- and two-loop parts. We checked that the effects we discuss in this subsection are dominated by the sfermion one-loop contributions. The two-loop corrections are discussed separately in the next subsection.

Since these contributions are identical in the NMSSM and the MSSM, the dependence of the M_W^{NMSSM} prediction on the sfermion sector parameters is studied in the MSSM limit. The comparison to the MSSM M_W prediction serves also as validation of our implementation. As analysed already in the context of the MSSM scan (see Sect. 5.7.2), the numerically largest SUSY contributions to the W boson mass come from the one-loop diagrams involving stops and sbottoms, and in the following we show the M_W prediction as a function of the (on-shell) stop sector parameters X_t (Fig. 5.20) and M_{SUSY} (Fig. 5.21 and Fig. 5.22). The left plot of Fig. 5.20 shows the NMSSM predictions in the MSSM limit (blue curves) as well as the MSSM predictions (red curves) for M_W as a function of the stop mixing parameter X_t ¹⁹. The parameters in Fig. 5.20 are $m_t =$

¹⁹The X_t parameter that we plot here is the on-shell parameter. As described in 5.4.2 the on-shell value is transformed into a $\overline{\text{DR}}$ value, which is used as input for `NMSSMTools` to calculate the Higgs masses. All numerical values given for X_t in this section refer to the on-shell parameters.

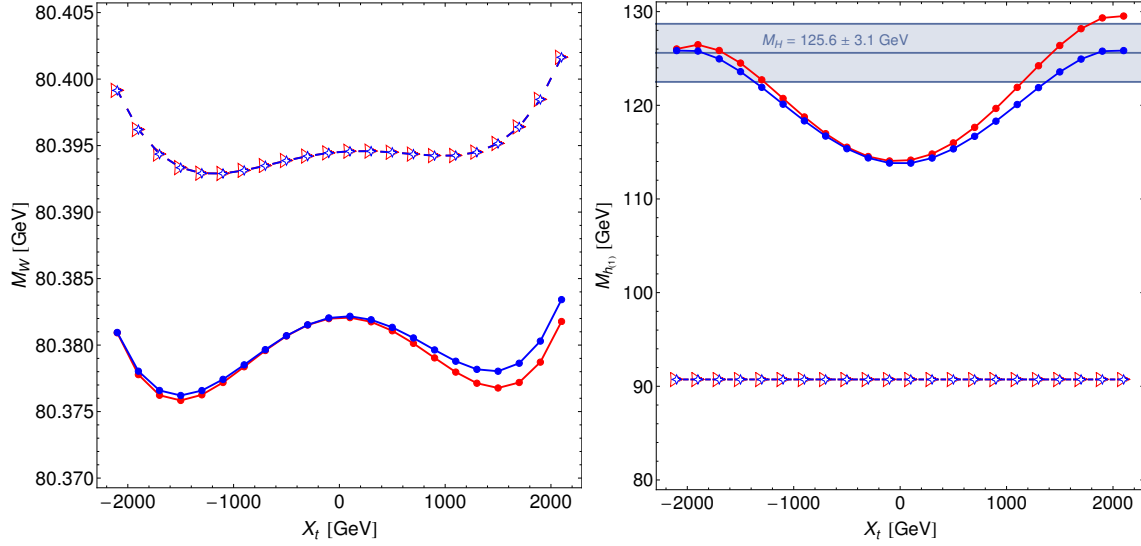


Figure 5.20: Comparison of the NMSSM predictions in the MSSM limit (blue curves) for the W boson mass (left plot) and the lightest \mathcal{CP} -even Higgs mass (right plot) with the MSSM predictions (red curves) plotted against the stop mixing parameter X_t . The parameters are given in the text. For the two dashed curves (small blue diamonds for the NMSSM predictions in the MSSM limit, and red triangles for the MSSM predictions) the tree-level Higgs masses are used. For the solid curves (with filled dots) loop-corrected Higgs masses are used: the NMSSM Higgs masses are calculated with `NMSSMTools`, and the MSSM Higgs masses calculated with `FeynHiggs`.

173.2 GeV, $\tan\beta = 20$, $\mu_{(\text{eff})} = 200$ GeV, $M_{\tilde{L}/\tilde{E}} = 500$ GeV, $M_{\tilde{Q}/\tilde{U}/\tilde{D}_{1,2}} = 1500$ GeV, $M_{\text{SUSY}} = M_{\tilde{Q}_3} = M_{\tilde{U}_3} = M_{\tilde{D}_3} = 1000$ GeV, $A_\tau = A_b = A_t$, $M_2 = 200$ GeV and $m_{\tilde{g}} = 1500$ GeV. For the additional NMSSM parameters we choose $\hat{m}_A = 1000$ GeV, $\lambda \rightarrow 0$, $K = \kappa/\lambda = 0.5$, $A_\kappa = -100$ GeV (the impact of A_κ on M_W in the MSSM-limit is negligible).

Our approach here is the following: We start from a NMSSM parameter point. We take the effective \mathcal{CP} -odd doublet mass \hat{m}_A or the parameter A_λ (here $\hat{m}_A = 1000$ GeV) as input to calculate the NMSSM Higgs boson spectrum. The charged Higgs mass (calculated in the NMSSM) is used as input for the calculation of the MSSM Higgs masses. As we discussed already in Sect. 5.3.4, this procedure ensures that the mass of the charged Higgs boson used in our M_W calculation is the same in the NMSSM and the MSSM, since we calculate the MSSM Higgs masses in `FeynHiggs` where the input parameter M_{H^\pm} is interpreted as an on-shell mass parameter. The other parameters which occur in both models ($\tan\beta$, the sfermion trilinear couplings A_f , and the soft mass parameters) are, apart from X_t , used with the same values as input for the calculation of the physical masses in the MSSM and the NMSSM. For X_t we take the difference between the on-shell value and the $\overline{\text{DR}}$ value into account as mentioned above. The MSSM parameter μ is identified with the NMSSM effective value μ_{eff} ²⁰. The mass eigenvalues of

²⁰From here on we will leave out the subscript 'eff' for the μ parameter in the NMSSM

the sfermions, the charginos and neutralinos are calculated from the mass matrices given in Sects. 2.2 and 2.3 both in the MSSM and the NMSSM (as described in Sect. 5.4).

For the two dashed curves in Fig. 5.20 (small blue diamonds for the NMSSM predictions in the MSSM limit and red open triangles for the MSSM predictions) the tree-level Higgs masses are used. For the solid curve (with filled dots) loop-corrected Higgs masses are used: the NMSSM Higgs masses are calculated with `NMSSMTools`, and the MSSM Higgs masses calculated with `FeynHiggs`. The corresponding predictions for the lightest \mathcal{CP} -even Higgs mass in the (N)MSSM are displayed in the right plot of Fig. 5.20. The blue band in the right plot shows the region $M_h/M_{h_1} = 125.6 \pm 3.1$ GeV (theoretical uncertainty of 3 GeV added quadratically to the experimental error, see above). The position of the curves relative to the blue M_H band depends strongly on the other parameters, which are fixed here. The NMSSM parameter points (with `NMSSMTools` Higgs masses) are allowed by `HiggsBounds` in the ranges $|X_t| \gtrsim 300$ GeV. For large X_t values ($|X_t| \gtrsim 1200$ GeV) the lightest Higgs mass is heavy enough to be interpreted as the signal at 125.6 GeV. While the tree-level Higgs masses agree exactly in the MSSM and the NMSSM in the MSSM-limit, we observe a difference between the masses for the lightest \mathcal{CP} -even Higgs calculated with `FeynHiggs` and with `NMSSMTools`, which is largest for $X_t \sim 2000$ GeV in this plot, where it amounts to ~ 3.7 GeV. This discrepancy arises since the higher-order corrections implemented in `FeynHiggs` are more complete than in `NMSSMTools`. The tree-level Higgs masses are only used in this plot. In all following plots (if nothing else is specified) the MSSM Higgs spectrum is calculated with `FeynHiggs` and the NMSSM Higgs spectrum is calculated with `NMSSMTools`.

Going back to the left plot of Fig. 5.20, we see that the M_W^{NMSSM} predictions in the MSSM-limit and the M_W^{MSSM} prediction coincide exactly if tree-level Higgs masses are used (which is an important check of our implementation). However, using loop-corrected masses, the difference between the `FeynHiggs` and `NMSSMTools` predictions for the lightest \mathcal{CP} -even Higgs mass leads to a difference in M_W of ~ 1.6 MeV. The effect of the difference in the M_W prediction induced by the different Higgs mass predictions is contained in the following plots in this section. This should be kept in mind, especially when we compare M_W^{NMSSM} with M_W^{MSSM} . The shape of the M_W predictions can be understood, remembering that the main contribution of the stop/sbottom sector can be associated with $\Delta\rho$ and hence depends strongly on the squark mixing. The SUSY contributions from the stop and sbottom sector to $\Delta\rho$ can be written in a compact form,

$$\begin{aligned} \Delta\rho^{\text{SUSY}} = \frac{3G_\mu}{8\sqrt{2}\pi^2} & \left(-\sin^2\theta_{\bar{t}}\cos^2\theta_{\bar{t}}F_0(m_{\bar{t}_1}^2, m_{\bar{t}_2}^2) - \sin^2\theta_{\bar{b}}\cos^2\theta_{\bar{b}}F_0(m_{\bar{b}_1}^2, m_{\bar{b}_2}^2) \right. \\ & + \cos^2\theta_{\bar{t}}\cos^2\theta_{\bar{b}}F_0(m_{\bar{t}_1}^2, m_{\bar{b}_1}^2) + \cos^2\theta_{\bar{t}}\sin^2\theta_{\bar{b}}F_0(m_{\bar{t}_1}^2, m_{\bar{b}_2}^2) \\ & \left. + \sin^2\theta_{\bar{t}}\cos^2\theta_{\bar{b}}F_0(m_{\bar{t}_2}^2, m_{\bar{b}_1}^2) + \sin^2\theta_{\bar{t}}\sin^2\theta_{\bar{b}}F_0(m_{\bar{t}_2}^2, m_{\bar{b}_2}^2) \right), \end{aligned} \quad (5.31)$$

with

$$F_0(x, y) = x + y - \frac{2xy}{x-y} \ln \frac{x}{y}, \quad F_0(x, x) = 0, \quad F_0(x, 0) = x. \quad (5.32)$$

The terms being sensitive to the splitting between the squarks of one flavour enter with

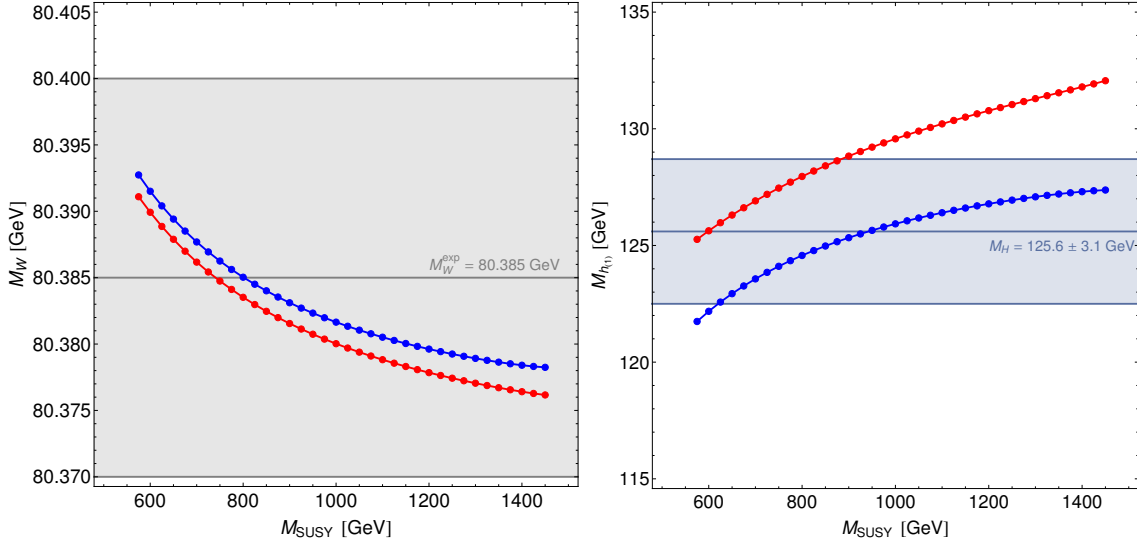


Figure 5.21: NMSSM predictions in the MSSM limit (blue curves) for the W boson mass (left plot) and the lightest \mathcal{CP} -even Higgs mass (right plot). The red curves show the MSSM predictions for comparison. The parameters are the same as in Fig. 5.20 but with $X_t = 2 M_{\text{SUSY}}$ and M_{SUSY} varied.

the opposite sign than the terms sensitive to the splitting between stops and sbottoms. Going from $X_t = 0$ to larger values of $|X_t|$ the contribution to M_W first decreases and increases again for large values ($\gtrsim 1500$ GeV) of $|X_t|$. For $X_t = 0$ the mixing in the stop sector is minimal. Increasing $|X_t|$, \tilde{t}_1 becomes lighter and \tilde{t}_2 heavier. With $A_b = A_t$ also the splitting between the \tilde{b}_1 and \tilde{b}_2 changes, however this effect is much less pronounced²¹. Therefore, when increasing $|X_t|$, the splitting between the two stops increases, as well as the splitting between \tilde{t}_2 and the two sbottoms. The splitting between \tilde{t}_1 and the sbottoms decreases first and then increases again, when \tilde{t}_1 gets lighter than the two sbottom states (which happens for $|X_t| \sim 300$ GeV). Thus, the first term in Eq. (5.31) gets larger (entering with a minus sign) and also the sum of the terms in the last two lines get larger (entering with a plus sign)²². The terms in the last two lines are always larger than the first term, resulting in a positive $\Delta\rho$ value. Increasing $|X_t|$ from 0 to 1500 GeV the difference in size between these two countervailing contributions gets smaller and the first negative term in Eq. (5.31) largely cancels the positive contributions leading to a decrease of M_W . For $|X_t| > 1500$ the difference increases again, the cancellation gets smaller, and M_W increases.

Besides X_t , the parameter most relevant for the stop and sbottom contributions is M_{SUSY} . For the same parameter point as in Fig. 5.20 we show the NMSSM M_W

²¹The splitting between the sbottoms is determined by $X_b = A_b - \mu \tan \beta$. For the chosen $\tan \beta$ and μ values it is smallest for $X_t = 2100$ GeV ($\implies X_b = -1890$ GeV) and is largest for $X_t = -2100$ GeV ($\implies X_b = -6090$ GeV).

²²The terms in the second line decrease first in the range $|X_t| = 0 - 300$ GeV, however the sum of the terms in the second and third line is getting larger for all $|X_t|$ values.

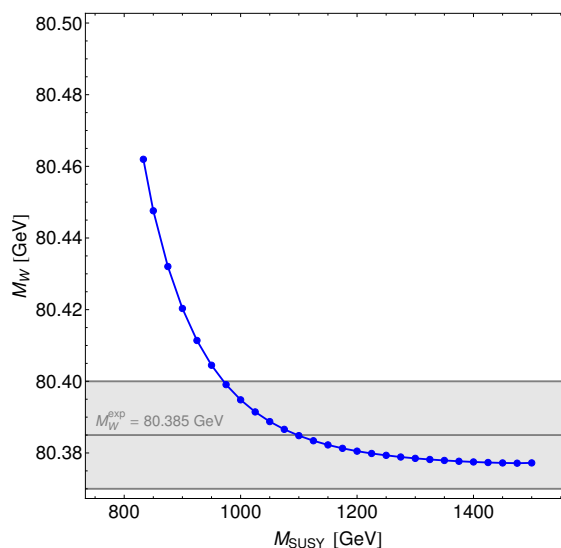


Figure 5.22: NMSSM prediction for the W boson mass in the MSSM limit as a function of M_{SUSY} . We choose $\tan\beta = 50$ and $\mu = 2000$ GeV keeping the other parameters as in Fig. 5.21.

prediction in the MSSM limit (and again for comparison the MSSM prediction) as a function of M_{SUSY} for $X_t = 2 M_{\text{SUSY}}$ in the left plot of Fig. 5.21. The right plot shows again the corresponding predictions for the lightest \mathcal{CP} -even Higgs in the NMSSM and the MSSM, evaluated with `NMSSMTools` or `FeynHiggs` respectively. We can see again a significant difference between these two evaluations, consisted with what we observed in Fig. 5.20. The difference in the Higgs masses is smaller for small M_{SUSY} values and gets larger for large M_{SUSY} values. Turning to the left plot, we see that for small M_{SUSY} the stop/sbottom sector gives a sizeable contribution to M_W , while and for large M_{SUSY} the stops and sbottoms decouple and their contribution to M_W decreases. Again we observe a difference between the NMSSM result in the MSSM-limit and the MSSM result, induced by the different Higgs mass evaluations. From here on, we will not always display the MSSM result for M_W (and the Higgs mass predictions) separately. We will show the MSSM prediction again for comparison when we come to the discussion of genuine NMSSM effects. Then it will be important to understand whether the difference between M_W^{NMSSM} and M_W^{MSSM} is in fact due to additional NMSSM contributions, or whether it is artificially induced by different Higgs mass evaluations. We will discuss this issue in more detail below.

For the parameter point in Fig. 5.21 the maximal M_W contribution from stops and sbottoms is ~ 15 MeV within the range of the plot. However the contributions from the stop/sbottom sector to M_W can generally be considerably larger, as we discussed in the last section. In order to demonstrate this here, we set $\tan\beta = 50$ and $\mu = 2000$ GeV keeping all other parameters as in Fig. 5.21. This parameter point is `HiggsBounds` allowed and the lightest Higgs falls in the range 125.6 ± 3.1 GeV for $M_{\text{SUSY}} > 1025$ GeV (within the plot range). For this choice of μ and $\tan\beta$ the spitting between the sbottoms

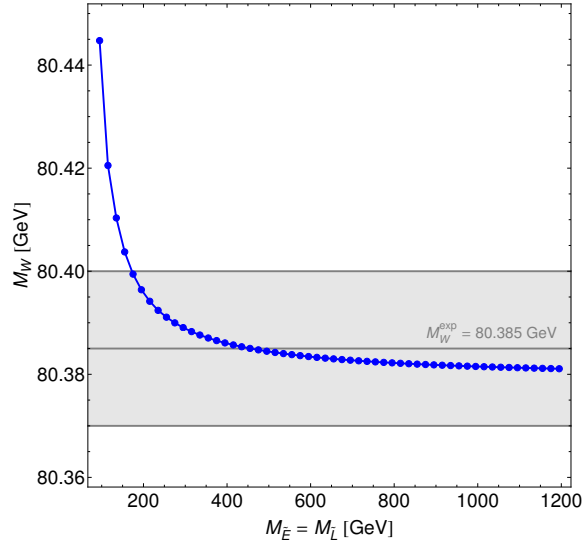


Figure 5.23: NMSSM predictions for the W boson mass in the MSSM limit. We choose $M_{\text{SUSY}} = 1200$ GeV, $X_t = 2 M_{\text{SUSY}}$, $X_l = 0$ ($l = e, \mu, \tau$), vary $M_{\tilde{E}} = M_{\tilde{L}}$ and keep the other parameters as in Fig. 5.20.

can get large, and this leads to a large M_W contribution, as demonstrated in Fig. 5.22. Here the maximal shift in M_W is ~ 90 MeV. Going even further down in M_{SUSY} the sbottom mass splitting and therewith the M_W contribution would increase further, however we decide to not show points with $m_{\tilde{b}_2}/m_{\tilde{b}_1} > 2.5$, in accordance the MSSM analysis in the last section. In Fig. 5.22 we show the experimental 1σ band from the W boson mass measurement. It is important to keep in mind that the curves depend sensitively also on the other (fixed) SUSY parameters, and one can not conclude in general that certain parameter regions of M_{SUSY} that lie outside the 1σ band for the parameters chosen in this plot, are in disagreement with experimental data.

As we have shown in the last section, the contribution of the squarks of the first two generations to M_W is small. It will not be shown here. We now turn directly to the M_W contribution from the slepton sector, shown in Fig. 5.23. For this plot we set $M_{\text{SUSY}} = 1200$ GeV, $X_t = 2 M_{\text{SUSY}}$, $X_l = 0$ ($l = e, \mu, \tau$) and we vary $M_{\tilde{E}} = M_{\tilde{L}}$, keeping the other parameters as in Fig. 5.20 (still in the MSSM-limit). The parameter points are **HiggsBounds** allowed, and the lightest Higgs falls in the range 125.6 ± 3.1 GeV. In accordance with the results shown in Fig. 5.11 we see here that the slepton sector can give sizeable contributions to M_W if the sleptons are very light (just above the LEP limit). For $M_{\tilde{E}} = M_{\tilde{L}} = 95$ GeV (corresponding to charged slepton masses of ~ 100 GeV and sneutrino masses of ~ 70 GeV) the M_W contribution from the slepton sector is ~ 60 MeV. The main effect comes from the $\Delta\rho$ contributions which are sensitive to the mass splitting between sleptons and sneutrinos.

5.8.2 Effect of SUSY two-loop corrections

In this subsection the size and parameter dependence of the SUSY two-loop corrections is analysed.

Fig. 5.24 shows the size of the $\mathcal{O}(\alpha\alpha_s)$ two-loop corrections. The parameters used here are $m_t = 173.2$ GeV, $\tan\beta = 2$, $\mu = 200$ GeV, $M_{\tilde{L}/\tilde{E}} = 1000$ GeV, $M_{\tilde{Q}/\tilde{U}/\tilde{D}_{1,2}} = 1500$ GeV, $A_\tau = A_b = 1000$ GeV, $M_2 = 600$ GeV, $m_{\tilde{g}} = 1500$ GeV (solid curves) and $m_{\tilde{g}} = 300$ GeV (dashed curves), $A_\lambda = 395$ GeV, $\lambda = 0.57$, $\kappa = 0.2$, $A_\kappa = -80$ GeV and we vary $M_{\text{SUSY}} = M_{\tilde{Q}_3} = M_{\tilde{U}_3} = M_{\tilde{D}_3}$. We show the results for three values of X_t : In the left plots we set $X_t = 2 M_{\text{SUSY}}$, in the middle ones $X_t = 0$ and in the right ones $X_t = -2 M_{\text{SUSY}}$. It should be stressed here that the parameters for these plots are chosen to demonstrate the possible size and the parameter dependence of the SUSY two-loop corrections, however they are partially excluded by experimental data: The parameter points in the left plots with $X_t = 2 M_{\text{SUSY}}$ are **HiggsBounds** allowed, whereas in the middle and the right plot, the chosen parameters are **HiggsBounds** excluded for most M_{SUSY} values. A gluino mass value of $m_{\tilde{g}} = 300$ GeV is clearly disfavoured by the negative LHC search results. The plots in Fig. 5.24 show the contribution to the W boson mass, δM_W , from the $\mathcal{O}(\alpha\alpha_s)$ two-loop corrections with gluon exchange (dark blue curves), with gluino exchange (orange curves) and from the mass-shift correction (pink curves). The shift δM_W has been obtained by calculating M_W^{NMSSM} twice, once including the corresponding two-loop corrections, and once without, and the two results have been subtracted from each other. Starting with the dark blue curves, we find that the gluon contributions lead to a maximal shift of ~ 3 MeV in M_W for all three choices of X_t and that the size of the gluon contributions decreases with increasing M_{SUSY} . Turning to the orange curves, we find that for $m_{\tilde{g}} = 1500$ GeV (solid curves) the δM_W shift, induced by the gluino two-loop corrections, is small (< 1 MeV) for $X_t = 0$ and $X_t = -2 M_{\text{SUSY}}$, while it is 3 – 4 MeV for $X_t = 2 M_{\text{SUSY}}$. Making the gluino light — choosing $m_{\tilde{g}} = 300$ GeV (dashed curves) — the gluino corrections can get large. For large positive squark mixing, $X_t = 2 M_{\text{SUSY}}$, they reach up to 17 MeV for small values of M_{SUSY} . The gluino corrections can lead to both a positive and a negative M_W shift, depending on the stop mixing parameter. Threshold effects occur for light gluinos and cause kinks in the dashed curves, as can be seen in the middle and the right plot. The gluon and gluino two-loop contributions are directly related to the mass-shift correction, which has to be incorporated in order to arrive at the complete result for the $\mathcal{O}(\alpha\alpha_s)$ contributions to $\Delta\rho^{\text{SUSY}}$. The pink curves show the impact of this additional correction term. Starting with the solid curves ($m_{\tilde{g}} = 1500$ GeV), we observe that for large stop mixing $X_t = \pm 2 M_{\text{SUSY}}$ the mass-shift corrections are positive and decrease with increasing M_{SUSY} . The maximal shift is ~ 4 (5.5) MeV for $X_t = 2 M_{\text{SUSY}}$ ($X_t = -2 M_{\text{SUSY}}$). For zero mixing the mass-shift corrections lead to a large negative shift in M_W (up to -12 MeV for small M_{SUSY}). For $m_{\tilde{g}} = 300$ GeV, the size of the mass-shift correction is smaller. The kinks, caused by threshold effects, can be observed (for the same M_{SUSY} values) also in the mass-shift corrections. Adding up the gluino and mass-shift corrections leads to a smooth curve and no kink is found in the full M_W prediction. This can be seen in Fig. 5.25, where we plot the sum of the gluon, gluino

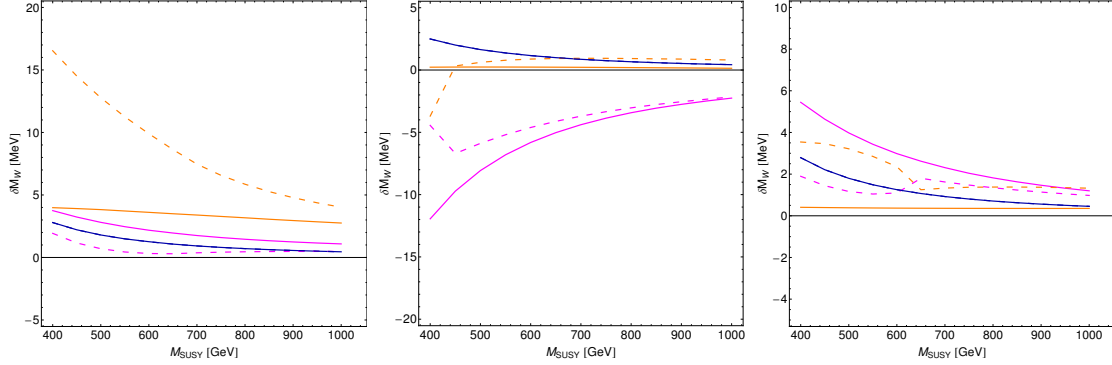


Figure 5.24: Size of the $\mathcal{O}(\alpha_s)$ two-loop corrections with gluon and gluino exchange. The solid curves correspond to $m_{\tilde{g}} = 1500$ GeV while the dashed curves correspond to $m_{\tilde{g}} = 300$ GeV. In the left plot we set $X_t = 2 M_{\text{SUSY}}$, in the middle one $X_t = 0$ and in the right one $X_t = -2 M_{\text{SUSY}}$. The plots show the contribution to the W boson mass, δM_W , from the $\mathcal{O}(\alpha_s)$ two-loop corrections with gluon exchange (dark blue curves), with gluino exchange (orange curves) and the mass-shift correction (pink curves) as a function of M_{SUSY} . The parameter points in the left plots with $X_t = 2 M_{\text{SUSY}}$ are **HiggsBounds** allowed. The parameter points in the middle plot with $X_t = 0$ and in the right plot with $X_t = -2 M_{\text{SUSY}}$ predict too low Higgs masses and are **HiggsBounds** excluded for most M_{SUSY} values. Note the different scales at the y-axis. The parameters used for these plots are given in the text.

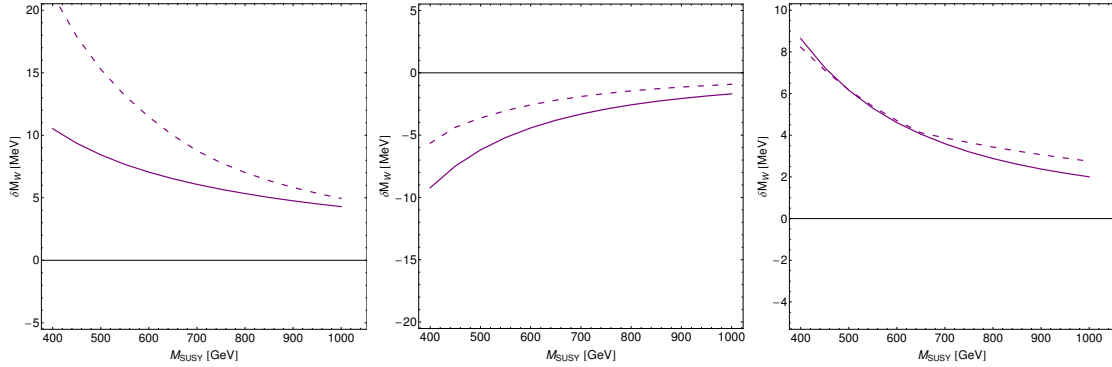


Figure 5.25: The plots show the full $\mathcal{O}(\alpha_s)$ two-loop corrections to M_W (sum of the corrections shown separately in Fig. 5.24) as a function of M_{SUSY} . The parameters are the same as in Fig. 5.24. The solid curves correspond to $m_{\tilde{g}} = 1500$ GeV while the dashed curves correspond to $m_{\tilde{g}} = 300$ GeV. In the left plot we set $X_t = 2 M_{\text{SUSY}}$, in the middle one $X_t = 0$ and in the right one $X_t = -2 M_{\text{SUSY}}$.

and mass-shift corrections (all parameters are the same as in Fig. 5.24). Generally one can see that for large M_{SUSY} all contributions decrease, showing the expected decoupling behaviour, however contributions from the $\mathcal{O}(\alpha_s)$ two-loop corrections up to a few MeV are still possible for $M_{\text{SUSY}} = 1000$ GeV.

The Yukawa-enhanced electroweak two-loop corrections of $\mathcal{O}(\alpha_t^2)$, $\mathcal{O}(\alpha_t \alpha_b)$, $\mathcal{O}(\alpha_b^2)$ to

$\Delta\rho$ (“Higgsino corrections”) can be included in our code, as we discussed in Sect. 5.3.4. To do so, we calculate the MSSM Higgs masses as described in Sect. 5.3.4 (taking the NMSSM charged Higgs mass as input for the MSSM Higgs mass calculation) and use them as input for the $\Delta\rho$ ($\mathcal{O}(\alpha_t^2)$, $\mathcal{O}(\alpha_t\alpha_b)$, $\mathcal{O}(\alpha_b^2)$) formula. The size of these contributions can be seen in Fig. 5.26.

Here, and in some of the following plots, we choose one of the benchmark points given in Ref. [212] (sometimes modified) as starting point for our study, which predict one of the \mathcal{CP} -even NMSSM Higgs bosons in the mass range of the observed Higgs signal. In Ref. [212] further aspects of these parameter points, such as the decay rates of the Higgs at ~ 125.6 GeV, are analysed.

We take the following parameters (modified version of the NMP2 benchmark point of [212]) $m_t = 173.2$ GeV, $\tan\beta = 2$, $\mu = 200$ GeV, $M_{\tilde{L}/\tilde{E}} = 1000$ GeV, $M_{\tilde{Q}/\tilde{U}/\tilde{D}_{1,2}} = 1000$ GeV, $M_{\tilde{Q}_3} = M_{\tilde{U}_3} = 700$ GeV, $M_{\tilde{D}_3} = 1000$ GeV, $A_\tau = A_b = 1000$ GeV, $M_2 = 200$ GeV, $m_{\tilde{g}} = 1500$ GeV, $A_\lambda = 405$ GeV, $\lambda = 0.6$, $\kappa = 0.18$, $A_\kappa = -10$ GeV, and we vary X_t . The left plot shows the NMSSM M_W prediction without Higgsino corrections (blue curve) and including Higgsino corrections (green curve) plotted against X_t . In the middle plot the shift δM_W induced by the Higgsino corrections (obtained by subtracting the M_W predictions with and without Higgsino corrections as shown in the left plot) is plotted against X_t . We see that the Higgsino corrections can enter the M_W prediction with both signs. The numerical effect of the M_W shift, induced by the Higgsino corrections, is relatively small (~ 1 MeV). It was shown in Ref. [160] that the contributions to M_W from the Higgsino corrections can be slightly larger (~ 5 MeV) for light \tilde{t}/\tilde{b} . The right plot shows the M_W prediction plotted against M_{h_1} . We can nicely see here that this scenario, in which the Higgs signal can be interpreted as the lightest \mathcal{CP} -even NMSSM Higgs, gives a W boson mass prediction in good agreement with the M_W measurement.

5.8.3 NMSSM Higgs sector contributions

While the effects of the one- and two-loop contributions discussed so far are identical in the MSSM and the NMSSM, we turn now to the discussion of genuine NMSSM effects, starting with the NMSSM Higgs sector.

In the MSSM the maximal value for the tree-level Higgs mass M_h (see Eq. (2.64)) is M_Z . In the NMSSM the tree-level Higgs mass M_{h_1} gets an additional contribution $\lambda^2 v^2 \sin^2 2\beta$, which can shift the tree-level Higgs mass upwards, compared to its MSSM value, and thus reduce the size of the radiative corrections needed to ‘push’ the lightest Higgs mass up to the mass of the experimentally observed Higgs boson. For $\lambda = 0.7$ and $\tan\beta = 2$ a tree-level value for M_{h_1} of 112 GeV is possible [212]. This additional tree-level contribution to the Higgs mass, as well as its impact on M_W are shown in Fig. 5.27. The parameters chosen here are $m_t = 173.2$ GeV, $\mu = 200$ GeV, $M_{\tilde{L}/\tilde{E}} = 500$ GeV, $M_{\tilde{Q}/\tilde{U}/\tilde{D}_{1,2}} = 1500$ GeV, $M_{\tilde{Q}_3} = M_{\tilde{U}_3} = M_{\tilde{D}_3} = 1000$ GeV, $X_t = 2000$ GeV, $A_\tau = A_b = A_t$, $M_2 = 200$ GeV, $m_{\tilde{g}} = 1500$ GeV, $\hat{m}_A = 450$ GeV, $\kappa = \lambda$ and $A_\kappa = -100$ GeV. We vary $\tan\beta$ and show the results for different values of λ . The red curves correspond to the MSSM-limit ($\lambda \rightarrow 0$) while for the other curves the λ value is given in the corresponding

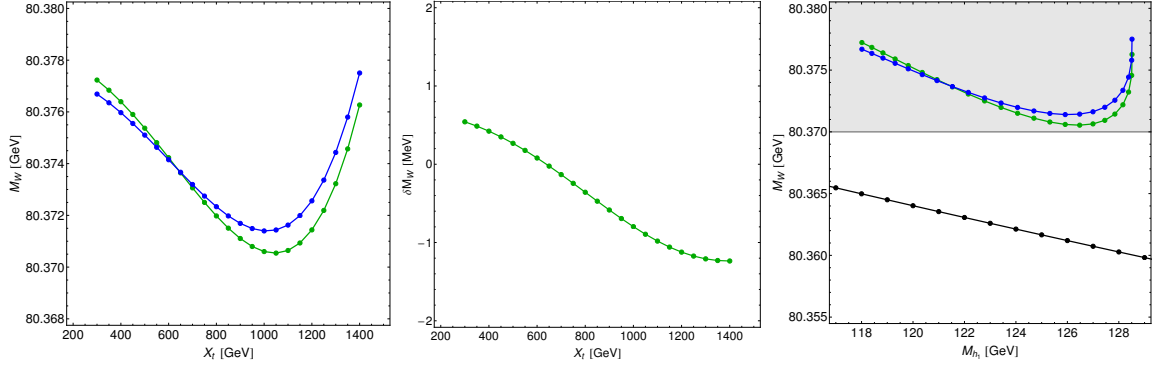


Figure 5.26: Size of the electroweak $\mathcal{O}(\alpha_t^2)$, $\mathcal{O}(\alpha_t\alpha_b)$, $\mathcal{O}(\alpha_b^2)$ SUSY two-loop corrections. The left plot shows the NMSSM M_W prediction without Higgsino corrections (blue curve) and including Higgsino corrections (green curve) plotted against X_t . In the middle plot the shift δM_W induced by the Higgsino corrections (obtained by subtracting the M_W predictions with and without Higgsino corrections as shown in the left plot) is plotted against X_t . The right plot shows the NMSSM M_W prediction without Higgsino corrections (blue curve) and including Higgsino corrections (green curve) plotted against the lightest \mathcal{CP} -even Higgs mass M_{h_1} . The black curve in the right plot indicates the SM M_W prediction with $M_{H^{\text{SM}}} = M_{h_1}$. The grey band indicates the 1σ region of the experimental W boson mass measurement. The parameters used for these plots are given in the text.

colour. The upper left plot shows the tree-level prediction for the lightest \mathcal{CP} -even Higgs mass M_{h_1} . As expected, the M_{h_1} prediction in the MSSM-limit approaches its maximal value M_Z for large $\tan\beta$. Increasing λ , the M_{h_1} prediction decreases for large $\tan\beta$, caused by doublet-singlet mixing terms. For small $\tan\beta$ one clearly sees the positive contribution from the term $\lambda^2 v^2 \sin^2 2\beta$ pushing the tree-level Higgs mass beyond M_Z for large λ .²³ The full M_{h_1} prediction (as calculated in `NMSSMTools`) can be seen in the upper right plot. Now we turn to the M_W contributions from the NMSSM Higgs and gauge boson sector, shown in the lower left plot. The shift δM_W displayed here is approximated by [156]

$$\delta M_W = -\frac{M_W^{\text{ref}}}{2} \frac{s_W^2}{c_W^2 - s_W^2} \Delta r^{\text{SUSY}} \quad (5.33)$$

where Δr^{SUSY} contains the contributions from the SUSY sector under consideration (here the contributions from the Higgs and gauge bosons) and the reference M_W value is set to $M_W^{\text{ref}} = M_W^{\text{exp}}$. The overall contribution from the Higgs sector is rather large and negative. As we will discuss in more detail below, the Higgs sector contributions here are predominantly SM-type contributions, (with $M_{H^{\text{SM}}}$ set to the corresponding Higgs mass value), however for large $\tan\beta$ and large λ the non-zero singlet component of M_{h_1} leads to

²³For one specific $\tan\beta$ value around 4, the contribution from the additional tree-level terms seems to cancel the one from doublet-singlet mixing, for all values of λ . Analytic confirmation of this cancellation is in progress.

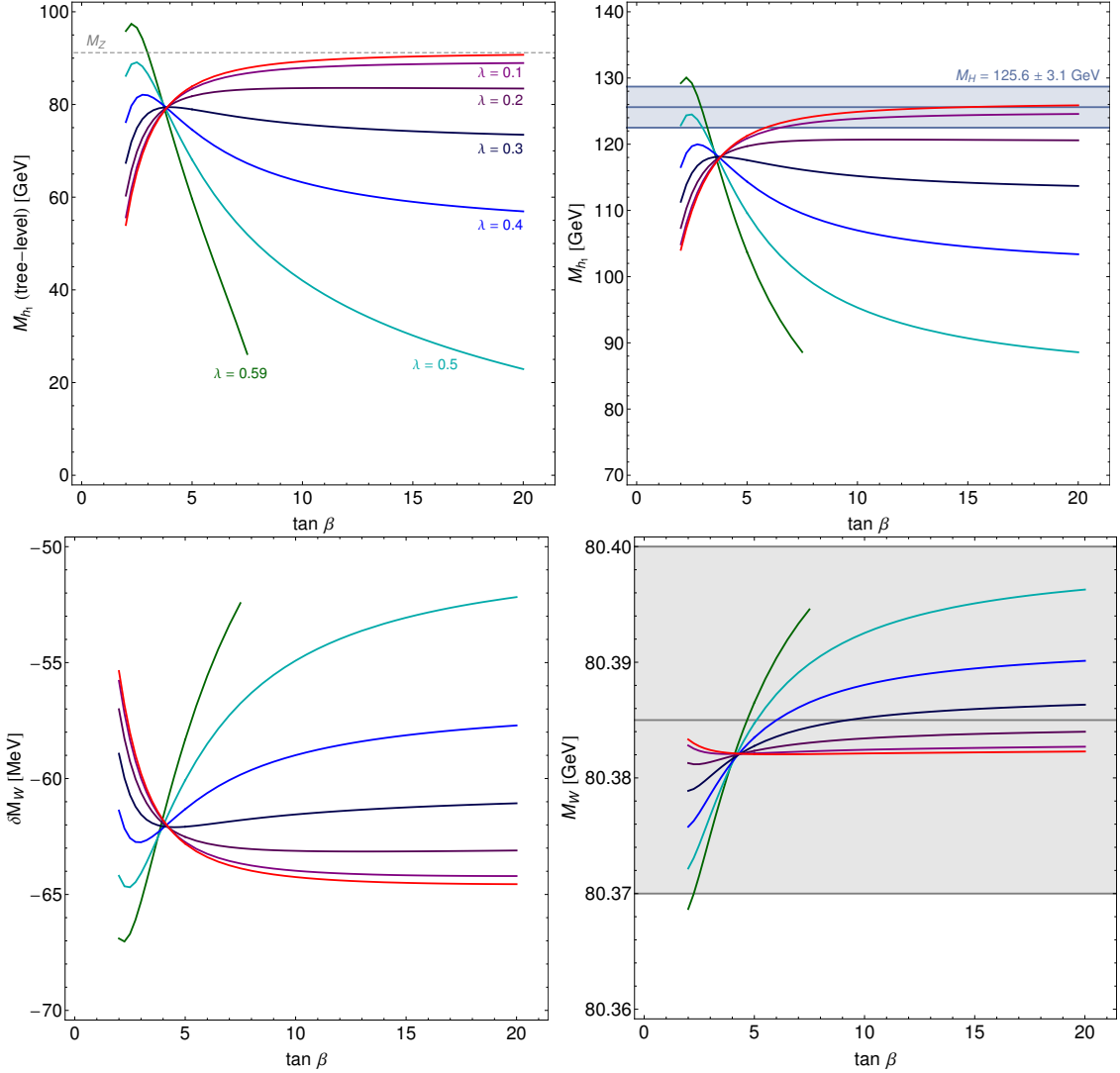


Figure 5.27: Higgs mass and M_W prediction as a function of $\tan\beta$. The red curves correspond to the MSSM-limit ($\lambda \rightarrow 0$) while for the other curves the λ values are given in the corresponding colour. The upper left plot shows the tree-level prediction for the lightest \mathcal{CP} -even Higgs mass M_{h_1} , the upper right plot shows M_{h_1} including radiative corrections (calculated in `NMSSMTools`), the lower left plot shows the shift δM_W (calculated as in Eq. (5.33)) from diagrams involving Higgs and gauge bosons, and the lower right plot shows the full M_W prediction. The parameters used for these plots are given in the text.

a prediction for δM_W slightly lower than the corresponding SM value. The prediction for M_W in the NMSSM is shown in the lower right plot. Larger values for M_{h_1} correspond to a lower predicted value for M_W , thus for small $\tan\beta$, where we find a significantly higher predicted value for M_{h_1} for large λ than in the MSSM-limit (arising from the additional tree-level term), we get a lower predicted value for M_W . For $\tan\beta = 2$ the difference

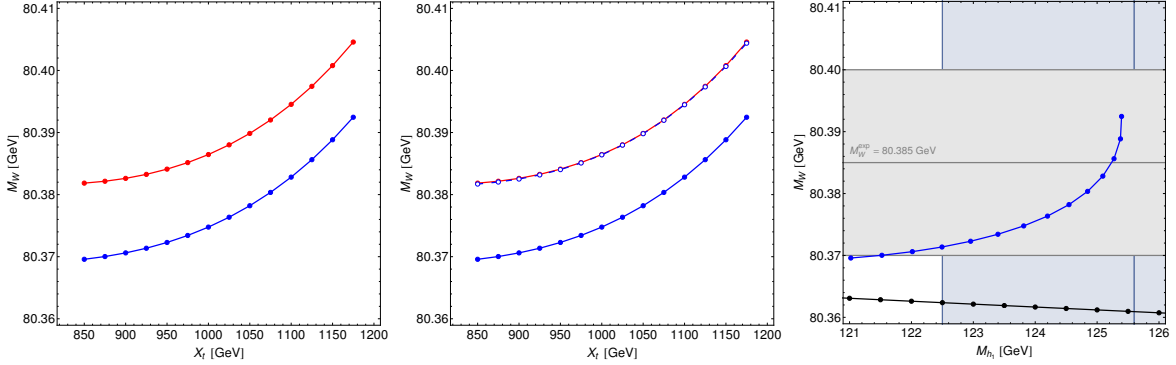


Figure 5.28: The left plot shows the M_W^{NMSSM} prediction (blue, solid curve) and the M_W^{MSSM} prediction (red) plotted against X_t . In the middle plot, the additional dashed blue curve corresponds to $M_W^{\text{NMSSM}} - M_W^{\text{SM}}(M_{h_1}) + M_W^{\text{SM}}(M_h)$ (M_{h_1} is the mass of the lightest \mathcal{CP} -even Higgs of the NMSSM and M_h is the mass of the light \mathcal{CP} -even Higgs of the MSSM). The right plots shows the M_W^{NMSSM} prediction plotted against the lightest \mathcal{CP} -even Higgs mass M_{h_1} . The black curve in the right plot indicates the SM M_W prediction with $M_{H^{\text{SM}}} = M_{h_1}$. The experimental M_W measurement is indicated by the grey band; the region $M_H = 125.6 \pm 3.1$ GeV is indicated by the blue band. The parameters are given in the text.

between the W boson mass prediction for $\lambda = 0.59$ and $\lambda \rightarrow 0$ is ~ 15 MeV. The parameter $\tan\beta$ enters also in the sfermion as well as in the chargino/neutralino sector. We checked that for the parameters here the $\tan\beta$ dependence of the stop/sbottom sector contributions is small, $\mathcal{O}(1)$ MeV). The contributions from the chargino/neutralino sector (which we will discuss in more detail below) enter with a positive sign and increase with $\tan\beta$. They give rise to a M_W shift of 1.5 ($\lambda = 0.59$) to 3.5 MeV (MSSM-limit) for $\tan\beta = 2$ and increase to ~ 11 MeV for $\tan\beta = 20$. This explains, why e.g. in the MSSM limit the difference $M_W(\tan\beta = 20) - M_W(\tan\beta = 2)$ is only about -1.5 MeV, even though the difference of the Higgs sector contribution $\delta M_W(\tan\beta = 20) - \delta M_W(\tan\beta = 2)$ is about -9 MeV.

We continue the study of the NMSSM Higgs sector contributions in Fig. 5.28. In the left plot we compare the NMSSM prediction for M_W (blue curve) with the MSSM prediction (red curve) which we obtained (here and in the following) by setting the `FeynHiggs` M_{H^\pm} input to the value of the charged Higgs mass calculated by `NMSSMTools`, while the other parameters which occur in both models are (apart from X_t , which is transformed between its on-shell and $\overline{\text{DR}}$ value, see above), used with the same values as input for the calculation of the physical masses in the MSSM and the NMSSM. The MSSM parameter μ is identified with the NMSSM effective value μ_{eff} . As a starting point we choose a modified version of the NMP3 benchmark point of [212], the exact parameters we use are $m_t = 173.2$ GeV, $\tan\beta = 2$, $\mu = 200$ GeV, $M_{\tilde{L}/\tilde{E}} = 1500$ GeV, $M_{\tilde{Q}/\tilde{U}/\tilde{D}_{1,2}} = 1000$ GeV, $M_{\tilde{V}_3} = M_{\tilde{Q}_3} = 530$ GeV, $M_{\tilde{D}_3} = 1000$ GeV, $A_\tau = A_b = 1000$ GeV, $M_2 = 370$ GeV, $m_{\tilde{g}} = 1500$ GeV, $A_\lambda = 395$ GeV, $\lambda = 0.57$, $\kappa = 0.2$, $A_\kappa = -80$ GeV, and we vary X_t . The NMSSM parameters are allowed by `HiggsBounds` and (for $X_t \gtrsim 900$ GeV) the

lightest \mathcal{CP} -even Higgs falls in the mass range of the observed Higgs signal. The MSSM prediction is plotted as a comparison to illustrate and discuss the NMSSM effects on M_W . Here (and in the following) we do not check any phenomenological constraints for the MSSM parameter point. The NMSSM prediction for M_W differs from the MSSM prediction by ~ 12 MeV. The chargino/neutralino contributions can enter with both signs, and we find that in this scenario the relatively small μ value causes negative corrections to Δr . On the other hand, small M_2 values tend to give positive contributions to Δr . For the chosen parameters, these two effects cancel and contributions from the chargino/neutralino sector are ~ 0 . Consequently different Higgs sector contributions give rise to the difference between the MSSM and the NMSSM curves. Any differences in the \mathcal{CP} -odd Higgs sector have a negligible impact on the M_W prediction (see also Ref. [163]). Since we set the charged Higgs masses equal to each other in the two models, differences can only come from the \mathcal{CP} -even Higgs sector. For this parameter point the second lightest Higgs ($M_{h_2} = 130$ GeV) has a large singlet component ($|U_{23}^H|^2 \simeq 95\%$), consequently the singlet components of h_1 and h_3 are small. h_3 is heavy and has no impact on the M_W prediction. Our procedure to calculate the Higgs masses in the MSSM and the NMSSM leads to the same charged Higgs masses, but to different predictions for the lightest \mathcal{CP} -even Higgs masses M_{h_1} and M_h . This difference arises from the different relations between the charged Higgs mass and the lightest \mathcal{CP} -even Higgs mass in the MSSM and the NMSSM. Further it also incorporates the (“technical”) difference due to the different radiative corrections included in `FeynHiggs` and `NMSSMTools` (as analysed above in the MSSM-limit). The middle plot of Fig. 5.28 shows in addition to the NMSSM prediction for M_W (blue) and the MSSM prediction (red), a blue dashed curve (with open dots). The dashed blue curve corresponds to $M_W^{\text{NMSSM}} - M_W^{\text{SM}}(M_{h_1}) + M_W^{\text{SM}}(M_h)$ ²⁴. As one can see the dashed blue curve lies on the red MSSM curve, thus here the difference between the MSSM and the NMSSM Higgs sector contributions to M_W arises from the SM-type Higgs sector contributions, in which different Higgs mass values are inserted. In principle there are different possibilities of how to relate an MSSM parameter point to a certain NMSSM parameter point. The way we chose the MSSM parameter point (for which we compare the predictions to those of the NMSSM parameter point) leads to the difference shown in the left plot of Fig. 5.28. We could have chosen the MSSM parameter point also in such a way that M_h agrees with M_{h_1} , in that case a possible difference between MSSM and NMSSM predictions may arise from different charged Higgs mass values (assuming differences in the neutralino sector are negligible). The right plot shows the M_W^{NMSSM} prediction plotted against the lightest \mathcal{CP} -even Higgs mass M_{h_1} . In this plot we display both the blue band indicating $M_{h_1} = 125.6 \pm 3.1$ GeV region, as well as the grey band showing the experimental 1σ band from the W boson mass measurement. The black curve in the right plot indicates the SM M_W prediction for $M_{H^{\text{SM}}} = M_{h_1}$.

²⁴The difference in the predictions for the lightest \mathcal{CP} -even Higgs masses in the MSSM and the NMSSM, which we subtract this way, includes both the difference between the different mass relations in the MSSM and the NMSSM, as well as the “technical” difference between the `FeynHiggs` and the `NMSSMTools` evaluation.

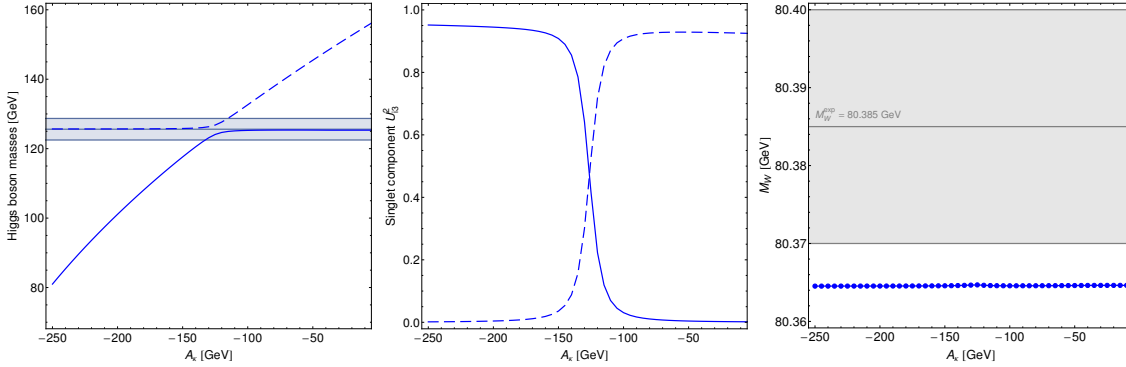


Figure 5.29: The left plot shows the prediction for M_{h_1} (solid curve) and M_{h_2} (dashed curve) as a function of A_κ . The region 125.6 ± 125.6 GeV is indicated as a blue band. The middle plot shows their singlet components U_{13}^2 (solid) and U_{23}^2 (dashed). The right plot shows the M_W^{NMSSM} prediction, here the grey band shows the experimental 1σ band from the W boson mass measurement. The parameters used for these plots are given in the text.

Now we want to investigate whether a singlet-doublet mixing (a genuine NMSSM feature) has an impact on the M_W prediction. Such a scenario is analysed in Fig. 5.29. Here we take a modified version of the NMP6 benchmark point of [212] as starting point; our parameters are $m_t = 173.2$ GeV, $\tan\beta = 2$, $\mu = 140$ GeV, $M_{\tilde{L}/\tilde{E}} = 1000$ GeV, $M_{\tilde{Q}/\tilde{U}/\tilde{D}_{1,2}} = 1000$ GeV, $M_{\tilde{Q}_3} = 800$ GeV, $M_{\tilde{U}_3} = 600$ GeV, $M_{\tilde{D}_3} = 1000$ GeV, $A_t = 1500$ GeV, $A_\tau = A_b = 1000$ GeV, $M_2 = 300$ GeV, $m_{\tilde{g}} = 1500$ GeV, $A_\lambda = 210$ GeV, $\lambda = 0.55$, $\kappa = 0.31$, and we vary A_κ . These parameters are allowed by `HiggsBounds`, and the Higgs signal can be interpreted as either h_1 or h_2 . The left plot shows the prediction for M_{h_1} (solid curve) and M_{h_2} (dashed). The corresponding singlet components U_{13}^2 (solid) and U_{23}^2 (dashed) are shown in the middle plot. The third \mathcal{CP} -even Higgs is heavy and has a negligible singlet component. For $A_\kappa \lesssim -170$ GeV, h_2 is doublet-like and has a mass in the region of the observed Higgs signal (indicated by the blue band). In the MSSM, scenarios which allow the interpretation of the Higgs signal as the heavy \mathcal{CP} -even Higgs involve always a (relatively light) charged Higgs. Due to changed mass relations between the Higgs bosons, it is possible in the NMSSM to have the second lightest \mathcal{CP} -even Higgs at 125.6 GeV together with a heavy charged Higgs. Therefore in the NMSSM the interpretation of the Higgs signal as the second lightest \mathcal{CP} -even Higgs is much less constrained by the LHC results from charged Higgs searches. The interpretation of the Higgs signal as h_2 is always accompanied by a lighter state with reduced couplings to vector bosons. In this plot the charged Higgs mass is 300 GeV. For $A_\kappa \gtrsim -100$ GeV, h_1 is doublet-like and has a mass in the region of the observed Higgs signal. In the intermediate region (-170 GeV $\lesssim A_\kappa \lesssim -100$ GeV) the two light \mathcal{CP} -even Higgs bosons are close in mass and “share” the singlet component. The right plot shows the NMSSM prediction for M_W , which is approximately flat. Accordingly, the parameter regions of A_κ corresponding to two different interpretations of the Higgs signal within the NMSSM lead to a (very similar) prediction for the W boson mass which is in

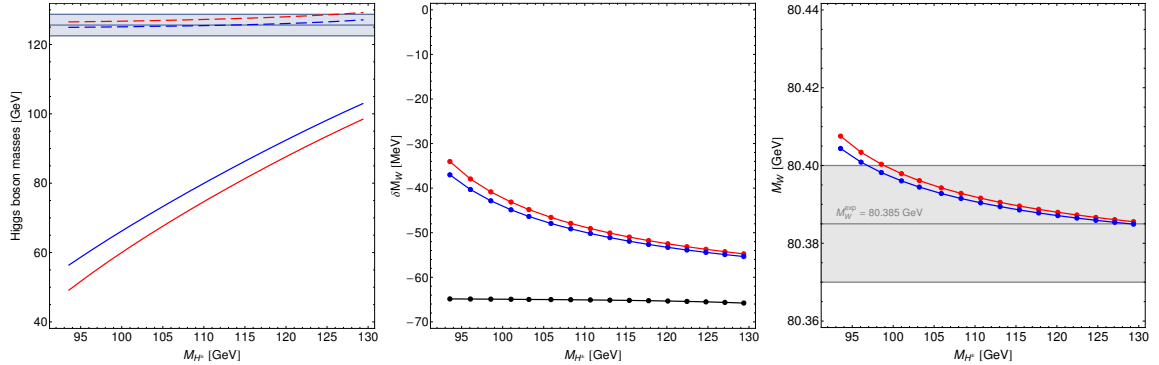


Figure 5.30: M_W contribution from a light charged Higgs. The left plot shows the prediction for the \mathcal{CP} -even Higgs boson masses in the NMSSM and in the MSSM as a function of the charged Higgs mass. The solid curves correspond to the mass of the lightest \mathcal{CP} -even Higgs in the NMSSM (blue) and the MSSM (red). The dashed curves correspond to the mass of the second lightest \mathcal{CP} -even Higgs in the NMSSM (blue) and the MSSM (red). The middle plot shows the shift δM_W (calculated as in Eq. (5.33)) induced by the Higgs and gauge boson sector in the NMSSM (blue), in the MSSM (red) and in the SM (black) with $M_{H^{\text{SM}}} = M_{h_2}$. The right plot shows the W boson mass prediction in the NMSSM (blue) and the MSSM (red). The parameters used for these plots are given in the text.

agreement with the experimental measurement of M_W (in this plot the M_W predictions is just below the experimental 1σ region, however making the particles which are not (or very little) affecting the Higgs sector (e.g. sleptons) lighter will improve the agreement with M_W^{exp}). Thus in this case, a strong doublet–singlet mixing does not lead to a visible effect in M_W .

We demonstrated so far that, taking Higgs search constraints and the Higgs discovery into account²⁵, the genuine NMSSM effects from the extended Higgs sector are quite small, and the Higgs sector contributions we analysed so far were dominated by SM-type contributions. This is true in the absence of a light charged Higgs, as we will discuss now. As we have seen in the MSSM analysis (see in particular Fig. 5.14) differences to the SM contribution can arise in the presence of light charged Higgs (together with a light \mathcal{CP} -even Higgs with small but non-zero couplings to vector bosons). These effects can of course also be observed in the NMSSM. Although this is not a genuine NMSSM effect, we want to demonstrate this contribution here. For Fig. 5.30 we choose the following parameters $m_t = 173.2$ GeV, $\tan\beta = 9.25$, $\mu = 200$ GeV, $M_{\tilde{L}/\tilde{E}} = 300$ GeV, $M_{\tilde{Q}/\tilde{U}/\tilde{D}_{1,2}} = 1500$ GeV, $M_{\tilde{Q}_3} = M_{\tilde{U}_3} = M_{\tilde{D}_3} = 1100$ GeV, $A_t = -2300$ GeV, $A_\tau = A_b = -1500$ GeV, $M_2 = 500$ GeV, $m_{\tilde{g}} = 1500$ GeV, $\lambda = 0.2$, $\kappa = 0.6$, $A_\kappa = -1370$ GeV, and we vary \hat{m}_A . The left plot Fig. 5.30 shows the predictions for the masses of the lightest two \mathcal{CP} -even Higgs bosons in the NMSSM (blue) and in the MSSM (red) as a

²⁵Neglecting experimental bounds one can have light \mathcal{CP} -Higgs bosons with a small singlet component, which would give large contributions to M_W . However this possibility will not be discussed here.

function of the charged Higgs mass. In both models the second lightest Higgs falls in the mass range 125.6 ± 3.1 GeV in this case. This scenario is excluded by the latest ATLAS results for charged Higgs searches [55]. To demonstrate the possible size of the contributions from a light charged Higgs, we show these plots anyway. The middle plot shows the shift δM_W (calculated as in Eq. (5.33)) induced by the Higgs and gauge boson sector in the NMSSM (blue) and in the MSSM (red). As one can see the difference in these contributions is quite small. The lightest \mathcal{CP} -even Higgs gives only a rather small contribution to M_W due to its reduced vector boson couplings. The SM-result for δM_W with $M_{H^{\text{SM}}} = M_{h_2}$ is shown in black. A significant difference between the SM contribution and the MSSM/NMSSM contributions can be observed for light M_{H^\pm} . The right plot shows the full M_W prediction in the NMSSM (blue) and in the MSSM (red).

5.8.4 Neutralino sector contributions

We start the discussion of the contributions from the NMSSM neutralino sector, which differs from the respective MSSM sector, with Fig. 5.31. As a starting point we choose a modified version of the NMP1 benchmark point of [212], the exact parameters are $m_t = 173.2$ GeV, $\tan \beta = 3$, $\mu = 200$ GeV, $M_{\tilde{L}/\tilde{E}} = 1000$ GeV, $M_{\tilde{Q}/\tilde{U}/\tilde{D}_{1,2}} = 1000$ GeV, $M_{\tilde{Q}_3} = M_{\tilde{U}_3} = 650$ GeV, $M_{\tilde{D}_3} = 1000$ GeV, $A_t = A_\tau = A_b = 1000$ GeV, $m_{\tilde{g}} = 1500$ GeV, $A_\lambda = 560$ GeV, $\lambda = 0.64$, $\kappa = 0.25$, $A_\kappa = -10$ GeV, and we vary M_2 . In the upper left plot, the blue curve shows the M_W^{NMSSM} prediction and the red curve the M_W^{MSSM} prediction. The difference between the NMSSM prediction and the MSSM prediction is small for $M_2 \lesssim 200$ GeV and increases for larger M_2 values. The origin of this difference is investigated in the other three plots of Fig. 5.31. As before our procedure to identify an MSSM point which can be compared to the NMSSM point implies different predictions for the lightest \mathcal{CP} -even Higgs mass. Here we subtract again the difference in the SM contributions, arising from the different Higgs mass predictions. The additional blue dashed curve (with open dots) in the upper right plot of Fig. 5.31 corresponds to $M_W^{\text{NMSSM, sub}} = M_W^{\text{NMSSM}} - M_W^{\text{SM}}(M_{h_1}) + M_W^{\text{SM}}(M_h)$. For large M_2 the difference between the NMSSM and the MSSM prediction for M_W can be fully explained by the difference in the (SM-type) Higgs mass contributions, which arise from inserting different predictions for M_{h_1} and M_h . However after subtracting the difference from the Higgs mass contributions we observe a sizeable difference between $M_W^{\text{NMSSM, sub}}$ and M_W^{MSSM} for small M_2 . This difference stems from different sizes of the chargino/neutralino sector contributions between the two SUSY models, which tend to compensate the difference between M_W^{NMSSM} and M_W^{MSSM} arising from the Higgs sector. This can be seen in the lower left plot, where we display the shift δM_W (calculated as in Eq. (5.33)) induced by the chargino/neutralino contributions in the MSSM (red) and in the NMSSM (blue). At $M_2 = 150$ GeV the chargino mass is ~ 100 GeV and thus just above the LEP limit. The δM_W contribution from the chargino/neutralino sector in the MSSM reaches 8.5 MeV in this plot, which is lower than the maximal MSSM contribution (of ~ 18 MeV for $m_{\tilde{\chi}_1^\pm} = 100$ GeV) depicted in Fig. 5.11. The reason is, that for the parameter point discussed here the slepton masses ($m_{\tilde{l}} \sim 1000$ GeV) are considerably larger than the ones used in the analysis

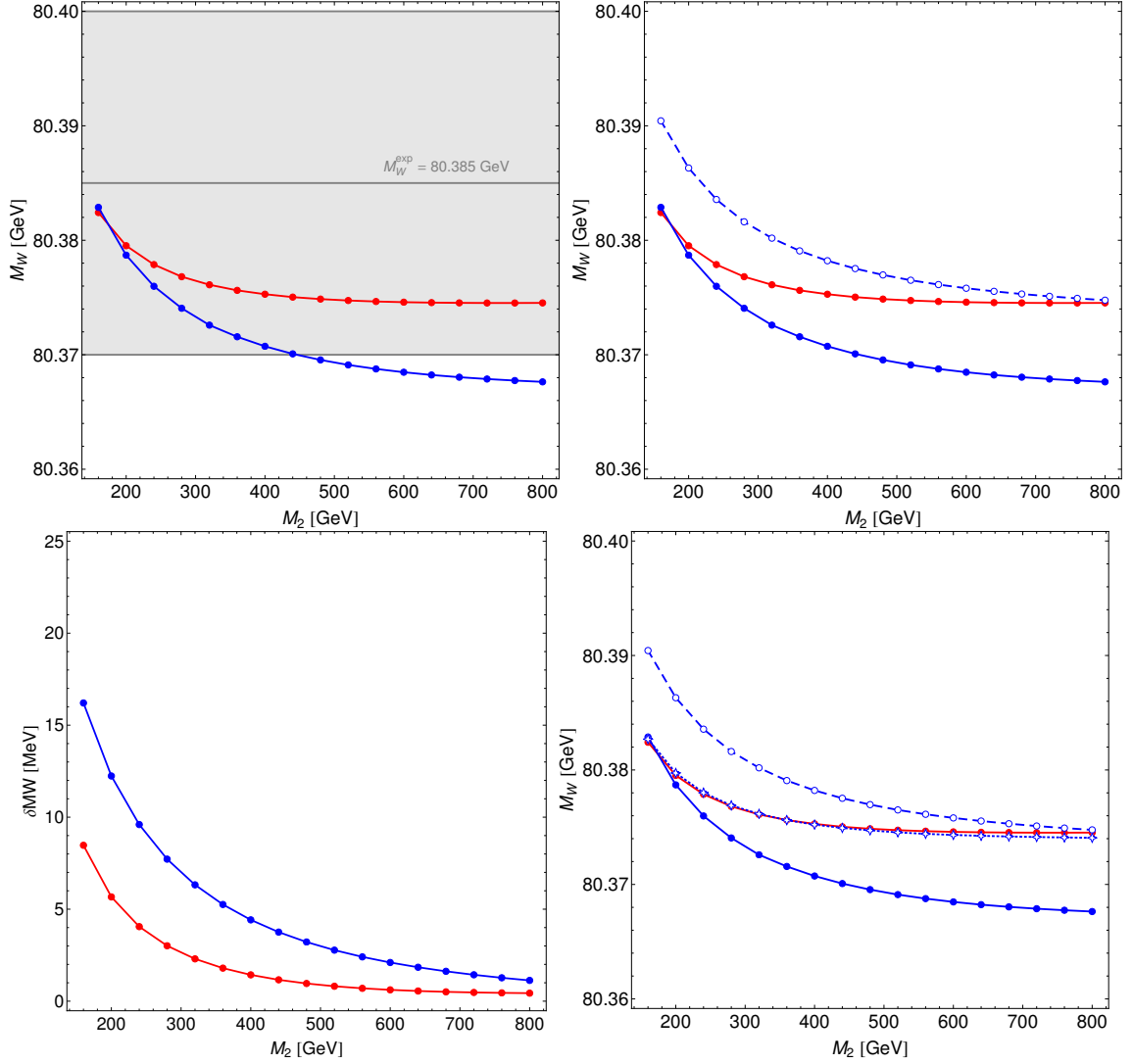


Figure 5.31: The upper left plot shows the M_W^{NMSSM} prediction (blue) and the M_W^{MSSM} prediction (red) as a function of M_2 . The experimental M_W measurement is indicated as a grey band. The upper right plot shows additionally a dashed blue curve (open dots) corresponding to $M_W^{\text{NMSSM, sub}} = M_W^{\text{NMSSM}} - M_W^{\text{SM}}(M_{h_1}) + M_W^{\text{SM}}(M_h)$. The lower left plot shows the shift in the W boson mass δM_W (calculated as in Eq. (5.33)) induced by the chargino/neutralino contributions in the MSSM (red) and in the NMSSM (blue). The lower right plot is similar to the upper right plot but it additionally contains the dotted blue curve (open diamonds) which corresponds to $M_W^{\text{NMSSM, sub}} - \delta M_W^{\text{NMSSM}} + \delta M_W^{\text{MSSM}}$ where δM_W is the shift in M_W induced by the chargino/neutralino contributions. The NMSSM parameter points are allowed by `HiggsBounds`, and M_{h_1} falls in the range 125.6 ± 3.1 GeV for $M_2 \lesssim 725$ GeV. The parameters used for these plots are given in the text.

in Fig. 5.11 ($m_{\tilde{t}} \sim 250$ GeV). In the NMSSM the maximal δM_W contribution from the chargino/neutralino sector is 16.5 MeV in Fig. 5.31 — significantly larger than in

the MSSM. Both in the MSSM and the NMSSM, the chargino/neutralino contributions decrease when increasing M_2 and therewith the chargino and neutralino masses, showing the expected decoupling behaviour. The largest difference between the NMSSM and the MSSM chargino/neutralino contributions is 8 MeV (at $M_2 = 160$ GeV). The difference comes from the neutralino sector, since the chargino sector is unchanged in the NMSSM with respect to the MSSM. We will discuss in more detail below (in the discussion of Figs. 5.32 -5.34) why the contributions from the neutralino sector are larger in the NMSSM than in the MSSM. The lower right plot of Fig. 5.31 is similar to the upper right plot, but it contains a fourth curve (blue dotted with open diamonds) which was obtained by subtracting the different chargino/neutralino contributions, thus it corresponds to $M_W^{\text{NMSSM,sub}} - \delta M_W^{\text{NMSSM}} + \delta M_W^{\text{MSSM}}$. This curve lies very close to the MSSM prediction. We have therefore identified the contributions causing the difference between the M_W^{NMSSM} and the M_W^{MSSM} predictions.

We continue with the discussion of the neutralino contributions to M_W in the NMSSM in Fig. 5.32. The chosen parameters are $m_t = 173.2$ GeV, $\tan\beta = 5.9$, $\mu = 200$ GeV, $M_{\tilde{L}/\tilde{E}} = 245$ GeV, $M_{\tilde{Q}/\tilde{U}/\tilde{D}_{1,2}} = 1500$ GeV, $M_{\tilde{Q}_3} = M_{\tilde{U}_3} = M_{\tilde{D}_3} = 1000$ GeV, $A_t \simeq 1966$ GeV, $A_\tau = A_b = 1000$ GeV, $m_{\tilde{g}} = 1500$ GeV, $\hat{m}_A = 1200$ GeV, $\lambda = 0.6$, $\kappa = 0.5\lambda$, $A_\kappa = -10$ GeV, and M_2 is varied. Again we get the MSSM prediction by setting the `FeynHiggs` M_{H^\pm} input to the value of the charged Higgs mass calculated by `NMSSMTools`. For this set of parameters this procedure leads to a scenario where the MSSM and the NMSSM Higgs boson sectors are very similar and both models predict the lightest \mathcal{CP} -even Higgs at ~ 125.6 GeV. The two states M_h and M_{h_1} are close in mass, the difference is $\lesssim 1$ GeV, and the resulting difference in M_W from the Higgs sector contributions is small ($\lesssim 0.5$ MeV). The upper left plot of Fig. 5.32 displays the W boson mass prediction in the NMSSM (blue) and in the MSSM (red). The difference between these two predictions is largest (7 MeV) for $M_2 = 150$ GeV and (almost) vanishes for large M_2 . Since differences in the Higgs sector contributions are very small, the difference between M_W^{NMSSM} and M_W^{MSSM} arises predominately from the differences in the neutralino sector. In the upper right plot we show the contribution to M_W (calculated as in Eq. (5.33)) arising from the chargino/neutralino sector in the NMSSM (blue) and the MSSM (red). The black dashed curve shows the difference between these two. Here the slepton mass scale is chosen lower, and consequently the MSSM chargino/neutralino contribution is closer to its maximal value, given in Fig. 5.11. As expected the difference in the chargino/neutralino contribution explains the difference between M_W^{NMSSM} and M_W^{MSSM} .

In order to investigate the reasons for the different predictions for the chargino/neutralino contributions we plot the masses of the lightest neutralino states in the NMSSM (blue) and the MSSM (red) in the lower left plot. The other MSSM/NMSSM neutralinos are heavier than 200 GeV and will hardly affect the M_W prediction. We set here the (unphysical) soft masses M_1 and M_2 equal in the MSSM and the NMSSM and identify the MSSM μ parameter with the effective μ of the NMSSM. The resulting predictions for the masses of $\tilde{\chi}_1^0$ and $\tilde{\chi}_2^0$ are a few GeV lower in the NMSSM than in the MSSM. The singlino components of the NMSSM neutralinos, $|N_{i5}|^2$ where N was defined in Eq. (2.75), are

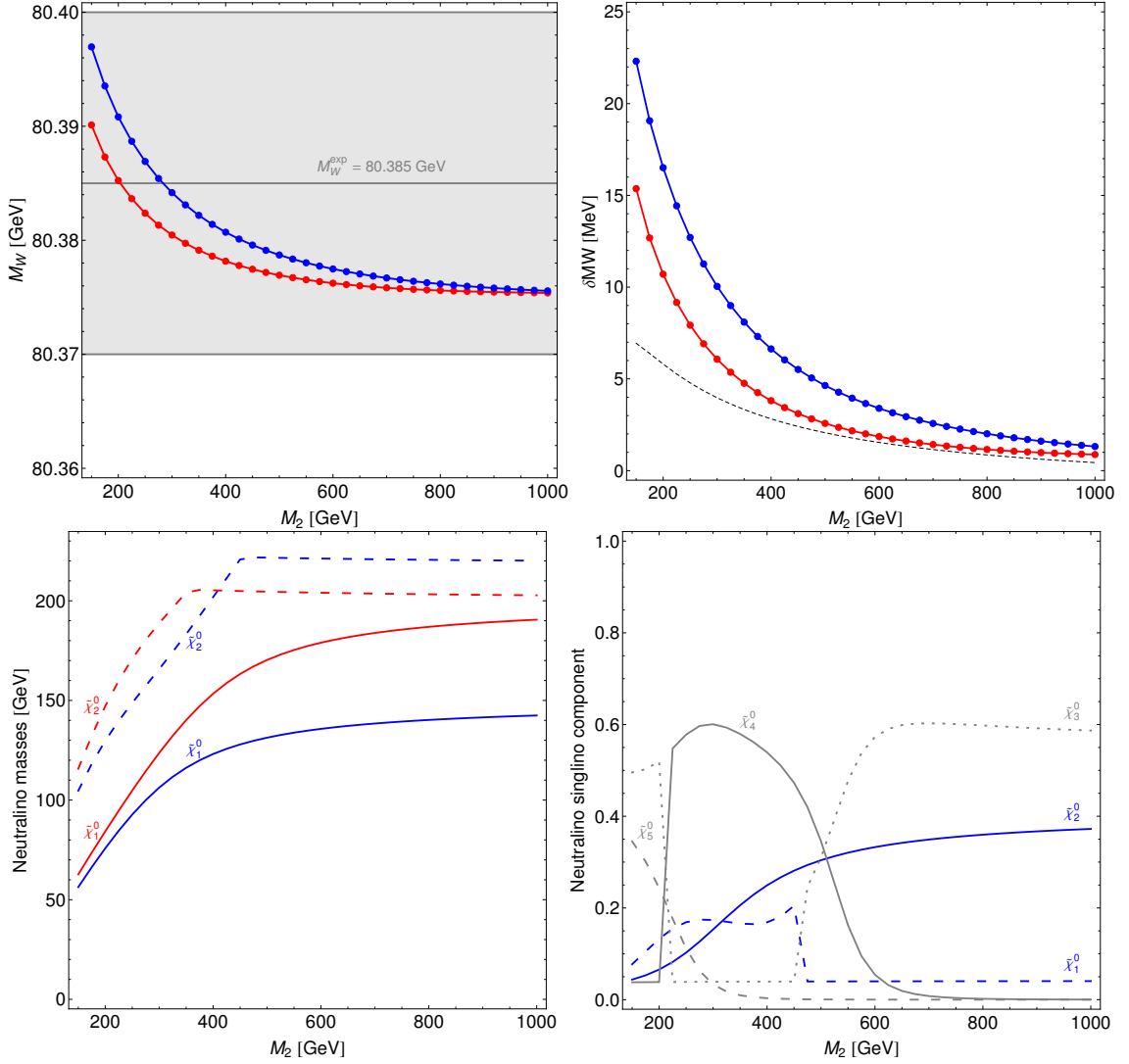


Figure 5.32: The upper left plot shows the M_W^{NMSSM} prediction in blue and the M_W^{MSSM} prediction in red as a function of M_2 . The upper right plot shows the shift δM_W from the chargino/neutralino contributions (calculated as in Eq. (5.33)) in the NMSSM (blue) and in the MSSM (red), the black dashed curve shows the difference between them. The neutralino masses and the neutralino singlet components are displayed in the lower row. The parameters (given in the text) are chosen such that the Higgs sectors of the MSSM and the NMSSM are very similar, both models are allowed by HiggsBounds and predict the lightest \mathcal{CP} -even Higgs (which is SM-like) close to 125.6 GeV.

shown in the lower right plot and we can observe a strong mixing between the five states. The singlet components of $\tilde{\chi}_1^0$ and $\tilde{\chi}_2^0$ are below 10% for $M_2 = 150$ GeV and increase to about 20 – 30% for $M_2 = 400$ GeV. The lighter neutralino states (with relatively small singlet component) lead to larger contributions from the neutralino sector to M_W in the NMSSM compared to the MSSM.

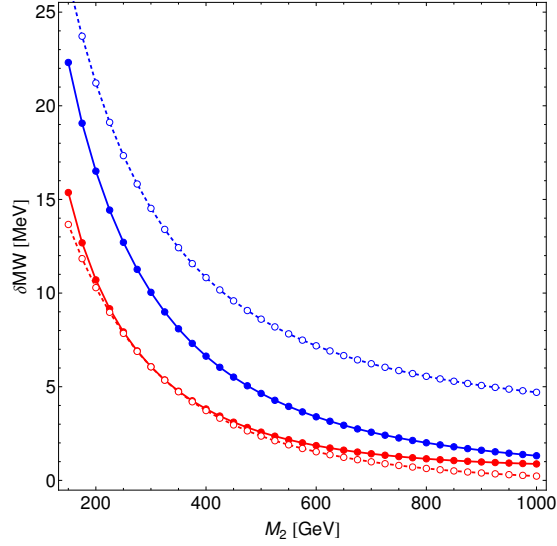


Figure 5.33: The plot shows the δM_W shifts in the NMSSM (blue curves) and in the MSSM (red curves), calculated taking the full chargino/neutralino contribution to Δr into account (solid curves) and using only the $\Delta\rho$ approximation (dashed curves). The parameters are chosen as in Fig. 5.32.

In the next step we analyse how well the full Δr contribution of the chargino/neutralino sector can be approximated by taking into account only the leading $-c_W^2/s_W^2 \Delta\rho$ (defined in Eq. (5.8)) term. The $\Delta\rho$ term contains only the W and Z boson self-energies at zero momentum transfer, thus this approximation neglects in particular the contributions from box, vertex and fermion self-energy diagrams containing charginos and neutralinos. The $\Delta\rho$ term corresponds to the T parameter of the S, T, U parameters [213, 214] often used to parameterise new physics contribution to electroweak precision observables. For the left plot of Fig. 5.33 we use the same parameters as in Fig. 5.32. Again the blue solid curve shows the δM_W shift as a function of M_2 , calculated as in Eq. (5.33) using the full $\Delta r_{\text{cha/neu}}^{\text{NMSSM}}$. The red solid curve shows the corresponding MSSM contribution using the full $\Delta r_{\text{cha/neu}}^{\text{MSSM}}$ (so the two solid curves are identical to the ones in the upper right plot of Fig. 5.32). The two dashed curves show the M_W contributions in the NMSSM (blue) and in the MSSM (red) if the chargino/neutralino contribution is approximated by the $\Delta\rho_{\text{cha/neu}}^{(\text{N})\text{MSSM}}$ terms:

$$\delta M_W = -\frac{M_W^{\text{ref}}}{2} \frac{s_W^2}{c_W^2 - s_W^2} \left(-\frac{c_W^2}{s_W^2} \right) \Delta\rho_{\text{cha/neu}}^{(\text{N})\text{MSSM}}. \quad (5.34)$$

In the MSSM the $\Delta\rho$ term containing charginos and neutralinos provides a very good approximation of the full Δr term in the intermediate range $200 \text{ GeV} \lesssim M_2 \lesssim 500 \text{ GeV}$. In the range of small and large M_2 values, $\Delta\rho$ slightly underestimates the full Δr contribution, the difference here is $\sim 2 \text{ MeV}$ for $M_2 = 150 \text{ GeV}$ and $\sim 0.6 \text{ MeV}$ for $M_2 = 1000 \text{ GeV}$. In the NMSSM the $\Delta\rho$ term gives a δM_W contribution which is larger ($\gtrsim 4 \text{ MeV}$) than the full Δr result for the full M_2 range plotted here. Also in

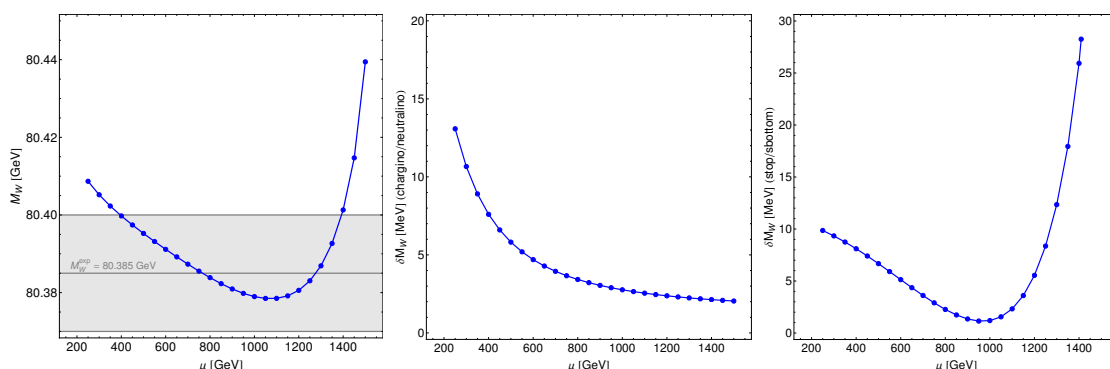


Figure 5.34: Dependence of the W boson mass prediction in the NMSSM on the μ parameter. The left plot shows the M_W^{NMSSM} prediction, the middle one the δM_W contribution from the chargino/neutralino sector and the right one shows the δM_W contribution from the stop/sbottom sector. The parameters are given in the text.

the case of large M_2 , the scenario shown here does not correspond to the decoupling limit of the chargino/neutralino sector because of the light Higgsino, $\mu = 200$ GeV. For $M_2 = 1000$ GeV the lightest neutralino has a mass of $M_2 = 140$ GeV, with a singlino component of $\sim 40\%$ and a Higgsino component of $\sim 60\%$. In this scenario the singlino-higgsino mixing leads to a positive contribution to $\Delta\rho$, but to a negative contribution to the Δr terms beyond $\Delta\rho$ (we checked that the contribution from the box diagrams is negligible for large M_2 values). We checked that going to large μ values, the chargino/neutralino sector decouples and all terms vanish. In this scenario the two effects largely cancel each other and for large M_2 one finds a small positive value for the full Δr result. This however depends on the chosen parameters and the admixture of the light neutralino, e.g. in the scenario discussed in Fig. 5.28 the negative contributions exceed the positive ones so that the full Δr result is negative for large M_2 .

In the last step we want to discuss the dependence of the M_W prediction in the NMSSM on the μ parameter, entering both in the sfermion sector and in the chargino/neutralino sector. The left plot of Fig. 5.34 shows the W boson mass prediction in the NMSSM as a function of μ ($=\mu_{\text{eff}}$). The parameters are chosen as $m_t = 173.2$ GeV, $\tan\beta = 20$, $M_{\tilde{L}/\tilde{E}} = 250$ GeV, $M_{\tilde{Q}/\tilde{U}/\tilde{D}_{1,2}} = 1500$ GeV, $M_{\tilde{Q}_3} = 500$ GeV, $M_{\tilde{U}_3} = 1500$ GeV, $M_{\tilde{D}_3} = 300$ GeV, $A_\tau = 0$ GeV, $A_t = A_b = -2185$ GeV, $M_2 = 150$ GeV, $m_{\tilde{g}} = 1500$ GeV, $\hat{m}_A = 1500$ GeV, $\lambda = 0.2$, $\kappa = 0.6$, $A_\kappa = -1370$ GeV, and μ is varied. The parameter points are HiggsBounds allowed and h_1 falls in the mass range 125.6 ± 3.1 GeV. Increasing μ the M_W^{NMSSM} prediction decreases first, reaches its minimum for $\mu \sim 1000$ GeV and then rapidly increases. This behaviour can be explained, looking at the contributions to M_W from the chargino/neutralino (here we take again the full Δr contributions into account) and from the stop/sbottom sector. The shift δM_W arising from charginos and neutralinos is shown in the middle plot of Fig. 5.34. The chargino/neutralino contribution is largest for small μ and decreases with increasing μ . We checked that also in this scenario, for small μ values, the $\Delta\rho$ contribution is larger than the full Δr contribution which we use here, however in this case the positive contri-

Contributions clearly dominate²⁶. Going to larger μ the masses of the (higgsino-like) chargino and neutralino states increase and the M_W contribution decreases. The shift δM_W arising from the stop/sbottom sector is shown in the right plot of Fig. 5.34. The contributions from the stop/sbottom sector (dominated by the $\Delta\rho$ contributions in Eq. (5.31)) get smaller when μ is increased up to $\mu \sim 1000$ GeV and then start to rise if μ is increased further. Increasing μ the splitting between the two sbottoms gets larger (while the stop masses stay nearly constant), which implies also an increase of the splitting between stops and sbottoms. The counteracting terms in Eq. (5.31) lead to the observed behaviour.

²⁶In this scenario the lightest neutralino has a small singlino component.

5.9 Summary

We have presented the currently most precise prediction for the W boson mass in the MSSM (for the general case of complex parameters) and the NMSSM and compared it with the state-of-the-art prediction in the SM. The evaluations in the MSSM and the NMSSM include the full one-loop result and all relevant higher-order corrections of SM and SUSY type.

Within the SM, interpreting the signal discovered at the LHC as the SM Higgs boson with $M_{H^{\text{SM}}} = 125.6$ GeV, there is no unknown parameter in the M_W prediction anymore. This yields $M_W^{\text{SM}} = 80.361$ GeV, which is somewhat below (but compatible at the level of about 1.5σ) with the current experimental value of $M_W^{\text{exp}} = 80.385 \pm 0.015$ GeV. The loop contributions from supersymmetric particles in general give rise to an upward shift in the prediction for M_W as compared to the SM case, which tend to bring the prediction into better agreement with the experimental result.

For the calculation of the M_W prediction, we made use of the highly automated programs `FeynArts`, `FormCalc` and `LoopTools`. In the case of the NMSSM, we developed a framework²⁷ consisting in particular of a new model file for the program `FeynArts` and a `Fortran` driver for the evaluation of the masses, mixing angles, etc. needed for the numerical evaluation. Numerous tests have been performed to verify the implementation; among other things we evaluated more than 150 loop-induced processes in the NMSSM and checked the results for UV-finiteness. In the present implementation for the MSSM we take the numerical values for the effective couplings and the MSSM Higgs boson masses from `FeynHiggs`. It is planned that the results for the M_W prediction in the MSSM will be implemented in or linked to `FeynHiggs`, such that in future the predicted M_W value can be used as input for the Higgs mass evaluation in `FeynHiggs`. In the NMSSM, currently the code `NMSSMTools` is used for the evaluation of the Higgs bosons masses.

In the MSSM, we performed scans over the parameter space and investigated the MSSM and SM predictions in the M_W - m_t plane, updating the earlier results in Ref. [156] while taking into account the existing constraints from Higgs and SUSY searches. We have analysed in this context the implications of the results of present and possible future searches for supersymmetric particles at the LHC. While the existing bounds on the gluino and the squarks of the first two generations have only a minor effect, more stringent bounds on the third generation squarks would have a drastic effect on the possible range of M_W values in the MSSM. In particular, assuming a lower bound of 500 GeV on the masses of the stops and sbottoms, the resulting range of predicted M_W values in the MSSM essentially reduces to the region that is best compatible with the experimental result. We have furthermore pointed out that even if the squarks are so heavy that their contribution to M_W becomes negligible, sizeable SUSY contributions to M_W are nevertheless possible if either charginos, neutralinos or sleptons are light.

²⁷This framework was developed first for the analysis presented in the next chapter, which has been published in Ref. [32]. In this thesis we decided to describe this framework in the context of the NMSSM M_W analysis, which we present first.

Besides the impact of limits from searches for supersymmetric particles, we have analysed the constraints arising from the Higgs signal at about 125.6 GeV. Within the MSSM this signal can be interpreted, at least in principle, either as the light or the heavy \mathcal{CP} -even Higgs boson. Concerning the interpretation in terms of the light \mathcal{CP} -even Higgs boson, the result for M_W turns out to be well compatible with the additional constraint that M_h should be in the mass range compatible with the signal. The main effect of this constraint is that it somewhat reduces the allowed range of predicted M_W values in the MSSM, improving in this way the overall compatibility with the experimental result for M_W . It is remarkable that also the rather exotic scenario where the mass of the heavy \mathcal{CP} -even Higgs boson is required to be in the range compatible with the observed signal (which is under pressure in particular from the recent ATLAS bound on light charged Higgs bosons) leads to predicted values for M_W that tend to be in better agreement with the experimental result than the SM one.

We have discussed the impact of the precision observable M_W in the context of possible future scenarios. The improved precision on M_W and m_t from future measurements at the LHC and in particular at a prospective Linear Collider (ILC) would significantly enhance the sensitivity to discriminate between the SM and the MSSM (as well as other BSM scenarios). Analysing in this context the impact of possible future LHC results in the stop sector on the M_W prediction, we have discussed a hypothetical scenario where a light stop has been detected at the LHC, while lower limits have been imposed on all other SUSY particles. We have demonstrated that, depending on the future central experimental value, a high-precision measurement of M_W could yield quite stringent *upper* bounds on the masses of the heavier stop and the lighter sbottom, which could be of great interest regarding the direct searches for those particles.

As a final step in the MSSM analysis, we have shown that the impact of a complex phase of the stop mixing parameter A_t , can have a sizeable effect on the sfermion one-loop contributions to M_W , in agreement with the results found in Ref. [156].

In the NMSSM, we started our analysis by demonstrating the size of the contributions from sfermions, in particular from stops/sbottoms and sleptons. Since the sfermion sector is unchanged in the NMSSM with respect to the MSSM, we have done this study in the MSSM-limit, yielding an important check of our NMSSM implementation. We have investigated the size of the SUSY two-loop corrections to M_W . The Yukawa-enhanced electroweak two-loop corrections of $\mathcal{O}(\alpha_t^2)$, $\mathcal{O}(\alpha_t\alpha_b)$, $\mathcal{O}(\alpha_b^2)$ give a numerically small contribution, while the $\mathcal{O}(\alpha\alpha_s)$ corrections can give sizeable contributions. Including these corrections, beyond the gluon exchange contributions, leads to an improved prediction for M_W^{NMSSM} compared to the previous result of Ref. [163].

We started the discussion of the genuine NMSSM effects with the Higgs sector contributions to M_W . The tree-level prediction for the lightest \mathcal{CP} -even Higgs mass gets an additional term in the NMSSM, which (for small $\tan\beta$) leads to an upward shift of the tree-level Higgs mass. Therefore, in that region, the radiative corrections needed to push the Higgs mass to 125.6 GeV can be smaller than in the MSSM, which implies that lighter stop masses and a smaller stop mixing are possible. We investigated a scenario where this additional tree-level term gives rise to a higher M_{h_1} prediction than in the

MSSM limit, which leads to a lower M_W prediction (the difference is ~ 15 MeV). We have investigated the effect of a strong doublet-singlet mixing between two Higgs bosons close in mass and found that it has only a minor impact on the M_W prediction. In the NMSSM the Higgs signal seen at the LHC can be interpreted both as the lightest and the second lightest \mathcal{CP} -even Higgs. Both interpretations give predictions for the W boson mass in good agreement with the M_W measurement. In the NMSSM the interpretation of the LHC signal as the second lightest \mathcal{CP} -even Higgs h_2 is possible together with either a light or a heavy charged Higgs. The second possibility makes this interpretation clearly less constrained in the NMSSM compared to the MSSM. Light charged Higgs bosons (together with a light \mathcal{CP} -even Higgs with reduced but non-zero couplings to gauge bosons) can (as in the MSSM) in principle give very significant contributions to M_W , in that case large deviations from the SM Higgs sector contributions occur. However scenarios with a light charged Higgs are under pressure from the LHC charged Higgs searches. Generally we find that taking all available constraints on the Higgs sector into account, the specific NMSSM effects of the Higgs sector to M_W are small.

The modified neutralino sector on the other hand, can lead to a sizeable difference between the W boson mass predictions in the NMSSM and the MSSM. The chargino/neutralino contributions to M_W can be larger in the NMSSM compared to the MSSM, in the scenario which we studied the difference reaches ~ 8 MeV. Assuming the same values for the soft mass parameters in the MSSM and the NMSSM and choosing $\mu = \mu_{\text{eff}}$, the mixing with the singlino leads to changed neutralino masses. If the lightest NMSSM states are lighter than the corresponding MSSM states, but have a relatively small singlino component it can cause M_W contributions larger than in the MSSM. While light wino/bino states typically give positive contributions, light higgsinos can give contributions entering with both signs. We compared the M_W prediction calculated with the full Δr to the one where the full result is approximated by $\Delta\rho$ and we found that in the NMSSM the differences can be sizeable. Taking only the $\Delta\rho$ term into account the full contributions can be over- or underestimated. Light neutralinos with a significant higgsino component tend to give a positive contribution to $\Delta\rho$ and a negative contribution to the Δr terms beyond $\Delta\rho$. Which of the contributions dominate, depends on the admixture of the light neutralinos.

Chapter 6

The diphoton decay channel in the MSSM and the NMSSM

The results in this chapter are based on Ref. [32] and in this work we largely follow that article. I have been heavily involved in obtaining the results presented in this chapter: I set up the framework for the MSSM scan. The NMSSM framework builds on a FeynArts model file for the NMSSM, as I discussed already in the last chapter. I did not set up the NMSSM framework, but I participated in finding good scan ranges (leading to a $R_{\gamma\gamma}$ enhancement) and in testing the framework. In both models I was stongly involved in analysing the mechanisms for an enhancement of the $\gamma\gamma$ rate compared to the SM (in particular I examined which parameter choices lead to a suppression of the Higgs coupling to $b\bar{b}$) and in plotting the results.

6.1 Introduction

In July 2012 ATLAS and CMS announced the spectacular discovery of a “Higgs-like” particle with a mass around $M_H \simeq 125$ GeV [1, 2]. A clear excess was detected in the two photon channel as well as in the $ZZ^{(*)}$ channel, whereas at that point the analyses in other channels were less mature.

Since July 2012, the discovery has been further confirmed and an excess has been seen also in other decay channels. Now the LHC experiments see evidence for a Higgs boson also in the $WW^{(*)}$ channel [84, 85] as well as in the $\tau\tau$ [87, 88] and $b\bar{b}$ [215, 216] channels. The LHC results are supplemented by the excess seen in $b\bar{b}$ by Tevatron [86].

At the time of the discovery, the observed rate in the $\gamma\gamma$ channel was considerably above the expectation for a SM Higgs both for ATLAS and CMS. By now the full 7 TeV and 8 TeV datasets have been analysed: the signal strength in the $\gamma\gamma$ channel measured by ATLAS [19] remains above the value expected in the SM (but is still compatible with the SM at the 2σ level), while the signal strength observed by CMS [20] is currently slightly below the SM level. While the statistical significance of the deviations from the SM prediction are at present not sufficient to draw a definite conclusion, they could point towards physics beyond the SM. The prime task is now to study the properties of the

discovered new particle and in particular to test whether the new particle is compatible with the Higgs boson of the SM or whether deviations from the SM predictions will be established.

In the analysis discussed in this chapter, we study possible alternatives to the SM, where the rates of the Higgs decays can be modified compared to the SM. We investigate the corresponding predictions in both the MSSM and the NMSSM, and compare them to the SM case. In particular, we evaluate the predictions for the production of a MSSM or NMSSM Higgs boson via gluon fusion, the main production channel at the LHC, followed by the decay into two photons.

This analysis was published shortly after the Higgs discovery in July 2012, therefore the main motivation was to investigate a possible enhancement of the two-photon rate over the SM prediction. This aspect is still of interest since also in the view of the latest data there is still considerable room for an enhanced $\gamma\gamma$ rate. Since this is a loop-induced process, new physics contributions affecting the $\gamma\gamma$ rate do not have to compete with a dominant SM tree-level contribution. As we will discuss in detail in chapter 7, the latest Higgs and low energy data (including results that were public by February 2014) still favours a slight enhancement of the $\gamma\gamma$ rate with respect to the SM.

We analyse potential enhancements of the production cross section times branching ratio over the corresponding SM prediction and we confront those predictions with the experimental data (available at that time). We discuss in detail how an enhanced $\gamma\gamma$ rate can be realised in the MSSM, and which *additional* mechanisms for an enhancement can occur in the NMSSM. We find that for a Higgs at 125 GeV sizeable enhancements of the $\gamma\gamma$ rate are possible in both models, with or without a corresponding enhancement of the $WW^{(*)}$ decay mode. On the other hand, both models allow also a $\gamma\gamma$ rate at the SM level or suppressed with respect to the SM. In both models the signal in this channel can be interpreted *either* as the lightest \mathcal{CP} -even Higgs *or* as the second-lightest \mathcal{CP} -even Higgs.

6.2 Framework of our analysis

6.2.1 General considerations

Since the NMSSM extends the MSSM in the Higgs and the neutralino sectors, differences to the MSSM are best probed in these two sectors. The processes playing the main role in the reported discovery of a Higgs boson at the LHC in July 2012 [1,2], namely production via gluon fusion and decay into two photons, are in fact processes that are particularly sensitive to possible deviations between the SM, the MSSM and the NMSSM. Some generic diagrams contributing to $gg \rightarrow h_i$ and to $h_i \rightarrow \gamma\gamma$ in the SM and in SUSY models are shown in Fig. 6.1. In the MSSM h_i denotes either h or H , while in the NMSSM h_i ($i = 1 \dots 3$) can be any of the three \mathcal{CP} -even Higgs states.

In this work we will compare the partial widths $\Gamma(h_i \rightarrow \gamma\gamma)$ and the branching ratios $\text{BR}(h_i \rightarrow \gamma\gamma)$ in the (N)MSSM with the SM prediction. In order to investigate the phenomenology at the LHC, besides the branching ratio also the Higgs production cross section has to be taken into account. The combined enhancement or suppression over the SM for a process $pp \rightarrow h_i \rightarrow X$ can therefore be summarised in the ratio¹

$$R_X^{h_i} = \frac{\sigma(pp \rightarrow h_i) \times \text{BR}(h_i \rightarrow X)}{\sigma(pp \rightarrow H^{\text{SM}}) \times \text{BR}(H^{\text{SM}} \rightarrow X)}. \quad (6.1)$$

If the Higgs production cross section is dominated by a single mechanism, such as gluon fusion which is often the case at the LHC, a common approximation is to use instead of $\sigma(pp \rightarrow h_i)$ the parton-level cross section $\hat{\sigma}(gg \rightarrow h_i)$. Neglecting the differences in kinematics, the decay width $\Gamma(h_i \rightarrow gg)$ has the same dependence as $\hat{\sigma}(gg \rightarrow h_i)$ on the couplings of the involved particles, and the dominant higher-order QCD corrections are expected to cancel out in the ratio². Making use of this approximation, Eq. (6.1) can be expressed as

$$R_X^{h_i} \simeq \frac{\Gamma(h_i \rightarrow gg) \times \text{BR}(h_i \rightarrow X)}{\Gamma(H^{\text{SM}} \rightarrow gg) \times \text{BR}(H^{\text{SM}} \rightarrow X)} = \frac{\Gamma(h_i \rightarrow gg) \times \Gamma(h_i \rightarrow X) \times \Gamma_{\text{tot}}(H^{\text{SM}})}{\Gamma(H^{\text{SM}} \rightarrow gg) \times \Gamma(H^{\text{SM}} \rightarrow X) \times \Gamma_{\text{tot}}(h_i)}. \quad (6.2)$$

This definition will be used to calculate $R_{\gamma\gamma}^{h_i}$ and $R_{WW}^{h_i}$ in the MSSM and in the NMSSM.

¹This ratio corresponds to the Higgs signal strength which is denoted μ in other chapters of this thesis.

²Non-negligible differences are mainly expected if the bottom loop contribution to $h_i \rightarrow gg$ dominates over the top loop contribution. In the case of the light \mathcal{CP} -even Higgs boson this can happen for very low M_A and moderate to large $\tan\beta$ values, whereas in the case of the heavy \mathcal{CP} -even Higgs boson this can happen for larger M_A and $\tan\beta \gtrsim 5$. Our results therefore exhibit an additional uncertainty in this part of the parameter space. Additional loop contributions from SUSY particles, while taken into account in our calculation, are usually subdominant and of lesser importance in this context.

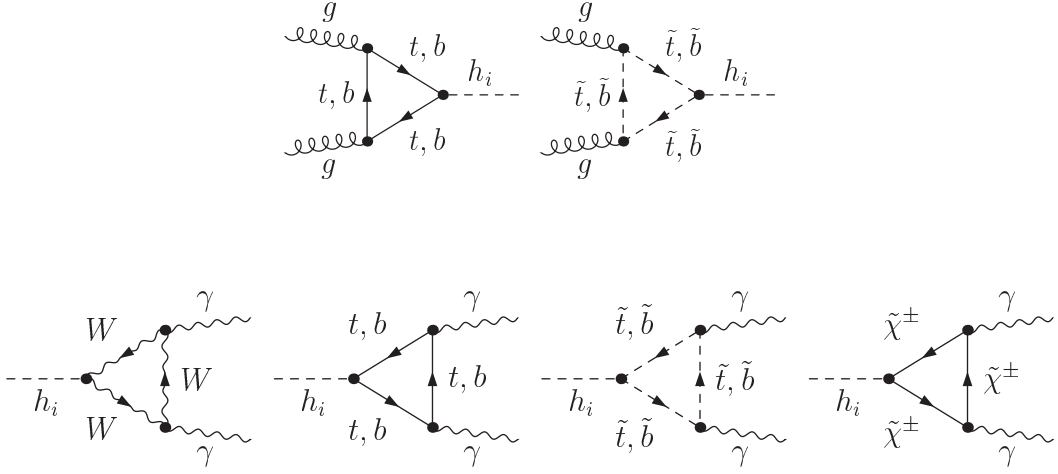


Figure 6.1: Generic diagrams contributing to $gg \rightarrow h_i$ (upper row) and to $h_i \rightarrow \gamma\gamma$ (lower row), where h_i denotes any neutral \mathcal{CP} -even Higgs boson in the (N)MSSM.

6.2.2 Computational framework

In the MSSM we evaluate the quantities of interest ($\Gamma(h/H \rightarrow \gamma\gamma)$, $\Gamma(h/H \rightarrow gg)$, Γ_{tot}) making use of the code `FeynHiggs` (version 2.8.6), which is also used to evaluate SM quantities given below.

The calculational framework in the NMSSM is similar to the one used for the M_W^{NMSSM} evaluation described in Sect. 5.4. Even though in this thesis we described the framework already in the context of the M_W^{NMSSM} prediction, it was originally set up first for the analysis of loop-induced Higgs decays in the NMSSM, presented in this chapter. We use the NMSSM `FeynArts` model file (see Sect. 5.4.4) to calculate the relevant Higgs production cross section in gluon fusion (approximated by $\Gamma(h/H \rightarrow gg)$, see above) and the decay width into two photons. The one-loop predictions for those processes correspond to the leading-order contributions, which are IR- and UV-finite without renormalisation (for a recent discussion of the renormalisation of the NMSSM Higgs sector, see [217]), so that the set-up mentioned above can immediately be applied for the investigation of these processes, important for NMSSM Higgs phenomenology at the LHC. To enable the numerical evaluation of observables, the analytic amplitudes of `FormCalc` can be exported to Fortran code, supplemented with a driver program to compute the necessary quantities (masses, mixings, etc.) from the fundamental parameters of the theory. The driver codes also provide standard facilities for numerical integration and the evaluation of master one-loop integrals through `LoopTools`. We have developed such a driver program for the NMSSM, which in its present state allows for Higgs and sparticle masses to be calculated either following the relations in Sect. 2.3, or using `NMSSMTools` (here we used version 2.3.5) [188] linked through a custom interface³. The NMSSM driver also offers the possibility to impose restrictions on the NMSSM parameter space resulting from the evaluation of various experimental or theoretical constraints. For instance, the

³See Sect. 5.4.2 for a brief discussion on the calculation of sparticle masses in `NMSSMTools`.

constraints implemented in `NMSSMTools` can be accessed, and direct constraints on the extended Higgs sector are available through an interface to `HiggsBounds` [195]. More details on the different constraints and how they are evaluated is given in Sect. 6.2.3 below.

6.2.3 Constraints on the parameter space

Before moving on to our numerical analysis, we briefly discuss the various phenomenological constraints which exist on the parameter space of the MSSM and the NMSSM. In the NMSSM we include the theoretical constraints described in Sect. 5.4.3. In both models we apply the LEP limits on SUSY particles as described in Sect. 5.4.3. The mass of the squarks of the first two generation is chosen to be $\gtrsim 750$ GeV, the mass of the gluino is 1200 GeV. The value chosen for the squark masses lies in the meanwhile excluded region, however the impact of these particles on our analysis is small, thus choosing a higher value (such as 1500 GeV) would only lead to minor changes of our results.

As in the previous chapter, we test limits from direct Higgs searches using the code `HiggsBounds`. However here we used `HiggsBounds` version 3.6.1, which was the most recent one at the time the analysis was conducted. This `HiggsBounds` version includes the results from Higgs searches at LEP and the Tevatron as well as from the LHC data presented in 2011 (referred to as `LHC2011`). Using only the `LHC2011` data the allowed mass range for a SM-like Higgs was still $\sim 114.4 \lesssim M_H \lesssim 127$ GeV. Including the 2012 data, the mass range for a SM-like Higgs is restricted to a small region around 125.6 GeV. In contrast to the newer `HiggsBounds` version described in Sect. 5.4.3, the version 3.6.1, which was used here, did not test every Higgs boson in a model. Only a single channel with the highest expected sensitivity was determined among all Higgs bosons of the model and the theory prediction was compared to the observation in this particular channel.

In this analysis we include the constraint from the anomalous magnetic moment of the muon, for which the measurement differs from the SM prediction by $\Delta a_\mu = a_\mu^{\text{exp}} - a_\mu^{\text{SM}} = (30.2 \pm 8.8) \times 10^{-10}$ [117, 118], which corresponds to more than 3σ (see Sect. 4.2.5). Employing new physics contributions to account for this deviation leads to bounds on the model parameters [218, 219]. The MSSM contribution is evaluated with `FeynHiggs`, where the leading two-loop contributions [220–222] are implemented. The dominant contributions to a_μ in the NMSSM are known including leading corrections up to the two-loop order [219]. For the numerical evaluation in the NMSSM we use `NMSSMTools`. As the 2σ allowed range for the SUSY contributions $\Delta a_\mu^{(\text{N})\text{MSSM}} = a_\mu^{(\text{N})\text{MSSM}} - a_\mu^{\text{SM}}$ we use $1.21 \times 10^{-9} < \Delta a_\mu^{(\text{N})\text{MSSM}} < 4.82 \times 10^{-9}$, which includes a theory uncertainty on the SUSY evaluation corresponding to 2.0×10^{-10} added in quadrature to the uncertainty quoted above. We note that both in the MSSM and in the NMSSM a positive value for μ/μ_{eff} is strongly favoured when a_μ is included as a constraint.

The MSSM analysis includes the constraint from $b \rightarrow s\gamma$, which is calculated in `FeynHiggs`. Within the NMSSM analysis a larger set of constraints from flavour physics

Observable	Exp. lower limit	Exp. upper limit	
$\text{BR}(B \rightarrow X_s \gamma)_{E_\gamma > 1.6 \text{ GeV}}$	3.03×10^{-4}	4.07×10^{-4}	[226]
$\text{BR}(B_s \rightarrow \mu^+ \mu^-)$	-	1.1×10^{-8}	[227]
$\text{BR}(B^\pm \rightarrow \tau \nu_\tau)$	0.79×10^{-4}	2.45×10^{-4}	[228]
ΔM_{B_s}	17.53 ps^{-1}	18.01 ps^{-1}	[229]
ΔM_{B_d}	0.499 ps^{-1}	0.515 ps^{-1}	[226]

Table 6.1: Experimentally allowed ranges at the 2σ level used for the flavour physics observables in the analysis presented in this chapter.

is included. A summary of flavour physics constraints on the NMSSM parameter space has been presented in [33]. In the present setup we use `NMSSMTools` (version 2.3.5) to evaluate the NMSSM theory predictions for the flavour physics observables. The corresponding experimental limits are listed in table 6.1⁴. Parameter-dependent theory uncertainties (taken from `NMSSMTools`) are added linearly to the intervals shown in the table before evaluating exclusion.

In theories with minimal flavour violation (MFV), which we are investigating here, the strongest constraints from flavour physics can usually be derived from B -physics observables such as $\text{BR}(B \rightarrow X_s \gamma)$, $\text{BR}(B_s \rightarrow \mu^+ \mu^-)$, $\text{BR}(B_u \rightarrow \tau^+ \nu_\tau)$, or from the mass mixings ΔM_s , ΔM_d [224, 225].

⁴Updated numbers for the flavour physics observables, as given e.g. in [223] (including in particular LHC measurements) were not available at the time when this analysis was performed. The same is true for the measurement of $\text{BR}(B_s \rightarrow \mu^- \mu^+)$ [115, 116], which is therefore not included here.

6.3 Numerical analysis

In this section we analyse numerically the phenomenologically important loop-induced Higgs decays of the neutral \mathcal{CP} -even Higgs bosons to two photons,

$$h_i \rightarrow \gamma\gamma \quad (i = 1, 2, 3) . \quad (6.3)$$

We investigate in particular to what extent the phenomenology of Higgs decays into two photons can differ in the MSSM and the NMSSM from the SM case, taking into account the existing constraints on the parameter space discussed above. Therefore we perform scans over the MSSM and NMSSM parameter spaces. Throughout this analysis, we fix:

$$\begin{aligned} M_{\tilde{E}_{1,2,3}} &= M_{\tilde{L}_{1,2,3}} = 250 \text{ GeV (to roughly comply with } \Delta a_\mu), \\ A_c &= A_s = A_u = A_d = A_\mu = A_e = A_t \\ m_{\tilde{g}} &= 1200 \text{ GeV.} \end{aligned} \quad (6.4)$$

While $M_{\text{SUSY}} = M_{\tilde{Q}_{1,2,3}} = M_{\tilde{U}_{1,2,3}} = M_{\tilde{D}_{1,2,3}}$ and M_2 are varied in the MSSM scan, in the NMSSM analysis they are fixed according to:

$$\begin{aligned} M_{\text{SUSY}} &= 1000 \text{ GeV,} \\ M_2 &= 400 \text{ GeV.} \end{aligned} \quad (6.5)$$

In the MSSM the tree-level Higgs sector can be specified by the two parameters M_{H^\pm} (or M_A) and $\tan\beta$. The NMSSM Higgs sector has larger freedom and requires additional input. We choose the following set of parameters to describe the NMSSM Higgs sector:

$$M_{H^\pm}, \tan\beta, \lambda, K \equiv \kappa/\lambda, A_\kappa . \quad (6.6)$$

The parameter M_{H^\pm} here in principle plays the same role as in the MSSM. However, since we employ `NMSSMTools` to calculate the Higgs masses, the input M_{H^\pm} is not defined in the on-shell renormalisation scheme, and must be understood as a tree-level input mass, which is translated into a value for A_λ using Eqs. (2.72), (2.73). The calculated physical M_{H^\pm} (including the higher order corrections) will therefore in general not be identical to the input value⁵. The parameters for which no values are given above, are chosen as input for the MSSM/NMSSM scans. In this analysis we restrict ourselves to the MSSM and NMSSM with real parameters. All complex phases are set to zero.

6.3.1 Decays of \mathcal{CP} -even Higgs bosons in the MSSM

Before we proceed to the NMSSM case, we study the two photon decays of the two \mathcal{CP} -even Higgs bosons, h and H , in the MSSM and compare to the SM.

⁵This feature would be avoided with an on-shell renormalisation of M_{H^\pm} , see e.g. [29, 217]. There are different possibilities how to relate MSSM with NMSSM parameter points. The method chosen here differs from the one used in Sect. 5.8 which implied that the value for the charged Higgs (pole) mass is identical in the MSSM and the NMSSM.

Parameter	Minimum	Maximum
M_{SUSY}	750	1500
$M_2 \simeq 2M_1$	200	500
$A_t = A_b = A_\tau$	-2400	2400
μ	200	3000
M_A	100	600
$\tan \beta$	1	60

Table 6.2: Parameter ranges for the MSSM scan. All parameters except $\tan \beta$ are given in GeV.

In order to study interesting regions of the MSSM parameter space, where differences in the diphoton channel between the MSSM and the SM can occur, we perform a random scan over the parameter ranges given in table 6.2. The remaining MSSM parameters are kept at the values specified in Eq. (7.1).

It should be noted that we allow for comparably high values for μ ; this is relevant for the possible size of some of the effects that we will discuss in detail below. However, such large values of μ , together with large values of $\tan \beta$, can lead to parameter combinations that show a non-stable behaviour in perturbation theory. In order to avoid parameter combinations that result in unacceptably large two-loop corrections in the evaluation of the Higgs boson self-energies and related quantities, we implement an upper limit on the corrections to the elements of the \mathbf{Z} matrix (see Ref. [29]). Comparing the one- and two-loop values of the respective diagonal elements, we require the following condition for the light \mathcal{CP} -even Higgs, $||Z_{11}^{2\text{-loop}}| - |Z_{11}^{1\text{-loop}}||/|Z_{11}^{1\text{-loop}}| < 0.25$, and analogously for the heavy \mathcal{CP} -even Higgs with the replacement $Z_{11} \rightarrow Z_{21}$. We found that this upper bound is effective for avoiding parameter regions that are considered unstable under higher-order corrections.

In Fig. 6.2 we show $\Gamma(h \rightarrow \gamma\gamma)$ in the top left and $\text{BR}(h \rightarrow \gamma\gamma)$ in the bottom left plot as a function of M_h . The corresponding plots for $H \rightarrow \gamma\gamma$ are given in the right column. The colour coding is as follows: all points in the scan which are allowed by the theoretical constraints and the direct search limits for sparticles [165] from LEP, as discussed above, are plotted in grey. Points which are also allowed by direct Higgs search limits (from `HiggsBounds` 3.6.1, i.e. including LHC_{2011}) are shown in blue (on top of the grey points). Finally, points which fulfil additionally the constraint from $(g-2)_\mu$ and $\text{BR}(b \rightarrow s\gamma)$ (both are here calculated with `FeynHiggs`) are plotted in black. The red (solid) curve in Fig. 6.2 shows the corresponding SM result with $M_{H^{\text{SM}}}$ set equal to the corresponding MSSM Higgs mass. It should be noted that here (and in all the following plots) different densities of points appearing in different regions have no physical meaning, as the point density is related to the specific procedure chosen for the

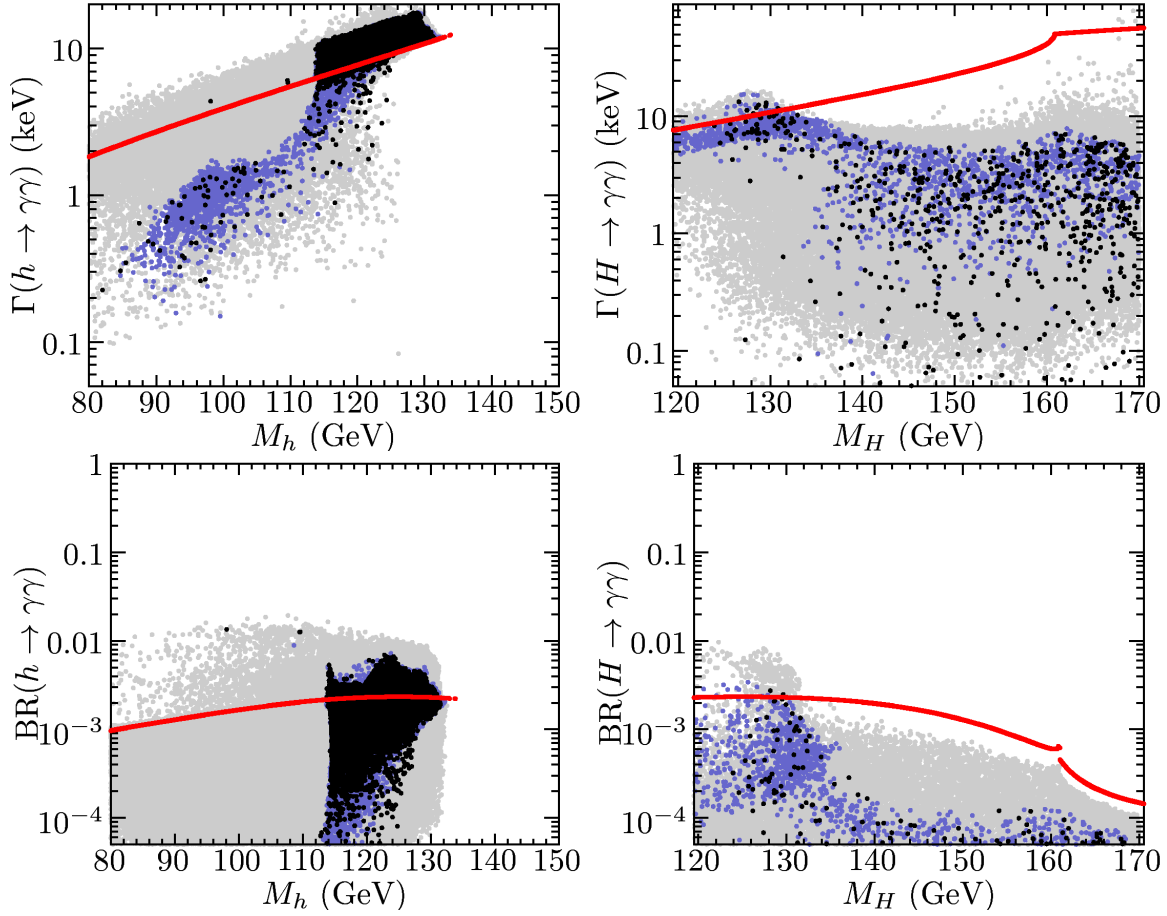


Figure 6.2: Results from the MSSM parameter scan for the partial widths $\Gamma(h, H \rightarrow \gamma\gamma)$ of h (left) and H (right), and the corresponding branching ratios. The full result of the scan (all points allowed by the theoretical constraints and the direct search limits for sparticles at LEP) is shown in grey. The blue points are compatible with the direct Higgs search limits (from `HiggsBounds` 3.6.1, i.e. including LHC_{2011}), while the black points in addition give a result in agreement with $(g-2)_\mu$ and $\text{BR}(b \rightarrow s\gamma)$. The solid (red) curve shows the respective quantities evaluated in the SM.

sampling of the SUSY parameter space.

We first focus on the light \mathcal{CP} -even Higgs boson, h , decaying into two photons. The extra particles in the MSSM yield additional loop contributions, which can both lower and raise $\Gamma(h \rightarrow \gamma\gamma)$ compared to the SM case. Below the LEP limit for a SM-like Higgs (for $M_h < 114.4$ GeV)⁶ most of the scenarios where $\Gamma(h \rightarrow \gamma\gamma) \geq \Gamma(H^{\text{SM}} \rightarrow \gamma\gamma)$ are ruled out by the direct Higgs search limits, but we also find a few allowed points in this region. For those h couples with about SM strength to gauge bosons, but is nevertheless not excluded due to a (much) suppressed coupling to b quarks, which

⁶We neglect here, and in the following plots in this chapter, the theory uncertainty of the Higgs boson mass evaluation, which for the light Higgs boson should be roughly at the level of 2–3 GeV [185].

weakens the corresponding LEP limit. In the following we focus on the mass region above the LEP limit. There we find scenarios in which $\Gamma(h \rightarrow \gamma\gamma)$ is enhanced by up to $\sim 70\%$ with respect to the SM. On the other hand, as can be seen from the lower left plot in Fig. 6.2, the $\text{BR}(h \rightarrow \gamma\gamma)$ can be enhanced by a factor ~ 3 over the SM in the same mass range (due to a suppression of the $b\bar{b}$ decay mode as discussed in more detail below). For the points that are allowed by all constraints the maximum enhancement of the branching ratio occurs around $M_h \sim 125$ GeV. For the same Higgs mass, values for $\text{BR}(h \rightarrow \gamma\gamma)$ at the SM rate or (strongly) suppressed compared to the SM are also possible.

The corresponding results for the heavy \mathcal{CP} -even MSSM Higgs boson are shown in the right column of Fig. 6.2. For $M_H \lesssim 130$ GeV we find viable points with a BR slightly larger than for a SM Higgs boson. For larger values of M_H one can see the behaviour expected from the decoupling properties of the MSSM, i.e. $\Gamma(H \rightarrow \gamma\gamma)$ and $\text{BR}(H \rightarrow \gamma\gamma)$ are both suppressed with respect to the SM, with the level of suppression increasing with M_H .

In Fig. 6.3 the results for $R_{\gamma\gamma}^h$ (left) and $R_{\gamma\gamma}^H$ (right) are shown, with the same colour coding as in Fig. 6.2. In order to make the results better visible we display them twice, on a logarithmic scale (upper row) and on a linear scale (lower row). The green curves in Fig. 6.3 show exclusion limits in the diphoton channel at 95% CL from data presented in 2011 data from ATLAS [230] (solid) and CMS [231] (dashed). The red lines are the limits from ATLAS (solid) and CMS (dashed) presented in July 2012 [1, 2] (based on $\sim 5 \text{ fb}^{-1}$ of 7 TeV data and $\sim 5 \text{ fb}^{-1}$ of 8 TeV data). The exclusion limits from ATLAS and CMS are displayed here explicitly for comparison, but only the LHC₂₀₁₁ data enters our analysis also as part of the constraints implemented in **HiggsBounds**. As explained above, **HiggsBounds** considers only the single channel with the highest *expected* sensitivity for determining 95% CL (combined) exclusion. In the considered region the expected sensitivity of the CMS search [231] happens to be slightly higher than the one from ATLAS [230], so that only the CMS limit actually has an effect in our analysis. The plot shows also some allowed points with $R_{\gamma\gamma}^h$ above the CMS 2011 exclusion curve. For these points another channel has a higher expected sensitivity, so that the $\gamma\gamma$ channel has not been selected by **HiggsBounds** for determining the 95% CL limit.

As one can see in the left column of Fig. 6.3, for $R_{\gamma\gamma}^h$ in principle a large enhancement, roughly up to a factor six, would be possible in the mass range $M_h = 114 \dots 130$ GeV (and an even stronger enhancement for lighter masses). Such large enhancements are now ruled out by the LHC searches. For the points that are allowed by all the considered constraints (which were available at the time) we find that in the region above the LEP limit for a SM-like Higgs a suppression of $R_{\gamma\gamma}^h$ by more than an order of magnitude is possible. On the other hand, a maximal enhancement of about ~ 3 times the SM value occurs for $M_h \approx 125$ GeV. Our results show that the MSSM could account for a Higgs signal around $M_h = 125$ GeV with a strength in the $\gamma\gamma$ channel of ~ 1.5 times the SM strength (compatible with the latest ATLAS measurement [19]), but also with a strength of ~ 0.8 times the SM strength (compatible with the latest CMS measurement [20]). The

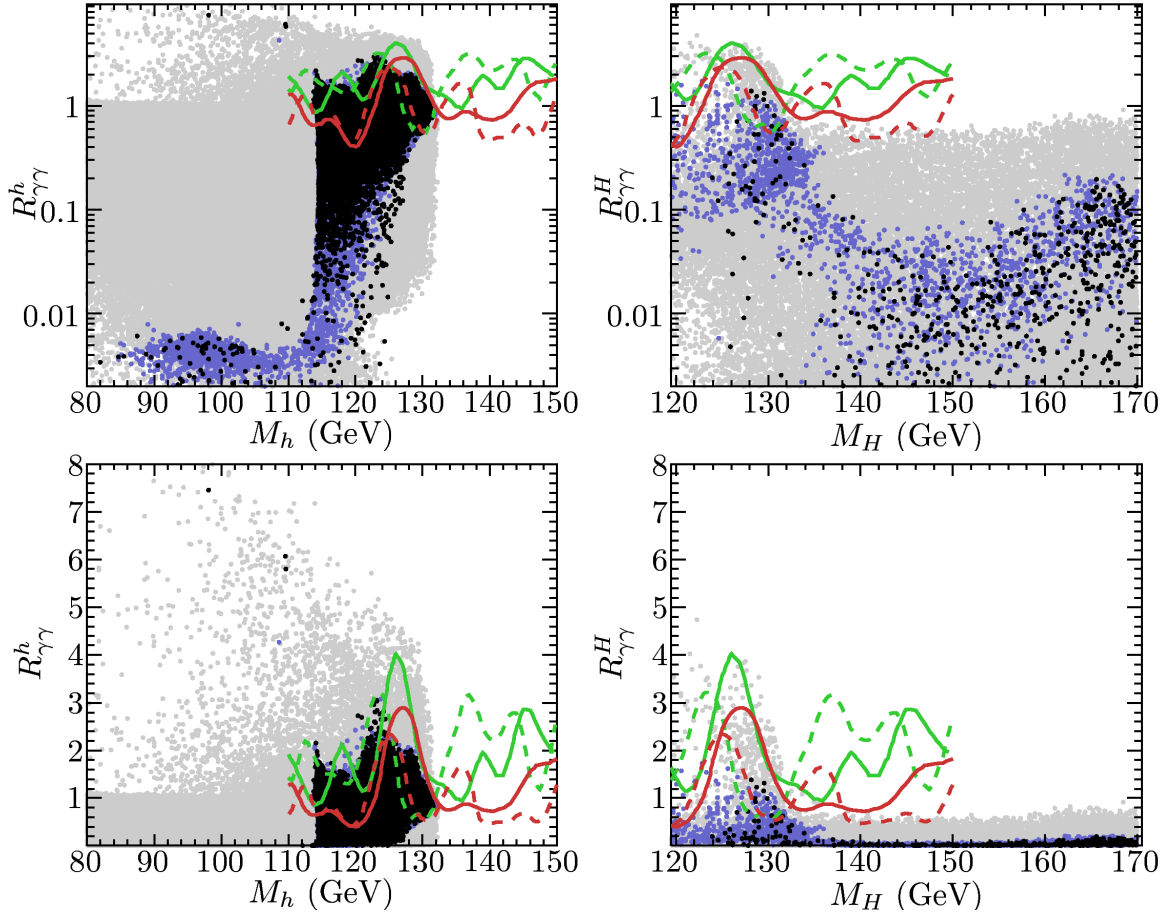


Figure 6.3: Results from the MSSM parameter scan on the ratios $R_{\gamma\gamma}^h$ for the light \mathcal{CP} -even Higgs boson h (left column) and $R_{\gamma\gamma}^H$ for the heavy \mathcal{CP} -even Higgs boson H (right column). The plots are displayed both on a logarithmic scale (upper row) and on a linear scale (lower row). The colour coding for the scan points is the same as in Fig. 6.2. The green lines are the corresponding limits from data presented in 2011 data from ATLAS [230] (solid) and from CMS [231] (dashed). The red lines are the limits from ATLAS (solid) and CMS (dashed) taken from [1, 2].

detailed origin of possible enhancements of $R_{\gamma\gamma}^h$ will be discussed below. Fig. 6.3 also shows that the possible size of the enhancement or suppression decreases for larger M_h ; for $M_h = 130$ GeV $R_{\gamma\gamma}^h$ is confined to values close to unity for the allowed points in the parameter space.

The right column of Fig. 6.3 shows the corresponding results for the heavy \mathcal{CP} -even Higgs. For $M_H \lesssim 130$ GeV the results for the heavy MSSM Higgs are qualitatively similar to the ones for the light \mathcal{CP} -even Higgs. In particular, also in this case a slight enhancement over the SM rate is possible for $M_H \approx 125$ GeV for the scan points that are in agreement with the collider constraints (the agreement with $(g-2)_\mu$ and the observables in the flavour sector could be improved by modifying some of the SUSY

parameters that do not directly influence Higgs phenomenology). Our results for $R_{\gamma\gamma}^H$ demonstrate that the discovery of a new boson in the $\gamma\gamma$ channel at a mass of about 125 GeV that was observed by ATLAS and CMS could also be interpreted within the MSSM as arising from the *heavier* \mathcal{CP} -even Higgs boson, as discussed in [48]. Such a scenario would imply that besides a possible signal at about 125 GeV there would be a lighter Higgs in the spectrum, having significantly suppressed couplings to gauge bosons. However here we want to remind the reader that this interpretation in the MSSM is meanwhile challenged by the recent ATLAS results from charged Higgs searches [55]. For $M_H \gtrsim 135$ GeV we always find $R_{\gamma\gamma}^H < 1$, in accordance with the decoupling properties of the MSSM.

The issue of a possible enhancement of $R_{\gamma\gamma}^h$ for a Higgs mass around 125 GeV has been discussed first in Refs. [208, 209], where in particular the contributions from light staus to $\text{BR}(h \rightarrow \gamma\gamma)$ and the suppression of $h \rightarrow b\bar{b}$ due to Higgs mixing effects have been emphasised. As seen above, we find that $\Gamma(h \rightarrow \gamma\gamma)$ can exceed its SM value, which is found to be an effect of the stau loop contributions. The most sizeable enhancements observed in $R_{\gamma\gamma}^h$, however, mainly arise from a suppression of the total width, which in the SM is dominated by the partial decay width into $b\bar{b}$. Suppressing the $b\bar{b}$ channel can therefore yield a significant reduction of the total MSSM width. Such a suppression can happen in two different ways. The reduced $hb\bar{b}$ coupling in the MSSM is given at tree-level by

$$\frac{g_{hb\bar{b}}}{g_{H^{\text{SM}}b\bar{b}}} = -\frac{\sin \alpha}{\cos \beta}, \quad (6.7)$$

where α is the mixing angle in the \mathcal{CP} -even Higgs sector (see Eq. (2.62)). In the decoupling limit ($M_A \gg M_Z$) the SM is recovered, i.e. $(-\sin \alpha / \cos \beta) \rightarrow 1$. Higher-order contributions from Higgs propagator corrections can approximately be included via the introduction of an effective mixing angle, corresponding to the replacement $\alpha \rightarrow \alpha_{\text{eff}}$ [232] (in our numerical analysis we treat propagator-type corrections of the external Higgs bosons in a more complete way, which is based on wave function normalisation factors that form the \mathbf{Z} matrix [29]). A suppression of the $h \rightarrow b\bar{b}$ channel thus occurs for small α_{eff} .

Genuine corrections to the $hb\bar{b}$ vertex can lead to another type of suppression. Beyond leading order, loop-induced Yukawa couplings of b quarks to the “wrong” Higgs doublet H_2 are induced. The modified $hb\bar{b}$ coupling can then be expressed as

$$\frac{g_{hb\bar{b}}}{g_{H^{\text{SM}}b\bar{b}}} = \frac{1}{1 + \Delta_b} \left(-\frac{\sin \alpha_{\text{eff}}}{\cos \beta} + \Delta_b \frac{\cos \alpha_{\text{eff}}}{\sin \beta} \right). \quad (6.8)$$

Via the quantity Δ_b [233–235] terms of $\mathcal{O}((\alpha_s \tan \beta)^n)$ and $\mathcal{O}((\alpha_t \tan \beta)^n)$ can be resummed. The most relevant contributions are given by

$$\Delta_b = \frac{2\alpha_s(m_t)}{3\pi} \tan \beta m_{\bar{g}} \mu I(m_{b_1}^2, m_{b_2}^2, m_{\bar{g}}^2) + \frac{\alpha_t(m_t)}{4\pi} \tan \beta A_t \mu I(m_{t_1}^2, m_{t_2}^2, |\mu|^2), \quad (6.9)$$

with

$$I(a, b, c) = -\frac{ab \ln(b/a) + ac \ln(a/c) + bc \ln(c/b)}{(a-c)(c-b)(b-a)}. \quad (6.10)$$

The dominant higher-order contribution to Δ_b are the QCD corrections, given in [236, 237]. Those contributions are not included in our analysis. While the loop-corrected $hb\bar{b}$ coupling, Eq. (6.8), approaches the tree-level coupling, Eq. (6.7), in the decoupling limit ($M_A \gg M_Z$), a suppression of $g_{hb\bar{b}}$ is possible for not too large M_A if Δ_b is numerically sizeable and positive.

We now turn to the alternative case where h is light and has suppressed couplings to gauge bosons, whereas the heavier \mathcal{CP} -even Higgs H is a SM-like Higgs boson. One finds a similar enhancement for $R_{\gamma\gamma}^H$, which is due to the suppression of $g_{Hb\bar{b}}$, if

$$\frac{g_{Hb\bar{b}}}{g_{H^{\text{SM}}b\bar{b}}} = \frac{\cos \alpha}{\cos \beta} \quad (6.11)$$

is small. Such an enhancement is restricted to the mass region $M_H \lesssim 130$ GeV, since for higher mass values the coupling of the heavy \mathcal{CP} -even Higgs to gauge bosons is suppressed, so that the partial width $\Gamma(H \rightarrow \gamma\gamma)$ is smaller than for the SM case, see Fig. 6.2. Accordingly, the scenarios with $R_{\gamma\gamma}^H > 1$ are only realised in a relatively small parameter region, for $M_A \lesssim 150$ GeV and intermediate $\tan \beta$. The scenario in which $R_{\gamma\gamma}^H$ is enhanced is complementary to the one giving an enhancement in $R_{\gamma\gamma}^h$ (as we checked explicitly). Consequently, a simultaneous enhancement in the diphoton channel for both \mathcal{CP} -even Higgs bosons is not possible.

A reduction of the total width, by the suppression of the $h, H \rightarrow b\bar{b}$ channel, can also affect the search for the Higgs boson in other channels. The correlation between the diphoton rate and the other decay rates (e.g. R_{bb}, R_{WW}) in the MSSM (as well as the dependence of the decay rates on the other MSSM parameters, such as A_t) is analysed in detail in chapter 7 in the context of a global fit.

6.3.2 Decays of \mathcal{CP} -even Higgs bosons in the NMSSM

We now turn to the NMSSM and analyse the diphoton decay in this model. There have been many approaches to interpret the discovered Higgs at ~ 125 GeV in the context of the NMSSM, for a recent analysis see e.g. Ref. [238], and more references can be found therein.

As before we consider the one-loop induced Higgs decay $h_{1,2} \rightarrow \gamma\gamma$, but now calculated using the NMSSM framework described in Sect. 6.2.2. We perform a scan over the NMSSM parameter space and evaluate the partial widths and branching ratios for this mode. The parameter ranges used for the scan are given in table 6.3. The remaining parameters are fixed as defined in Eq. (7.1) and Eq. (6.5). It should be noted that the ranges in table 6.3 are not meant to cover the full NMSSM parameter space. The effects discussed above that can cause an enhancement of $R_{\gamma\gamma}^{h,H}$ in the MSSM can be realised also in the context of the NMSSM. In the present analysis we are interested in genuine NMSSM effects, which go beyond the MSSM phenomenology. Such genuine NMSSM effects arise in particular from the mixing of the Higgs doublet fields with the Higgs singlet. To be specific, we consider scenarios that are characterised by large values of M_{H^\pm} , corresponding to the SM+singlet limit of the NMSSM (see Sect. 2.3).

We furthermore restrict μ_{eff} and $\tan\beta$ to relatively small values, while our MSSM scan (compare table 6.2) extended to rather large values of μ and $\tan\beta$ and focussed on the region of relatively low values of M_A . The parameters are chosen such that the mechanisms for enhancing $R_{\gamma\gamma}^{h,H}$ realised in the MSSM do not play a role, putting the emphasis on the genuine NMSSM effects.

Parameter	Minimum	Maximum	
$A_t = A_b = A_\tau$	-2 400	2 400	GeV
μ_{eff}	150	250	GeV
M_{H^\pm}	500	1 000	GeV
$\tan\beta$	2.6	6	
λ	0.5	0.7	
K	0.3	0.5	
A_κ	-100	-5	GeV

Table 6.3: Parameter ranges used for the \mathcal{CP} -even Higgs decay scan in the NMSSM.

The results for $h_{1,2} \rightarrow \gamma\gamma$ are shown in Fig. 6.4 (h_3 is always heavy and plays no role in our analysis). The colour coding is similar as in Fig. 6.2: all displayed points satisfy the theoretical constraints and the LEP mass limits on SUSY particles (grey). Points which in addition fulfil the direct Higgs exclusion limits from colliders (from `HiggsBounds` 3.6.1, i.e. including `LHC2011`) are drawn in blue, and points which satisfy all the constraints, in particular also those from Δa_μ and flavour physics (now evaluated with `NMSSMTools`), are shown in black. The red curve shows the corresponding SM result, obtained by setting $M_{H^{\text{SM}}} = m_{h_{1,2}}$, respectively.

We choose to study m_{h_1} in a range from 80 GeV up to its maximum around 135 GeV. Allowed points with $m_{h_1} < 80$ GeV are also found in the scan, but the large singlet component of these very light Higgs bosons gives rise to a quite different phenomenology, which we do not investigate in detail here. For masses close to 140 GeV, the number of allowed points is seen to decrease, which illustrates that only quite specific choices of the input parameters give m_{h_1} close to the maximum. This, as well as other features with local under- (over-) density of points in certain regions, can simply be viewed as sampling artefacts, i.e. the point density has no physical meaning. For h_2 we study the mass interval $120 \text{ GeV} < m_{h_2} < 170 \text{ GeV}$, which means there is an overlap with the region considered for m_{h_1} . To go even higher in m_{h_2} is not particularly interesting for our purposes, since when the two-body decay $h_2 \rightarrow WW^{(*)}$ is open the loop-induced $h_2 \rightarrow \gamma\gamma$ decay becomes suppressed, as is also clearly visible in the figure (and a Higgs in this mass range can of course not explain the observed signal).

Fig. 6.4 shows that $\Gamma(h_i \rightarrow \gamma\gamma)$ is always smaller than (or at most equal to) its SM value for the points in our scan. This means in particular that our scan, for which we

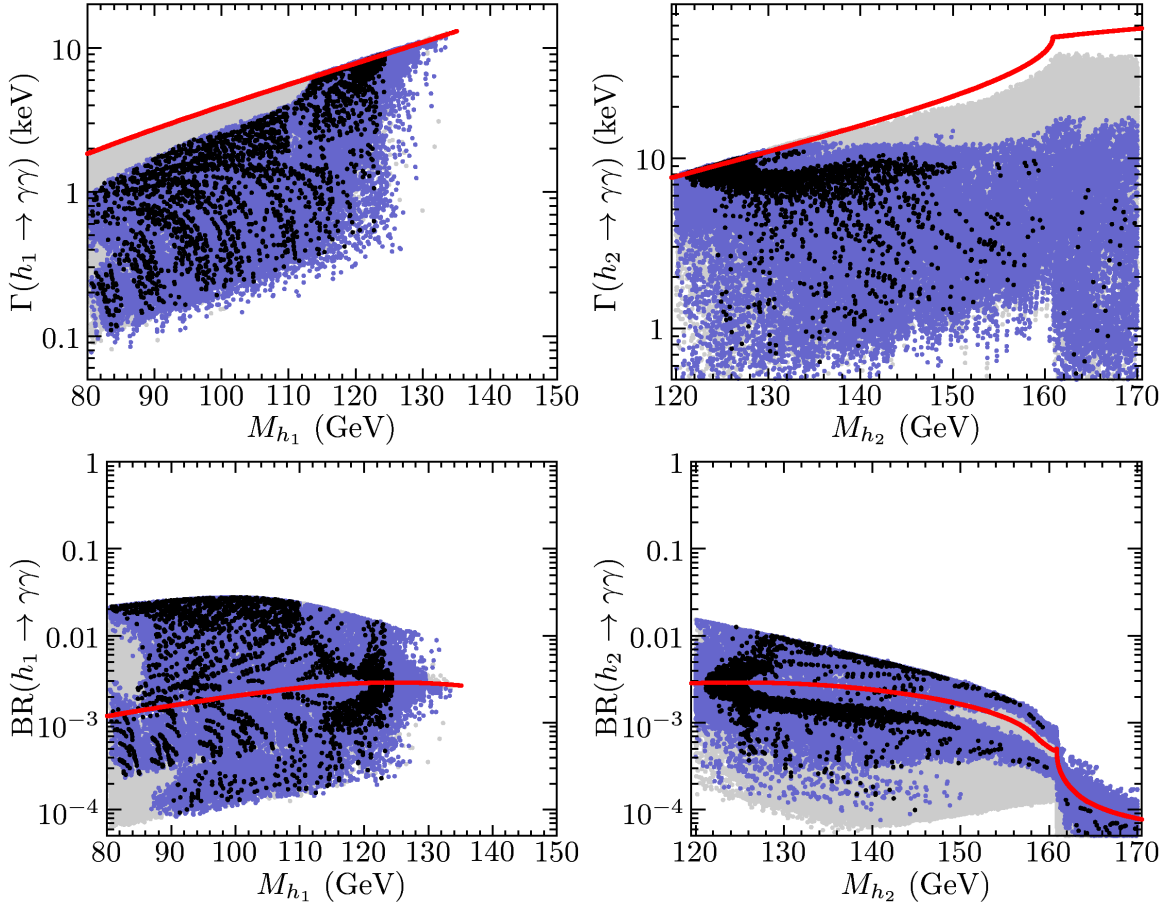


Figure 6.4: Results from the NMSSM parameter scan (see text) for the partial widths $\Gamma(h_i \rightarrow \gamma\gamma)$ and the corresponding branching ratios of h_1 (left) and h_2 (right). All points in the figure fulfil the theoretical constraints defined in Sect. 5.4.3. In addition, the blue points satisfy direct Higgs search limits from colliders (from `HiggsBounds` 3.6.1, i.e. including LHC_{2011}), while the black points are in agreement with all theoretical and experimental constraints. The solid (red) curve shows the respective quantities evaluated in the SM.

have fixed the slepton masses to large values (see Eq. (7.1)), does not contain points with light staus (the contribution of light staus was discussed in the MSSM context above). For $m_{h_2} \gtrsim 140$ GeV, the partial width does not reach the full SM value, which shows that this mass region is not accessible for a fully SM-like h_2 . Taking into account the collider constraints, we also see that, as in the MSSM, a SM-like Higgs boson with $m_{h_1} < 114.4$ GeV is excluded as a consequence of the LEP limits. Despite the smaller NMSSM width for $\Gamma(h_i \rightarrow \gamma\gamma)$ compared to the SM, Fig. 6.4 shows that an enhancement of the branching ratio with up to an order of magnitude over the SM is possible. The results are similar for h_1 and h_2 in the overlapping mass region.

As in the case of the MSSM we now analyse $R_{\gamma\gamma}^{h_i}$. The total widths appearing in

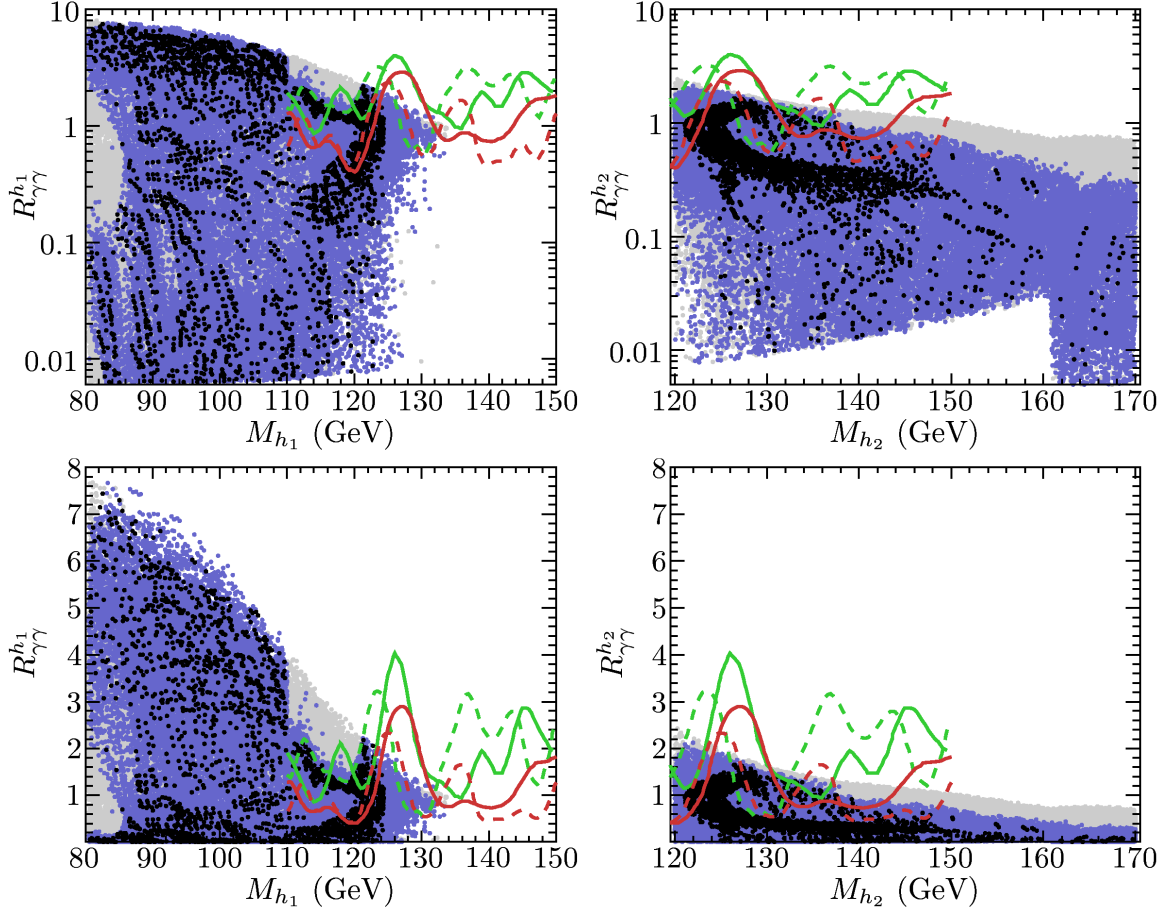


Figure 6.5: Results from the NMSSM parameter scan on the ratio $R_{\gamma\gamma}^{h_i}$ for the two lightest Higgs bosons h_1 (left column) and h_2 (right column). The plots are displayed both on a logarithmic scale (upper row) and on a linear scale (lower row). The colour coding for the scan points is the same as in Fig. 6.4. The green lines show exclusion limits on this channel at 95% CL from LHC₂₀₁₁ data from ATLAS [230] (solid) and from CMS [231] (dashed). The red lines are the new limits from ATLAS (solid) and CMS (dashed) taken from [1, 2].

Eq. (6.2) are calculated in an approximate way according to

$$\Gamma_{\text{tot}}(h_i) = \frac{1}{m_{h_i}} \text{Im} \left[\Sigma_{h_i}(m_{h_i}^2) \right] + \Gamma(h_i \rightarrow WW^{(*)}) + \Gamma(h_i \rightarrow \gamma\gamma) + \Gamma(h_i \rightarrow gg), \quad (6.12)$$

where $\Sigma_{h_i h_i}$ denotes the one loop self energy of h_i . The inclusion of the off-shell decays, as well as the loop-induced processes, in the total width is essential for a realistic prediction.

The results for $R_{\gamma\gamma}^{h_1}$ and $R_{\gamma\gamma}^{h_2}$ from the scan over the NMSSM parameter space are shown in Fig. 6.5. As before, we show the plots both on a logarithmic and a linear scale. Looking first at h_1 , the figure shows that a sizeable enhancement over the SM rate is possible over the whole mass range from $m_{h_1} = 80$ GeV to $m_{h_1} = 130$ GeV. For the range of Higgs masses below the SM limit, $m_{h_1} < 114.4$ GeV, points with a

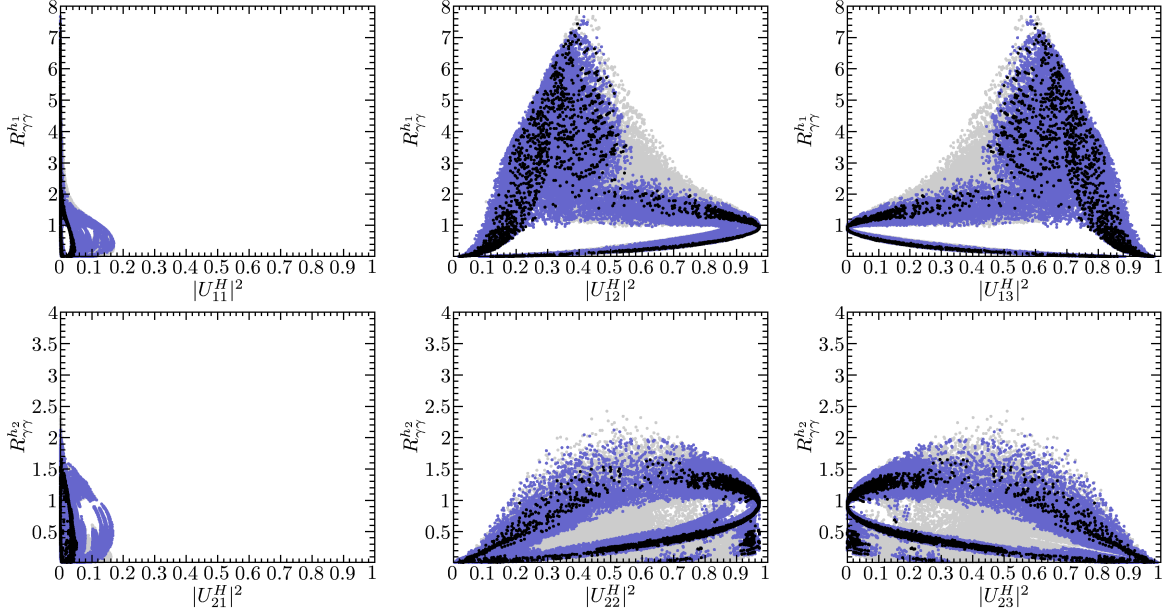


Figure 6.6: Results from the NMSSM parameter scan on $R_{\gamma\gamma}^{h_i}$ and the elements U_{ij}^H of the \mathcal{CP} -even Higgs mixing matrix for h_1 (top) and h_2 (bottom). The colour coding is the same as in Fig. 6.4.

significant enhancement $R_{\gamma\gamma}^{h_1} \gtrsim 7$ are observed, in accordance with the results of [239] (see also [240]).

Turning to h_2 , the results for $R_{\gamma\gamma}^{h_2}$ are similar to those for $R_{\gamma\gamma}^{h_1}$ in the common mass range; the observed maximal enhancement is $R_{\gamma\gamma}^{h_2} \gtrsim 2$ for m_{h_2} in the range from 120 GeV to 125 GeV. A smaller enhancement over the SM is possible for all $m_{h_2} < 145$ GeV. As m_{h_2} approaches 160 GeV, where the on-shell decay $h_2 \rightarrow WW^{(*)}$ opens, the rate drops to $R_{\gamma\gamma}^{h_2} < 1$.

It is clearly visible that the NMSSM (similarly to the MSSM) can also produce points with a large suppression of $R_{\gamma\gamma}$. Concerning the case $R_{\gamma\gamma}^{h_i} > 1$, we see that the NMSSM can produce an enhancement compatible with an excess over the SM rate, as seen by ATLAS, either for h_1 or h_2 in the mass region around 125 GeV.

In order to identify the conditions under which a significant NMSSM enhancement of $R_{\gamma\gamma}^{h_i}$ is possible — as explained above, this is a genuine NMSSM effect that goes beyond the mechanisms discussed above for the MSSM — we show in Fig. 6.6 the dependence of $R_{\gamma\gamma}^{h_i}$ on the composition of h_i as defined in Eq. (2.70). Fig. 6.6 shows that an important requirement for $R_{\gamma\gamma}^{h_i} > 1$ is that $U_{i1}^H \simeq 0$, which means that the corresponding Higgs mass eigenstate lacks a H_1 component. In the limit $U_{i1}^H \rightarrow 0$ (corresponding to $\alpha_{\text{eff}} \rightarrow 0$ in the MSSM) the otherwise dominant decay channels $h_i \rightarrow b\bar{b}$ and $h_i \rightarrow \tau\tau$ vanish, thereby increasing $\text{BR}(h_i \rightarrow \gamma\gamma)$. Since U^H is unitary, the general sum rule

$$\sum_j |U_{ij}^H|^2 = 1 \quad (6.13)$$

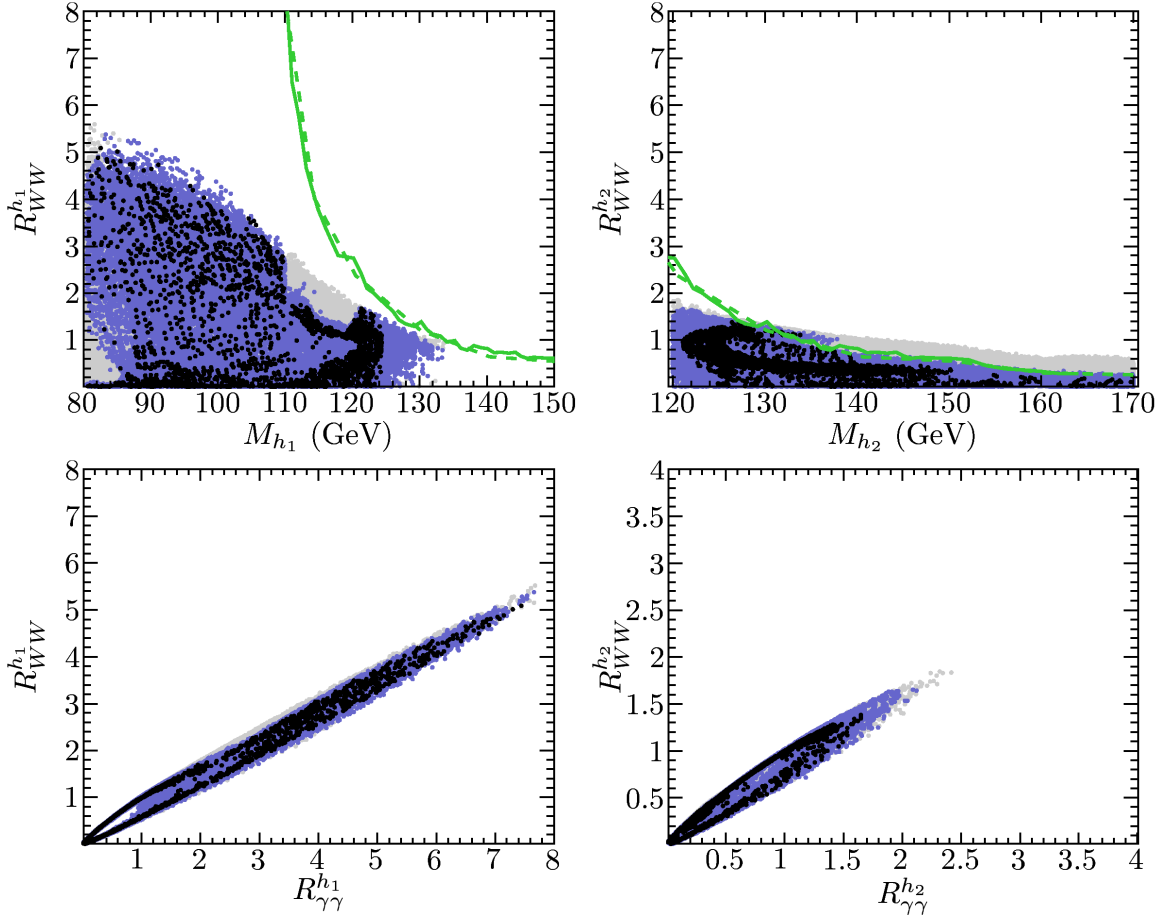


Figure 6.7: Results from the NMSSM parameter scan on the ratios $R_{WW}^{h_i}$ ($i = 1, 2$) for the NMSSM Higgs bosons h_1 (left column) and h_2 (right column). The plots in the upper row show $R_{WW}^{h_i}$ as a function of the respective Higgs mass. The 95% CL exclusion limits for the $WW^{(*)}$ channel from LHC₂₀₁₁ data from ATLAS [241] (solid line) and CMS [242] (dashed line) are also shown. The plots in the lower row show the correlation of $R_{WW}^{h_i}$ and $R_{\gamma\gamma}^{h_i}$. The colour coding is the same as in Fig. 6.4.

implies that points with $U_{i1}^H = 0$ must have $|U_{i2}^H|^2 + |U_{i3}^H|^2 = 1$. From Fig. 6.6 it can be seen that a configuration that maximises $R_{\gamma\gamma}^{h_i}$ would be

$$|U_{i1}^H|^2 = 0, \quad |U_{i2}^H|^2 \simeq 0.4, \quad |U_{i3}^H|^2 \simeq 0.6 .$$

Unlike the case of Higgs doublet mixing resulting in a small α_{eff} in the MSSM (which requires a low value for M_A and a high μ), in the NMSSM the enhancement of $R_{\gamma\gamma}^{h_i}$ is caused by a sizeable singlet component of h_i . The observed $R_{\gamma\gamma}^{h_i}$ enhancement is therefore a genuine feature of the NMSSM which is still present even in the SM+singlet limit. On the other hand, in the MSSM limit (where $|U_{i3}^H|^2 = 0$) points from our scan show only very small $R_{\gamma\gamma}^{h_i}$ enhancements. This is a consequence of the fact that we have restricted our scan in the NMSSM to large M_{H^\pm} , large slepton and squark masses, as well as to

relatively small values of $\tan \beta$ and μ_{eff} , which corresponds to a parameter region in the MSSM that is complementary to the one used for our MSSM scan.

In the NMSSM the decay $h_i \rightarrow \gamma\gamma$ is usually dominated by contributions from loops containing W bosons (the same is true in the MSSM), and we expect a corresponding correlation of $R_{\gamma\gamma}^{h_i}$ with the (off-shell) decays $h_i \rightarrow WW^{(*)}$ and $h_i \rightarrow ZZ^{(*)}$. This is studied in Fig. 6.7, where we give results for the tree-level decays $h_{1,2} \rightarrow WW^{(*)}$ using the same colour coding as above. As expected, a sizeable enhancement is possible for $R_{WW}^{h_i}$, in particular for h_1 , and a strong positive correlation between $R_{WW}^{h_i}$ and $R_{\gamma\gamma}^{h_i}$ is visible. The possibility of a simultaneous enhancement of these two modes can again be understood as an effect of the large suppression of the main fermionic coupling $h_i b\bar{b}$, which leads to an enhancement of the respective branching ratios. Despite the positive correlation between $R_{WW}^{h_i}$ and $R_{\gamma\gamma}^{h_i}$ it is nevertheless possible to have both a slight enhancement of $R_{\gamma\gamma}^{h_i}$ and a slight suppression of $R_{WW}^{h_i}$.

6.4 Summary

In this chapter we have presented an analysis, comparing the predictions for Higgs boson production in gluon fusion, the main production channel at the LHC, and its subsequent decay into two photons in the SM, the MSSM, and the NMSSM. In the context of the NMSSM we have furthermore analysed the $WW^{(*)}$ channel, which is strongly correlated with the $\gamma\gamma$ mode.

While for the predictions in the SM and the MSSM we have used the well-known code `FeynHiggs`, for the predictions in the NMSSM we have used a framework consisting in particular of an appropriate model file for the program `FeynArts`. In this thesis we described the framework already in chapter 5, however it was originally developed first for the analysis of loop-induced decays in the NMSSM, presented in this chapter.

We have presented results for Higgs-boson production in gluon fusion and its decays into $\gamma\gamma$ (and $WW^{(*)}$)⁷ within the MSSM and the NMSSM, normalised to the SM prediction. We have analysed in detail possible mechanisms for the enhancement (but also the suppression) of those channels in both models. In this context we have investigated in particular whether an enhancement of the $\gamma\gamma$ rate for a Higgs mass of about 125 GeV is compatible with limits on the parameter space arising from theoretical constraints as well as from the limits from direct searches for supersymmetric particles, from the Higgs searches at LEP, the Tevatron and the LHC (based on the data presented in 2011), from electroweak precision observables and from flavour physics (which existed at the time this analysis was conducted). Performing parameter scans in both models, we have then confronted the points passing all the above constraints with the results of the Higgs searches in the $\gamma\gamma$ channel that have been announced by ATLAS and CMS in July 2012, leading to the announcement of the discovery of a ‘‘Higgs-like’’ boson. We have found that an enhanced rate of Higgs production and decay to two photons can easily be realised in the MSSM as well as in the NMSSM. At the same time both models also permit a rate at the SM level or below. This holds not only for the lightest \mathcal{CP} -even Higgs boson in the models, but also for the second lightest \mathcal{CP} -even Higgs boson in both the MSSM and the NMSSM. In this latter interpretation in both models the lightest \mathcal{CP} -even Higgs boson possesses a strongly suppressed coupling to gauge bosons and escapes all existing direct searches.

Within the MSSM we have analysed the mechanisms that can lead to an enhanced $\gamma\gamma$ rate in comparison to the SM prediction. Besides the presence of light scalar taus, in particular a suppression of the $b\bar{b}$ decay mode results in an enhanced $\gamma\gamma$ rate. This suppression can either be caused by Higgs-boson propagator corrections entering the effective mixing angle, or by the so-called Δ_b corrections.

Within the NMSSM the above mentioned mechanisms can naturally be realised, and we focused on *additional* mechanisms that are *genuine* for the NMSSM. We found that in particular the doublet-singlet mixing can result in a substantial suppression of the $b\bar{b}$ mode, resulting again in an enhancement in the $\gamma\gamma$ rate with respect to the SM

⁷In this chapter we presented results for $WW^{(*)}$ only in the NMSSM. In the next chapter we will show results for $WW^{(*)}$ also in the MSSM.

prediction.

In the data analysed by July 2012 both LHC experiments saw an enhancement of the diphoton channel compared to the SM. Including more data, the signal strength in the $\gamma\gamma$ channel observed by ATLAS [19] remains above the value expected in the SM, while the signal strength observed by CMS [20] is currently slightly below the SM level. It remains exciting to see how this (slight) discrepancy will be resolved with more data and whether a deviation from the SM will be established, which could point towards physics beyond the SM.

Chapter 7

Fitting the MSSM to the observed Higgs signal

In this chapter we present a study performed in 2012, which was published in Ref. [49], as well as an updated version of this study. I made significant contributions to all results presented in this chapter. I participated in developing and testing the framework for the original (2012) analysis: I set up the first version of the scan code and implemented the experimental Higgs rate measurements. I was involved in analysing the data and in producing the figures. The computer code used for the updated analysis was not written by me, but I analysed the data and produced the (updated) results shown in this chapter. The plots in Figs. 7.1, 7.2 and 7.3 have been obtained from my collaborators.

7.1 Motivation

In the previous chapter we discussed that the interpretation of the new state as the light \mathcal{CP} -even Higgs boson of the MSSM is a viable possibility (called the “light Higgs case” in the following), but that also the interpretation as the heavy \mathcal{CP} -even Higgs boson (called the “heavy Higgs case”) is in principle possible. As discussed above the latter interpretation is challenged by the latest ATLAS charged Higgs search limit (which was not available at the time the analysis for the heavy Higgs case was performed).

The question arises whether the MSSM (or another model beyond the SM) can give a prediction of the production cross sections and decay rates of the observed Higgs boson that yields a better description of the data than the one provided by the SM. The main aim of this work is to investigate whether, and if so by how much, the MSSM can improve the theoretical description of the experimental data, and potentially which parts of the parameter space of the MSSM are favoured by the experimental data in the various Higgs search channels.

Because of the large number of free parameters, the MSSM Higgs search results at LEP [243], the Tevatron [244,245] and the LHC [55,69,70,246–251] have been interpreted in certain benchmark scenarios [54,252–254] (of which the m_h^{\max} scenario has been most widely used). However, in order to investigate potentially favoured regions in the MSSM

parameter space a scan over the relevant SUSY parameters has to be performed. A complete scan over the in principle more than a hundred free parameters of the MSSM parameter space is technically unfeasible. One therefore needs to focus on a certain subset of parameters. Very ambitious scans for the pMSSM with 19 free parameters (pMSSM–19, see [255] for details) have been performed [53, 256]. However, on the one hand it is difficult to sample such a multi-dimensional parameter space sufficiently densely, on the other hand it is well known that several of the parameters of the pMSSM–19 hardly affect Higgs phenomenology. We therefore focus in this paper on a smaller set of parameters, namely the pMSSM with the seven free parameters that we regard as most relevant for the phenomenology of Higgs and flavour physics (pMSSM–7, see below for details on these parameters). This 7-dimensional parameter space, which as we will demonstrate captures most of the allowed Higgs phenomenology of the MSSM, can be sampled quite well with $\mathcal{O}(10^7)$ scan points.

In our analysis we perform fits in the MSSM both for the interpretation of the LHC signal in terms of the light and the heavy \mathcal{CP} -even Higgs of the MSSM and we compare the fit results with the SM case. In the original analysis conducted at the end of 2012, we took into account the results of the Higgs rate measurements in the individual search channels and the Higgs mass measurements from ATLAS and CMS at 7 and 8 TeV centre-of-mass energy that were publicly available at that time. In this thesis we also present an update for the light Higgs case which includes the latest ATLAS and CMS results relevant for our analysis (incorporating the results which were public by February 2014), including in particular some analyses using the full 2012 data set. We furthermore included the Higgs rate measurements of the Tevatron. The updated fit is performed using the code `HiggsSignals` [257]. Besides the Higgs signal strengths and mass measurements, we included the most relevant set of low-energy observables, $\text{BR}(b \rightarrow s\gamma)$, $\text{BR}(B_s \rightarrow \mu^+\mu^-)$, $\text{BR}(B_u \rightarrow \tau\nu_\tau)$, $(g-2)_\mu$ and the mass of the W boson, M_W , in our fit and we apply constraints from Higgs searches and limits on the SUSY particle masses.

7.2 Framework for our analysis

In this section, each subsection is divided into two parts: First we describe our original analysis (done in 2012) and in the second part we shortly comment on the updated analysis. In the latter part we focus on changes in the new analysis compared to the original one. It is understood that everything which is not explicitly mentioned in the description of the update is unchanged with respect to the original analysis.

7.2.1 pMSSM parameter scans

Original 2012 analysis: pMSSM–7scan

As a first and general simplification we restrict ourselves to the MSSM with real parameters. We choose to only vary the parameters most relevant for the Higgs phenomenology. The tree-level values for the predictions of the MSSM Higgs sector quantities are determined by $\tan\beta$ and the \mathcal{CP} -odd Higgs-boson mass M_A . Consequently, we choose these two parameters as free parameters. Beyond tree-level, the main correction to the Higgs boson masses stems from the t/\tilde{t} sector, and for large values of $\tan\beta$ also from the b/\tilde{b} sector. In the sfermion sector we choose to vary $M_{\tilde{q}_3} \equiv M_{\tilde{Q}_3} = M_{\tilde{U}_3} = M_{\tilde{D}_3}$, $M_{\tilde{l}_3} \equiv M_{\tilde{E}_3} = M_{\tilde{L}_3}$ and $A_f \equiv A_t = A_b = A_\tau$. We also take the higgsino mass parameter μ (entering also in the off-diagonal elements of the sfermion mass matrix) as a free scan parameter. As final scan parameter the gaugino mass parameter M_2 is chosen.

The pMSSM–7 parameter space is sampled by performing random scans (using uniform distributions) over the seven input parameters in the ranges given in table 7.1. The two cases where either h or H corresponds to the observed signal are treated in two separate scans, and the results are discussed in parallel below. Each scan starts with $\mathcal{O}(10^7)$ randomly chosen points with a flat distribution over the parameter ranges. Dedicated, smaller, sampling is then performed to map the interesting regions of parameter space¹. In practice, the full parameter ranges from table 7.1 are taken only for the light Higgs case, while for the heavy Higgs case we limit $M_A < 200$ GeV and $\tan\beta < 30$ (still using the full ranges for the other parameters), which improves the sampling efficiency in the relevant mass region for M_H . Additionally the top quark pole mass is sampled from a Gaussian distribution with $m_t = 173.2 \pm 0.9$ GeV, using a cutoff at $\pm 2\sigma$.

The other MSSM parameters are fixed according to

$$\begin{aligned}
 M_{\tilde{E}_{1,2}} &= M_{\tilde{L}_{1,2}} = 300 \text{ GeV} \\
 M_{\tilde{Q}_{1,2}} &= M_{\tilde{U}_{1,2}} = M_{\tilde{D}_{1,2}} = 1000 \text{ GeV} \\
 A_c &= A_s = A_u = A_d = A_\mu = A_e = A_f \\
 m_{\tilde{g}} &= 1000 \text{ GeV}.
 \end{aligned}
 \tag{7.1}$$

The choices for the first and second generation squarks and the gluino place their masses roughly at the level currently probed at the LHC. Somewhat larger values would only

¹The reader should keep in mind here (and in the following) that the point density has no statistical meaning.

Parameter	Minimum	Maximum
M_A [GeV]	90	1000
$\tan \beta$	1	60
μ [GeV]	200	3000
$M_{\tilde{q}_3}$ [GeV]	200	1500
$M_{\tilde{l}_3}$ [GeV]	200	1500
A_f [GeV]	$-3 M_{\tilde{q}_3}$	$3 M_{\tilde{q}_3}$
M_2 [GeV]	200	500

Table 7.1: Ranges used for the free parameters in the pMSSM-7 scan.

have a minor impact on our analysis. The values for the first and second generation slepton mass parameters were chosen to provide rough agreement with the anomalous magnetic moment of the muon.

For the evaluation of the sparticle and Higgs masses we use the code `FeynHiggs` (version 2.9.4) [29, 185–187]. The residual Higgs mass uncertainty from this calculation (i.e. from missing higher order corrections) is assumed to be around 2–3 GeV, depending on the considered region of parameter space [185]. We are interested in parameter points that give a Higgs mass prediction, for either M_h or M_H , close to the observed LHC signal. We therefore constrain the analysis in a first step to points with M_h or M_H in the region 121 – 129 GeV. In order to avoid configurations in parameter space that give an unstable perturbative behavior in the Higgs mass calculation, we use a criterion (which was introduced and motivated in Sect. 6.3.1) based on the \mathbf{Z} -matrix (as defined in [29]) and exclude points for which $||Z_{k1}^{2L}| - |Z_{k1}^{1L}|| / |Z_{k1}^{1L}| > 0.1$. Here $k = 1$ (2) is set for a SM-like light (heavy) Higgs. This criterion is similar (even slightly stricter) than the one we applied in Sect. 6.3.1.

Updated analysis

An updated analysis is presented for the light Higgs case only. In this analysis, we choose

$$\begin{aligned}
 M_{\tilde{E}_{1,2}} &= M_{\tilde{L}_{1,2}} = M_{\tilde{l}_3} \\
 M_{\tilde{Q}_{1,2}} &= M_{\tilde{U}_{1,2}} = M_{\tilde{D}_{1,2}} = 1500 \text{ GeV} \\
 m_{\tilde{g}} &= 1500 \text{ GeV}.
 \end{aligned}$$

Setting the soft masses for the sleptons of the first two generations equal to $M_{\tilde{l}_3}$ (which we scan over) instead of fixing it to 300 GeV is particularly relevant for the fit of the anomalous magnetic moment of the muon, as we will discuss later. The masses of the squarks of the first and second generation and the gluon are set to 1500 GeV to be in

better agreement with the current LHC limits. We perform a scan (starting with 5×10^6 randomly generated points) over the same 7 pMSSM parameters, as in our original work. The scan range for μ was extended to 100 – 4000 GeV, keeping the other scan ranges as in table 7.1. We select scan points for which the lightest \mathcal{CP} -even Higgs falls in the mass range $M_{h_1} = 125.7 \pm 3$ GeV.

7.2.2 Constraints on the parameter space

Original 2012 analysis

We apply the essentially model-independent limits on sfermion and chargino masses, typically at the level of ~ 100 GeV from direct searches at LEP (as summarised in the PDG review [165]). Furthermore, we require that the lightest supersymmetric particle (LSP) is the lightest neutralino. The exclusion limits from Higgs searches at LEP, the Tevatron, and the LHC (which were published before July 2012) are taken into account using `HiggsBounds` version 3.8.0 [195, 196]. It should be noted, that this `HiggsBounds` version tests, for each parameter point, the model predictions only against the *single* channel with the highest expected sensitivity for an exclusion.

Updated analysis

For the updated analysis we use `HiggsBounds` version 4.2.0beta, which is not publicly available yet². This `HiggsBounds` version (as the one described in Sect. 5.4.3) performs the exclusion test separately for each Higgs boson in the model. All relevant LHC Higgs analyses (available up to February 2014) are included in this `HiggsBounds` version, in particular the limits from the MSSM Higgs searches presented in Ref. [55] (ATLAS search for charged Higgs bosons) and Ref. [248] (CMS search for neutral Higgs bosons decaying into τ pairs). For the light Higgs case the latter one is particularly important. A theoretical uncertainty of 3 GeV on the Higgs mass calculation is included when determining the `HiggsBounds` exclusion.

7.2.3 χ^2 fits

Original 2012 analysis

In order to investigate how well (compared to the SM) the MSSM can describe the observed data and to obtain an indication of what the favoured regions of the MSSM parameter space are, we use a simple statistical treatment of the data where the different observables are taken into account by calculating, for every parameter point in the scan, a global χ^2 function

$$\chi^2 = \sum_{i=1}^{n_{\text{LHC}}} \frac{(\mu_i - \hat{\mu}_i)^2}{\sigma_i^2} + \sum_{i=1}^{n_{\text{Tev}}} \frac{(\mu_i - \hat{\mu}_i)^2}{\sigma_i^2} + \frac{(M_{h,H} - \hat{M}_H)^2}{\sigma_{\hat{M}_H}^2} + \sum_{i=1}^{n_{\text{LEO}}} \frac{(O_i - \hat{O}_i)^2}{\sigma_i^2}. \quad (7.2)$$

²This `HiggsBounds` version contains besides the results in the last publicly available version (version 4.1.0) the CMS result from the search for neutral Higgs bosons decaying into τ pairs [248].

Quantities with a hat denote experimental measurements, and unhatted quantities the corresponding model predictions for the Higgs signal strength modifiers, μ_i , the Higgs mass $M_{(h,H)}$ and the low-energy observables (LEO), O_i . The different observables entering Eq. (7.2) are described in more detail below. The combined uncertainties σ_i contain the known theory and experimental uncertainties. Correlations are neglected here, since they were for most cases not publicly available. The total number of degrees of freedom, ν , is counted in the naive way as $\nu = n_{\text{obs}} - n_{\text{para}}$, where $n_{\text{obs}} = n_{\text{LHC}} + n_{\text{Tev}} + 1 + n_{\text{LEO}}$ (for LHC, Tevatron, the Higgs boson mass, and low-energy observables); n_{para} is the number of model parameters. In the SM we have $n_{\text{para}} = 1$ (the Higgs mass), and for both MSSM analyses $n_{\text{para}} = 7$. In the following part, we will go through the terms of Eq. (7.2) and describe which values enter the χ^2 formula.

The measured signal strength modifiers provide the main dataset to which we fit the MSSM Higgs sector. In total we include 37 observables, where $n_{\text{LHC}} = 34$ are from the LHC experiments and $n_{\text{Tev}} = 3$ provide supplementary information from the Tevatron³. The best fit signal strength modifiers of ATLAS and CMS are given for different Higgs masses, corresponding to the values measured by the individual experiments, i.e. we interpret the experimental discoveries by ATLAS and CMS as being compatible, and due to a single new state. The Tevatron data, which does not admit a mass measurement from the observed excess on its own, is evaluated for $\hat{M}_H = 125$ GeV. All values are extracted directly from the quoted experimental references, with one exception: ATLAS has not provided a measurement for the signal strength modifier of $H \rightarrow ZZ^{(*)}$ separately for the 7 and 8 TeV data, but only for the combination (the 7 TeV values are available from a previous analysis). In order to compare to our 8 TeV predictions, these values are therefore calculated from the 7 TeV and 7 + 8 TeV data under the assumption of independent Gaussian measurements, following the procedure outlined in [258]. This should lead to an uncertainty on the estimated 8 TeV rate of the same order as the overall uncertainty from neglecting the (unknown) correlations.

The MSSM predictions for the signal strength modifiers are evaluated according to

$$\mu_i = \frac{\sum_k \omega_{ik} \sigma_k(pp \rightarrow h, H) \times \text{BR}(h, H \rightarrow i)}{\sum_k \omega_{ik} \sigma_k^{\text{SM}}(pp \rightarrow h, H) \times \text{BR}^{\text{SM}}(h, H \rightarrow i)}, \quad (7.3)$$

where $\sigma_k(pp \rightarrow h, H)$ denotes the contribution to the Higgs production cross section from partonic subprocess k , evaluated at the predicted Higgs mass. The production modes considered are gluon-gluon fusion (gg), vector boson fusion (VBF), associated vector boson production (Vh, VH), and associated $t\bar{t}h(H)$ production (see Sect. 4.2.1). The experimental efficiencies ω_{ik} have only been published by ATLAS and CMS for the $\gamma\gamma$ analysis; by CMS in the case of the subcategories, and by ATLAS for the inclusive result. We make use of these numbers when they are available. For all other channels we have to use the “naive” efficiencies deducible from the analysis description (e.g. for a VBF-type analysis tagging two forward jets, we set $\omega = 1$ for the VBF cross section,

³The measured rates, which are taken into account, can be seen in Fig. 7.1 and Fig. 7.3 where we present the results, see discussion below.

whereas all other modes have $\omega = 0$). In channels where the mass resolution is not good enough to separate contributions from different Higgs bosons, we approximate the contributions from H and the \mathcal{CP} -odd Higgs A by adding their signal rates. We do not add the rates of the \mathcal{CP} -even Higgs bosons, whose joint contributions to the signal could include interference effects. Our analysis is therefore limited to the case with a single \mathcal{CP} -even Higgs boson close to the observed signal. Since the \mathcal{CP} -odd Higgs does not have tree-level couplings to vector bosons (and hence also a reduced coupling to photons), it gives a negligible contribution to the channels with vector bosons in the Higgs production and/or decay. Effectively, the \mathcal{CP} -odd Higgs therefore only plays a role for the inclusive (0/1 jet) $\tau^+\tau^-$ channels. In these channels it can easily dominate over the H contribution for large values of $\tan\beta$. In the light Higgs case, we find that the masses of h and A differ by $M_A - M_h \gtrsim 50$ GeV in the favoured region (see below). Thus we do not take any contributions to the h rates from the \mathcal{CP} -odd Higgs into account.

The cross section predictions entering Eq. (7.3) are calculated, both in the MSSM and the SM, using `FeynHiggs` (version 2.9.4). In `FeynHiggs`, the results of the LHC Higgs cross section working group for the SM cross sections are implemented [259–261] (where the gg production cross sections are taken from [262]). The corresponding MSSM production cross-sections are obtained in the effective-coupling approximation [263]. The gg production cross section follows the description in [264], where results of [265–268] were used. The decay width evaluation includes a full one-loop correction for the decay to fermions [192, 269]; see [264] for more details on the other channels.

In addition to the signal strength modifiers, we include a χ^2 contribution from the measured Higgs mass \hat{M}_H . Averaging the ATLAS and CMS mass measurements (at that time), we obtain $\hat{M}_H = 125.7$ GeV. We use a $\sigma_{\hat{M}_H} = 3$ GeV total uncertainty, which accounts for both the theoretical uncertainties from missing higher orders and for the experimental uncertainty.

In addition to the measurements related to the LHC Higgs signal, we include $n_{\text{LEO}} = 5$ low-energy observables (LEO) in the fit. These are listed in table 7.2, which summarises the experimental values⁴ and the corresponding SM theory predictions (evaluated for $M_H^{\text{SM}} = 125.7$ GeV and $m_t = 173.2$ GeV). The flavour physics observables are evaluated (both in the SM and the MSSM) using `SuperIso` (version 3.2) [272–274], which in particular contains the results for $\text{BR}(B \rightarrow X_s \gamma)$ based on the NNLO calculation of [275]. Our fit includes also the anomalous magnetic moment of the muon, $a_\mu = \frac{1}{2}(g - 2)_\mu$. We use `SuperIso` to calculate the MSSM contribution δa_μ to the anomalous magnetic moment of the muon including the dominant two-loop contributions [220–222] (we have

⁴We note that the Belle Collaboration has reported a new (lower) measurement of $\text{BR}(B_u \rightarrow \tau \nu_\tau)$ that is in better agreement with the SM (and also with models with two Higgs doublets, like the MSSM) [270]. While we do not take this new result into account in our overall fit results, in the following we do comment briefly on its possible effects. The measurement of $\text{BR}(B_s \rightarrow \mu^- \mu^+)$ [115, 116] became public shortly after this analysis was conducted. Therefore here only an upper limit on $\text{BR}(B_s \rightarrow \mu^+ \mu^-)$ is included. Both of these results are included in the updated analysis. We do not include the BaBar result on $\bar{B} \rightarrow D^{(*)} \tau^- \bar{\nu}_\tau$ [271], which shows (combining the D and $D^{(*)}$ measurements) a 3.4σ deviation from the SM prediction, which can not be explained in the MSSM either.

Observable	Experimental value	SM value
$\text{BR}(B \rightarrow X_s \gamma)$	$(3.43 \pm 0.21 \pm 0.07) \times 10^{-4}$ [223]	$(3.08 \pm 0.22) \times 10^{-4}$
$\text{BR}(B_s \rightarrow \mu^+ \mu^-)$	$< 4.2 \times 10^{-9}$ [276]	$(3.55 \pm 0.38) \times 10^{-9}$
$\text{BR}(B_u \rightarrow \tau \nu_\tau)$	$(1.66 \pm 0.33) \times 10^{-4}$ [223]	$(1.01 \pm 0.29) \times 10^{-4}$
δa_μ	$(30.2 \pm 9.0) \times 10^{-10}$ [117, 118, 277]	–
M_W	(80.385 ± 0.015) GeV [76, 100]	(80.363 ± 0.004) GeV

Table 7.2: Original 2012 analysis: The experimental values and (SM) theory predictions for low-energy observables (LEO) used to constrain the MSSM parameter space.

cross-checked those results with `FeynHiggs` and found good agreement). As a final observable we include the MSSM prediction for the W boson mass into the fit. As we saw in Sect. 5.6, the SM prediction shows a $\sim 1.5\sigma$ deviation from the latest experimental value. Here our MSSM evaluation of M_W is done using `FeynHiggs`, where the full SM result [143] is supplemented with the leading corrections from the \tilde{t}/\tilde{b} sector [157, 158, 164]. We did not yet have the `Fortran` code for the M_W calculation, presented in chapter 5, available at the time this fit was performed⁵. A comparison with the best available MSSM evaluation [35] shows that corrections > 10 MeV can be missed if some uncoloured SUSY particles are light⁶. We assign a theory uncertainty of 15 MeV to our M_W evaluation and conservatively combine it with the experimental uncertainty linearly. Thus in total we take an uncertainty of ± 30 MeV into account.

Updated analysis

A major change compared to the original analysis arises from the fact that we use the code `HiggsSignals` version 1.2.0 [257] for the calculation of the χ^2 contribution from the Higgs signal strength modifiers in the various decay channels and the Higgs mass, $\chi_{\text{HS}}^2 = \chi_\mu^2 + \chi_{M_H}^2$. The quantity χ_μ^2 is calculated as described in Ref. [257], taking correlated systematic uncertainties into account. Including also the low-energy observables, we calculated the total χ^2 as

$$\chi^2 = \chi_{\text{HS}}^2 + \sum_{i=1}^{n_{\text{LEO}}} \frac{(O_i - \hat{O}_i)^2}{\sigma_i^2}. \quad (7.4)$$

⁵The `Mathematica` code is too slow to be included in a scan with $\mathcal{O}(10^7)$ points.

⁶The contributions from light sleptons can even be significantly larger (up to ~ 60 MeV) when all sleptons have masses just above the LEP limit as we have shown in chapter 5, which requires $M_{\tilde{E}} = M_{\tilde{L}} \sim 100$ GeV together with a small mixing in the slepton sector (the mixing has to be quite small to keep m_{τ_1} above the LEP limit). Such parameter points are not present here, since we choose $M_{\tilde{I}_3} > 200$ GeV and $M_{\tilde{E}_{1,2}} = M_{\tilde{L}_{1,2}} = 300$ GeV ($M_{\tilde{E}_{1,2}} = M_{\tilde{L}_{1,2}} = M_{\tilde{I}_3}$) in the original (updated) analysis. A similar argument holds for the chargino/neutralino contributions, since we choose $M_2 > 200$ GeV.

Observable	Experimental value	SM value
$\text{BR}(B \rightarrow X_s \gamma)$	$(3.43 \pm 0.21 \pm 0.07) \times 10^{-4}$ [223]	$(3.08 \pm 0.22) \times 10^{-4}$
$\text{BR}(B_s \rightarrow \mu^+ \mu^-)$	$(2.9 \pm 0.7) \times 10^{-9}$ [116]	$(3.87 \pm 0.5) \times 10^{-9}$
$\text{BR}(B_u \rightarrow \tau \nu_\tau)$	$(1.14 \pm 0.22) \times 10^{-4}$ [279]	$(0.80 \pm 0.12) \times 10^{-4}$
δa_μ	$(30.2 \pm 9.0) \times 10^{-10}$ [117, 118, 277]	–
M_W	(80.385 ± 0.015) GeV [76, 100]	(80.361 ± 0.004) GeV

Table 7.3: Updated analysis: The experimental values and (SM) theory predictions for low-energy observables (LEO).

In our update the signal strength modifiers from $n_{\text{LHC}} + n_{\text{Tev}} = 80$ Higgs decay channels are included, out of which 9 are from Tevatron and 71 from the LHC⁷. Additionally we include $n_{M_H} = 4$ Higgs mass measurements from ATLAS and CMS. The theory predictions for the μ_i are obtained with `HiggsSignals` (using `FeynHiggs` input) taking efficiencies into account when they are available. For more information on the χ^2 calculation in `HiggsSignals` and the included experimental data, we refer to [257, 278].

The same flavour observables are included as in the original analysis. Updated SM values for B physics observables are calculated in `SuperIso-3.3` for $M_{H\text{SM}} = 125.7$ GeV and $m_t = 173.2$ GeV and are summarised together with the experimental measurements in table 7.3⁸. In the updated analysis the measurement of $\text{BR}(B_s \rightarrow \mu^+ \mu^-)$ by CMS and LHCb [116] is included. Further we use an updated value for $\text{BR}(B_u \rightarrow \tau \nu_\tau)$, including the latest Belle result [270].

⁷The measured rates, which are taken into account, can be seen in Fig. 7.2 where we present the results, which will be discussed below.

⁸The SM M_W value is slightly different from the one in table 7.2, due to small changes in the input values for SM parameters. We set the SM parameters here to the `FeynHiggs` default values. While here the M_W prediction in the MSSM is obtained from `FeynHiggs`, we plan to use the `Fortran` code presented in chapter 5 in a future update of this analysis.

	LHC only			LHC+Tev		
	χ^2/ν	χ_ν^2	p	χ^2/ν	χ_ν^2	p
SM	27.6/34	0.81	0.77	31.0/37	0.84	0.74
h	23.3/28	0.83	0.72	26.8/31	0.86	0.68
H	26.0/28	0.93	0.57	33.1/31	1.07	0.37

	LHC+LEO			LHC+Tev+LEO		
	χ^2/ν	χ_ν^2	p	χ^2/ν	χ_ν^2	p
...	41.6/39	1.07	0.36	45.3/42	1.08	0.34
...	26.7/33	0.81	0.77	30.4/36	0.84	0.73
...	35.5/33	1.08	0.35	42.4/36	1.18	0.21

Table 7.4: Original 2012 analysis: Global χ^2 results with ν degrees of freedom from the fits of the SM and the MSSM with either h or H as the LHC signal, the reduced $\chi_\nu^2 \equiv \chi^2/\nu$, and the corresponding p -values. The number of degrees of freedom are evaluated naively as $\nu = n_{\text{obs}} - n_{\text{param}}$.

	LHC+Tev			LHC+Tev+LEO		
	χ^2/ν	χ_ν^2	p	χ^2/ν	χ_ν^2	p
SM	87.5/83	1.05	0.35	102.8/88	1.17	0.17
h	84.3/77	1.09	0.27	87.2/82	1.06	0.33

Table 7.5: Updated analysis: Global χ^2 results with ν degrees of freedom from the fits of the SM and the MSSM light Higgs case, the reduced $\chi_\nu^2 \equiv \chi^2/\nu$, and the corresponding p -values.

7.3 Results

In this section we will describe the results from the original analysis and the update for the light Higgs case in parallel. We will typically start our discussions by showing results for the light Higgs case of the original 2012 analysis, then we present the corresponding results of the updated analysis, before turning to the heavy Higgs case (again of the original analysis⁹).

In table 7.4 we present the results of our fits (original 2012 analysis) in terms of total

⁹We did not update the analysis for the heavy Higgs case yet.

χ^2 values (with ν degrees of freedom), the reduced $\chi^2_\nu \equiv \chi^2/\nu$, and the corresponding p -values¹⁰. Since ν is derived via the naive counting, the *absolute* numbers of the p -values should not be over-interpreted; the *relative* numbers, however, give a good impression of the *relative* goodness of the fits. For the SM and each MSSM interpretation (the cases of either h or H as the observed signal) we present four different fits: one taking the complete dataset (LHC+Tevatron+LEO) into account, one where the low-energy observables (LEO) are left out, one where the Tevatron data are left out, and finally the fit where only LHC observables are considered. When the fit is performed using only the high-energy collider data, both with and without the Tevatron results, the obtained χ^2 values of the best fit points are quite similar between the SM and the two MSSM interpretations, where the fit in the heavy Higgs case becomes slightly worse after the inclusion of the Tevatron data. When low energy observables are included, the SM and the heavy Higgs case fits become somewhat worse. In the latter case this can be understood from the potentially larger contributions of light Higgs bosons to B -physics observables. For the SM fit the reason lies in the fact that the SM prediction for $(g-2)_\mu$ differs by more than 3σ from the experimental value. Still we find that the SM provides a good fit to the full dataset, with $p_{\text{SM}} = 0.34$. On the other hand, concerning the MSSM it should be kept in mind that we did not fit the second generation slepton masses, which could potentially further improve the a_μ fit. For the complete fit, the corresponding p -values in the MSSM cases are $p_h = 0.73$ ($p_H = 0.21$) for the h (H) interpretations, respectively, which are both acceptable p -values. Thus for the light Higgs case the MSSM gives a slightly better fit to the Higgs and low-energy data than the SM.

Now we turn to the discussion of the fit results of the updated analysis, which are summarised in table 7.5. We show the results this time only for two separate cases: once using the full data set (LHC+Tevatron+LEO) and once leaving out low-energy data (LHC+Tevatron). Generally we find that after the inclusion of the additional LHC Higgs data (and the new B physics measurements), the fit quality is somewhat lower both in the SM and in the MSSM (light Higgs case) compared to our previous results. For the fit using only the collider data, we find that (as before) the χ^2 values of the MSSM best fit point (with h interpretation of the Higgs signal) is very similar to the SM value. Both the SM and the MSSM provide quite a good fit to the data with $p_{\text{SM}} = 0.35$ and $p_h = 0.27$. It is not surprising that also in the updated analysis the SM fit gets worse when the low-energy data is included. The largest χ^2 contribution comes from the $(g-2)_\mu$ deviation, which is unchanged compared to the original analysis. In the MSSM, the p -value increases slightly when low-energy data is included, it is $p_h = 0.33$ for the full fit of our updated analysis. Overall, the data at this point shows no clear preference for the MSSM over the SM (or the other way round). While the MSSM fit for the light Higgs case yields a lower total χ^2 value than the SM, this comes at the expense

¹⁰The p -value provides information about the goodness of a fit, by quantifying the discrepancy between the observed data and what one would expect from a certain hypothesis (e.g. a certain model: SM, MSSM light Higgs case, ...). To be more precise it gives the probability that a test statistic is in equal or worse agreement with the expectation from the hypothesis than the actual data. Thus large p -values show a good agreement of the expectation from the hypothesis with the data, whereas small p -values correspond to a poor agreement. More details can be found e.g. in the ‘‘Statistics’’ review in Ref. [165]

of additional parameters, so that the difference in the p -value is rather moderate.

Channel	\sqrt{s} [TeV]	μ_h	χ_h^2	Pull	μ_H	χ_H^2	Pull	
ATLAS	$b\bar{b}$	7	0.98	0.05	0.22	0.83	0.02	0.15
ATLAS	$\tau\tau$	7	0.98	0.11	0.33	2.46	1.67	1.29
ATLAS	WW	7	0.99	0.69	0.83	1.25	1.50	1.22
ATLAS	WW	8	0.99	2.31	-1.52	1.25	1.19	-1.09
ATLAS	$\gamma\gamma$	7	1.41	0.95	-0.98	1.10	1.94	-1.39
ATLAS	$\gamma\gamma$	8	1.42	0.18	-0.43	1.10	0.87	-0.93
ATLAS	ZZ	7	0.99	0.02	-0.13	1.25	0.02	0.16
ATLAS	ZZ	8	0.99	0.01	-0.09	1.25	0.09	0.31
CMS	$b\bar{b}$ (VH)	7	0.98	0.10	0.32	0.83	0.04	0.19
CMS	$b\bar{b}$ (VH)	8	0.98	0.25	0.50	0.83	0.13	0.36
CMS	$b\bar{b}$ (ttH)	7	0.98	0.72	0.85	0.83	0.61	0.78
CMS	$\tau\tau$ (0/1 jets)	7	0.97	0.00	-0.02	2.72	1.43	1.20
CMS	$\tau\tau$ (0/1 jets)	8	0.97	0.57	-0.76	2.81	0.20	0.44
CMS	$\tau\tau$ (VBF)	7	1.04	4.12	2.03	0.61	2.92	1.71
CMS	$\tau\tau$ (VBF)	8	1.04	4.24	2.06	0.61	3.03	1.74
CMS	$\tau\tau$ (VH)	7	1.04	0.01	0.09	0.61	0.00	-0.02
CMS	$\gamma\gamma$ (Dijet loose)	8	1.45	1.04	1.02	1.15	0.76	0.87
CMS	$\gamma\gamma$ (Dijet tight)	8	1.48	0.01	0.12	1.19	0.00	-0.06
CMS	$\gamma\gamma$ (Untagged 0)	8	1.44	0.00	-0.02	1.13	0.07	-0.26
CMS	$\gamma\gamma$ (Untagged 1)	8	1.42	0.01	-0.09	1.10	0.16	-0.39
CMS	$\gamma\gamma$ (Untagged 2)	8	1.41	0.18	0.42	1.09	0.02	0.14
CMS	$\gamma\gamma$ (Untagged 3)	8	1.41	1.80	-1.34	1.09	2.32	-1.52
CMS	$\gamma\gamma$ (Dijet)	7	1.48	1.80	-1.34	1.19	2.21	-1.49
CMS	$\gamma\gamma$ (Untagged 0)	7	1.44	0.89	-0.94	1.14	1.24	-1.11
CMS	$\gamma\gamma$ (Untagged 1)	7	1.41	0.65	0.81	1.10	0.23	0.48
CMS	$\gamma\gamma$ (Untagged 2)	7	1.41	0.35	0.59	1.09	0.10	0.32
CMS	$\gamma\gamma$ (Untagged 3)	7	1.41	0.01	-0.07	1.09	0.07	-0.27
CMS	WW (0/1 jets)	7	0.98	0.40	0.64	1.23	1.09	1.04
CMS	WW (0/1 jets)	8	0.98	0.05	0.22	1.23	0.36	0.60
CMS	WW (VBF)	7	1.05	1.12	1.06	1.39	1.47	1.21
CMS	WW (VBF)	8	1.05	0.03	-0.17	1.39	0.00	0.01
CMS	WW (VH)	7	1.05	1.50	1.22	1.39	1.78	1.33
CMS	ZZ	7	0.99	0.21	0.45	1.25	0.69	0.83
CMS	ZZ	8	0.99	0.08	0.28	1.25	0.43	0.65
LHC	Higgs mass [GeV]		126.1	0.02	0.13	125.8	0.00	0.03
Tevatron	$b\bar{b}$	1.96	0.98	2.13	-1.46	0.83	2.82	-1.68
Tevatron	$\gamma\gamma$	1.96	1.24	0.88	-0.94	0.97	1.08	-1.04
Tevatron	WW	1.96	0.87	0.24	0.49	1.11	0.49	0.70
LEO	$\text{BR}(B \rightarrow X_s \gamma) \times 10^4$		3.41	0.00	-0.03	4.38	2.12	1.46
LEO	$\text{BR}(B_s \rightarrow \mu^+ \mu^-) \times 10^9$		2.79	0.00	0.00	2.24	0.00	0.00
LEO	$\text{BR}(B_u \rightarrow \tau \nu_\tau) \times 10^4$		0.98	2.37	-1.54	0.80	3.78	-1.94
LEO	$\delta a_\mu \times 10^9$		2.58	0.24	-0.49	1.34	3.48	-1.87
LEO	M_W [GeV]		80.379	0.04	-0.19	80.383	0.00	-0.05

Table 7.6: Original 2012 analysis: Best fit results (for the complete fit) with corresponding χ^2 contributions and pulls for each observable.

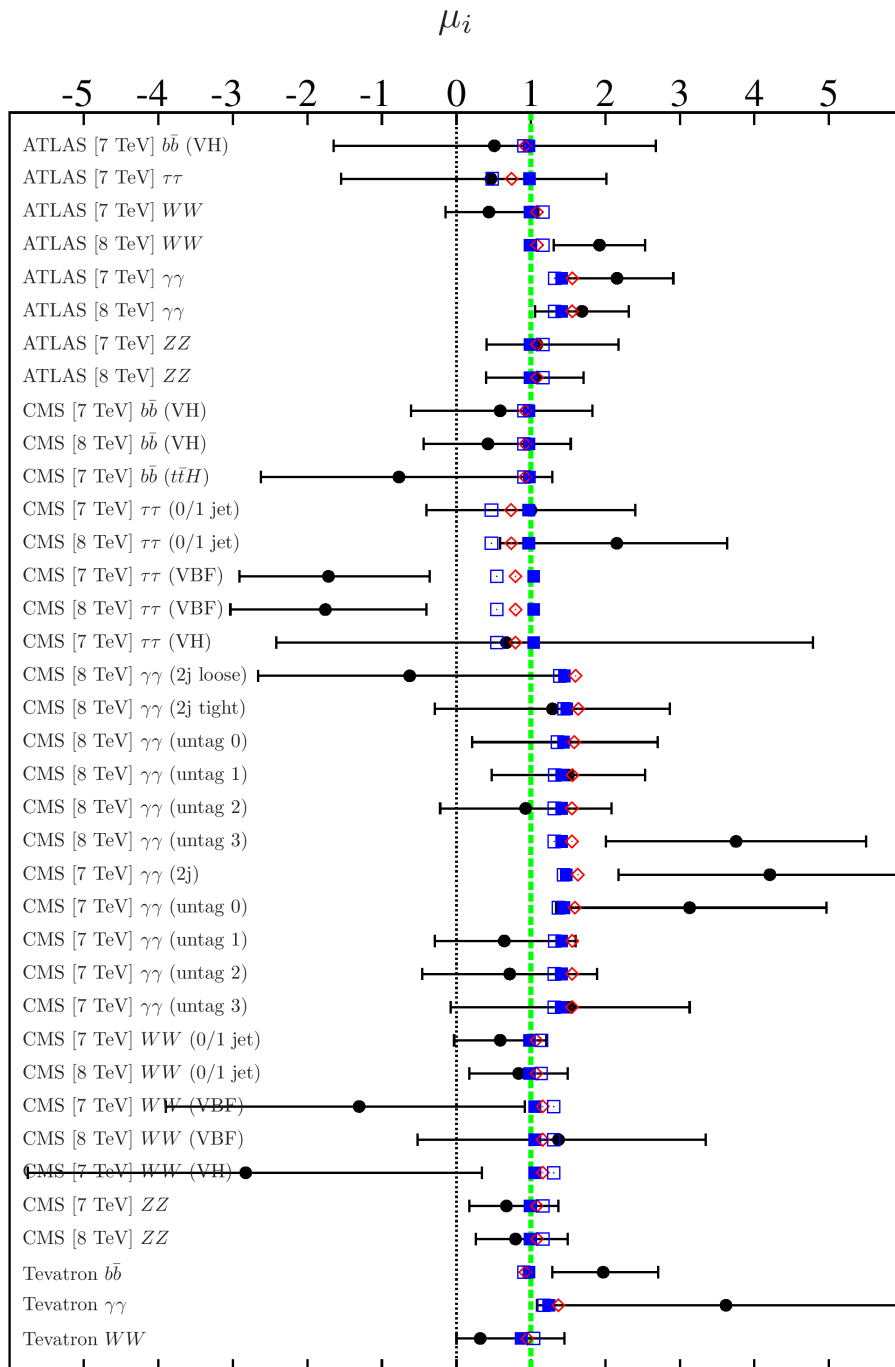


Figure 7.1: Original 2012 analysis: Fit results for the signal strength modifiers, μ_i , in the case that the light \mathcal{CP} -even Higgs is interpreted as the new boson discovered at the LHC (light Higgs case). The experimental data is shown as black dots (with error bars). The other symbols show best fit points, corresponding to the full fit (LHC+Tevatron+LEO) (blue solid squares), without the Tevatron data (blue open squares), and without LEO (red diamonds).

LEO	O_i	χ_h^2	Pull
$\text{BR}(B \rightarrow X_s \gamma) \times 10^4$	3.55	0.03	0.18
$\text{BR}(B_s \rightarrow \mu^+ \mu^-) \times 10^9$	3.66	0.77	0.88
$\text{BR}(B_u \rightarrow \tau \nu_\tau) \times 10^4$	0.78	2.00	-1.41
$\delta a_\mu \times 10^9$	2.76	0.09	-0.29
M_W [GeV]	80.382	0.01	-0.10

Table 7.7: Updated analysis: Best fit results (for the complete fit) with corresponding χ^2 contributions and pulls for the low energy observables.

Starting with the best fit for the h case, we show in Fig. 7.1 the different best fit points using all available data (LHC, Tevatron, LEO) (blue solid squares), leaving out LEO (red diamonds) or leaving out the Tevatron data (blue open squares). The comparison of these three different types of results allows to trace the origin of possible trends in the fitted parameters. The experimental data on the signal strength modifiers in the different channels (as indicated in the figure) is shown as black dots, with the error bars corresponding to $\pm 1 \sigma$ uncertainties on $\hat{\mu}$. The values for the best fit point of the complete fit (LHC, Tevatron, LEO) are also presented in tabular form in table 7.6. From here we can determine some characteristics of the best fit point, such as an enhanced rate in the $\gamma\gamma$ final state and nearly SM rates for the other channels. Leaving out the Tevatron data a (small) suppression of the fermionic final states can be observed. The fitted rates demonstrate that the pMSSM-7 is able to accommodate the main trends in the LHC/Tevatron data. However large deviations from the SM predictions can not be explained in the MSSM (see discussion in Sect. 4.2.2). Comparing the best fit points with/without LEO, we find a qualitatively very similar behaviour. In table 7.6 we also give the details on the results for the low-energy observables¹¹. In the light Higgs case, the only relevant contribution to the total χ^2 comes from $\text{BR}(B_u \rightarrow \tau \nu_\tau)$. The best-fit value of $\text{BR}(B_s \rightarrow \mu^+ \mu^-)$ lies somewhat below the SM prediction. This feature is indeed found for most of our favoured region. We have checked that this trend is present already without taking the χ^2 contribution of $\text{BR}(B_s \rightarrow \mu^+ \mu^-)$ itself into account, see also the discussion in [280]. Interestingly, the best-fit value for $\text{BR}(B_s \rightarrow \mu^+ \mu^-)$ is in very good agreement with the recent LHC measurement [115, 116] (which was not included in the fit of the original analysis).

The results for the best fit point of the updated analysis are shown in Fig. 7.2. The black dots with error bars display the measurements for the signal strength modifiers in the 80 channels which are included in `HiggsSignals` version 1.2.0. The corresponding predictions of the MSSM best-fit point of the full fit (including LHC, Tevatron and low-energy data) are shown as red, solid squares. One can see that the predictions of the MSSM best-fit point for the signal strength modifiers are ~ 1 (the SM value) for all decay channels, apart from the $\gamma\gamma$ channel. The rate in the $\gamma\gamma$ decay channel is enhanced by $\sim 20\%$. As we will discuss in more detail below, light staus (leading to an enhanced $\gamma\gamma$

¹¹The pull values are defined as (predicted value - observed value)/(uncertainty).

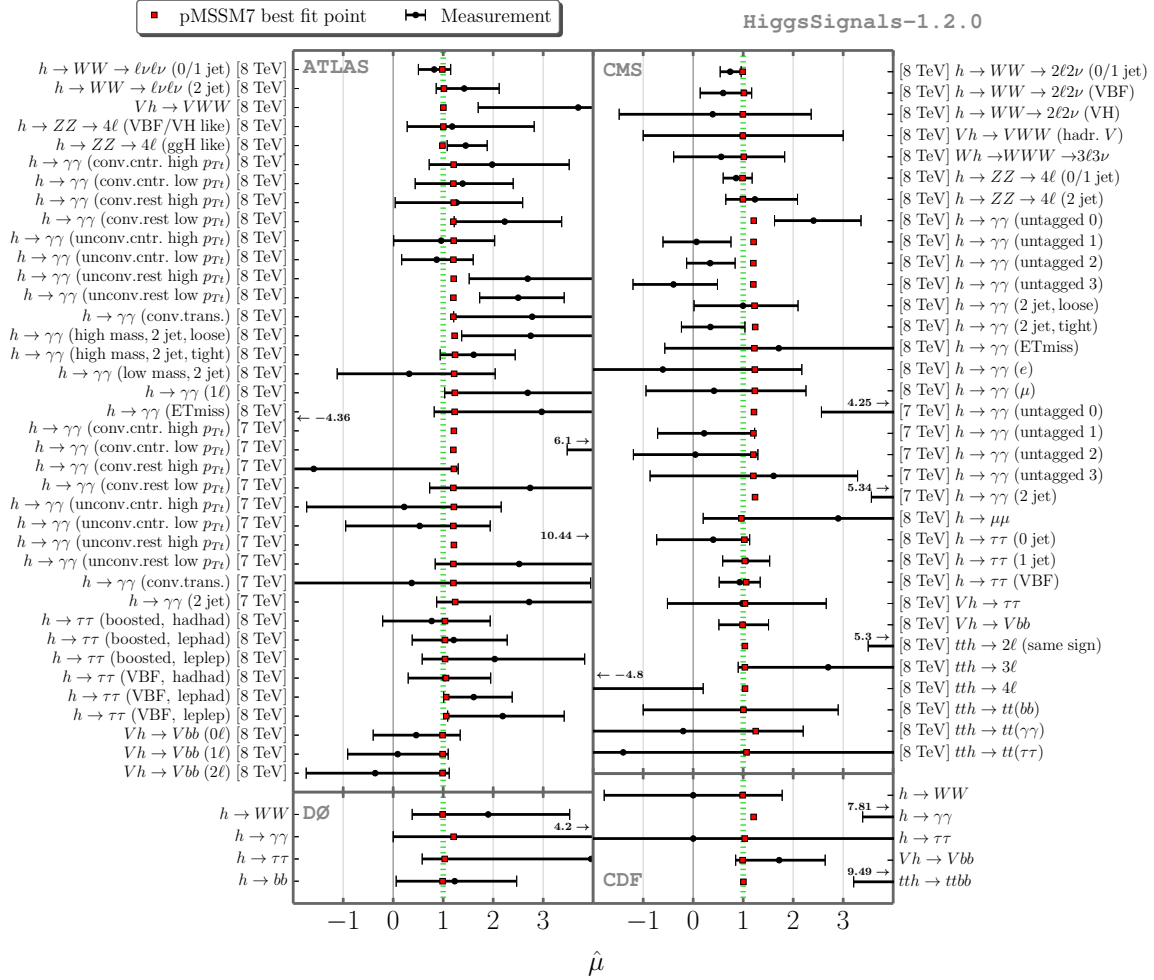


Figure 7.2: Updated analysis: Fit results of the updated analysis for the signal strength modifiers, μ_i , in the light Higgs case. The experimental data is shown as black dots (with error bars). The red solid squares indicate the best fit point of the full fit (LHC+Tevatron+LEO).

rate) are (indirectly) favoured by the $(g-2)_\mu$ measurement (which favours light selectrons and smuons), since lepton mass universality is assumed in the updated analysis. We checked that also the best-fit point of the fit taking collider data only (without low-energy observables) shows a slightly enhanced $\gamma\gamma$ rate (by $\sim 10\%$). Table 7.7 shows the predictions of the best-fit point for the low-energy observables and the corresponding χ^2 contributions. After the inclusion of the Belle result [270] the χ^2 contribution of $\text{BR}(B_u \rightarrow \tau\nu_\tau)$ is slightly reduced (even though the MSSM prediction is even lower than in the original analysis), however it still accounts for the largest χ^2 contribution out of the low-energy observables. Using *just* the Belle result ($0.96 \pm 0.26 \times 10^{-4}$) instead of the world average would substantially reduce the χ^2 contribution and lead to a better MSSM fit. Including the measurement for $\text{BR}(B_s \rightarrow \mu^+\mu^-)$, instead of just an upper limit, gives

a non-vanishing χ^2 contribution. Further we find that setting $M_{\tilde{E}_{1,2}} = M_{\tilde{L}_{1,2}} = M_{\tilde{l}_3}$ leads to an improved prediction for $(g-2)_\mu$. The total χ^2 contribution from all low-energy observables remains at roughly the same value as in the original 2012 analysis.

The best fit points for the heavy Higgs case are presented in Fig. 7.3 (numerical values in table 7.6). As the figure shows, essentially the same best fit point (albeit with different total χ^2 values) is obtained for the different cases with/without LEO. The rates we find in the heavy Higgs case are similar to the ones in the light Higgs case. Leaving out the Tevatron data, however, has a larger qualitative impact on the results, and the best-fit point in this case has rates close to zero in the $b\bar{b}$ channel. In table 7.6 we also give the results for the low-energy observables in the heavy Higgs case. One can see that the relatively small value of the Higgs mass scale in this case leads to non-negligible χ^2 contributions from $\text{BR}(B \rightarrow X_s \gamma)$ and $\text{BR}(B_u \rightarrow \tau \nu_\tau)$, where the latter would substantially improve for a value close to the new Belle result. Also the SUSY contribution to a_μ turns out to be relatively small, giving a sizeable contribution to the total χ^2 (which is however affected by our choice in the original fit to keep the slepton mass parameters fixed). Concerning $\text{BR}(B_s \rightarrow \mu^+ \mu^-)$ it should be noted that, as in the light Higgs case, the preferred value is below the SM result, which again holds for most of the favoured region.

We now turn from the global fit properties and the best fit points to a more detailed analysis of the scan results. From here on we will always consider the complete fit, including LHC, Tevatron and LEO data. Starting again with the original analysis, Fig. 7.4 shows distributions of $\Delta\chi_h^2 = \chi_h^2 - \chi_{h,\min}^2$ (light Higgs case) for the different signal rates. The colour coding is as follows: all points analysed in the scan (which pass theoretical consistency checks and have one \mathcal{CP} -even Higgs boson in the interval around the observed signal) are shown in grey. The blue points in addition fulfil constraints at 95% CL from direct Higgs searches applied by `HiggsBounds` version 3.8.0. The signal rates are calculated as the inclusive Higgs production cross section (evaluated at $\sqrt{s} = 8$ TeV) times the decay rate, normalised to the SM predictions

$$R_X^{h,H} = \frac{\sum_i \sigma_i(pp \rightarrow h, H) \times \text{BR}(h, H \rightarrow X)}{\sum_i \sigma_i^{\text{SM}}(pp \rightarrow h, H) \times \text{BR}^{\text{SM}}(h, H \rightarrow X)}. \quad (7.5)$$

The only final state for which we consider a different observable than the fully inclusive Higgs production is $b\bar{b}$, where the sum is only taken over the cross sections for $(h, H)Z$ and $(h, H)W^\pm$ associated production. As described above, for the inclusive $\tau^+\tau^-$ channels we consider the contribution of both H and A when these are close in mass. To make it clear when this is the case, we denote the joint (inclusive) rate as $R_{\tau\tau}^{H/A}$. We also define a common rate for vector boson final states $R_{VV} \equiv R_{WW} = R_{ZZ}$. We do not include the experimental efficiencies for the $\gamma\gamma$ channel in Eq. (7.5), since the efficiencies are different for the two experiments. These are however used for the different predictions entering the fit (as described above). Investigating the best fit rates in some more detail, we find in the original analysis

$$R_{VV}^h = 0.99_{-0.02}^{+0.22}, \quad R_{\gamma\gamma}^h = 1.42_{-0.38}^{+0.12}, \quad R_{bb}^h = 0.98_{-0.10}^{+0.03}, \quad R_{\tau\tau}^h = 0.98_{-0.94}^{+0.01}. \quad (7.6)$$

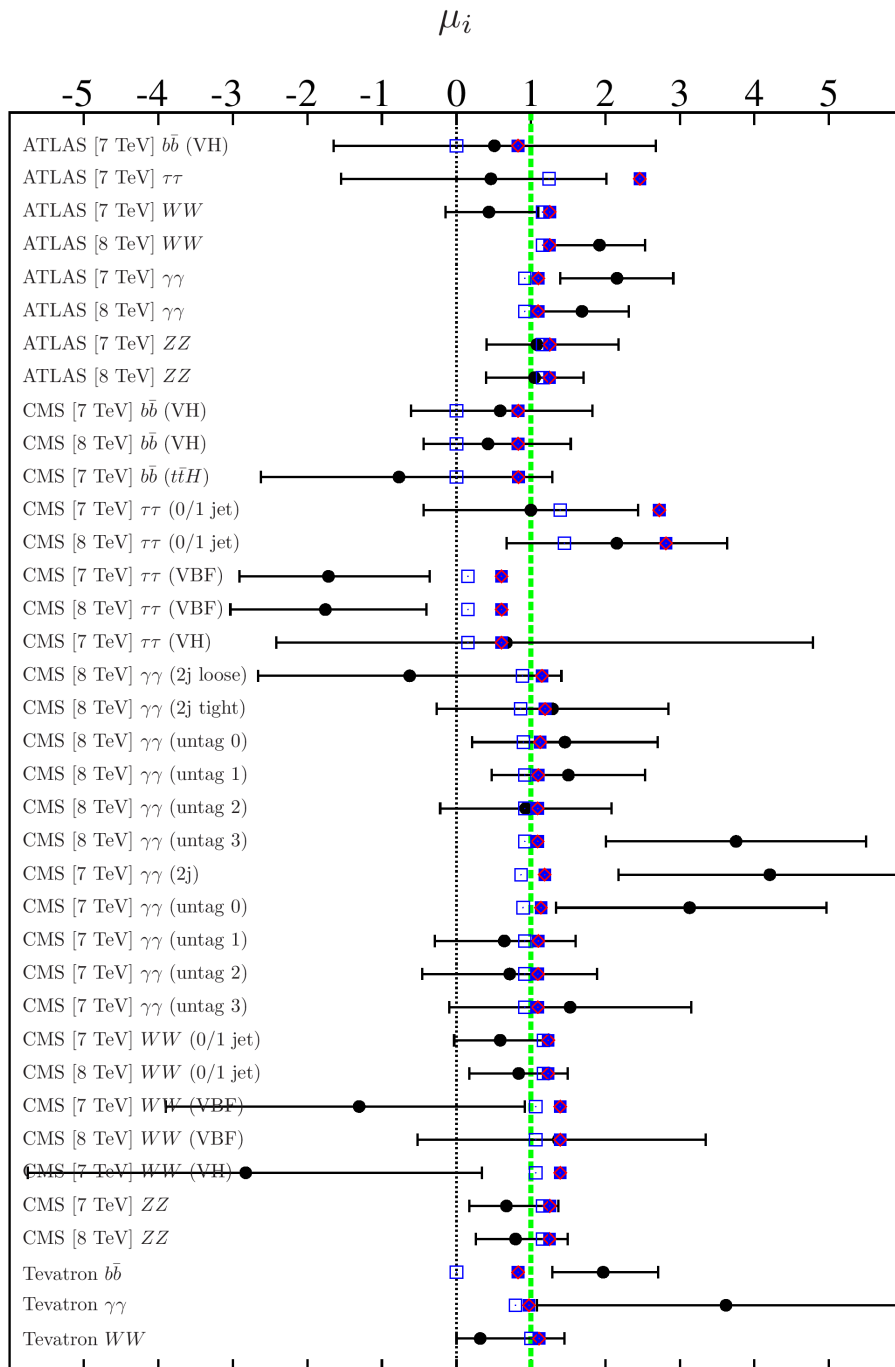


Figure 7.3: Fit results for the signal strength modifiers, μ_i , in the case that the heavy \mathcal{CP} -even Higgs is interpreted as the new boson seen at the LHC (heavy Higgs case). The experimental data is shown as black dots (with error bars). The other symbols show best fit points, corresponding to the full fit (LHC+Tevatron+LEO) (blue solid squares), without the Tevatron data (blue open squares), and without LEO (red diamonds).

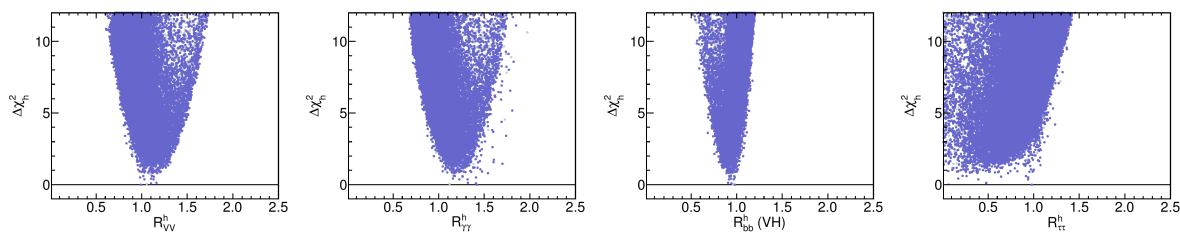


Figure 7.4: Original 2012 analysis: Distributions of $\Delta\chi_h^2$ versus the different signal rates (defined in the text) for the light Higgs case (we refer to the χ^2 value of the complete fit). The colours show all points in the scan (grey), and points that pass the direct Higgs search constraints from HiggsBounds version 3.8.0 (blue).

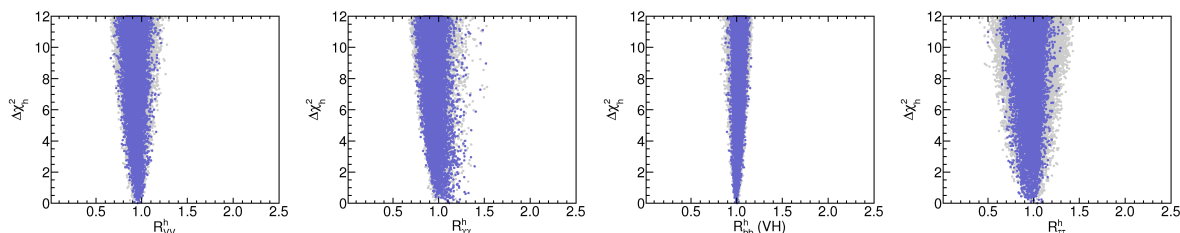


Figure 7.5: Updated analysis: Distributions of $\Delta\chi_h^2$ versus the different signal rates for the light Higgs case (we refer to the χ^2 value of the complete fit). The colours show all points in the scan (grey), and points that pass the direct Higgs search constraints from HiggsBounds version 4.2.0beta (blue).

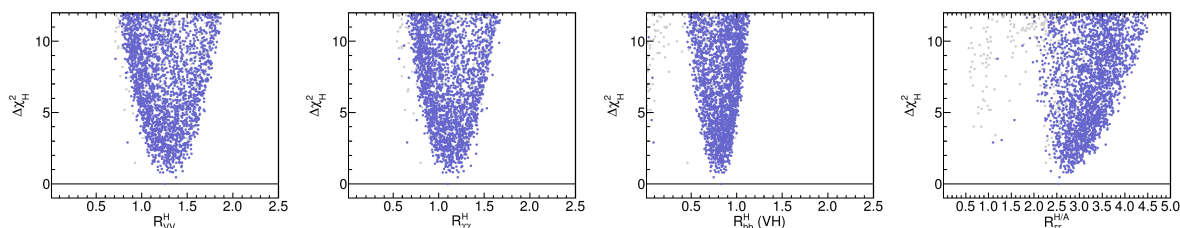


Figure 7.6: Original 2012 analysis: $\Delta\chi_H^2$ versus the different signal rates (defined in the text) for the heavy Higgs case (we refer to the χ^2 value of the complete fit). Colour coding the same as in Fig. 7.4.

where the uncertainty intervals are extracted from the range with $\Delta\chi_h^2 < 1$ (corresponding to 68% confidence intervals in the Gaussian case). For $R_{\tau\tau}^h$ we observe a distribution which is very flat near the minimum. This indicates a low sensitivity in the fit to constraints from $\tau^+\tau^-$ final states, and it permits substantially reduced $\tau^+\tau^-$ rates at a very low additional χ^2 contribution. We will see that this has changed substantially in the update where the most recent data from the $\tau\tau$ channel by ATLAS [88] and CMS [87] is included.

The results for the updated fit are presented in Fig. 7.5. It is clearly visible that including the latest experimental measurements from ATLAS and CMS (with reduced

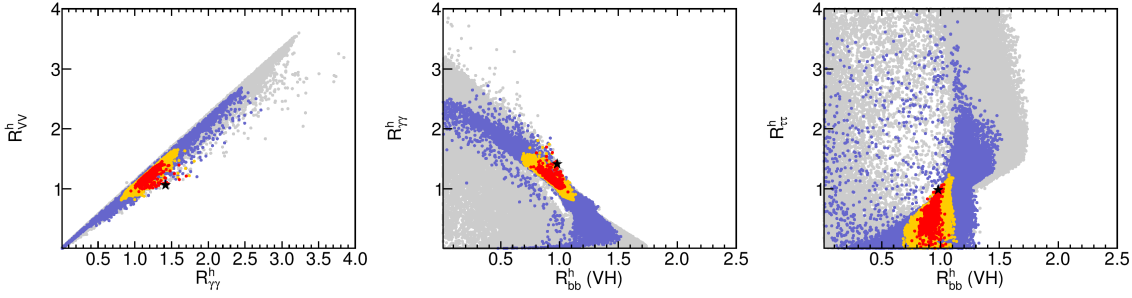


Figure 7.7: Original 2012 analysis: Correlations between signal rates for the light Higgs case. The colour coding follows that of Fig. 7.4, with the addition of the favoured regions with $\Delta\chi_h^2 < 2.3$ (red) and $\Delta\chi_h^2 < 5.99$ (yellow). The best fit point is indicated by a black star.

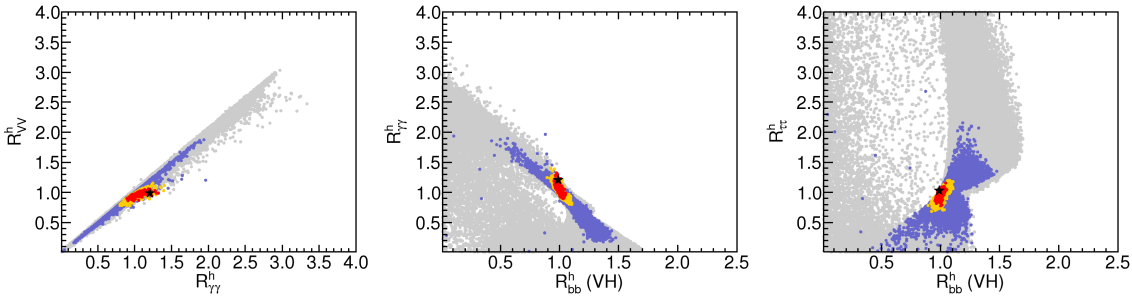


Figure 7.8: Updated analysis: Correlations between signal rates for the light Higgs case. The colour coding follows that of Fig. 7.5, with the addition of the favoured regions with $\Delta\chi_h^2 < 2.3$ (red) and $\Delta\chi_h^2 < 5.99$ (yellow). The best fit point is indicated by a black star.

uncertainties) leads to significantly narrower $\Delta\chi_h^2$ distributions, especially for R_{VV}^h , R_{bb}^h and $R_{\tau\tau}^h$. The best fit rates are:

$$R_{VV}^h = 0.99_{-0.10}^{+0.04}, \quad R_{\gamma\gamma}^h = 1.21_{-0.28}^{+0.11}, \quad R_{bb}^h = 0.97_{-0.02}^{+0.06}, \quad R_{\tau\tau}^h = 1.03_{-0.20}^{+0.05}. \quad (7.7)$$

Results for the heavy Higgs case are shown in Fig. 7.6. The resulting $\Delta\chi_H^2$ distributions for individual R_X are similar to those for $\Delta\chi_h^2$ (of the original analysis), except for $R_{\tau\tau}$, where the additional contribution from the A boson strongly enhances this quantity over the corresponding result in the light Higgs case. Extracting the results for the minimal χ^2 in the same way as for the light Higgs case, we obtain

$$R_{VV}^H = 1.25_{-0.07}^{+0.30}, \quad R_{\gamma\gamma}^H = 1.10_{-0.06}^{+0.18}, \quad R_{bb}^H = 0.83_{-0.12}^{+0.05}, \quad R_{\tau\tau}^{H/A} = 2.54_{-0.17}^{+0.31}. \quad (7.8)$$

More information about the phenomenology of the pMSSM-7 Higgs sector can be found from the correlations between the different rates. This is shown in Fig. 7.7 for the light Higgs case (original analysis). Compared to the one-dimensional χ^2 distributions of Fig. 7.4, this figure introduces two new colours that are used in the following to show regions close to the minimum χ^2 . We highlight points for which $\Delta\chi_{h,H}^2 < 2.3$

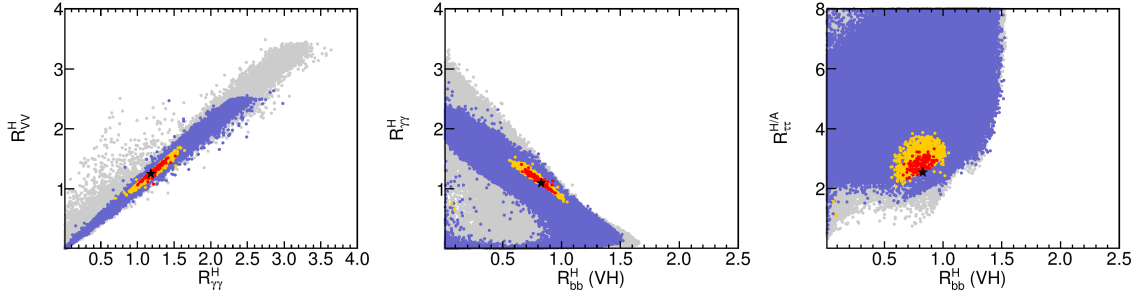


Figure 7.9: Original 2012 analysis: Correlations between signal rates in the heavy Higgs case. Colours similar to Fig. 7.7, but here representing $\Delta\chi_{H}^2 < 2.3$ (red) and $\Delta\chi_{H}^2 < 5.99$ (yellow). The black star indicates the best fit point for the heavy Higgs case.

(red) and $\Delta\chi_{h,H}^2 < 5.99$ (yellow). In the Gaussian limit these correspond to 68% (95%) confidence regions in two dimensions. We shall refer to these points simply as the *favoured region/points*, or sometimes *most favoured region/points* when $\Delta\chi_{h,H}^2 < 2.3$ is discussed. The best fit point is indicated in the figures by a black star.

The left plot of Fig. 7.7 shows the strong, positive, correlation between R_{VV}^h and $R_{\gamma\gamma}^h$ (compare Fig. 6.7 for a corresponding analysis in the NMSSM). In most of the viable parameter space we find $R_{\gamma\gamma}^h > R_{VV}^h$. The favoured region contains points with fully correlated rates in the interval $0.9 \lesssim R_{\gamma\gamma, VV}^h \lesssim 1.6$, but also solutions with lower degree of correlation, where a $\gamma\gamma$ enhancement (up to $R_{\gamma\gamma}^h \sim 1.8$) is accompanied by a much smaller (or no) enhancement of R_{VV}^h . In the second plot of Fig. 7.7 we compare the results of $R_{\gamma\gamma}^h$ and R_{bb}^h (we remind the reader that the latter rate is calculated using the VH production mode only) and we find an anticorrelation between these two rates. As we discussed in the last chapter, this can be understood from the fact that the $h, H \rightarrow b\bar{b}$ decay gives the largest contribution to the total width for a Higgs boson in this mass range, both in the SM and (typically) also in the MSSM. A reduction of the $h, H \rightarrow b\bar{b}$ partial width is therefore effectively a reduction of the total decay width, which leads to a simultaneous enhancement of the branching ratios into the subdominant final states. We already discussed this mechanism to enhance the $\gamma\gamma$ rate in detail in Sect. 6. As we can see here the reduction of the total width also affects other rates, like R_{VV}^h . The third (right) plot in Fig. 7.7 shows the weak correlation of $R_{\tau\tau}^h$ to R_{bb}^h , where in principle any value of $R_{\tau\tau}^h < 1$ is found in the favoured region for $R_{bb}^h \lesssim 1$.

The rate correlations for the updated fit can be seen in Fig. 7.8. The general trends are the same as in the original analysis. We see that the regions of allowed (blue) points are smaller, e.g. points with $R_{\gamma\gamma}^h > 2$, as were still allowed in our 2012 analysis, are excluded by `HiggsBounds` version 4.2.0beta. Also the size of the (most) favoured regions is clearly reduced. The favoured region still extends to $R_{\gamma\gamma}^h \sim 1.5$, while for the other rates it is restricted to values close to 1. This can easily be understood, looking at the $\Delta\chi^2$ distributions in Fig. 7.5, where one can see that small deviations of R_{bb}^h , $R_{\tau\tau}^h$ and R_{VV}^h from their minimum values (close to 1) entail significant additional χ^2 contributions. A (slight) enhancement of $R_{\gamma\gamma}^h$ without a simultaneous suppression of R_{bb}^h can arise from

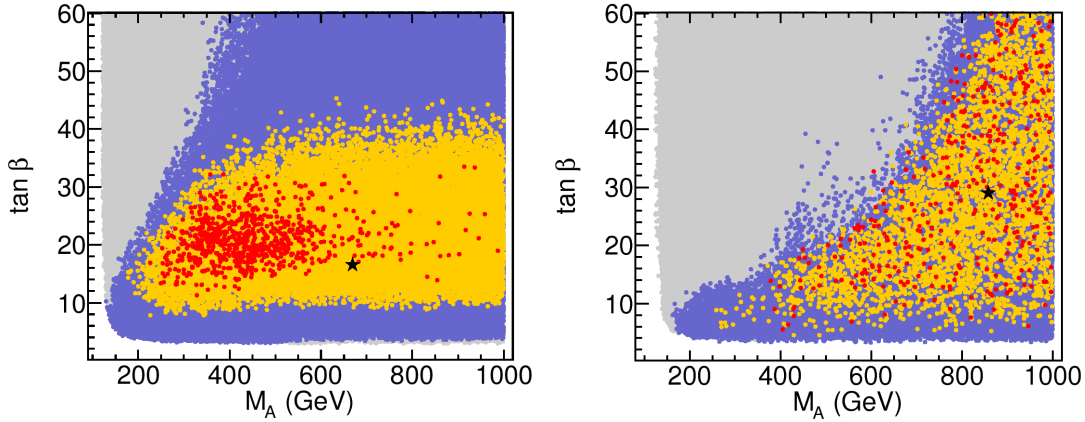


Figure 7.10: Higgs sector tree-level parameters (M_A , $\tan\beta$) in the light Higgs case for the original 2012 fit (left) and the updated fit (right).

light staus in the loop-induced $h \rightarrow \gamma\gamma$ decay, as we already mentioned in the previous chapter. This possibility, which is favoured by the current data, will be discussed in more detail below.

Turning to Fig. 7.9, we show the rate correlations for the heavy Higgs case (original analysis). Similar results as in the light Higgs case are visible in the heavy Higgs data, with the notable difference in the $\tau^+\tau^-$ rate, mainly due to the inclusion of the contribution from the \mathcal{CP} -odd Higgs A . The favoured regions are found at values for $R_{\tau\tau}^{H/A}$ between 2 and 4, while R_{bb}^H remains below 1.

We now briefly discuss what mechanisms can alter the branching ratios in the manner observed, and what the consequences are for the favoured regions of the MSSM parameter space. In Fig. 7.10 we show the scan results for the light Higgs case in the plane of the Higgs sector tree-level parameters (M_A , $\tan\beta$), where the results of the original (updated) fit are shown in the left (right) plot. Starting with the left plot one can note the region at low M_A , high $\tan\beta$ which is excluded by direct MSSM Higgs searches (mainly $H/A \rightarrow \tau^+\tau^-$). The excluded region appears smaller in this plane than the corresponding results published by the experiments [246, 281], since their results are shown only for one particular benchmark scenario (the so-called m_h^{\max} scenario [253]). We see that the regions of very high $\tan\beta \gtrsim 40$, and also low $\tan\beta \lesssim 8$, are disfavoured by the fit. At high $\tan\beta$ this results from a poor fit to $(g-2)_\mu$ and flavour observables, whereas for low $\tan\beta$ the fit to the LHC Higgs observables becomes worse. For low $\tan\beta$ it also becomes increasingly difficult to fit the relatively high Higgs mass value. Low values of M_A are disfavoured by the fit results. The region in which we find points with M_h close to the observed signal starts at $M_A \gtrsim 150$ GeV. The preferred region starts at $M_A \gtrsim 170$ GeV (and the most favoured region at $M_A \gtrsim 230$ GeV). Taking the rate information into account therefore suggests somewhat higher mass scales for the MSSM Higgs sector than what is required by the $\hat{M}_H \sim 125.7$ GeV Higgs mass measurement alone [48]. The relatively large M_A values imply that the MSSM is in the decoupling region ($M_A \gg M_Z$), where the light Higgs has (almost) SM-like couplings. Note that this is already a con-

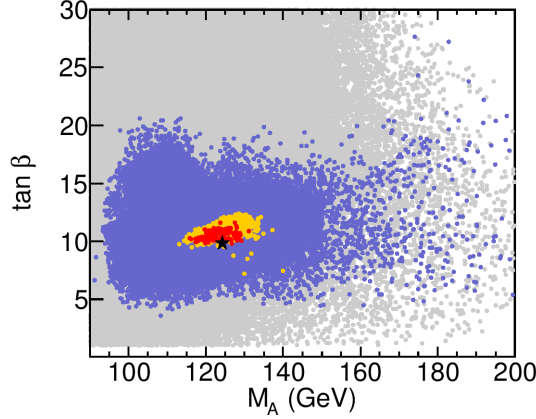


Figure 7.11: Original 2012 analysis: Higgs sector tree-level parameters (M_A , $\tan\beta$) in the heavy Higgs case.

sequence of the mass measurement alone and therefore no large deviations from the SM predictions are expected. This agrees with our findings in Fig. 7.1. It is not surprising that the rate measurements push the MSSM even further in the decoupling limit, given the high quality of the SM fit to the LHC data.

Turning to the right plot, we see that in the updated analysis a significantly larger part of the parameter plane (low M_A /high $\tan\beta$) is excluded by the experimental limits included in `HiggsBounds` version 4.2.0beta. This exclusion is dominated by the constraints from the updated MSSM $H/A \rightarrow \tau^+\tau^-$ search by CMS [248]. The updated rate measurements push the favoured and most favoured regions further in the decoupling limit, starting now at $M_A \gtrsim 250$ GeV and $M_A \gtrsim 400$ GeV respectively. While in the original analysis $\tan\beta$ values $\gtrsim 40$ and $\lesssim 8$ were disfavoured, we observe that the favoured range for $\tan\beta$ opens up in the updated analysis. For $M_{\tilde{E}_{1,2}} = M_{\tilde{L}_{1,2}} = 300$ GeV (as we had in the original analysis) and $\tan\beta > 40$ the MSSM contributions to $(g-2)_\mu$ are too large to explain the deviation between the SM and the measured value, leading to a large $\chi_{(g-2)_\mu}^2$ contribution and therefore a worse fit. By setting $M_{\tilde{E}_{1,2}} = M_{\tilde{L}_{1,2}} = M_{\tilde{I}_3}$ in the updated fit, we find a better prediction for $(g-2)_\mu$ in the region of large $\tan\beta$ ¹². In the original analysis we had approximately twice as many scan points as in the update. With more points the density of the yellow/red points in the right plot will increase. However we remind the reader that the point density has no physical meaning.

For the heavy Higgs case, as shown in Fig. 7.11, the situation is very different. Low values for M_A are preferred, and the favoured region in $(M_A, \tan\beta)$ is much smaller than for the light Higgs case: $110 \text{ GeV} \lesssim M_A \lesssim 140 \text{ GeV}$ and $7 \lesssim \tan\beta \lesssim 13$. Even though H can be very SM-like in this scenario, this situation is very different from the decoupling limit in the light Higgs case since it implies that all five MSSM Higgs bosons are light.

While in the heavy Higgs scenario the low preferred values for M_A typically lead

¹²In the updated fit, points with large $\tan\beta$ values that have a small $\chi_{(g-2)_\mu}^2$ have typically $M_{\tilde{E}_{1,2}} = M_{\tilde{L}_{1,2}} \gtrsim 400$ GeV.

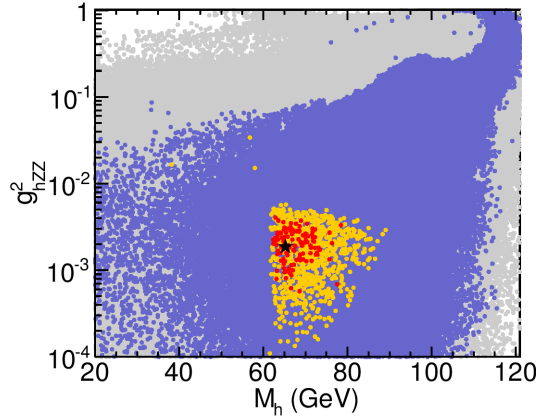


Figure 7.12: Original 2012 analysis: Effective coupling squared g_{hZZ}^2 of the lightest MSSM Higgs boson to a Z boson pair, as a function of the lightest Higgs mass M_h in the heavy Higgs case.

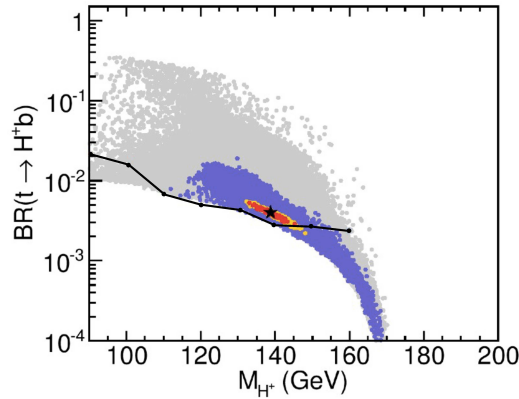


Figure 7.13: Original 2012 analysis: Branching ratio of the top quark into a charged Higgs boson and a bottom quark in the heavy Higgs case. The experimental upper limit [55] on this decay mode is indicated as black line.

to a situation where H , A , and H^\pm are rather close in mass, the lightest Higgs boson, h , can have a significantly lower mass, as illustrated in Fig. 7.12. As we see from this figure, points with $M_h < 90$ GeV have a very small effective coupling to vector bosons, $g_{hZZ}^2 \ll 1$, which explains why such light Higgs bosons are compatible with the Higgs search limits from LEP. The bulk of the favoured region in this case is found for $60 \text{ GeV} \lesssim M_h \lesssim 90 \text{ GeV}$, with an effective coupling squared to vector bosons at the sub-percent level. Another feature which is clearly visible in the `HiggsBounds` allowed points (blue) is the degradation of the limit around $M_h \sim 98$ GeV, which was caused by a slight excess of events observed at LEP in that mass region. While a scenario in which the Higgs signal at the LHC is interpreted as the heavy \mathcal{CP} -even Higgs, together with $M_h \sim 98$ GeV is in principle possible (see also [48, 51]), it is clearly not favoured by our rate analysis.

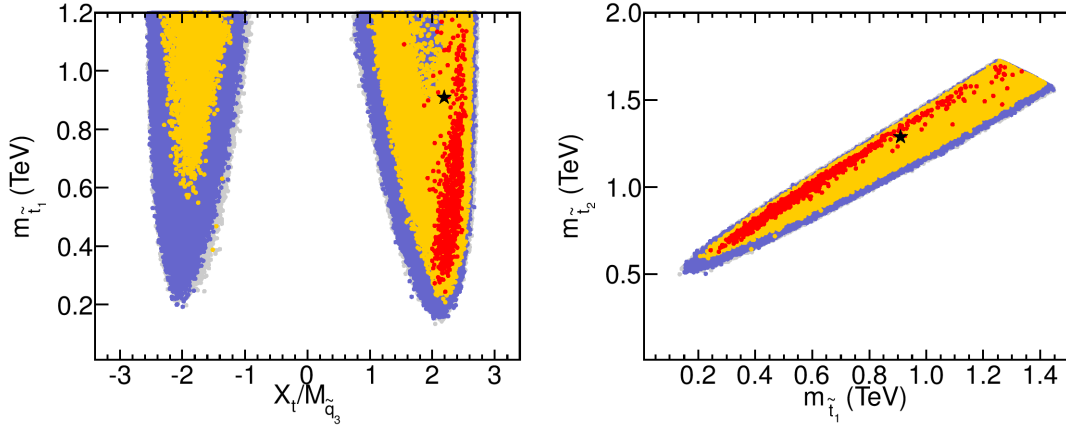


Figure 7.14: Original 2012 analysis: Stop mixing parameter $X_t/M_{\tilde{q}_3}$ vs. the light stop mass (left), and the light vs. heavy stop masses (right) in the light Higgs case.

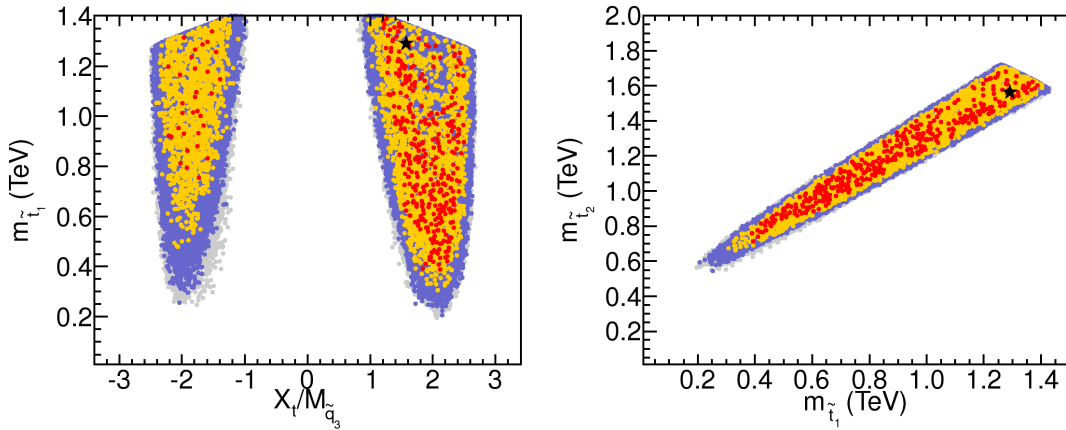


Figure 7.15: Updated analysis: Stop mixing parameter $X_t/M_{\tilde{q}_3}$ vs. the light stop mass (left), and the light vs. heavy stop masses (right) in the light Higgs case.

In the heavy Higgs case only values of the charged Higgs boson mass below the top mass ($M_{H^\pm} < m_t$) are found, which offers the possibility to test this scenario at the LHC by searching for charged Higgs bosons in top quark decays. We therefore show in Fig. 7.13 the fit results for $\text{BR}(t \rightarrow bH^+)$ as a function of M_{H^\pm} . The current upper limit on this decay mode [55] (published after this analysis was performed) sets very stringent constraints on this interpretation. Comparing the limit presented by ATLAS, which is displayed in Fig. 4.6 (and which is additionally shown as a black line in Fig. 7.13) with the favoured region obtained from the fit, one sees that the most favoured region (and most of the favoured region) is excluded at the 95% CL. However there are still allowed (blue) points not excluded by the limit of Ref. [55], for which the mass of the heavy \mathcal{CP} -even Higgs is close to the observed signal. We are currently working on an update to investigate to what extent the interpretation of the signal in terms of the heavy \mathcal{CP} -even Higgs in the MSSM is still viable.

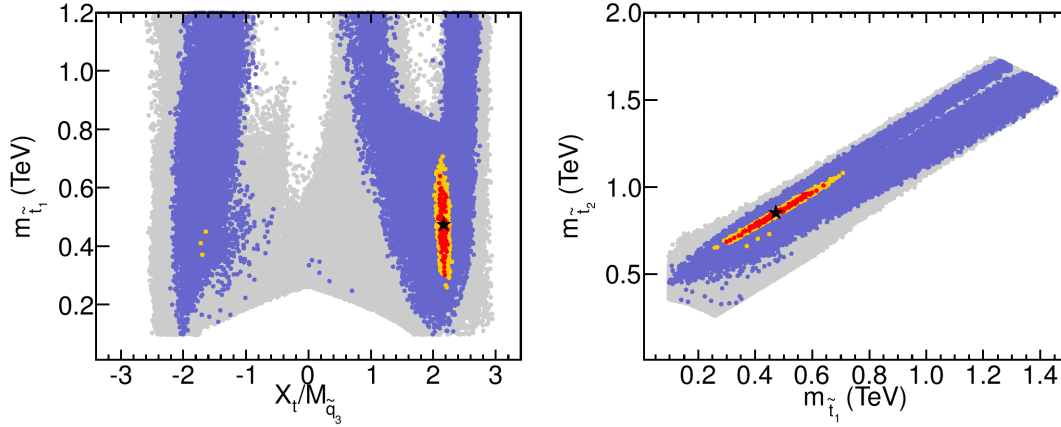


Figure 7.16: Original 2012 analysis: Stop mixing parameter $X_t/M_{\tilde{q}_3}$ vs. the light stop mass (left), and the light vs. heavy stop masses (right) in the heavy Higgs case.

The most relevant parameters for higher-order corrections in the MSSM Higgs sector are the soft SUSY-breaking parameters in the stop sector. In Fig. 7.14 we show (for the original analysis) $X_t/M_{\tilde{q}_3}$ vs. the light stop mass (left plot) and the light vs. the heavy stop mass (right plot) in the light Higgs case. In the left plot one can see that the case of zero stop mixing in the MSSM is excluded by the observation of a Higgs at $M_h \sim 125.6$ GeV (unless $M_{\tilde{q}_3}$ is very large), and that values of $|X_t/M_{\tilde{q}_3}|$ between ~ 1 and ~ 2.5 must be realised if $M_{\tilde{q}_3}$ is at the TeV scale. For the most favoured region we find $X_t/M_{\tilde{q}_3} = 2 - 2.5$. It should be noted here that large values of $|A_t|$ ($|A_t| \gtrsim \sqrt{6} M_{\tilde{q}_3}$) could potentially lead to charge and colour breaking minima [282–288]. We checked that applying a cut at $|A_t| \gtrsim \sqrt{6} M_{\tilde{q}_3}$ would still leave most points of the favoured region. Concerning the value of the lightest scalar top mass, the overall smallest values are found at $m_{\tilde{t}_1} \sim 200$ GeV, in agreement with [48]. Even taking the rate information into account, the (most) favoured values start at $m_{\tilde{t}_1} \gtrsim 200$ GeV for positive X_t . Such a light \tilde{t}_1 is accompanied by a somewhat heavier \tilde{t}_2 , as can be seen in the right plot of Fig. 7.14. Still, values of $m_{\tilde{t}_1} \sim 200$ GeV are realised for $m_{\tilde{t}_2} \sim 600$ GeV, which would mean that both stop masses are rather light, offering interesting possibilities for the LHC. The highest favoured $m_{\tilde{t}_1}$ values we find are ~ 1.4 TeV. These are the maximal values reached in our scan, but from Fig. 7.14 it appears plausible that the favoured region extends to larger values of both stop masses. Such a scenario would be extremely difficult to access at the LHC. For the interpretation of these results it is important to remember that we have assumed a universal value for the soft mass parameters in the scalar top and bottom sector. Relaxing this assumption would potentially lead to larger regions of parameter space in which all applied constraints can be satisfied and which provide a good fit result.

Turning to the updated fit, we see in Fig. 7.15 that the most favoured region for $X_t/M_{\tilde{q}_3}$ widens and that red points can be found for $X_t/M_{\tilde{q}_3} = 1 - 2.5$, as well as for

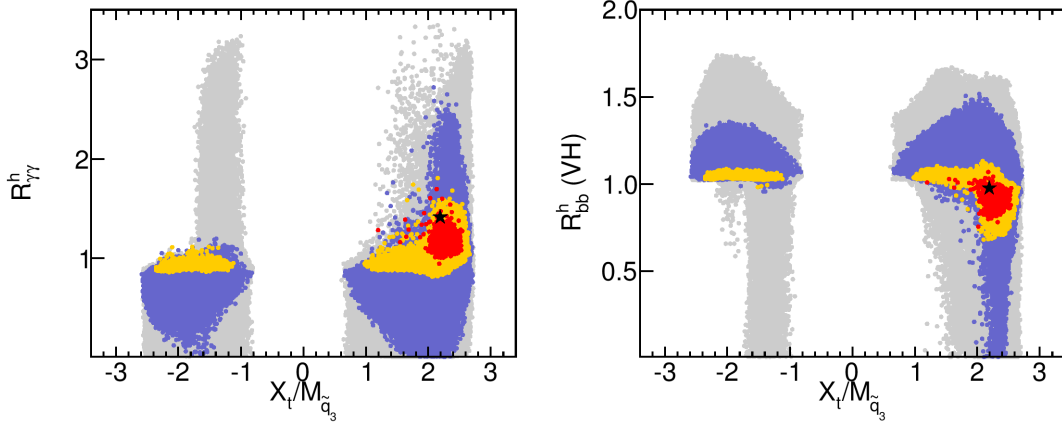


Figure 7.17: Original 2012 analysis: Dependence of the rates $R_{\gamma\gamma}^h$ and R_{bb}^h (VH) on the stop mixing parameter $X_t/M_{\tilde{q}_3}$ for the light Higgs case.

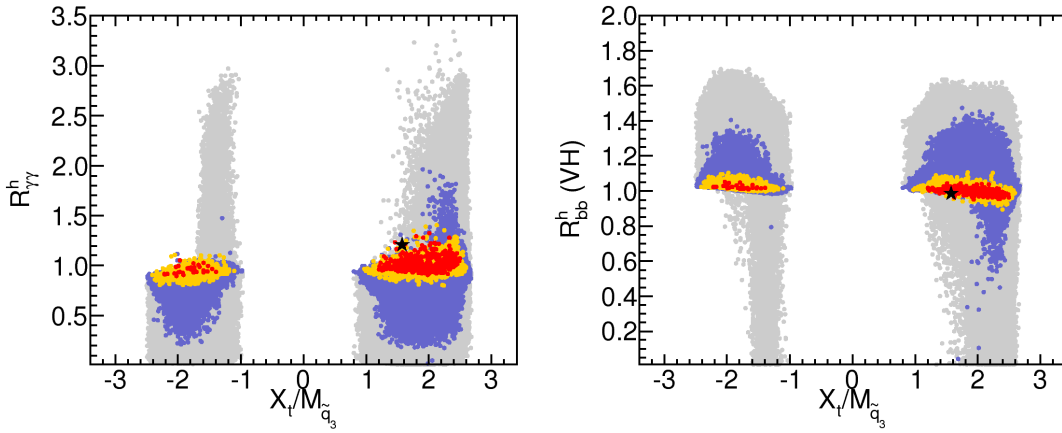


Figure 7.18: Updated analysis: Dependence of the rates $R_{\gamma\gamma}^h$ and R_{bb}^h (VH) on the stop mixing parameter $X_t/M_{\tilde{q}_3}$ for the light Higgs case.

negative X_t ¹³. This is connected to the fact that a suppression of $b\bar{b}$ is no longer favoured, as we will demonstrate below. While the best fit point has heavy stops (with masses close to the upper scan limit) the (most) favoured region goes down to significantly lower $m_{\tilde{t}_1}$ values. The favoured (most favoured) region starts at $m_{\tilde{t}_1} \gtrsim 300$ GeV ($m_{\tilde{t}_1} \gtrsim 400$ GeV), i.e. somewhat higher values than in the original analysis.

The results for the scalar top masses in the heavy Higgs case (original analysis) look quite similar to the light Higgs case, but with substantially smaller favoured regions, which are nearly solely realised for positive X_t with $X_t/M_{\tilde{q}_3} = 2$ – 2.3 , as can be seen in Fig. 7.16. The favoured values of $m_{\tilde{t}_1}$ range between ~ 250 GeV and ~ 700 GeV, whereas the preferred range of the heavy stop extends from $m_{\tilde{t}_2} \sim 650$ GeV to $m_{\tilde{t}_2} \sim 1100$ GeV.

¹³In Fig. 7.15 we extended the plotted range to large $m_{\tilde{t}_1}$ values, to include the best-fit point in the plot. The edges for large $m_{\tilde{t}_1}$ indicate the upper scan limits. The same feature would be visible in Fig. 7.14 if the plotting range were extended to larger $m_{\tilde{t}_1}$ masses.

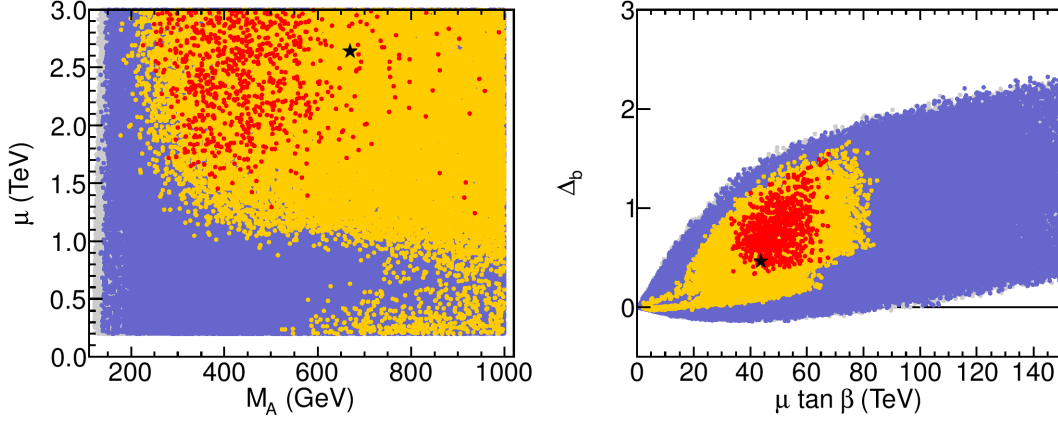


Figure 7.19: Original 2012 analysis: Correlation of the μ parameter to the value of M_A (left), and dependence of Δ_b corrections on $\mu \tan \beta$ (right), both in the light Higgs case.

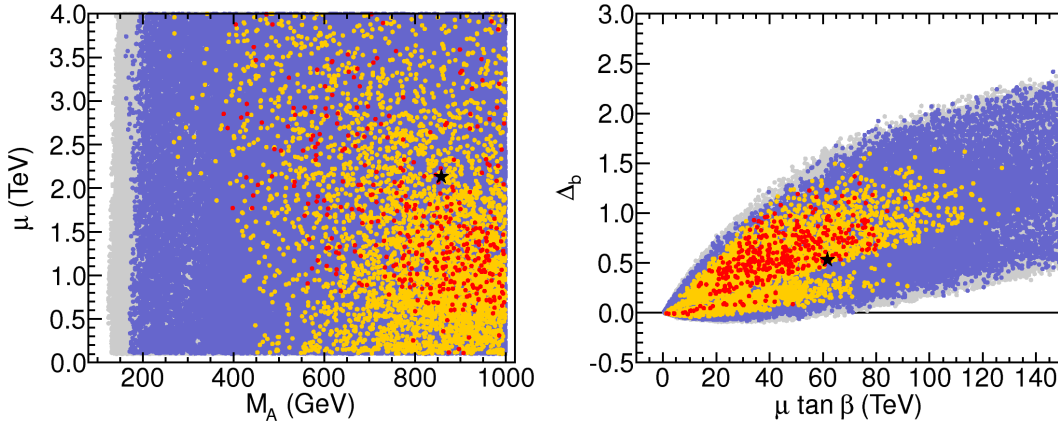


Figure 7.20: Updated analysis: Correlation of the μ parameter to the value of M_A (left), and dependence of Δ_b corrections on $\mu \tan \beta$ (right), both in the light Higgs case.

We now turn to the analysis of rates as a function of the underlying MSSM parameters. This comparison allows to analyse the various mechanisms that are responsible for the observed slight differences in the decay rates with respect to the SM values.

In Fig. 7.17 (original analysis) we analyse the correlation between the ratio $X_t/M_{\tilde{q}_3}$ and $R_{\gamma\gamma}^h$ (left) or R_{bb}^h (VH) (right) in the light Higgs case (for the original 2012 analysis). It can be seen that the enhancement in the $\gamma\gamma$ channel is only substantial for $X_t/M_{\tilde{q}_3} \gtrsim 2$, where values of up to $R_{\gamma\gamma}^h \sim 1.7$ can be reached in the favoured region. As we discussed in the previous chapter such an enhancement can have two sources: a suppression of $\Gamma(h \rightarrow b\bar{b})$ — the largest contribution to the total width — or a direct enhancement of $\Gamma(h \rightarrow \gamma\gamma)$. That the first mechanism is (in the original analysis) indeed responsible for a substantial part of the scenarios with an enhancement of $R_{\gamma\gamma}^h$ can be seen in the right plot of Fig. 7.17, which together with the middle plot of Fig. 7.7 illustrates that the enhancement in the $\gamma\gamma$ channel in the favoured regions is accompanied by some sup-

pression of the $b\bar{b}$ channel. This suppression/enhancement is realised for large, positive values of $X_t/M_{\tilde{q}_3}$.

Fig. 7.18 displays the results for the updated analysis. The most favoured region contains points in the range $0.9 \lesssim R_{\gamma\gamma}^h \lesssim 1.3$, however — contrary to the original 2012 fit — the $\gamma\gamma$ enhancement is essentially not caused by a suppressed $b\bar{b}$ rate. Since a suppression of R_{bb}^h is no longer favoured by the updated fit, the clear preference for large, positive $X_t/M_{\tilde{q}_3}$, which we saw in the original analysis, is less pronounced in the fit of the updated analysis.

As analysed in Sect. 6.3.1, a suppression of $b\bar{b}$ can happen in different ways: A suppression of the $h \rightarrow b\bar{b}$ channel occurs for scenarios with small α_{eff} . Furthermore, genuine corrections to the $hb\bar{b}$ vertex entering via the quantity $\Delta_b \propto \mu \tan \beta$ [233–235, 289]¹⁴, can give rise to suppression of the $h \rightarrow b\bar{b}$ channel, see Eq. (6.8). While the loop-corrected coupling $g_{hb\bar{b}}$, as given in Eq. (6.8), approaches the SM coupling in the decoupling limit ($M_A \gg M_Z$), a suppression of $g_{hb\bar{b}}$ is possible for M_A not too large provided that Δ_b is numerically sizeable and positive. We analyse this in Fig. 7.19 (original analysis). The left plot in this figure shows that the most favoured regions are obtained for $\mu > 1$ TeV, and that the combination of small μ and $M_A \lesssim 500$ GeV is disfavoured. The corresponding Δ_b values are shown in the right plot as a function of $\mu \tan \beta$. The most favoured regions are found in the range $0.3 \lesssim \Delta_b \lesssim 1.5$, for correspondingly large values of $\mu \tan \beta \sim 30$ –70 TeV. Note that the large values for the Δ_b corrections do not pose problems with perturbativity, since they tend to reduce the bottom Yukawa coupling. It should be noted that the Δ_b corrections in Eq. (6.8) have another important effect: while in the absence of those contributions a small value of α_{eff} would give rise to a simultaneous suppression of the Higgs couplings to $b\bar{b}$ and to $\tau^+\tau^-$, the Δ_b corrections differ from the corresponding contributions to the $g_{h\tau^+\tau^-}$ coupling. This implies in particular that the $g_{h\tau^+\tau^-}$ coupling may be suppressed while the $g_{hb\bar{b}}$ coupling remains unsuppressed (and vice versa).

The updated results in Fig. 7.20 show no preference for large μ (large Δ_b) values. This is expected, since a suppression of $b\bar{b}$ is no longer favoured. The most favoured region of the updated fit includes points with Δ_b values in the range from 0 to ~ 1.3 GeV. In the left plot we can see (as before) that the favoured regions is pushed to higher M_A values.

For the second mechanism, a direct enhancement of the $\Gamma(h \rightarrow \gamma\gamma)$ width, it is known that other SUSY particles can play an important role. One possibility that has been discussed in the literature is to have very light scalar taus [208, 209]. The effect of light scalar taus can also be observed in our analysis, as can be seen in Fig. 7.21 and Fig. 7.22. Here we show $\Gamma(h, H \rightarrow \gamma\gamma)/\Gamma(h, H \rightarrow \gamma\gamma)_{\text{SM}}$ as a function of $m_{\tilde{\tau}_1}$. We start the discussion with the light Higgs case shown in Fig. 7.21. In the original 2012 analysis, shown in the left plot, for $m_{\tilde{\tau}_1} \sim 100$ GeV the enhancement over the SM width reaches 50% in the favoured region. Even lower values of $m_{\tilde{\tau}_1}$ (which are allowed by limits from direct searches, see [165]) are forbidden in our scan from the requirement that the LSP is the lightest neutralino, together with the lower limit of $M_2 \geq 200$ GeV

¹⁴The dominant contributions to Δ_b beyond one-loop order are the QCD corrections, given in [290]. Those two-loop contributions are not included in our analysis.

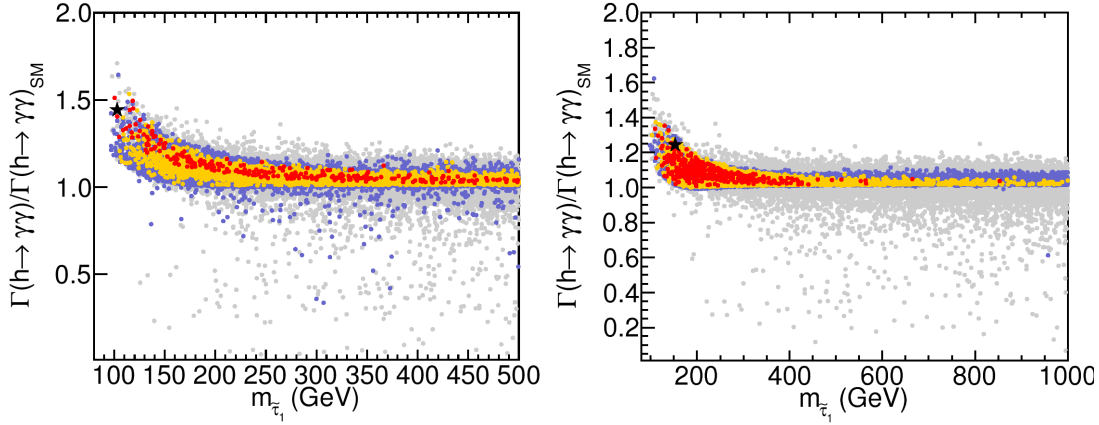


Figure 7.21: Enhancement of the $h \rightarrow \gamma\gamma$ partial width in the presence of light staus for the light Higgs case. The left plot shows the result of the 2012 analysis, the right plot shows the update.

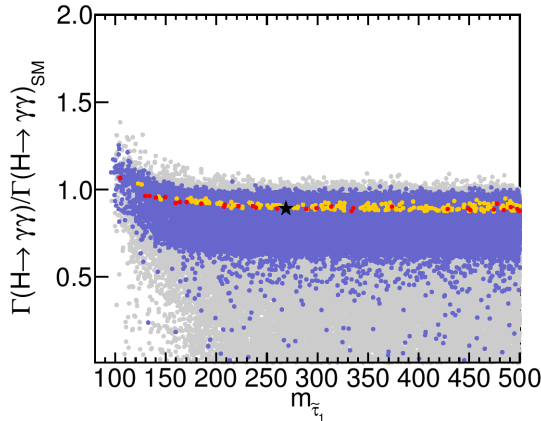


Figure 7.22: Original 2012 analysis: Enhancement of the $h \rightarrow \gamma\gamma$ partial width in the presence of light staus for the heavy Higgs case.

and the GUT relation between M_1 and M_2 . Relaxing these assumptions would allow for a larger enhancement of $\Gamma(h \rightarrow \gamma\gamma)/\Gamma(h \rightarrow \gamma\gamma)_{\text{SM}}$, as is clear from the sharp rise of this rate seen in Fig. 7.21 for low $m_{\tilde{\tau}_1}$. For $m_{\tilde{\tau}_1} \gtrsim 300$ GeV a decoupling to the SM rate is observed. Through the contributions of light scalar taus it is thus possible to accommodate enhanced values of $R_{\gamma\gamma}^h$, while maintaining R_{bb}^h and R_{VV}^h at the SM level. While the best fit point has $m_{\tilde{\tau}} \sim 100$ GeV, the most favoured region covers the entire $m_{\tilde{\tau}}$ range.

Also in the updated analysis (right plot of Fig. 7.21) the preference for light staus is clearly visible. Since the latest $b\bar{b}$ measurements restrict the R_{bb}^h to values close to 1, light staus are the dominant source of the $R_{\gamma\gamma}^h$ enhancement. Even though $R_{\gamma\gamma}^h \sim 1$ belongs to the most favoured region, heavy staus ($\gtrsim 600$ GeV) are less favoured by the fit. This feature stems from the fit to $(g-2)_\mu$, since in the updated fit we choose

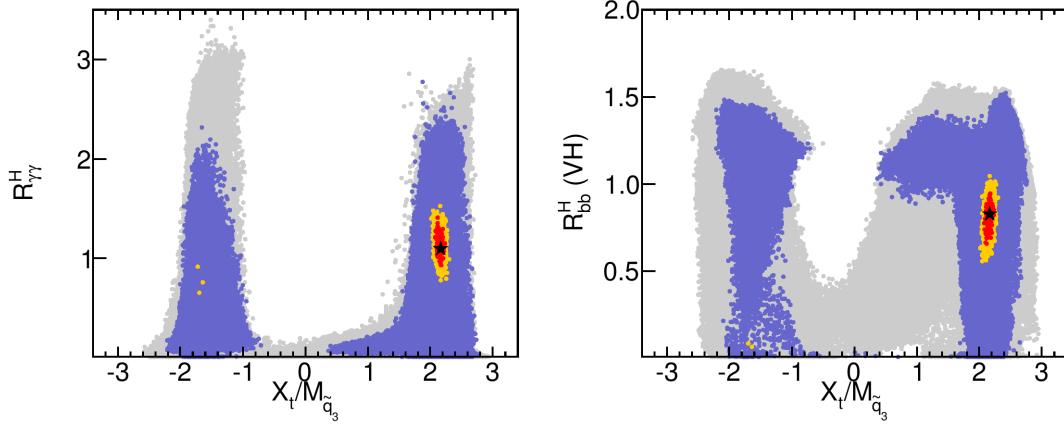


Figure 7.23: Original 2012 analysis: Dependence of the rates $R_{\gamma\gamma}^H$ and R_{bb}^H (VH) on the stop mixing parameter $X_t/M_{\tilde{q}_3}$ for the heavy Higgs case.

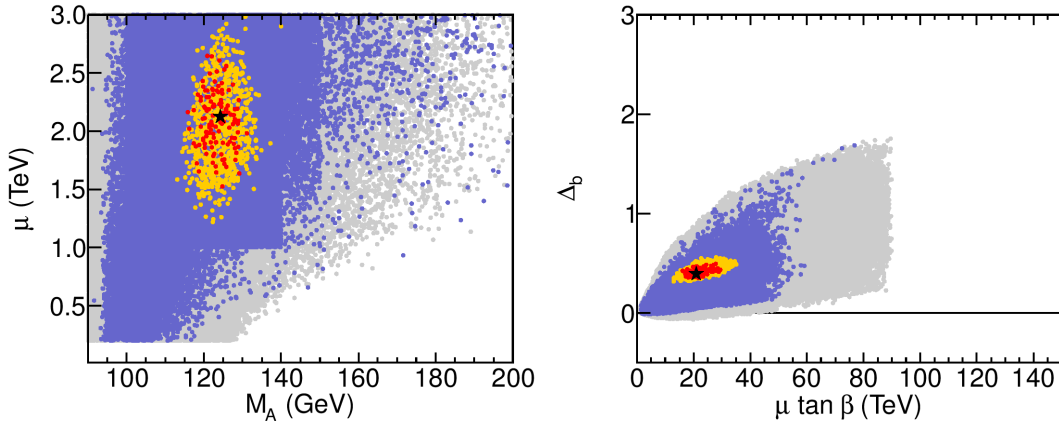


Figure 7.24: Original 2012 analysis: Correlation of the μ parameter to the value of M_A (left), and dependence of Δ_b corrections on $\mu \tan \beta$ (right), both in the heavy Higgs case.

$$M_{\tilde{E}_{1,2}} = M_{\tilde{L}_{1,2}} = M_{\tilde{t}_3}.$$

In the heavy Higgs case, on the other hand, as shown in the right plot of Fig. 7.22, the favoured region is located close to one, and light staus do not contribute to a possible enhancement of $R_{\gamma\gamma}^H$.

Similarly to the light Higgs case, we investigate the dependence of the rates on the stop sector parameters for the heavy Higgs case. The results are shown in Fig. 7.23. As in Fig. 7.16, the favoured regions are given for large and positive $X_t/M_{\tilde{q}_3}$, where we find $0.8 \lesssim R_{\gamma\gamma}^H \lesssim 1.6$ and a corresponding suppression of $0.6 \lesssim R_{bb}^H \lesssim 1.0$. The Δ_b corrections can also in this case be largely responsible for the suppression of the R_{bb}^H rate, as we show in Fig. 7.24. Here one can see that in the heavy Higgs scenario only values of Δ_b between ~ 0.3 and ~ 0.6 are favoured, which are realised for $10 \text{ TeV} \lesssim \mu \tan \beta \lesssim 35 \text{ TeV}$, i.e. smaller values than in the light Higgs case (of the original 2012 analysis).

In order to summarise the discussion on favoured MSSM parameter regions, we list in

Parameter	Light Higgs case			Light Higgs case			Heavy Higgs case		
	Original 2012 fit			Updated fit			Original 2012 fit		
	Best fit			Best fit			Best fit		
M_A [GeV]	300	669	860	398	858	(1000)	120.5	124.2	128.0
$\tan \beta$	15	16.5	26	9.8	29	(60)	9.7	9.8	10.8
μ [GeV]	1900	2640	(3000)	845	2128	3824	1899	2120	2350
$M_{\tilde{q}_3}$ [GeV]	450	1100	(1500)	637	1424	1481	580	670	740
$M_{\tilde{l}_3}$ [GeV]	250	285	(1500)	230	356	463	(200)	323	(1500)
A_f [GeV]	1100	2569	3600	1249	2315	3524	1450	1668	1840
M_2 [GeV]	(200)	201	450	(200)	229	(500)	(200)	304	370
M_h [GeV]	122.2	126.1	127.1	124.6	125.5	126.4	63.0	65.3	72.0
M_H [GeV]	280	665	860	386	858	(1000)	123.9	125.8	126.4
M_{H^\pm} [GeV]	310	673	860	405	858	(1000)	136.5	138.8	141.5

Table 7.8: Best fit parameter values (in the respective middle column) and ranges for $\Delta\chi_{h,H}^2 < 1$. Values in parentheses indicate that the limit of the scan range has been reached.

table 7.8 the parameter values for the best fit points (of the complete fit). We also give the parameter ranges corresponding to $\Delta\chi_{h,H}^2 < 1$. For several of the parameters this range extends to the limits of our scanned interval. Cases like this have been indicated in table 7.8 with parentheses around the corresponding numbers. One can see that in most cases the ranges with $\Delta\chi_{h,H}^2 < 1$ are quite wide. In the original analysis, one exception is $\tan \beta$, which is relatively tightly constrained (at least at the level of $\Delta\chi_{h,H}^2 < 1$) in the light Higgs case, and even more so in the heavy Higgs case. However the $\tan \beta$ range got significantly wider for the updated fit. For the updated fit $M_{\tilde{l}_3}$ is constrained to relatively small values, which is in particular an effect of $(g-2)_\mu$ as we analysed above. In the heavy Higgs case, as discussed above, also the masses of the additional Higgs bosons are relatively tightly constrained. More precise experimental data would be needed to achieve tighter constraints on the other fitted parameters which enter the MSSM Higgs phenomenology via loop corrections. The fact that even in the more “exotic” scenario, where the observed signal is interpreted in terms of the heavier \mathcal{CP} -even Higgs of the MSSM, the values of individual SUSY parameters are only moderately constrained by the fit illustrates that a reasonably good description of the data can be achieved without the need of tuning certain parameters to specific values. It remains to be studied how much this will change when updating also the analysis for the heavy Higgs case.

7.4 Summary

We have analysed the compatibility of the Minimal Supersymmetric Standard Model (MSSM) with the recent discovery of a Higgs boson at the LHC. To this end we have studied the low-energy (phenomenological) pMSSM-7 parameter space, where we allowed the seven parameters most relevant for Higgs and flavour phenomenology to vary freely.

A random parameter scan over the seven free parameters with $\mathcal{O}(10^7)$ scan points has been performed. For each scan point, a χ^2 function was evaluated, taking into account the measured rates in the individual Higgs search channels from ATLAS, CMS, and the Tevatron, the best-fit mass values of the LHC experiments, as well as the following low-energy observables: $\text{BR}(B \rightarrow X_s \gamma)$, $\text{BR}(B_s \rightarrow \mu^+ \mu^-)$, $\text{BR}(B_u \rightarrow \tau \nu_\tau)$, $(g-2)_\mu$ and M_W . In this chapter we presented the original analysis performed in the end of 2012, where we took 37 Higgs boson rate measurements into account. We also showed the results of an undated analysis making use of the code `HiggsSignals` containing the most recent Higgs rate measurements (90 in total).

Starting with the original 2012 analysis, we find that the SM yields a good fit to the data, with a χ^2 per degree of freedom around unity. The precise value depends on whether low-energy observables and/or the Tevatron data are included in the fit. Turning to the MSSM, we find that the pMSSM-7 provides a good fit to the Higgs and low-energy data in the case that the light \mathcal{CP} -even Higgs is interpreted as the new state at ~ 125.6 GeV. In the updated analysis the quality both of the SM and the MSSM (light Higgs case) fits gets slightly worse, however both models still provide a good fit to the current data. In the case that the heavy \mathcal{CP} -even Higgs boson is interpreted as the newly discovered state the fit is still acceptable, but somewhat worse than in the light Higgs case, once Tevatron and low-energy data is included. In the original analysis, the two MSSM best-fit points have a total χ^2/ν of 30.4/36 (42.4/36) for the light (heavy) Higgs case, respectively, after the inclusion of LHC, Tevatron and low-energy data. The corresponding SM value for χ^2/ν is 45.3/42. In the updated fit the MSSM (light Higgs case) the best-fit point has a χ^2/ν of 87.2/82, while for the SM we find 102.8/88, thus the MSSM (light Higgs case) provides an equally good description of the data as the SM — the overall fit quality is even slightly better.

The largest χ^2 contribution in the SM comes from the inclusion of $(g-2)_\mu$, which shows a more than 3σ deviation from the SM prediction. Regarding the comparison of the results for the light Higgs case and the heavy Higgs case in the MSSM it should be noted that a sizeable part of the additional χ^2 contribution in the heavy Higgs case results from the $\text{BR}(B_u \rightarrow \tau \nu_\tau)$ measurement and from $(g-2)_\mu$. The agreement between theory and experiment for $\text{BR}(B_u \rightarrow \tau \nu_\tau)$ would improve with the inclusion of the new Belle measurement. The χ^2 contribution arising from $(g-2)_\mu$ for the heavy Higgs case of the MSSM could be improved if the second generation slepton parameters would be treated as additional free fit parameters or be set equal to the third generation slepton parameters (as we did in the updated analysis of the light Higgs case).

Thus, while the best description of the data is achieved if the new state discovered at the LHC is interpreted as the light \mathcal{CP} -even Higgs boson of the MSSM, the more “exotic”

interpretation in terms of the heavier \mathcal{CP} -even Higgs of the MSSM is also permitted by the data (at the time the original analysis was performed), even if the results from the Higgs searches at the LHC are supplemented with results from the Tevatron Higgs searches and with results from flavour physics and electroweak precision data. As we discussed earlier in this thesis, the latter interpretation would imply that also the other four Higgs bosons of the MSSM would be rather light. So far no additional Higgs boson has been seen at the LHC and stringent constraints on this scenario were set, in particular from charged Higgs searches. We are planning to update also the analysis of the heavy Higgs case, to see whether this interpretation can still provide a viable description of the current data.

In the light Higgs case, we find for the best-fit point of the full fit an enhancement of production times branching ratio for the $\gamma\gamma$ channels of about 40% (in the original analysis) and 20% (in the updated analysis) with respect to the SM prediction. Also in the heavy Higgs case a (small) enhancement of $\gamma\gamma$ is found. The rates in the $\gamma\gamma$ and VV channels are strongly correlated, however in most cases with the possibility of a stronger enhancement (or smaller suppression) in the $\gamma\gamma$ channel. Between the $\gamma\gamma$ channel and the $b\bar{b}$ channel an anti-correlation can be observed. This shows that a $\gamma\gamma$ enhancement can arise from a suppression of the $b\bar{b}$ channel. A suppression of the $b\bar{b}$ channel can (for both interpretations of the Higgs signal) be caused by a large value of Δ_b , which can reach values exceeding unity. In the original analysis the MSSM fits (both for the light and the heavy Higgs case) favour a scenario where the $b\bar{b}$ rate is suppressed, at least over parts of the preferred regions, while in the update fit a $b\bar{b}$ suppression is disfavoured. In the updated analysis the favoured regions for R_{bb}^h , $R_{\tau\tau}^h$ and R_{VV}^h are all restricted to values very close to 1 (the SM value).

In the light Higgs case, the $\gamma\gamma$ channel can be enhanced by the contribution of light scalar taus to the decay process. In the case where the lightest scalar tau mass is as low as ~ 100 GeV, we find an enhancement of up to 50% from this mechanism. This mechanism to enhance the $\gamma\gamma$ rate is favoured in the updated analysis. In the updated fit we assume a universal slepton mass parameter, consequently the $(g-2)_\mu$ measurement which favours light selectrons and smuons implies that also light staus are favoured.

For the scalar top masses, we find that the favoured regions start at $m_{\tilde{t}_1} \sim 200$ GeV and $m_{\tilde{t}_2} \sim 600$ GeV in the light Higgs case and at somewhat higher masses in the updated analysis. The mixing in the scalar top sector must exceed $|X_t/M_{\tilde{q}_3}| \sim 1$ for $M_{\tilde{q}_3}$ values within our scanned parameter range, where (in the original analysis) the most favoured region has $X_t/M_{\tilde{q}_3} = 2 - 2.5$. This region is wider in the updated analysis, since a $b\bar{b}$ suppression is no longer favoured. Similar values for the lower bounds on the scalar top masses are found in the heavy Higgs case. However, for this case we find that the favoured regions are also bounded from above by (roughly) $m_{\tilde{t}_2} \lesssim 1$ TeV.

It is evident from our analysis (as demonstrated e.g. by Figs. 7.1, 7.2 and 7.3), that the fitted rates in the MSSM interpretations are not significantly different from the SM predictions. Therefore very precise measurements of the rates of the observed Higgs boson will be necessary to gain sensitivity for distinguishing a MSSM Higgs boson from the SM one. New data for the ATLAS and CMS Higgs analyses will come next year.

It will be particularly important to investigate on the one hand potential deviations of the rates from the SM predictions and on the other hand the outcome of searches for additional non SM-like Higgs bosons. Confronting these results with predictions in the MSSM will show whether this model, whose unambiguous prediction of a light (and potentially SM-like) Higgs boson seems to be well supported by the current data, will continue to provide a good description of nature also in the future.

Chapter 8

Constraining SUSY scenarios using simplified models

The content of this chapter is based on Ref. [291]. I was strongly involved in the development of the code Fastlim and in all results presented in this chapter. I implemented and validated some of the analyses. I participated in generating the efficiency tables: I checked our event generation setup (done in MadGraph 5 [292] with Pythia 6 [78] using MLM merging) and I contributed with a code, reading the ATOM output and generating the efficiency tables in the Fastlim format. I generated the cross-section tables. I participated in the coding of Fastlim: I implemented e.g. the function calculating the CLs values, the files containing the information about the experimental analyses and parts of the output function. I was strongly involved in obtaining the results shown in Sect. 8.5 (the constraints from direct searches on the parameter space of “natural” SUSY models): I generated the grids, ran SUSY-HIT and FastLim and plotted the results. I partially used templates which I got from my collaborators.

8.1 Introduction

In the three years of the LHC operation, ATLAS and CMS conducted many direct SUSY searches, and limits on the SUSY parameter space have been set (as discussed in Sect. 4.2.3). The experimental collaborations have so far interpreted their results in specific models, e.g. the CMSSM, or various simplified models, while large parts of the high-dimensional SUSY parameter space remain unexplored. In phenomenological studies of SUSY models, as the ones presented in the previous chapters, it would be desirable to include the LHC constrains from direct SUSY searches.

Testing a BSM parameter point against direct LHC search results is generally possible. This is however a computationally intensive effort which requires generating (Monte-Carlo) events, running a detector simulation program and finally estimating the efficiencies in the signal regions of the searches of interest. In total it can take a few hours to test a single model point. The impact of LHC searches on certain BSM scenarios which have not been addressed by the LHC experiments, has been studied by several authors

following this procedure, see e.g. Refs. [293–296] (a more comprehensive list of references can be found in Ref. [291]). However, it is obvious that the number of parameter points which can be tested in this way is very limited by time and computing power. Testing each point of a large parameter scan is not feasible.

We have developed a new tool (**Fastlim**) which is simple to use and can calculate a conservative limit on a parameter point of a BSM model in less than a minute. The program makes use of simplified models, which provide the basis to decouple the (slow) Monte Carlo (MC) event generation and simulation steps necessary to estimate the efficiencies, from the (much faster) limit setting steps. The idea to use simplified models to constrain more complex models, has already been discussed in the literature [94, 297, 298]. In the first version of the code we implemented searches and topologies relevant for R-parity conserving SUSY models. The program can be generalised to R-parity violating models as well as to non-SUSY models, but in this chapter we will focus on R-parity conserving SUSY models.

The input of the program are the masses and decay branching ratios of SUSY particles which must be given in the **SLHA** [299] format. **Fastlim** does not perform any MC simulation. Instead, the program *reconstructs* the visible cross section, for each signal region of the implemented analyses, from the contributions of the relevant simplified event topologies, by interpolating the pre-calculated efficiency tables and the cross section tables, which are provided together with the program. The visible cross section in each signal region can be compared to the reported upper limit to decide whether a parameter point is excluded. In this approach, the reconstructed visible cross section can only be underestimated because only the available simplified topologies and searches are considered. Including additional topologies may only strengthen the bounds.

In order to demonstrate the utility of the program we study the constraints from the ATLAS 2013 missing energy searches on the “natural” SUSY parameter space, a class of SUSY models where the particles closely tied to the Higgs boson mass are relatively light, while the rest of the particle spectrum is assumed to be beyond the reach of the LHC. **Fastlim** version 1.0 contains a set of event topologies which can cover the “natural” SUSY model parameter space, however the same topologies appear also in other interesting SUSY models.

8.2 Methodology

8.2.1 The traditional “recasting” approach

In a cut-and-count based analysis, experimentalists define several sets of selection cuts, called signal regions, such that the SM events falling into these regions are suppressed whilst the signal events are enhanced. Based on their observation, the experiments provide the 95% CL upper limit on the number of allowed SUSY events over the SM background in signal region a . On the other hand, the SUSY contribution to the signal region a , $N_{\text{SUSY}}^{(a)}$, can be calculated as

$$N_{\text{SUSY}}^{(a)} = \epsilon^{(a)} \cdot \sigma_{\text{SUSY}} \cdot \mathcal{L}_{\text{int}}, \quad (8.1)$$

where $\epsilon^{(a)}$ is the efficiency for the signal region a , σ_{SUSY} is the inclusive SUSY cross section and \mathcal{L}_{int} is the integrated luminosity used in the analysis. Comparing the theoretical prediction with the reported upper limit, one can test the considered SUSY model point.

The efficiency and the cross section depend in general on the whole SUSY particle mass spectrum and the couplings. For the calculation of the SUSY cross section several public tools are available, e.g. `PROSPINO` [300] and `NLL fast` [301–305]. The efficiency must be estimated by a MC simulation, according to

$$\epsilon^{(a)} = \lim_{N_{\text{MC}} \rightarrow \infty} \frac{\# \text{ of events falling in signal region } a}{\# \text{ of generated events}}. \quad (8.2)$$

Therefore — in a first step — SUSY events have to be generated using an event generator like `Herwig` [77], `Pythia` [78, 79] or `MadGraph` [292]. The event samples are then passed to a fast detector simulation code (e.g. `Delphes` [306] and `PGS` [307]) which should be tuned beforehand to reproduce as accurately as possible the detector response and object reconstruction criteria for that analysis. Finally signal region cuts must be implemented, and the efficiency can then be estimated according to Eq. (8.2) using the detector level events.

This method is generic and in principle applicable to any model. However tuning the detector simulation, defining the reconstructed objects (often on a per analysis basis) and validating the code for the efficiency estimation, is a cumbersome task which becomes increasingly difficult as the analyses become more elaborate and the number of analyses increases¹. Another disadvantage of this method is the computation time. Neglecting the time needed to implement and validate the setup, the running time for the whole procedure, including the event generation and efficiency estimation, can easily take up to an hour per model point (of which the largest part of the time is used for the event generation/detector simulation). This becomes a crucial problem when a parameter scan is performed, requiring large computing facilities. In order to overcome this problem, leveraging on the idea of simplified topologies, we take a different approach, which is described in the next subsection.

¹There is a program, called `ATOM` [308], which takes an event file as input and evaluates the efficiencies, for a set of well-validated analyses, taking detector effects into account. A similar program is `CheckMate` [309]. For our work we make use of the `ATOM` framework, as we will explain below.

8.2.2 A new approach to calculate the visible cross section

We start by rewriting $N_{\text{SUSY}}^{(a)}$: the SUSY contribution can also be expressed as the sum of the contributions of all event topologies,

$$N_{\text{SUSY}}^{(a)} = \sum_i^{\text{all topologies}} \epsilon_i^{(a)} \cdot \sigma_i \cdot \mathcal{L}_{\text{int}}, \quad (8.3)$$

where $\epsilon_i^{(a)}$ is the efficiency for topology i (e.g. $i = pp \rightarrow \tilde{g}\tilde{g} \rightarrow qq\tilde{\chi}_1^0qq\tilde{\chi}_1^0, \dots$), which can be calculated in the same way as in Eq. (8.2) but using only the events with topology i . The cross section for topology i , σ_i , can be written as the product of the production cross section and the branching ratios for the decay chains (assuming the narrow width approximation holds). For instance, the visible cross section, $\sigma_{\text{vis}}^{(a)} \equiv N_{\text{SUSY}}^{(a)}/\mathcal{L}_{\text{int}}$, can be written as,

$$\begin{aligned} \sigma_{\text{vis}}^{(a)} = & \\ & \epsilon_{\tilde{g} \rightarrow qq\tilde{\chi}_1^0: \tilde{g} \rightarrow qq\tilde{\chi}_1^0}^{(a)}(m_{\tilde{g}}, m_{\tilde{\chi}_1^0}) \cdot \sigma_{\tilde{g}\tilde{g}}(m_{\tilde{g}}, m_{\tilde{q}}) \cdot (\text{BR}_{\tilde{g} \rightarrow qq\tilde{\chi}_1^0})^2 + \\ & \epsilon_{\tilde{q} \rightarrow q\tilde{\chi}_1^0: \tilde{q} \rightarrow q\tilde{\chi}_1^0}^{(a)}(m_{\tilde{q}}, m_{\tilde{\chi}_1^0}) \cdot \sigma_{\tilde{q}\tilde{q}}(m_{\tilde{g}}, m_{\tilde{q}}) \cdot (\text{BR}_{\tilde{q} \rightarrow q\tilde{\chi}_1^0})^2 + \\ & \epsilon_{\tilde{g} \rightarrow qq\tilde{\chi}_1^0: \tilde{q} \rightarrow q\tilde{\chi}_1^0}^{(a)}(m_{\tilde{g}}, m_{\tilde{q}}, m_{\tilde{\chi}_1^0}) \cdot \sigma_{\tilde{g}\tilde{q}}(m_{\tilde{g}}, m_{\tilde{q}}) \cdot \text{BR}_{\tilde{g} \rightarrow qq\tilde{\chi}_1^0} \cdot \text{BR}_{\tilde{q} \rightarrow q\tilde{\chi}_1^0} + \\ & \dots \end{aligned} \quad (8.4)$$

Unlike the $\epsilon_i^{(a)}$, the $\epsilon_i^{(a)}$ do not depend on all SUSY parameters but only on the masses and couplings of the particles appearing in topology i . The couplings modify only the angular distributions of the final state particle, but hardly alter the p_T of the final state objects. Since the LHC searches (which are still sufficiency inclusive) are not very sensitive to these effects, the dependence of the efficiency on the couplings is typically small [298]. In Eq. (8.4), the masses relevant to the efficiencies are written out explicitly.

If the decay chains in the topology i are sufficiency short, the $\epsilon_i^{(a)}$ depend only on few mass parameters. For such topologies, one can pre-calculate (using the recasting method described in Sect. 8.2.1) the $\epsilon_i^{(a)}(\mathbf{m}_i)$ for every grid point in the parameter space, $\mathbf{m}_i = \{m_i^{(1)}, m_i^{(2)}, \dots\}$, and tabulate the values. Once such tables are available, one can obtain the $\epsilon_i^{(a)}$ for any parameter point by interpolating between the grid points and by reconstructing the visible cross section according to Eq. (8.4), without having to generate MC events. In practice, it is computationally feasible to generate the efficiency tables only for topologies involving two or three different SUSY particles². Therefore, some of topologies might be neglected by the formula in Eq. (8.4) and in this case the reconstructed visible cross section is underestimated. This means that the derived limit is conservative. Detailed information on the currently available efficiency tables will be given in Sect. 8.4.2.

²In certain cases, topologies with more than three SUSY particles may be approximated by two or three dimensional topologies, as will be described in Sect. 8.3.3.

Similarly to the efficiency tables, **Fastlim** contains pre-calculated cross section tables for various production modes (more details in Sect. 8.3.1), and the cross section for any parameter point can be obtained by interpolation.

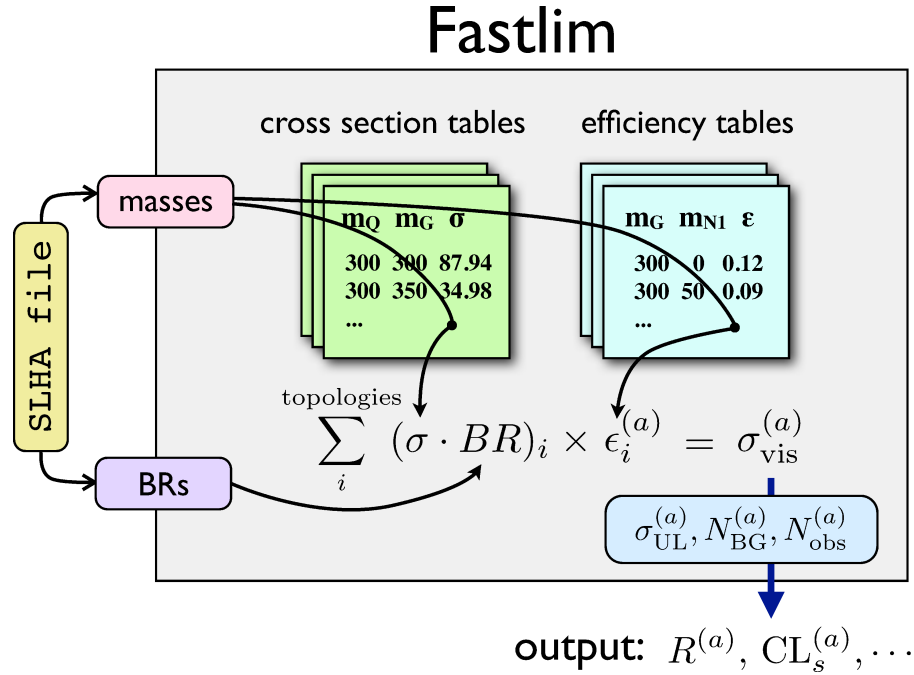


Figure 8.1: The structure of FastLim.

8.3 Functionality of the program Fastlim

This section explains the code `Fastlim`. More details (in particular how to use the program) can be found in [291].

8.3.1 The calculational procedure

The calculation procedure is as follows: The program goes through all the event topologies, starting with the SUSY particles specified in the main program file (e.g. $\tilde{g}\tilde{g}, \tilde{t}_1\tilde{t}_1, \dots$), and collects the branching ratios of each decay mode of the SUSY particles from the input SLHA file³. The cross sections are then obtained for the given production modes by interpolating the cross section tables. The cross sections of the event topologies, σ_i are calculated by multiplying the corresponding production cross sections with the branching ratios. In the next step, a loop through all the event topologies is performed, where the program checks whether efficiency tables exist for the event topology under consideration. If the corresponding efficiency tables are found, the efficiencies for all the signal regions are obtained by interpolation. The topologies, for which no efficiency tables are found, are not considered. The visible cross section for the topology, $\sigma_i^{(a)}$, is then calculated by multiplying the cross section and the efficiency. Summing over all topologies gives the total visible cross section, $\sigma_{\text{vis}}^{(a)}$, for the signal region a for each

³Here we make use of the code `PySLHA` [310] to extract the masses and branching ratios from the SLHA file

implemented analysis. Some relevant information has previously been extracted from the experimental papers, including the 95% confidence level (CL) upper limit on the visible cross section, $\sigma_{\text{UL}}^{(a)}$, the contribution of the SM background, $N_{\text{BG}}^{(a)}$, together with its uncertainty, the observed data, $N_{\text{obs}}^{(a)}$, and the luminosity used for the analysis. A convenient measure for the exclusion is the ratio between the visible cross section and its 95% CL upper limit

$$R^{(a)} \equiv \frac{\sigma_{\text{vis}}^{(a)}}{\sigma_{\text{UL}}^{(a)}}.$$

The model point is excluded at the 95% CL if $R^{(a)} > 1$. The program can also calculate the $CL_s^{(a)}$ variable [311] by comparing $N_{\text{obs}}^{(a)}$ and $N_{\text{BG}}^{(a)} + N_{\text{SUSY}}^{(a)}$ taking their uncertainties into account. The $CL_s^{(a)}$ provides a conservative exclusion p -value and the model point is excluded at the 95% CL if $CL_s^{(a)} < 0.05$.

The program outputs $R^{(a)}$ for all the signal regions and provides $CL_s^{(a)}$ if specified. If $R^{(a)} > 1$, it tells the user that the tested parameter point is excluded by signal region a . In the output it is also shown how much of the total cross section is covered by the implemented event topologies. This information is crucial, since the exclusion limit can be significantly underestimated, if the cross section of the implemented topologies is substantially smaller than the total SUSY cross section. A schematic diagram for the calculation procedure is shown in Fig. 8.1.

The efficiency and cross section tables are provided in the form of a standard text file so that new tables can be added straightforwardly. The efficiency tables installed in `Fastlim` 1.0 are generated by us using `MadGraph` 5 and `ATOM`. More details how the efficiency tables are obtained are given in the beginning of Sect. 8.4.2. The cross section tables should be provided for each production mode and centre of mass energy. In `Fastlim` 1.0, $\tilde{g}\tilde{g}$, $\tilde{g}\tilde{q}$, $\tilde{q}\tilde{q}$ and $\tilde{q}\tilde{q}^*$ cross sections and uncertainties are generated by `NLLfast` [301–305] combining different PDF sets, following the prescription described in Ref. [312]. For the stop and sbottom pair productions, the cross sections are taken from the values given by the SUSY Cross Section Working Group [313].

8.3.2 Nomenclature of the event topologies

We defined a naming scheme, such that each topology has a unique name. Since we will use these names later, we will shortly explain them here.

We assume that the SUSY particles are pair produced and that each SUSY particle decays into at most one other SUSY particle. This assumption is true for most R-parity conserving models⁴, but it is also realised in a large class of R-parity violating models. We use lower case letters for R-even particles and upper case letters for R-odd particles. The names for R-even and R-odd particles are given in Table 8.1.

By using the particle names in Table 8.1, one can assign a unique name to each event topology. Considering for example the event topology $pp \rightarrow \tilde{g}\tilde{g}$ followed by $\tilde{g} \rightarrow qq\tilde{\chi}_1^0$ on one side and $\tilde{g} \rightarrow tb\tilde{\chi}_1^\pm, \tilde{\chi}_1^\pm \rightarrow W^\pm\tilde{\chi}_1^0$ on the other: the string `GqqN1` describes the

⁴We do not consider the SUSY particle decays into three or more SUSY particles.

Particle	g	A	Z	h	H	A	W^\pm	H^\pm	q	t	b	e	μ	τ	ν
Name	g	gam	z	h	h2	h3	w	hp	q	t	b	e	m	ta	n
Particle	\tilde{g}	$\tilde{\chi}_1^0 \cdots \tilde{\chi}_4^0$	$\tilde{\chi}_1^\pm, \tilde{\chi}_2^\pm$	\tilde{q}	\tilde{t}_1, \tilde{t}_2	\tilde{b}_1, \tilde{b}_2	\tilde{e}	$\tilde{\mu}$	$\tilde{\tau}_1, \tilde{\tau}_2$	$\tilde{\nu}, \tilde{\nu}_\tau$					
Name	G	N1 \cdots N4	C1, C2	Q	T1, T2	B1, B2	E	M	TAU1, TAU2	NU, NUT					

Table 8.1: The names for the R-even (top) and R-odd (bottom) particles.

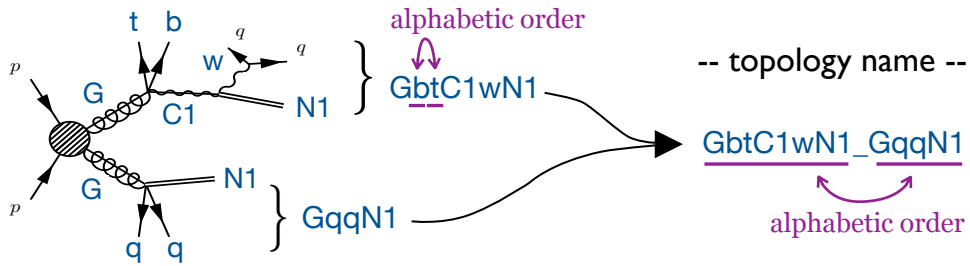


Figure 8.2: The naming scheme for the event topology.

first first decay chain and is generated by joining the particle names. In each decay, the mother SUSY particle comes first and the daughter SUSY particle comes, if existing, at the end. The SM particles are placed in between, in alphabetic order. With this rule, the string assigned to the second decay chain is uniquely determined as $GbtC1wN1$. Finally we connect the two strings in the alphabetic order and insert “_” in between, which defines the name $GbtC1wN1_GqqN1$ for this event topology (see Fig. 8.2).

In order to reduce the length of the topology name, we do not specify the decay of the SM particles because the decay branching ratios for the SM particles are fixed and independent of the SUSY parameters⁵. We also do not distinguish between light (s)quark flavours. Finally, we do not distinguish between particles and anti-particles.

8.3.3 Further approximations

Treatment of Soft Decays

Several SUSY models predict partially degenerate SUSY mass spectra. Examples are higgsino LSP scenarios, where higgsinos have similar masses, leading to almost degenerate $\tilde{\chi}_1^\pm$, $\tilde{\chi}_2^0$ and $\tilde{\chi}_1^0$. If one SUSY particle decays to another which has a similar mass, the SM particles produced in the decay tend to be very soft. These SM particles may not be observed in the detector because of the low detector acceptance and the recon-

⁵A possibility to take deviations in Higgs branching ratios from the SM values into account can be included in future `Fastlim` releases.

struction efficiencies. Even if such objects are reconstructed, they will hardly affect the signal region efficiencies since high- p_T cuts are employed in the SUSY searches. Therefore it is useful to truncate such a decay from a topology and redefine the topology as a shorter effective event topology, if this decay is associated with two nearly degenerate SUSY particles. Let us consider for example the topology `GbbC1qqN1_GbbC1qqN1`. If the chargino, `C1`, and the neutralino, `N1`, are mass degenerate, its efficiencies would be very similar to those of `GbbN1_GbbN1` because the light quarks from the chargino decays will be too soft to be separated from soft QCD radiation. Therefore (if the efficiency tables for `GbbC1qqN1_GbbC1qqN1` are not available) one can instead take the efficiencies from the `GbbN1_GbbN1` tables. In the current version of the program such a possibility is implemented by default for `N1`, `N2` and `C1` if their mass splitting is smaller than 10 GeV. Note that this replacement may introduce topologies in which the electric charge appears to be not conserved. For example, truncating `C1qqN1` in `GbbN1_GbtC1qqN1` introduces `GbbN1_GbtN1`.

Topologies with Similar Decay Structure

In general the \tilde{t}_2 and \tilde{t}_1 decay kinematics depend on their $\tilde{t}_{L,R}$ admixture. The top quarks coming from stop decays may be polarised depending on the $\tilde{t}_{L,R}$ admixture of the stop. However the `Fastlim` code provides the efficiencies only for unpolarised top quarks. Therefore the two topologies `T1tN1_T1tN1` and `T2tN1_T2tN1` are identical apart from the stop mass. We provide the efficiency tables only for `T1tN1_T1tN1` but use them for both `T1tN1_T1tN1` and `T2tN1_T2tN1`. The same efficiency tables can be used also for `B1tN1_B1tN1` and `B2tN1_B2tN1`, which may arise after truncating the soft chargino decays in `B1tC1qqN1_B1tC1qqN1` and `B2tC1qqN1_B2tC1qqN1`, respectively.

Reduction of Multidimensional Topologies

Let us now consider the event topology `GtT1tN1_GtT2tN1`, which involves four on-shell SUSY particles: `G`, `T2`, `T1`, `N1`. Thus in principle it requires four dimensional efficiency tables. However, if for example `T1` and `T2` are close in mass⁶ to each other, one may use the three-dimensional efficiency tables of `GtT1tN1_GtT1tN1`. By default, the efficiencies for `GtT1tN1_GtT2tN1` are taken from those for `GtT1tN1_GtT1tN1` if $(m_{\tilde{t}_2} - m_{\tilde{t}_1})/m_{\tilde{t}_2} < 0.1$. In that case, the average mass, $(m_{\tilde{t}_2} + m_{\tilde{t}_1})/2$, is used for the mass of the intermediate particle between `G` and `N1` in the interpolation.

⁶This is in principle possible, however many SUSY models require a large splitting in the stop sector in order to predict a realistic value for the Higgs boson mass.

8.4 Fastlim version 1.0

Name	Short description	E_{CM}	\mathcal{L}_{int}	# SRs
ATLAS_CONF_2013_024	0 lepton + 6(2 b-)jets + MET [Heavy stop]	8	20.5	3
ATLAS_CONF_2013_035	3 leptons + MET [EW production]	8	20.7	6
ATLAS_CONF_2013_037	1 lepton + 4(1 b-)jets + MET [Medium/heavy stop]	8	20.7	5
ATLAS_CONF_2013_047	0 leptons + 2-6 jets + MET [squarks & gluinos]	8	20.3	10
ATLAS_CONF_2013_048	2 leptons (+ jets) + MET [Medium stop]	8	20.3	4
ATLAS_CONF_2013_049	2 leptons + MET [EW production]	8	20.3	9
ATLAS_CONF_2013_053	0 leptons + 2 b-jets + MET [Sbottom/stop]	8	20.1	6
ATLAS_CONF_2013_054	0 leptons + ≥ 7 -10 jets + MET [squarks & gluinos]	8	20.3	19
ATLAS_CONF_2013_061	0-1 leptons + ≥ 3 b-jets + MET [3rd gen. squarks]	8	20.1	9
ATLAS_CONF_2013_062	1-2 leptons + 3-6 jets + MET [squarks & gluinos]	8	20.3	13
ATLAS_CONF_2013_093	1 lepton + bb(H) + Emiss [EW production]	8	20.3	2

Table 8.2: The analyses available in `Fastlim` version 1.0. The units for the centre of mass energy, E_{CM} , and the integrated luminosity, \mathcal{L}_{int} , are TeV and fb^{-1} , respectively. The number of signal regions in each analysis and the references are also shown.

8.4.1 The available analyses

Most of the standard E_T^{miss} (MET)-based searches published by ATLAS in 2013 are available in the first `Fastlim` version. The list of the available analyses together with short descriptions, the centre of mass energies, the luminosities and the number of signal regions in the analysis are listed in Table 8.2. The SUSY searches carried out by CMS will be included in a future release.

We have implemented the analyses given in Table 8.2 into the `ATOM` framework. The validation has been done using the cut-flow tables provided by ATLAS (when they are available⁷), and the validation results can be found in Refs. [291,314].

8.4.2 The implemented event topologies

The efficiency tables installed in `Fastlim` have been generated as follows: $5 \cdot 10^4$ events have been generated using `MadGraph 5` [292] for each grid point in the respective mass plane (independent of the topology and the mass spectrum). The samples include up to one extra hard parton emission at the matrix element level, matched to the parton

⁷In the cases where no cut-flow tables were available, we validated our implementations by checking two independent implementations or by comparing to the simplified model exclusion plots.

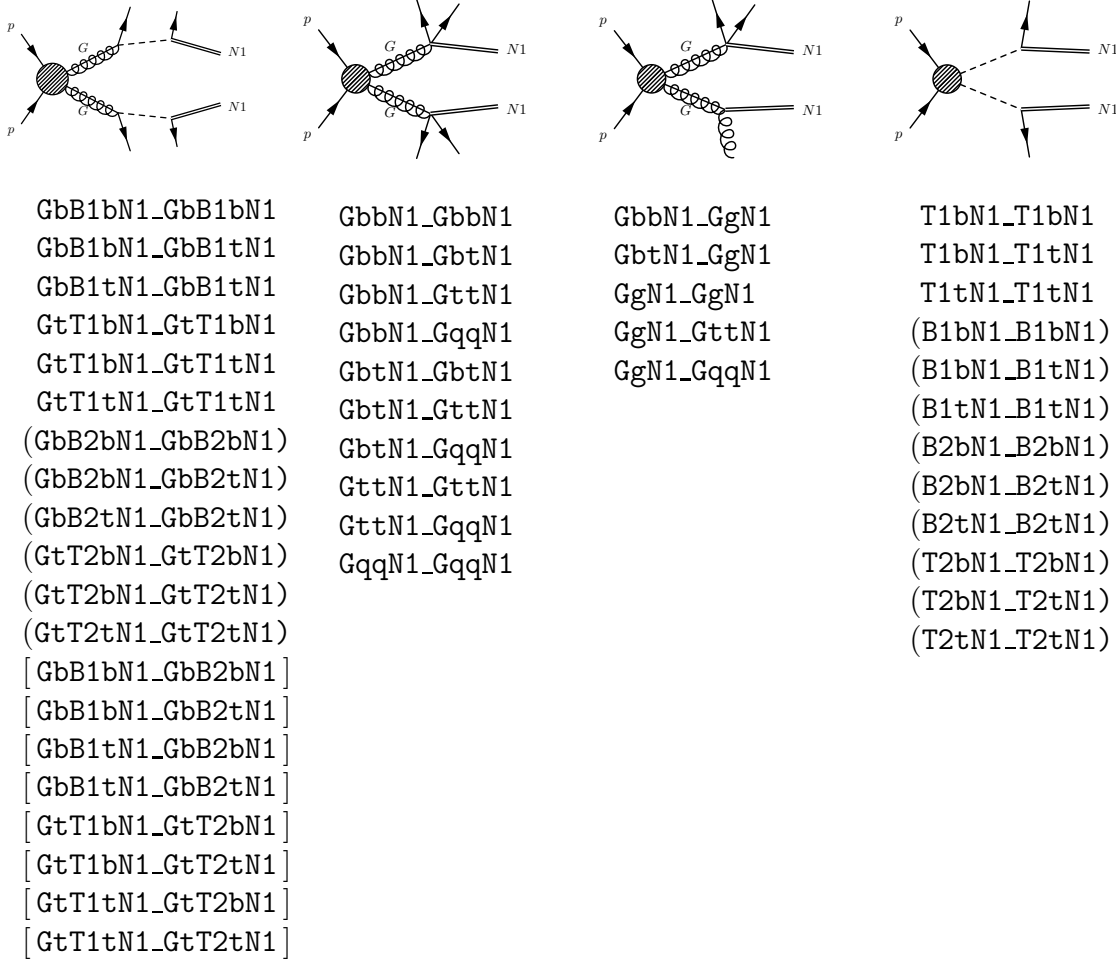


Figure 8.3: The event topologies whose efficiency tables are implemented in `Fastlim` version 1.0. The round bracket means that the efficiencies for the topology can be taken from the efficiency tables for one of the other topologies in the same group. On the other hand, the square bracket means that the efficiencies can be obtained only when the two intermediate SUSY masses are close ($m_{B1} \simeq m_{B2}$ or $m_{T1} \simeq m_{T2}$).

shower (carried out by `Pythia 6` [78]) using the MLM merging scheme [315], where the merging scale is set at $m_{\text{SUSY}}/4$ with m_{SUSY} being the mass of the heavier SUSY particle in the production. The event files are then passed to `ATOM` [308], which evaluates the efficiencies for various signal regions (of the analyses given in Sect. 8.4.1) taking the detector effects into account.

`Fastlim 1.0` contains the efficiency tables for a set of event topologies which are listed in Fig. 8.3. These topologies provide a good coverage of the “natural” SUSY model parameter space, as we will show explicitly in Sect. 8.5. In Fig. 8.3, round brackets indicate that the efficiencies for this topology can be taken from one of the other topologies in the same group (e.g. the topology `T2tN1_T2tN1` can use the efficiency tables of `T1tN1_T1tN1`

as discussed in Sect. 8.3.3). The square bracket means that the efficiencies of this event topology can be obtained from another topology only if the condition $m_{\mathbf{B1}} \simeq m_{\mathbf{B2}}$ or $m_{\mathbf{T1}} \simeq m_{\mathbf{T2}}$ is satisfied (see Sect. 8.3.3 for more details.). There are several event topologies in which the electric charge appears not to be conserved. These topologies can appear after the soft decays are truncated as mentioned in Sect. 8.3.3. We include also the loop induced decay $\mathbf{G} \rightarrow \mathbf{gN1}$ (via a stop-top loop), which can have a sizeable branching fraction if the two-body modes and $\mathbf{GttN1}$ are kinematically forbidden. The rate of this decay is enhanced if the stop and higgsino masses are small and the trilinear coupling A_t is large. These conditions may be found in “natural” SUSY models.

Although the event topologies are chosen to cover “natural” SUSY models, many of the topologies appear also in other models. A large rate of the gluino pair production is relatively common in a wide range of the SUSY models because the gluino has the largest colour factor among the MSSM particles. Many high-scale models tend to predict light stops, since in the RGE running of the Higgs soft SUSY breaking parameter \tilde{m}_2 down to lower scales, radiative corrections occur involving terms proportional to the squared stop masses (as we will show explicitly in Sect. 8.5). The electroweak symmetry breaking conditions suggest that the stops should be light, since otherwise large cancellations would be needed (see also Sect. 2.2.10).

Additional topologies are being evaluated and will become available soon. The incorporation of externally produced efficiency maps for additional topologies is straightforward.

8.5 Constraints from direct searches on “natural” SUSY models

In this section, we study the constraints from direct SUSY searches conducted by ATLAS on “natural” SUSY models (a well studied region of the SUSY parameter space [57, 316–324]) using `Fastlim`.

The requirements for “natural” SUSY can be investigated based on the electroweak symmetry breaking condition

$$M_Z^2 = -2(\tilde{m}_2^2 + |\mu|^2) + \mathcal{O}(\cot^2 \beta), \quad (8.5)$$

which follows from the requirement that the Higgs potential (see Eq. (2.54)) has a minimum which breaks the electroweak symmetry. This condition implies that the parameter μ controlling the higgsino mass, and the soft mass of the up-type Higgs, \tilde{m}_2 , should not be too far from M_Z at the electroweak scale, otherwise a precise cancellation is required among these parameters. The most relevant one- and two-loop corrections to the mass \tilde{m}_2 stem from stops and gluinos. Consequently these SUSY particles should not be too far away from the electroweak scale, and we define “natural” SUSY models as a class of spectra where only the gluino, left-handed stops and sbottoms, right-handed stops and higgsinos (whose masses are given by the parameters $m_{\tilde{g}}$, M_{Q_3} , M_{U_3} and μ) are at energy scales accessible at the LHC while the other sparticles are assumed to be heavy (since the fine tuning condition (8.5) is not very sensitive to their masses). For the study below we fix the soft masses of the other sparticles at 3 TeV⁸.

We calculate the sparticle spectrum and branching ratios using `SUSY-HIT` [325]. For the results in this section, we generated two-dimensional grids (with $\sim 500 - 1000$ points) covering slices of “natural” SUSY parameter space. The constraints presented below are obtained by interpolating (with `Mathematica`) between the grid points. By using `Fastlim` performing the whole study presented in this section with 4836 parameter points took 18.7 hours (14 seconds per model point on average) on a single computer.

In Fig. 8.4, we show the direct SUSY search constraints on the (M_{U_3}, μ) plane. For one specific analysis the 95% CL exclusion is obtained by comparing the calculated value for the visible cross section for a certain parameter point with its 95% CL upper limit (see Eq. (8.3.1)) in the signal region which has the highest sensitivity. We do not combine several signal regions. In the left plot of Fig. 8.4 (and in following plots of that type) we show (superimposed) the 95% CL exclusion regions from several analyses.

In this model only the right-handed stop and the higgsinos are light, while all other particles are decoupled; we fix the other parameters as $M_{Q_3} = m_{\tilde{g}} = 3$ TeV, $\tan \beta = 10$, $X_t \equiv A_t - \mu \cot \beta = 0$. The right plot of Fig. 8.4 shows the cross section coverage

$$\text{Coverage} = \frac{\sum_i^{\text{implemented}} \sigma_i}{\sigma_{\text{tot}}}, \quad (8.6)$$

where the numerator is the sum of the cross sections of the topologies implemented in

⁸Throughout this section we set: $M_1 = M_2 = M_{Q,D,U_{12}} = M_{D_3} = 3000$ GeV, $X_b = X_t$.

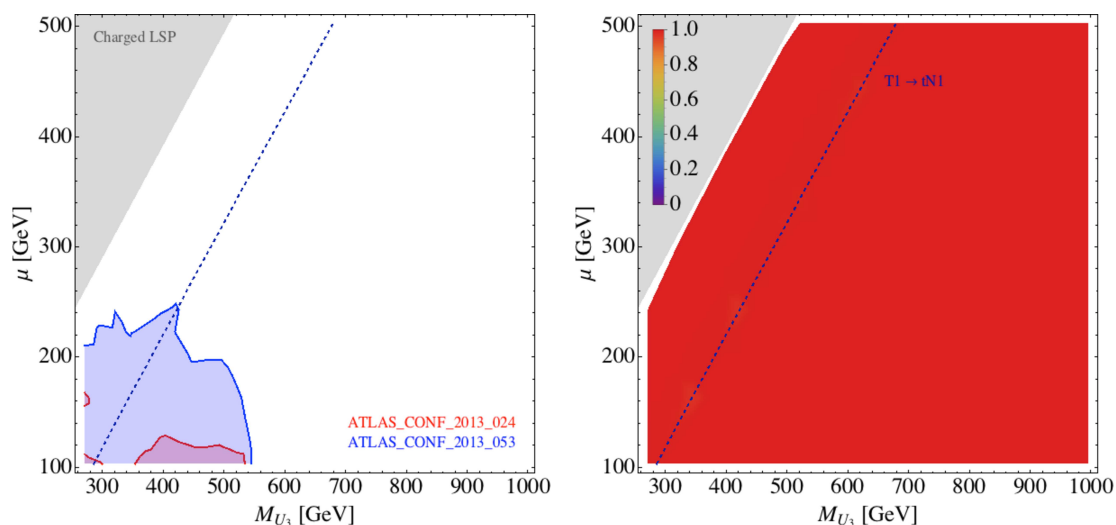


Figure 8.4: Constraints from direct SUSY searches on the (M_{U_3}, μ) plane. The other parameters are $m_{\tilde{g}} = M_{Q_3} = 3000$ GeV, $\tan\beta = 10$ and $X_t = 0$. The left plot shows the exclusion regions from the analyses listed in the plot. The right plot shows the cross section coverage, as defined in Eq. (8.6). The blue dashed line represents the kinematical threshold of the $T1 \rightarrow \tau N1$ decay.

Fastlim 1.0 (as specified in Sect. 8.4.2). As can be seen, **Fastlim** has a almost perfect coverage on this parameter slice.

In this model, the dominant processes are $T1bN1_T1bN1$, $T1bN1_T1\tau N1$ and $T1\tau N1_T1\tau N1$, after truncating the soft decays among the higgsino states, meaning $C1, N2 \rightarrow N1$. All three of these decays are governed by the top Yukawa coupling. The blue dashed line represents the kinematical limit of the $T1 \rightarrow \tau N1$ decay. The topology $T1bN1_T1bN1$ (arising after the truncation of $C1$ on both decay branches) dominates on the left hand side of this line. On the right hand side, the phase space and symmetry factors give the relation $\sigma(T1bN1_T1\tau N1) > \sigma(T1bN1_T1bN1) > \sigma(T1\tau N1_T1\tau N1)$. In the grey region, the \tilde{t}_1 becomes lighter than the $\tilde{\chi}_1^0$, thus the spectrum has a charged LSP. We therefore do not consider this region. The white gap in the right plot of Fig. 8.4 between the grey and the coloured region results from the grid spacing and the **Mathematica** interpolation. This artefact would disappear with a finer grid.

The left plot of Fig. 8.4 shows the constraints from the SUSY searches implemented in **Fastlim** 1.0 (see Table 8.2). In this plot (and the following ones of the same type) only the names of the analyses providing an exclusion are listed on the plot, using the same colour as the exclusion contour. The exclusion regions are plotted in descending order, starting with the top one in the list. As can be seen, only the analyses ATLAS_CONF_2013_024 and ATLAS_CONF_2013_053 exclude a region in this mass plane. ATLAS_CONF_2013_024 is designed to constrain the $T1\tau N1_T1\tau N1$ topology targeting the fully-hadronic top decays. Because $T1\tau N1_T1\tau N1$ is subdominant here, the constraint from this analysis is weaker than the corresponding exclusion plot in Ref. [326] assuming

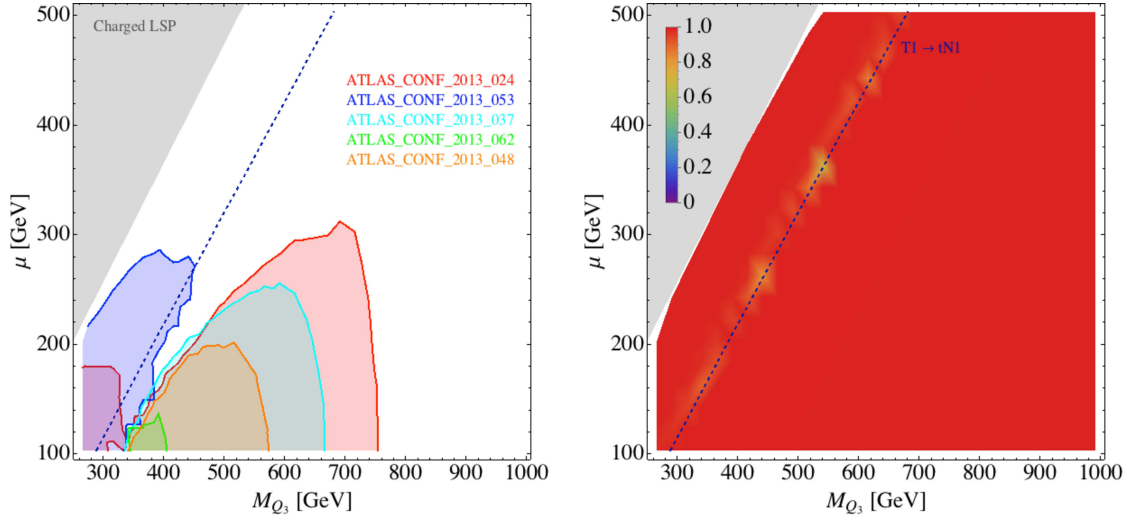


Figure 8.5: Constraints from direct SUSY searches on the (M_{Q_3}, μ) plane. The other parameters are $m_{\tilde{g}} = M_{U_3} = 3000$ GeV, $\tan\beta = 10$ and $X_t = 0$. The left plot shows the exclusion regions from the analyses listed in the plot. The right plot shows the cross section coverage, as defined in Eq. (8.6). The blue dashed line represents the kinematical threshold of the $T1 \rightarrow \tau N1$ decay.

$\text{Br}(\tilde{t}_1 \rightarrow t\tilde{\chi}_1^0) = 1$. ATLAS_CONF_2013_053 (looking for exactly two jets originating from b -quarks), on the other hand, has been designed for the $B1bN1_B1bN1$ topology. Since in this “natural” SUSY model, $T1bN1_T1bN1$ has the largest/second largest rate among the possible topologies depending on the parameter region, this analysis gives a strong exclusion. It roughly excludes $M_{U_3} < 500$ GeV with $\mu < 200$ GeV.

Fig. 8.5 shows the exclusion (left plot) and the cross section coverage (right plot) for the (M_{Q_3}, μ) plane. The other parameters are chosen as $M_{U_3} = m_{\tilde{g}} = 3$ TeV, $X_t = 0$ and $\tan\beta = 10$. The small M_{Q_3} values result in both light \tilde{t}_L and light \tilde{b}_L . The \tilde{t}_L is slightly heavier than the \tilde{b}_L because of the contribution from the top quark mass to Eq. (2.43). Here again the blue dashed line represents the kinematical threshold of the $T1 \rightarrow \tau N1$ decay. On the left hand side of the blue dashed line, $T1bN1_T1bN1$ and $B1bN1_B1bN1$ dominate. If kinematically allowed (on the right hand side of the blue line) the \tilde{t}_L and \tilde{b}_L decay preferably to t_R and \tilde{H}_2 while the $T1 \rightarrow bN1$ and $B1 \rightarrow bN1$ modes are instead suppressed by the bottom Yukawa coupling. The right plot of Fig. 8.5 shows that the coverage is slightly below 100% near the $T1 \rightarrow \tau N1$ kinematical threshold line, where the three-body $T1 \rightarrow qqB1$ decay via an off-shell W boson takes a small branching fraction.

From the left plot of Fig. 8.5, one can see that ATLAS_CONF_2013_053 mainly constrains the left hand side of the blue dashed line. This can be understood because the analysis is tailored for the $T1bN1_T1bN1$ and $B1bN1_B1bN1$ topologies. On the other side of the blue dashed line, the $T1tN1_T1tN1$ and $B1tN1_B1tN1$ topologies dominate, and in this region, ATLAS_CONF_2013_024 (and ATLAS_CONF_2013_037) are particularly constraining because they are designed for the hadronic-hadronic (and hadronic-leptonic)

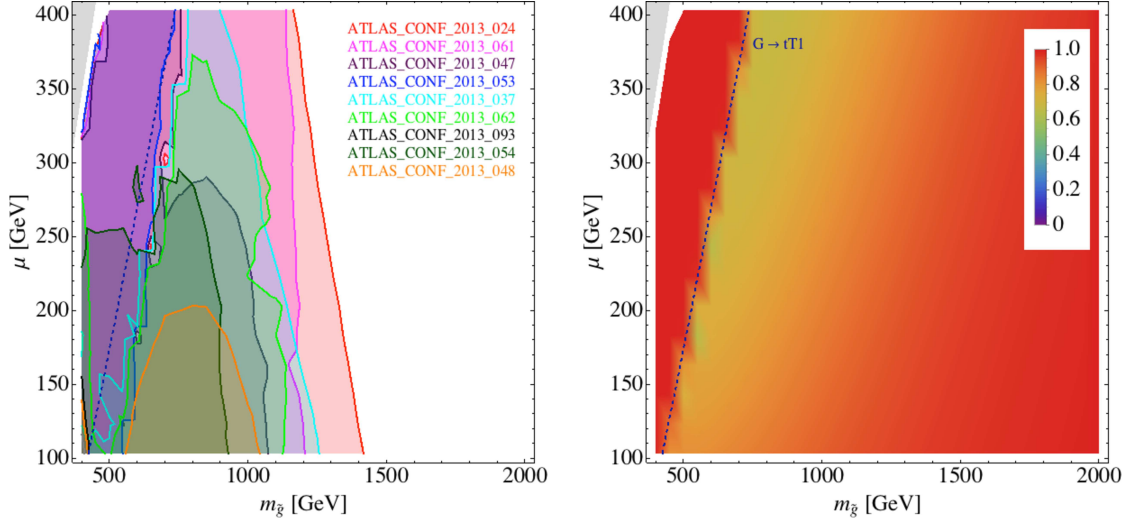


Figure 8.6: Constraints from direct SUSY searches on the $(m_{\tilde{g}}, \mu)$ plane. The other parameters are $M_{U_3} = 3000$ GeV, $\tan\beta = 10$ and $X_t = 0$. M_{Q_3} is chosen such that the \tilde{t}_1 mass is in the middle between the \tilde{g} and $\tilde{\chi}_1^0$ mass ($M_{Q_3} \simeq (m_{\tilde{t}_1}^2 - m_t^2)^{1/2}$ with $m_{\tilde{t}_1} = (m_{\tilde{g}} + \mu)/2$). The left plot shows the exclusion regions from the analyses listed in the plot. The right plot shows the cross section coverage, as defined in Eq. (8.6). The blue dashed line represents the kinematical threshold of the $G \rightarrow tT1$ decay.

top modes for the $T1tN1_T1tN1$ topology. ATLAS_CONF_2013_024 excludes M_{Q_3} values from ~ 400 up to 750 GeV for $\mu \lesssim 250$ GeV at the 95% CL. Because of the transition between different dominant decay modes, there is a gap in the exclusion region near the blue dashed line. In this particular region, $M_{Q_3} = 400$ GeV and $\mu = 200$ GeV is still allowed by all the analyses implemented in **Fastlim**.

Fig. 8.6 shows the exclusion (left plot) and the cross section coverage (right plot) in the $(m_{\tilde{g}}, \mu)$ plane. Here, we set $M_{U_3} = 3$ TeV, $\tan\beta = 10$, $X_t = 0$. M_{Q_3} is chosen such that the \tilde{t}_1 mass is roughly in the middle between the \tilde{g} and $\tilde{\chi}_1^0$ mass: $M_{Q_3} \simeq (m_{\tilde{t}_1}^2 - m_t^2)^{1/2}$ with $m_{\tilde{t}_1} = (m_{\tilde{g}} + \mu)/2$. This condition links the stop and sbottom masses to the gluino and higgsino masses. This connection is also visible from the line indicating the kinematical threshold for the $G \rightarrow tT1$ decay. The right plot of Fig. 8.6 shows that the coverage degrades to $\sim 70\%$ at the right hand side of the $G \rightarrow tT1$ threshold line. In this region, asymmetric gluino decays e.g. $GbB1tN1_GtT1tN1$ are relevant. This topology requires four-dimensional grids and is therefore not implemented in **Fastlim**.

Nevertheless, one can see from the left plot of Fig. 8.6 that many analyses exclude regions in this parameter slice because of the large cross section of the gluino pair production. Among them, ATLAS_CONF_2013_024 and ATLAS_CONF_2013_061 yield the most stringent constraints. Since ATLAS_CONF_2013_024 mainly constrains the $T1tN1_T1tN1$ and $B1tN1_B1tN1$ topologies, the bound from this analysis on the gluino mass gradually decreases as the stop and sbottom masses increase with the higgsino mass value. Here, ATLAS_CONF_2013_024 excludes $m_{\tilde{t}_1} \lesssim 750$ GeV. On the other hand, the

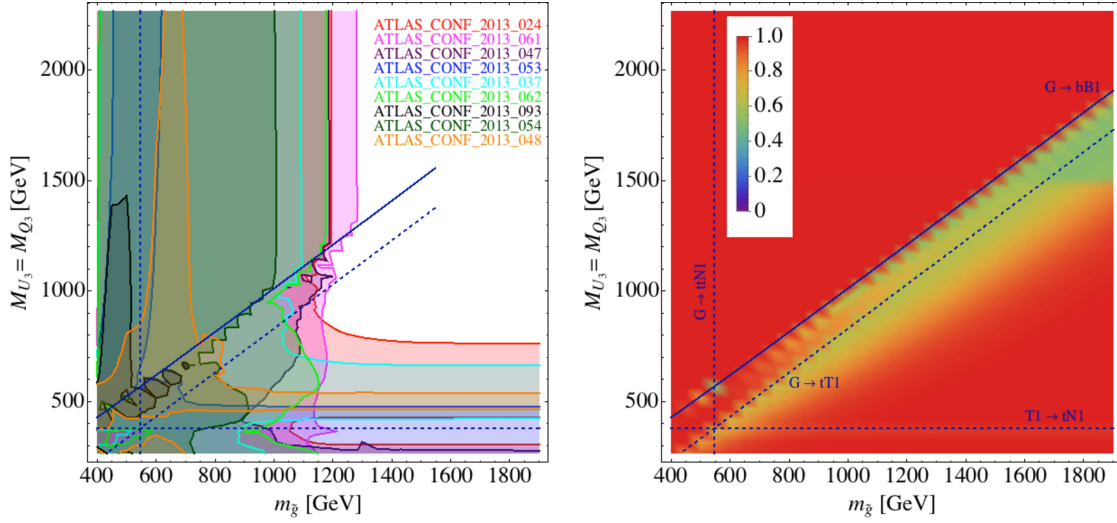


Figure 8.7: Constraints from direct SUSY searches on the $(m_{\tilde{g}}, M_{U_3/Q_3})$ plane. We set $\tan\beta = 10$, $\mu = 200$ GeV and $X_t = 0$. The left plot shows the exclusion regions from the analyses listed in the plot. The right plot shows the cross section coverage, as defined in Eq. (8.6). The blue lines represent kinematical thresholds.

limit from ATLAS_CONF_2013_061 is almost independent of the higgsino mass. This analysis looks for events with 0-1 lepton plus ≥ 3 b -jets, targeting the gluino pair production processes with the gluino decaying to the third generation quarks either through an on- and off-shell \tilde{t}_1 or \tilde{b}_1 . The analysis roughly excludes a 1.2 TeV gluino regardless of the value of μ at the 95% CL.

We now look at the constraint on the $(m_{\tilde{g}}, M_{U_3/Q_3})$ plane, where we take $M_{U_3} = M_{Q_3}$, $\mu = 200$ GeV, $\tan\beta = 10$, $X_t = 0$. The right plot of Fig. 8.7 shows that the cross section coverage decreases to $\sim 60\%$ in the region around the $G \rightarrow t\bar{t}1$ threshold line. Here, as before, the asymmetric gluino decays (e.g. $Gb\bar{b}1bN1_Gt\bar{t}1tN1$ in the region slightly above the $G \rightarrow t\bar{t}1$ threshold line, and e.g. $Gb\bar{b}1bN1_GttN1$ slightly below the line) become sizeable. One can see from the left plot of Fig. 8.7 that the exclusions on the gluino mass and the stop mass are roughly independent of each other. The gluino mass is excluded up to 1280 GeV, almost independently of the stop mass⁹. The most stringent constraint on the gluino mass comes from ATLAS_CONF_2013_061. The soft mass parameters for the third generation squarks are, on the other hand, constrained up to 750 GeV where the strongest limit comes again from the ATLAS_CONF_2013_024 analysis, constraining the stop production processes independently of the gluino mass.

In Fig. 8.8, we investigate the $\tan\beta$ dependence of the M_{Q_3} limit. In this parameter plane, the cross section coverage is $\sim 100\%$ everywhere. The other parameters are fixed as $\mu = 200$ GeV, $X_t = 0$ and $M_{U_3} = m_{\tilde{g}} = 3$ TeV. This parameter plane intersects

⁹Here (and more generally in the discussion of the plots in this section) the exclusion refers to the 95% CL exclusion given by the analysis that is most sensitive in that region.

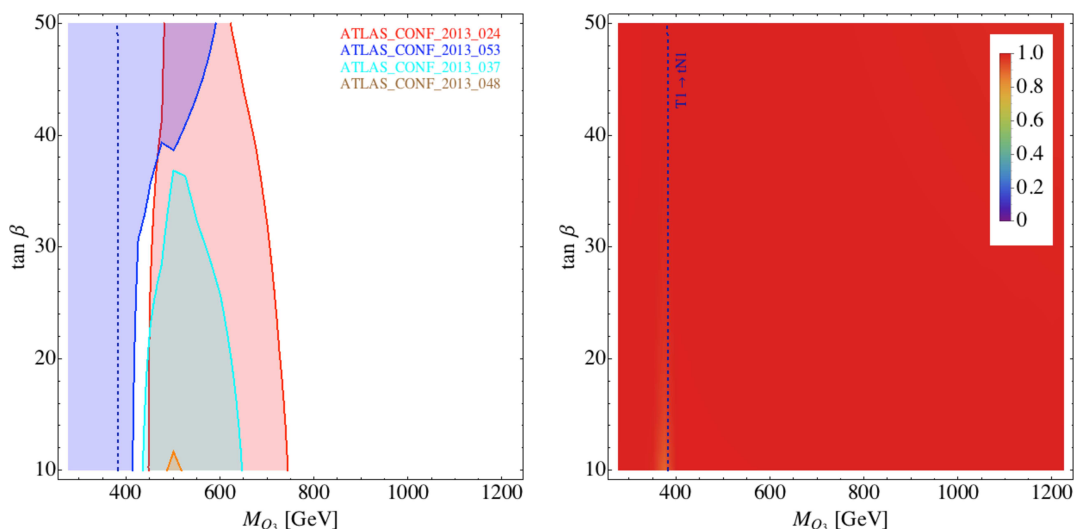


Figure 8.8: Constraints from direct SUSY searches on the $(M_{Q_3}, \tan \beta)$ plane. The other parameters are $M_{U_3} = m_{\tilde{g}} = 3000$ GeV, $\mu = 200$ GeV and $X_t = 0$. The left plot shows the exclusion regions from the analyses listed in the plot. The right plot shows the cross section coverage, as defined in Eq. (8.6). The blue dashed line represents the kinematical threshold of the $T1 \rightarrow \tau N1$ decay.

the one of Fig. 8.5 at $\mu = 200$ GeV and $\tan \beta = 10$. The gap observed in the left plot of Fig. 8.5 around $M_{Q_3} \simeq 400$ GeV, $\mu = 200$ GeV is also visible here. The size of $\tan \beta$ affects the branching fractions of the $T1 \rightarrow \mathbf{b}N1$ and $B1 \rightarrow \mathbf{b}N1$ modes since these decays are dictated by the bottom Yukawa coupling. From $\tan \beta = 10$ to 50, $\text{BR}(B1 \rightarrow \mathbf{b}N1)$ changes from 0% to 28% (for $M_{Q_3} \simeq 500$ GeV). Because of this effect, the constraint from ATLAS_CONF_2013_053 gets stronger as $\tan \beta$ increases. Consequently, the gap closes for $\tan \beta \gtrsim 40$. In the large M_{Q_3} region, the strongest limit comes again from ATLAS_CONF_2013_024, designed for $T1 \rightarrow \mathbf{t}N1$ modes. However, increasing $\tan \beta$ the $T1 \rightarrow \mathbf{t}N1/B1 \rightarrow \mathbf{t}N1$ rates decrease ($T1 \rightarrow \mathbf{b}N1/B1 \rightarrow \mathbf{b}N1$ rates increase), and the exclusion from ATLAS_CONF_2013_024 gets weaker: varying $\tan \beta$ from 10 to 50, the limit on M_{Q_3} changes from 750 GeV to 620 GeV.

We finally show the exclusion for the $(A_t, (M_{U_3}^2 + M_{Q_3}^2)^{1/2})$ parameter plane in Fig. 8.9. Considering a model where the parameters are defined at a scale Λ , the radiative correction (to the RGE running) lead to the up-type Higgs soft mass term [327]¹⁰

$$\delta \tilde{m}_2^2 \simeq -\frac{3y_t^2}{8\pi^2} (M_{U_3}^2 + M_{Q_3}^2 + |A_t|^2) \log \left(\frac{\Lambda}{m_{\tilde{t}}} \right). \quad (8.7)$$

Thus in the $(A_t, (M_{U_3}^2 + M_{Q_3}^2)^{1/2})$ parameter plane, the distance from the origin roughly provides an indication for the size of the fine tuning. We take $M_{U_3} = M_{Q_3}$ in the

¹⁰Radiative electroweak symmetry breaking was briefly discussed in Sect. 2.2.10. In this formula the running of the soft masses is neglected.

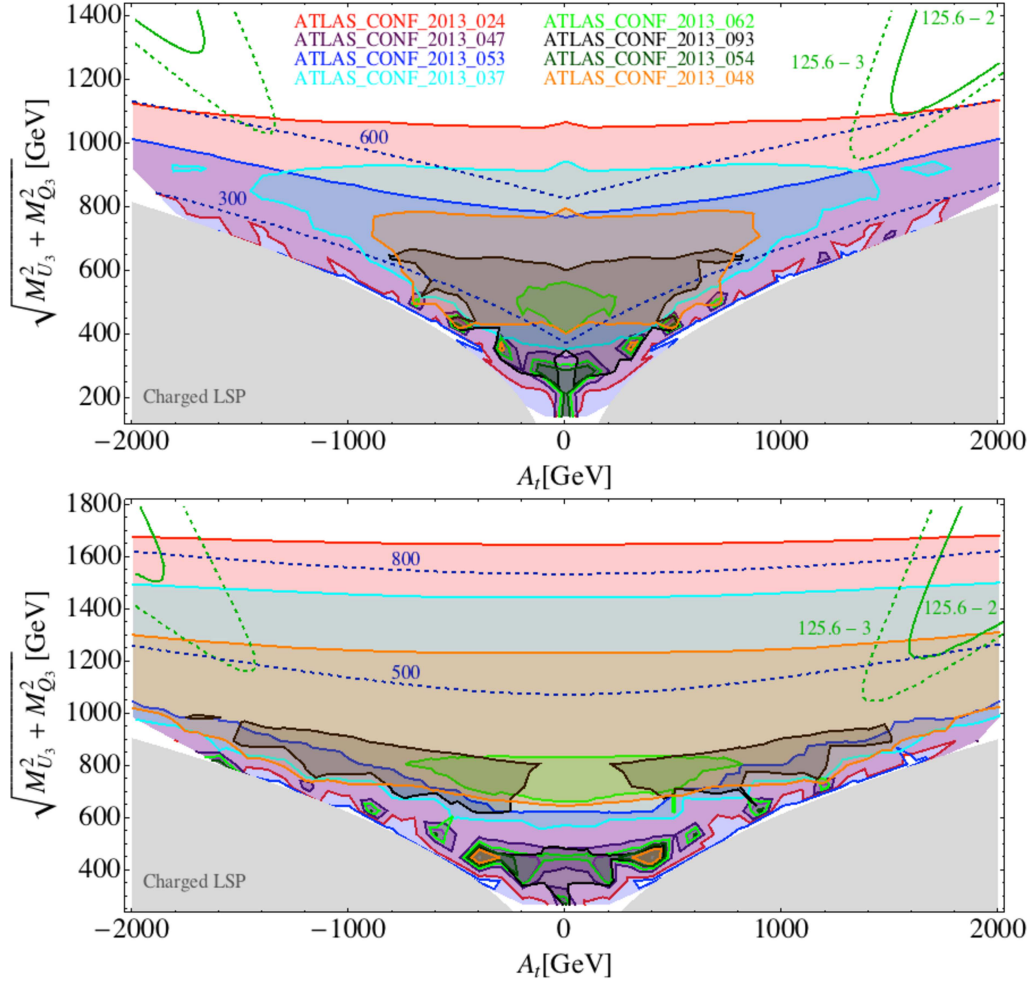


Figure 8.9: Constraints from direct SUSY searches on the $(A_t, (M_{U_3}^2 + M_{Q_3}^2)^{1/2})$ plane. In the upper plot we choose $M_{U_3} = M_{Q_3}$ and in the lower one $M_{U_3} = 2 M_{Q_3}$. The other parameters are $m_{\tilde{g}} = 3000$ GeV, $\tan \beta = 10$, $\mu = 100$ GeV. Both plots show the exclusion regions from the analyses listed in the upper plot. The blue dashed curves show the \tilde{t}_1 mass contours. The green curves represent the Higgs mass contours, where we allow 3 (dashed) and 2 (solid) GeV deviation from the central observed value 125.6 GeV. Note the difference in scale on the y-axis.

upper plot, whereas $M_{U_3} = 2 M_{Q_3}$ is chosen in the lower plot. The other parameters are $m_{\tilde{g}} = 3000$ GeV, $\mu = 100$ GeV, $\tan \beta = 10$.

As can be seen, ATLAS_CONF_2013_024 again places the most stringent limit on the soft mass for the third generation squarks, both for the $M_{U_3}/M_{Q_3} = 1$ and $M_{U_3}/M_{Q_3} = 2$ cases. The blue dashed lines show the \tilde{t}_1 mass contours. One can see that the exclusion limit on $(M_{U_3}^2 + M_{Q_3}^2)^{1/2}$ does not change much when A_t is varied, even though the limit on the \tilde{t}_1 mass changes from 780 to 600 GeV when varying $|A_t|$ from 0 to 2 TeV (for $(M_{U_3}^2 + M_{Q_3}^2)^{1/2} \simeq 1$ TeV) in the $M_{U_3}/M_{Q_3} = 1$ scenario. The mass splitting between \tilde{t}_1

and \tilde{t}_2 get larger when $|A_t|$ is increased. However, the changes in the cross section times efficiency from the $\tilde{t}_1\tilde{t}_1^*$ and $\tilde{t}_2\tilde{t}_2^*$ processes tend to cancel each other, and the resulting visible cross sections are relatively stable against the variation of $|A_t|$. For $M_{U_3}/M_{Q_3} = 2$ scenario, \tilde{t}_1 is mostly composed of \tilde{t}_L and the dependence of the \tilde{t}_1 mass on the $|A_t|$ variation itself is rather mild.

The green curves show the Higgs mass contours, where we allow for 3 (dashed) and 2 (solid) GeV deviation from the central observed value 125.6 GeV, taking the theory uncertainties into account. We have calculated the Higgs mass using `FeynHiggs 2.9.4` [29]. In the $M_{U_3}/M_{Q_3} = 1$ scenario, most of the parameter space is constrained more stringently by the Higgs mass measurement than by direct SUSY searches. On the other hand, in the $M_{U_3}/M_{Q_3} = 2$ scenario the ATLAS_CONF_2013_024 analysis excludes (at 95% CL) a significant part of the parameter space where the Higgs mass condition is satisfied.

8.6 Summary and future plans

In this chapter we described a new computer tool, `Fastlim`, and we demonstrate its usability by discussing a first application. `Fastlim` can calculate limits from direct LHC searches on the BSM parameter space. The first version of this tool can be used to constrain R-parity conserving SUSY models, but the structure of the program allows for a generalisation also to other BSM models. The key idea of the program is that it reconstructs the visible cross section (in the signal regions of the considered analyses) by adding up the contributions from different simplified event topologies. This approach enables the user to get visible cross sections without running any Monte-Carlo event generation or detector simulation. Our program takes an `SLHA` input file and then reads off, and interpolates between, pre-calculated cross section tables and efficiency tables (for simplified model topologies), which are provided with the code.

We presented a minimal and intuitive naming scheme, which assigns a unique name to every event topology. Further we discussed useful approximations, which enhance the applicability of `Fastlim`.

As a first application of our program, we study the sensitivity of the recent direct SUSY searches, performed at the LHC at 8 TeV, to the parameter space of “natural” SUSY models. We have shown the constraints from the ATLAS 2013 missing energy searches on two dimensional parameter slices of “natural” SUSY models. We found that direct LHC SUSY searches (at 8 TeV) can give more stringent constraints than the observation of a Higgs signal at ~ 125.6 GeV in some regions of the “natural” SUSY parameter space. This was not the case when the exclusion from the 7 TeV data was analysed [316].

Adding additional topologies and experimental analyses in the `Fastlim` framework is straightforward. We are working on producing efficiency tables for more topologies, which will be included in future updates, thus extending the applicability of the program. Recasting LHC analyses to extend the number of topologies became a coordinated effort [328], and we hope that efficiency tables of other authors will become available and can be included in the `Fastlim` framework. In particular we hope that the experimental collaborations will directly provide their efficiencies in a table format so that their results can be included and thus reinterpreted in a wide range of the SUSY models.

Once enough topologies will be available, `Fastlim` can be used also for phenomenological studies of the MSSM (or NMSSM) parameter space as the ones presented in the previous chapters of this thesis. Currently `Fastlim` needs in average 14 seconds per parameter point, and we are aiming to increase the speed of the program further in future releases.

Chapter 9

Conclusions

In this thesis we presented various complementary possibilities to employ the experimental measurements in order to test models beyond the SM. We derived constraints on the MSSM and the NMSSM model parameters and we investigated preferred parameter regions, by confronting their predictions with the experimental results from precision measurements (of M_W and m_t), Higgs measurements and direct SUSY searches.

Both the MSSM and the NMSSM provide an excellent description of the data provided by collider experiments. Their parameter spaces are narrowed down by the different experimental results, thus sharpening the predictions made by these SUSY models. The discovery of a Higgs boson with a mass of ~ 125.6 GeV implies (if interpreted as the light \mathcal{CP} -even Higgs) that in the MSSM the \mathcal{CP} -odd Higgs mass, M_A has to be in the decoupling region, which automatically causes the Higgs couplings to be SM-like. In such a case a significant improvement of the precision of the Higgs decay rate measurements will be necessary to get sensitivity for distinguishing the MSSM from the SM. This interpretation requires a large splitting in the stop sector. Very light stops are disfavoured by this interpretation (and are also challenged by the direct LHC searches, as we shall see below), however we found that stop masses down to ~ 200 GeV are still allowed by the Higgs mass constraint. In models with extended Higgs sectors, such as the NMSSM, the bounds, imposed by the mass of the discovered Higgs boson, are less stringent and a viable interpretation of the Higgs discovery in the non-decoupling regime, in terms of the second lightest Higgs of the model, is possible. This interpretation involves the existence of another Higgs boson with a mass below the LHC signal and reduced couplings to vector bosons.

The direct searches for SUSY particles have been unsuccessful so far, pushing parts of the SUSY particle spectrum (in particular gluinos and squarks of the first two generations) to relatively high masses. Studying the impact of direct search limits on the “natural” SUSY parameter space, we have seen that in this scenario also light stops and sbottoms are put to the test by the latest results, but there are still regions in the parameter space, not yet reached by the current searches. In a general pMSSM scenario light stops and sbottoms are presumably significantly less constrained by the current searches. We are planning to investigate the impact of the LHC limits from direct searches on the pMSSM parameter space in a future study. Electroweak precision observables, such as

M_W , can enhance the sensitivity for discriminating between different models and give additional indirect constraints, supplementing the ones from Higgs physics and direct searches. We found that the M_W prediction in SUSY models is very well compatible with the measurement, taking into account constraints from the Higgs boson discovery and direct SUSY searches. More stringent limits on the masses of stops and sbottoms (or a measurement of these masses) will drastically sharpen the M_W prediction in SUSY models. We have shown that an improved measurement of M_W could yield bounds on the masses of SUSY particles, which could be of great interest for direct searches — demonstrating the strength of the interplay between these complementary methods.

More details on the work presented in this thesis are summarised in the following.

Electroweak precision observables

In the first part of this thesis (containing original research) we provided the currently most precise prediction for the W boson mass in the MSSM and the NMSSM. We presented our one-loop computation of M_W in the MSSM (for the general case of complex parameters) and in the NMSSM. We combine our one-loop result with all relevant available higher order corrections. To make use of the sophisticated SM result, we split the (N)MSSM results into a SM-type part, containing the state-of-the-art SM prediction with all relevant loop corrections, and a SUSY part, consisting of the one-loop results and the known leading two-loop corrections. This procedure ensures that the full SM result is recovered in the decoupling limit. Furthermore it facilitates the extensions to other models beyond the SM. We have performed the one-loop calculation using the tools `FeynArts`, `FormCalc` and `LoopTools` which allow to carry out one-loop calculations with a high degree of automation. In the case of the NMSSM, we employed a new `FeynArts` model file, presented in Ref. [32]. The MSSM prediction has been encoded in `Mathematica` and `Fortran` format, while the NMSSM prediction is so far only available as `Mathematica` code. `Mathematica` provides the flexibility that allows us to analyse the functions at an analytic level, while `Fortran` is significantly faster and therefore suitable for large scans.

We demonstrated that the SUSY contributions to M_W typically give rise to an upward shift, generally improving the agreement of the theoretical prediction with the experimental measurement compared to the SM, where a 1.5σ deviation is found. For our MSSM analysis we performed a large scan over the parameter space (taking into account constraints from Higgs and SUSY searches) to study the overall behaviour of M_W , while in the NMSSM analysis we focussed on a few interesting benchmark scenarios. The largest SUSY contributions stem from the stop/sbottom sector. Thus more stringent constraints on third generation squarks would severely decrease the possible M_W range in the (N)MSSM. Even if stops and sbottoms are heavy, we found that sizeable contributions to M_W are possible if either chargino, neutralinos or sleptons are light. Furthermore we have shown that both in the MSSM and the NMSSM, the interpretations of the LHC Higgs signal in terms of either the lightest or the second lightest \mathcal{CP} -even Higgs both imply a prediction for M_W in good agreement with the experimental value. We studied the impact of the precision observable M_W in the context of possible future scenarios and

found that an improved accuracy of M_W and m_t measurements, which could be obtained with the ILC, would significantly enhance the sensitivity to discriminate between the SM and new physics models. A hypothetical scenario in which a light stop, but no other SUSY particle, is discovered at the LHC has been discussed and we demonstrated that in this case a high-precision M_W measurement could provide stringent upper bounds on the masses of the other third generation squarks. In the context of the MSSM we have also shown that a complex phase in the sfermion sector can lead to a significant shift in the W boson mass prediction, confirming earlier results given in Ref. [156]. Finally we investigated the pure NMSSM effects on M_W and found that in particular the extended neutralino sector can lead to M_W contributions that are larger than in the MSSM case.

Higgs physics

In the second part of this thesis we analysed different interpretations of the discovered Higgs signal in the context of SUSY models. Therefore we performed scans over the relevant regions in parameter space, taking constraints from Higgs and SUSY searches, flavour physics and electroweak measurements into account. As a first important result we found that both the MSSM and the NMSSM permit the interpretation of the Higgs at ~ 125.6 GeV in terms of the lightest or second lightest \mathcal{CP} -even Higgs boson of the respective SUSY model. In the MSSM the interpretation of the Higgs signal in terms of the heavier Higgs implies the presence of a light charged Higgs and is therefore very constrained by the latest ATLAS results from charged Higgs searches [55]. One part of our study concerns a possible enhancement of the $\gamma\gamma$ rate compared to the SM. We found that both the MSSM and the NMSSM can accommodate a Higgs at ~ 125.6 GeV which decays into two photons at the level of the SM or higher. An enhancement of the $\gamma\gamma$ rate can result either from a suppression of the $b\bar{b}$ decay mode (in which case also the other sub-dominant decay modes are affected) or directly from an enhancement of the $\gamma\gamma$ width. A direct enhancement of the width is caused by light staus, giving additional contributions to the loop-induced Higgs decay into two photons (without causing relevant modifications of the Higgs production rate via gluon fusion). In the MSSM a suppression of the $b\bar{b}$ rate can arise either from Higgs boson propagator corrections entering the effective mixing angle α_{eff} or by large Δ_b corrections, which parameterise the modifications in the Higgs coupling to $b\bar{b}$ caused by a loop-induced coupling of b quarks to the 'wrong' Higgs doublet. The NMSSM possesses an additional mechanism to suppress the $b\bar{b}$ decay and thus enhance the two photon rate, namely via singlet-doublet mixing.

Within the MSSM we have performed fits for the two MSSM interpretations of the Higgs signal, taking into account the measured Higgs rates in the various decay channels, the measured Higgs mass and low-energy observables. In this thesis we presented a fit, conducted at the end of 2012, including the results which were publicly available at that time, as well as an update for the 'light Higgs case' (interpretation of the signal at ~ 125.6 in terms of the light \mathcal{CP} -even Higgs) including the latest data. In the updated analysis, we observed an overall good fit-quality in the MSSM, as well as for the SM, where the MSSM fit for the interpretation of the signal at ~ 125.6 in terms of the light

\mathcal{CP} -even Higgs is slightly better than the SM one. The SM fit gets somewhat worse if low-energy observables are included. This is a consequence of the deviation between the SM prediction and the measurement of the anomalous magnetic moment of the muon. All rates predicted by the MSSM best-fit point are quite close to the SM values, apart from the two-photon rate, which is enhanced by $\sim 20\%$. A suppression of the $b\bar{b}$ Higgs decay is no longer favoured by the latest LHC measurements, and consequently the $\gamma\gamma$ enhancement is caused by light staus. A good MSSM fit is found for relatively large ranges of the MSSM parameters illustrating that in the MSSM a good description of the latest data is achieved, without the need of tuning any parameters to specific values. The parameter which is most constrained by our fit is the slepton soft mass parameter. While light staus are favoured by the $\gamma\gamma$ enhancement, light smuons and selectrons are preferred by the measured value of $(g-2)_\mu$.

Direct SUSY searches

In the last part of this thesis we studied the impact of direct SUSY searches. In order to calculate the exclusion limits also for models not covered in the experimental analyses, we developed the tool **FastLim**. This program reconstructs the visible cross section, which can be compared to the upper limits quoted in the experimental papers, by adding up the contributions from different simplified event topologies (e.g. $pp \rightarrow \tilde{g}\tilde{g} \rightarrow qq\tilde{\chi}_1^0qq\tilde{\chi}_1^0$, $pp \rightarrow \tilde{q}\tilde{q} \rightarrow q\tilde{\chi}_1^0q\tilde{\chi}_1^0$, ...). **FastLim** allows a fast estimation of the conservative limits from direct LHC searches, without performing Monte Carlo event generation. This is achieved by reading off pre-calculated cross section tables and efficiency tables for simplified model topologies, involving not more than three SUSY particles. As a proof of concept of this approach, we implemented recent ATLAS SUSY searches and presented their impact on the parameter space of “natural” SUSY models. The implemented simplified event topologies provide a very good cross section coverage of the “natural” SUSY parameter space. We found that direct LHC SUSY searches (at 8 TeV) can give more stringent constraints than the observation of a Higgs signal at ~ 125.6 GeV in some regions of the “natural” SUSY parameter space. The code structure of **FastLim** is very flexible, and additional efficiency tables can be included straightforwardly. Once we implemented enough topologies, we plan to use **FastLim** to investigate the impact of direct search limits on the pMSSM parameter space.

Bibliography

- [1] **ATLAS** Collaboration, G. Aad et al., *Observation of a new particle in the search for the Standard Model Higgs boson with the ATLAS detector at the LHC*, *Phys.Lett.* **B716** (2012) 1–29, [[arXiv:1207.7214](#)].
- [2] **CMS** Collaboration, S. Chatrchyan et al., *Observation of a new boson at a mass of 125 GeV with the CMS experiment at the LHC*, *Phys.Lett.* **B716** (2012) 30–61, [[arXiv:1207.7235](#)].
- [3] F. Englert and R. Brout, *Broken Symmetry and the Mass of Gauge Vector Mesons*, *Phys.Rev.Lett.* **13** (1964) 321–323.
- [4] P. W. Higgs, *Broken Symmetries and the Masses of Gauge Bosons*, *Phys.Rev.Lett.* **13** (1964) 508–509.
- [5] P. W. Higgs, *Broken symmetries, massless particles and gauge fields*, *Phys.Lett.* **12** (1964) 132–133.
- [6] G. Guralnik, C. Hagen, and T. Kibble, *Global Conservation Laws and Massless Particles*, *Phys.Rev.Lett.* **13** (1964) 585–587.
- [7] S. Glashow, *Partial Symmetries of Weak Interactions*, *Nucl.Phys.* **22** (1961) 579–588.
- [8] S. Weinberg, *A Model of Leptons*, *Phys.Rev.Lett.* **19** (1967) 1264–1266.
- [9] A. Salam, *Weak and Electromagnetic Interactions*, *Conf.Proc.* **C680519** (1968) 367–377.
- [10] P. Ramond, *Dual Theory for Free Fermions*, *Phys.Rev.* **D3** (1971) 2415–2418.
- [11] A. Neveu and J. Schwarz, *Factorizable dual model of pions*, *Nucl.Phys.* **B31** (1971) 86–112.
- [12] Y. Golfand and E. Likhtman, *Extension of the Algebra of Poincare Group Generators and Violation of p Invariance*, *JETP Lett.* **13** (1971) 323–326.
- [13] D. Volkov and V. Akulov, *Is the Neutrino a Goldstone Particle?*, *Phys.Lett.* **B46** (1973) 109–110.

-
- [14] J. Wess and B. Zumino, *Supergauge Transformations in Four-Dimensions*, *Nucl.Phys.* **B70** (1974) 39–50.
- [15] J. Wess and B. Zumino, *A Lagrangian Model Invariant Under Supergauge Transformations*, *Phys.Lett.* **B49** (1974) 52.
- [16] R. Haag, J. T. Lopuszanski, and M. Sohnius, *All Possible Generators of Supersymmetries of the S-Matrix*, *Nucl.Phys.* **B88** (1975) 257.
- [17] **CDF** Collaboration, F. Abe et al., *Observation of top quark production in $\bar{p}p$ collisions*, *Phys.Rev.Lett.* **74** (1995) 2626–2631, [[hep-ex/9503002](#)].
- [18] **DØ** Collaboration, S. Abachi et al., *Observation of the top quark*, *Phys.Rev.Lett.* **74** (1995) 2632–2637, [[hep-ex/9503003](#)].
- [19] **ATLAS** Collaboration. ATLAS-CONF-2013-012.
- [20] **CMS** Collaboration. CMS-PAS-HIG-13-001.
- [21] M. E. Peskin and D. V. Schroeder, *An Introduction to Quantum Field Theory*, 1995.
- [22] A. Denner, *Techniques for calculation of electroweak radiative corrections at the one loop level and results for W physics at LEP-200*, *Fortsch.Phys.* **41** (1993) 307, [[0709.1075](#)].
- [23] M. Böhm, A. Denner, and H. Joos, *Gauge theories of the strong and electroweak interaction*, 2001.
- [24] S. P. Martin, *A Supersymmetry primer*, [hep-ph/9709356](#).
- [25] I. Aitchison, *Supersymmetry in Particle Physics*, 2007.
- [26] R. K. Ellis, W. J. Stirling, and B. R. Webber, *QCD and Collider Physics*, 1996.
- [27] O. Stål, *Physics at the High-Energy Frontier - Phenomenological Studies of Charged Higgs Bosons and Cosmic Neutrino Detection*, 2009. PhD thesis.
- [28] P. Drechsel, *Countertermbeiträge zum anomalen magnetischen Moment des Myons im MSSM*, 2012. Diplomarbeit.
- [29] M. Frank, T. Hahn, S. Heinemeyer, W. Hollik, H. Rzehak, et al., *The Higgs Boson Masses and Mixings of the Complex MSSM in the Feynman-Diagrammatic Approach*, *JHEP* **0702** (2007) 047, [[hep-ph/0611326](#)].
- [30] A. Fowler, *Higher order and CP-violating effects in the neutralino and Higgs boson sectors of the MSSM*, 2010. PhD thesis.

-
- [31] U. Ellwanger, C. Hugonie, and A. M. Teixeira, *The Next-to-Minimal Supersymmetric Standard Model*, *Phys.Rept.* **496** (2010) 1–77, [arXiv:0910.1785].
- [32] R. Benbrik, M. Gomez Bock, S. Heinemeyer, O. Stål, G. Weiglein, and L. Zeune, *Confronting the MSSM and the NMSSM with the Discovery of a Signal in the two Photon Channel at the LHC*, *Eur.Phys.J.* **C72** (2012) 2171, [arXiv:1207.1096].
- [33] F. Mahmoudi, J. Rathsman, O. Stål, and L. Zeune, *Light Higgs bosons in phenomenological NMSSM*, *Eur.Phys.J.* **C71** (2011) 1608, [arXiv:1012.4490].
- [34] L. Zeune, *Precise predictions for the W boson mass in models beyond the Standard Model*, 2011. Diplomarbeit.
- [35] S. Heinemeyer, W. Hollik, G. Weiglein, and L. Zeune, *Implications of LHC search results on the W boson mass prediction in the MSSM*, *JHEP* **1312** (2013) 084, [arXiv:1311.1663].
- [36] J. Küblbeck, M. Böhm, and A. Denner, *Feyn Arts: Computer Algebraic Generation of Feynman Graphs and Amplitudes*, *Comput.Phys.Commun.* **60** (1990) 165–180.
- [37] A. Denner, H. Eck, O. Hahn, and J. Küblbeck, *Compact Feynman rules for Majorana fermions*, *Phys.Lett.* **B291** (1992) 278–280.
- [38] A. Denner, H. Eck, O. Hahn, and J. Küblbeck, *Feynman rules for fermion number violating interactions*, *Nucl.Phys.* **B387** (1992) 467–484.
- [39] J. Küblbeck, H. Eck, and R. Mertig, *Computer algebraic generation and calculation of Feynman graphs using FeynArts and FeynCalc*, *Nucl.Phys.Proc.Suppl.* **29A** (1992) 204–208.
- [40] T. Hahn, *Generating Feynman diagrams and amplitudes with FeynArts 3*, *Comput.Phys.Commun.* **140** (2001) 418, [hep-ph/0012260].
- [41] T. Hahn and C. Schappacher, *The Implementation of the Minimal Supersymmetric Standard model in FeynArts and FormCalc*, *Comput.Phys.Commun.* **143** (2002) 54–68, [hep-ph/0105349].
- [42] **Super-Kamiokande** Collaboration, Y. Fukuda et al., *Evidence for oscillation of atmospheric neutrinos*, *Phys.Rev.Lett.* **81** (1998) 1562–1567, [hep-ex/9807003].
- [43] **WMAP** Collaboration, E. Komatsu et al., *Seven-Year Wilkinson Microwave Anisotropy Probe (WMAP) Observations: Cosmological Interpretation*, *Astrophys.J.Suppl.* **192** (2011) 18, [arXiv:1001.4538].
- [44] **Planck** Collaboration, P. Ade et al., *Planck 2013 results. XVI. Cosmological parameters*, arXiv:1303.5076.

-
- [45] A. G. Cohen, A. De Rujula, and S. Glashow, *A Matter - antimatter universe?*, *Astrophys.J.* **495** (1998) 539–549, [[astro-ph/9707087](#)].
- [46] L. Girardello and M. T. Grisaru, *Soft Breaking of Supersymmetry*, *Nucl.Phys.* **B194** (1982) 65.
- [47] S. Dimopoulos and S. D. Thomas, *Dynamical relaxation of the supersymmetric CP violating phases*, *Nucl.Phys.* **B465** (1996) 23–33, [[hep-ph/9510220](#)].
- [48] S. Heinemeyer, O. Stål, and G. Weiglein, *Interpreting the LHC Higgs Search Results in the MSSM*, *Phys.Lett.* **B710** (2012) 201–206, [[arXiv:1112.3026](#)].
- [49] P. Bechtle, S. Heinemeyer, O. Stål, T. Stefaniak, G. Weiglein, et al., *MSSM Interpretations of the LHC Discovery: Light or Heavy Higgs?*, *Eur.Phys.J.* **C73** (2013) 2354, [[arXiv:1211.1955](#)].
- [50] A. Bottino, N. Fornengo, and S. Scopel, *Phenomenology of light neutralinos in view of recent results at the CERN Large Hadron Collider*, *Phys.Rev.* **D85** (2012) 095013, [[arXiv:1112.5666](#)].
- [51] M. Drees, *A Supersymmetric Explanation of the Excess of Higgs-Like Events at the LHC and at LEP*, *Phys.Rev.* **D86** (2012) 115018, [[arXiv:1210.6507](#)].
- [52] K. Hagiwara, J. S. Lee, and J. Nakamura, *Properties of 125 GeV Higgs boson in non-decoupling MSSM scenarios*, *JHEP* **1210** (2012) 002, [[arXiv:1207.0802](#)].
- [53] A. Arbey, M. Battaglia, A. Djouadi, and F. Mahmoudi, *The Higgs sector of the phenomenological MSSM in the light of the Higgs boson discovery*, *JHEP* **1209** (2012) 107, [[arXiv:1207.1348](#)].
- [54] M. Carena, S. Heinemeyer, O. Stål, C. Wagner, and G. Weiglein, *MSSM Higgs Boson Searches at the LHC: Benchmark Scenarios after the Discovery of a Higgs-like Particle*, *Eur. Phys. J.* **C73** (2013) 2552, [[arXiv:1302.7033](#)].
- [55] **ATLAS** Collaboration. ATLAS-CONF-2013-090.
- [56] J. E. Kim and H. P. Nilles, *The mu Problem and the Strong CP Problem*, *Phys.Lett.* **B138** (1984) 150.
- [57] L. J. Hall, D. Pinner, and J. T. Ruderman, *A Natural SUSY Higgs Near 126 GeV*, *JHEP* **1204** (2012) 131, [[arXiv:1112.2703](#)].
- [58] H. Anlauf, *Radiative Corrections in Gauge Theories*, 2001. Lecture notes.
- [59] W. Pauli and F. Villars, *On the invariant regularization in relativistic quantum theory*, *Rev. Mod. Phys.* **21** (1949) 434–444.
- [60] G. 't Hooft and M. Veltman, *Regularization and Renormalization of Gauge Fields*, *Nucl.Phys.* **B44** (1972) 189–213.

-
- [61] G. Passarino and M. Veltman, *One Loop Corrections for e^+e^- Annihilation into $\mu^+\mu^-$ in the Weinberg Model*, *Nucl.Phys.* **B160** (1979) 151.
- [62] T. Hahn and M. Perez-Victoria, *Automatized one loop calculations in four-dimensions and D-dimensions*, *Comput.Phys.Commun.* **118** (1999) 153–165, [[hep-ph/9807565](#)].
- [63] F. del Aguila, A. Culatti, R. Munoz-Tapia, and M. Perez-Victoria, *Constraining differential renormalization in Abelian gauge theories*, *Phys.Lett.* **B419** (1998) 263–271, [[hep-th/9709067](#)].
- [64] G. Altarelli and G. Parisi, *Asymptotic Freedom in Parton Language*, *Nucl.Phys.* **B126** (1977) 298.
- [65] F. Siegert, *Monte-Carlo event generation for the LHC*, 2010. PhD thesis.
- [66] A. Bethani, *Neutral Higgs boson searches in the $H \rightarrow \tau\tau \rightarrow \mu\mu$ decay channel*, 2013. PhD thesis.
- [67] **ATLAS** Collaboration. See: <https://twiki.cern.ch/twiki/bin/view/AtlasPublic/SupersymmetryPublicResults>.
- [68] **CMS** Collaboration. See: <https://twiki.cern.ch/twiki/bin/view/CMSPublic/PhysicsResultsSUS>.
- [69] **ATLAS** Collaboration. See: <https://twiki.cern.ch/twiki/bin/view/AtlasPublic/HiggsPublicResults>.
- [70] **CMS** Collaboration. See: <https://twiki.cern.ch/twiki/bin/view/CMSPublic/PhysicsResultsHIG>.
- [71] **ALEPH** Collaboration, A. Heister et al., *Search for supersymmetric particles with R parity violating decays in e^+e^- collisions at \sqrt{s} up to 209 GeV*, *Eur.Phys.J.* **C31** (2003) 1–16, [[hep-ex/0210014](#)].
- [72] **DELPHI** Collaboration, J. Abdallah et al., *Searches for supersymmetric particles in e^+e^- collisions up to 208 GeV and interpretation of the results within the MSSM*, *Eur.Phys.J.* **C31** (2003) 421–479, [[hep-ex/0311019](#)].
- [73] **OPAL** Collaboration, G. Abbiendi et al., *Search for anomalous production of dilepton events with missing transverse momentum in e^+e^- collisions at $\sqrt{s} = 183$ GeV to 209 GeV*, *Eur.Phys.J.* **C32** (2004) 453–473, [[hep-ex/0309014](#)].
- [74] **L3** Collaboration, P. Achard et al., *Search for scalar leptons and scalar quarks at LEP*, *Phys.Lett.* **B580** (2004) 37–49, [[hep-ex/0310007](#)].
- [75] **ALEPH, DELPHI, L3, OPAL, LEP Electroweak Working Group**, *A Combination of preliminary electroweak measurements and constraints on the standard model*, [hep-ex/0612034](#).

-
- [76] **Tevatron Electroweak Working Group**, *2012 Update of the Combination of CDF and DØ Results for the Mass of the W Boson*, arXiv:1204.0042.
- [77] M. Bahr, S. Gieseke, M. Gigg, D. Grellscheid, K. Hamilton, et al., *Herwig++ Physics and Manual*, *Eur.Phys.J.* **C58** (2008) 639–707, [arXiv:0803.0883].
- [78] T. Sjostrand, S. Mrenna, and P. Z. Skands, *PYTHIA 6.4 Physics and Manual*, *JHEP* **0605** (2006) 026, [hep-ph/0603175].
- [79] T. Sjostrand, S. Mrenna, and P. Z. Skands, *A Brief Introduction to PYTHIA 8.1*, *Comput.Phys.Commun.* **178** (2008) 852–867, [arXiv:0710.3820].
- [80] **ATLAS Collaboration**, S. M. Consonni, *Higgs search at ATLAS*, arXiv:1305.3315.
- [81] **LHC Higgs Cross Section Working Group**, S. Heinemeyer, et al., *Handbook of LHC Higgs Cross Sections: 3. Higgs Properties*, arXiv:1307.1347. See: <https://twiki.cern.ch/twiki/bin/view/LHCPhysics/CrossSections>.
- [82] **ATLAS Collaboration**. ATLAS-CONF-2013-013.
- [83] **CMS Collaboration**, S. Chatrchyan et al., *Measurement of the properties of a Higgs boson in the four-lepton final state*, arXiv:1312.5353.
- [84] **ATLAS Collaboration**. ATLAS-CONF-2013-030.
- [85] **CMS Collaboration**, S. Chatrchyan et al., *Measurement of Higgs boson production and properties in the WW decay channel with leptonic final states*, *JHEP* **01** (2014) 096, [arXiv:1312.1129].
- [86] **Tevatron New Physics Higgs Working Group, CDF, DØ**, *Updated Combination of CDF and DØ Searches for Standard Model Higgs Boson Production with up to 10.0 fb⁻¹ of Data*, arXiv:1207.0449.
- [87] **CMS Collaboration**, S. Chatrchyan et al., *Evidence for the 125 GeV Higgs boson decaying to a pair of τ leptons*, arXiv:1401.5041.
- [88] **ATLAS Collaboration**. ATLAS-CONF-2013-108.
- [89] **ATLAS Collaboration**. ATLAS-CONF-2013-034.
- [90] **ATLAS Collaboration**. ATLAS-CONF-2013-014, ATLAS-COM-CONF-2013-025.
- [91] **CMS Collaboration**. CMS-PAS-HIG-13-005.
- [92] **ATLAS Collaboration**, G. Aad et al., *Evidence for the spin-0 nature of the Higgs boson using ATLAS data*, *Phys.Lett.* **B726** (2013) 120–144, [arXiv:1307.1432].
- [93] **CMS Collaboration**. CMS-PAS-HIG-13-016.
- [94] D. S. Alves, E. Izaguirre, and J. G. Wacker, *Where the Sidewalk Ends: Jets and Missing Energy Search Strategies for the 7 TeV LHC*, *JHEP* **1110** (2011) 012, [arXiv:1102.5338].

-
- [95] **ATLAS** Collaboration, H. Okawa, *Interpretations of SUSY Searches in ATLAS with Simplified Models*, [arXiv:1110.0282](#).
- [96] **CMS** Collaboration, S. Chatrchyan et al., *Interpretation of Searches for Supersymmetry with simplified Models*, *Phys.Rev.* **D88** (2013) 052017, [[arXiv:1301.2175](#)].
- [97] R. Mahbubani, M. Papucci, G. Perez, J. T. Ruderman, and A. Weiler, *Light non-degenerate squarks at the LHC*, [arXiv:1212.3328](#).
- [98] **CDF** Collaboration, T. Aaltonen et al., *Precise measurement of the W-boson mass with the CDF II detector*, [arXiv:1203.0275](#).
- [99] **DØ** Collaboration, V. M. Abazov et al., *Measurement of the W Boson Mass with the DØ Detector*, [arXiv:1203.0293](#).
- [100] **ALEPH, DELPHI, L3, OPAL, SLD, LEP Electroweak Working Group, SLD Electroweak Group, SLD Heavy Flavour Group**, S. Schael, et al., *Precision electroweak measurements on the Z resonance*, *Phys.Rept.* **427** (2006) 257–454, [[hep-ex/0509008](#)]. See: <http://lepewwg.web.cern.ch/LEPEWWG/>.
- [101] **Tevatron Electroweak Working Group, CDF, DØ**, *Combination of CDF and DØ results on the mass of the top quark using up to 5.8 fb⁻¹ of data*, [arXiv:1107.5255](#).
- [102] **ATLAS, CMS** Collaborations. ATLAS-CONF-2013-102, CMS PAS TOP-13-005.
- [103] **ATLAS** Collaboration. ATLAS-CONF-2013-046.
- [104] **ATLAS** Collaboration. ATLAS-CONF-2013-077.
- [105] **CMS** Collaboration, S. Chatrchyan et al., *Measurement of the top-quark mass in $t\bar{t}$ events with lepton+jets final states in pp collisions at $\sqrt{s} = 7$ TeV*, *JHEP* **1212** (2012) 105, [[arXiv:1209.2319](#)].
- [106] **CMS** Collaboration, S. Chatrchyan et al., *Measurement of the top-quark mass in $t\bar{t}$ events with dilepton final states in pp collisions at $\sqrt{s} = 7$ TeV*, *Eur.Phys.J.* **C72** (2012) 2202, [[arXiv:1209.2393](#)].
- [107] **CMS** Collaboration, S. Chatrchyan et al., *Measurement of the top-quark mass in all-jets $t\bar{t}$ events in pp collisions at $\sqrt{s}=7$ TeV*, [arXiv:1307.4617](#).
- [108] **CMS** Collaboration, S. Chatrchyan et al., *Measurement of masses in the $t\bar{t}$ system by kinematic endpoints in pp collisions at $\sqrt{s} = 7$ TeV*, *Eur.Phys.J.* **C73** (2013) 2494, [[arXiv:1304.5783](#)].
- [109] **CMS** Collaboration. CMS-PAS-TOP-12-030.
- [110] **ATLAS, CDF, CMS, DØ** Collaborations, *First combination of Tevatron and LHC measurements of the top-quark mass*, [arXiv:1403.4427](#).

- [111] S. Heinemeyer, S. Kraml, W. Porod, and G. Weiglein, *Physics impact of a precise determination of the top quark mass at an e^+e^- linear collider*, *JHEP* **0309** (2003) 075, [[hep-ph/0306181](#)].
- [112] P. Z. Skands and D. Wicke, *Non-perturbative QCD effects and the top mass at the Tevatron*, *Eur.Phys.J.* **C52** (2007) 133–140, [[hep-ph/0703081](#)].
- [113] A. H. Hoang and I. W. Stewart, *Top Mass Measurements from Jets and the Tevatron Top-Quark Mass*, *Nucl.Phys.Proc.Suppl.* **185** (2008) 220–226, [[arXiv:0808.0222](#)].
- [114] M. Baak, A. Blondel, A. Bodek, R. Caputo, T. Corbett, et al., *Study of Electroweak Interactions at the Energy Frontier*, [arXiv:1310.6708](#).
- [115] **LHCb** Collaboration, R. Aaij et al., *Measurement of the $B_s^0 \rightarrow \mu^+\mu^-$ branching fraction and search for $B^0 \rightarrow \mu^+\mu^-$ decays at the LHCb experiment*, *Phys.Rev.Lett.* **111** (2013) 101805, [[arXiv:1307.5024](#)].
- [116] **CMS, LHCb** Collaborations, *Combination of results on the rare decays $B_{(s)}^0 \rightarrow \mu^+\mu^-$ from the CMS and LHCb experiments*, Tech. Rep. CMS-PAS-BPH-13-007. CERN-LHCb-CONF-2013-012, CERN, Geneva, Jul, 2013.
- [117] M. Davier, A. Hoecker, B. Malaescu, and Z. Zhang, *Reevaluation of the Hadronic Contributions to the Muon $g - 2$ and to $\alpha(M_Z^2)$* , *Eur.Phys.J.* **C71** (2011) 1515, [[arXiv:1010.4180](#)].
- [118] **Muon G-2** Collaboration, G. Bennett et al., *Final Report of the Muon E821 Anomalous Magnetic Moment Measurement at BNL*, *Phys.Rev.* **D73** (2006) 072003, [[hep-ex/0602035](#)].
- [119] O. Stål, G. Weiglein, and L. Zeune. In preparation.
- [120] A. Sirlin, *Radiative Corrections in the $SU(2)_L \times U(1)$ Theory: A Simple Renormalization Framework*, *Phys.Rev.* **D22** (1980) 971–981.
- [121] W. Marciano and A. Sirlin, *Radiative Corrections to Neutrino Induced Neutral Current Phenomena in the $SU(2)_L \times U(1)$ Theory*, *Phys.Rev.* **D22** (1980) 2695.
- [122] A. Djouadi and C. Verzegnassi, *Virtual Very Heavy Top Effects in LEP / SLC Precision Measurements*, *Phys. Lett.* **B195** (1987) 265.
- [123] A. Djouadi, *$\mathcal{O}(\alpha_s)$ Vacuum Polarization Functions of the Standard Model Gauge Bosons*, *Nuovo Cim.* **A100** (1988) 357.
- [124] B. Kniehl, *Two Loop Corrections to the Vacuum Polarizations in Perturbative QCD*, *Nucl. Phys.* **B347** (1990) 86.
- [125] F. Halzen and B. Kniehl, *Δr beyond one loop*, *Nucl. Phys.* **B353** (1991) 567.
- [126] B. Kniehl and A. Sirlin, *Dispersion relations for vacuum polarization functions in electroweak physics*, *Nucl. Phys.* **B371** (1992) 141.

-
- [127] B. Kniehl and A. Sirlin, *On the effect of the $t\bar{t}$ threshold on electroweak parameters*, *Phys. Rev.* **D47** (1993) 883.
- [128] A. Freitas, W. Hollik, W. Walter, and G. Weiglein, *Complete fermionic two loop results for the $M_W - M_Z$ interdependence*, *Phys.Lett.* **B495** (2000) 338–346, [[hep-ph/0007091](#)]. [Erratum-ibid. **B570** (2003) 260-264].
- [129] A. Freitas, W. Hollik, W. Walter, and G. Weiglein, *Electroweak two loop corrections to the $M_W - M_Z$ mass correlation in the standard model*, *Nucl.Phys.* **B632** (2002) 189–218, [[hep-ph/0202131](#)]. [Erratum-ibid. **B666** (2003) 305-307].
- [130] M. Awramik and M. Czakon, *Complete two loop electroweak contributions to the muon lifetime in the standard model*, *Phys. Lett.* **B568** (2003) 48, [[hep-ph/0305248](#)].
- [131] M. Awramik and M. Czakon, *Complete two loop bosonic contributions to the muon lifetime in the standard model*, *Phys. Rev. Lett.* **89** (2002) 241801, [[hep-ph/0208113](#)].
- [132] A. Onishchenko and O. Veretin, *Two-loop bosonic electroweak corrections to the muon lifetime and $M_W - M_Z$ interdependence*, *Phys. Lett.* **B551** (2003) 111, [[hep-ph/0209010](#)].
- [133] M. Awramik, M. Czakon, A. Onishchenko, and O. Veretin, *Bosonic corrections to Δr at the two loop level*, *Phys. Rev.* **D68** (2003) 053004, [[hep-ph/0209084](#)].
- [134] L. Avdeev, J. Fleischer, S. Mikhailov, and O. Tarasov, *$\mathcal{O}(\alpha\alpha_s^2)$ correction to the electroweak ρ parameter*, *Phys.Lett.* **B336** (1994) 560, [[hep-ph/9406363](#)].
- [135] K. G. Chetyrkin, J. H. Kuhn, and M. Steinhauser, *Corrections of order $\mathcal{O}(G_F M_t^2 \alpha_s^2)$ to the ρ parameter*, *Phys. Lett.* **B351** (1995) 331, [[hep-ph/9502291](#)].
- [136] K. G. Chetyrkin, J. Kuhn, and M. Steinhauser, *QCD corrections from top quark to relations between electroweak parameters to order α_s^2* , *Phys. Rev. Lett.* **75** (1995) 3394, [[hep-ph/9504413](#)].
- [137] K. Chetyrkin, J. Kuhn, and M. Steinhauser, *Three loop polarization function and $\mathcal{O}(\alpha_s^2)$ corrections to the production of heavy quarks*, *Nucl.Phys.* **B482** (1996) 213, [[hep-ph/9606230](#)].
- [138] M. Faisst, J. H. Kuhn, T. Seidensticker, and O. Veretin, *Three loop top quark contributions to the ρ parameter*, *Nucl. Phys.* **B665** (2003) 649, [[hep-ph/0302275](#)].
- [139] K. Chetyrkin, M. Faisst, J. H. Kuhn, P. Maierhofer, and C. Sturm, *Four-Loop QCD Corrections to the ρ Parameter*, *Phys.Rev.Lett.* **97** (2006) 102003, [[hep-ph/0605201](#)].
- [140] R. Boughezal and M. Czakon, *Single scale tadpoles and $\mathcal{O}(G_F m_t^2 \alpha_s^3)$ corrections to the ρ parameter*, *Nucl.Phys.* **B755** (2006) 221, [[hep-ph/0606232](#)].
- [141] J. van der Bij, K. Chetyrkin, M. Faisst, G. Jikia, and T. Seidensticker, *Three loop leading top mass contributions to the ρ parameter*, *Phys.Lett.* **B498** (2001) 156–162, [[hep-ph/0011373](#)].

- [142] R. Boughezal, J. Tausk, and J. van der Bij, *Three-loop electroweak correction to the ρ parameter in the large Higgs mass limit*, *Nucl.Phys.* **B713** (2005) 278–290, [hep-ph/0410216].
- [143] M. Awramik, M. Czakon, A. Freitas, and G. Weiglein, *Precise prediction for the W boson mass in the standard model*, *Phys.Rev.* **D69** (2004) 053006, [hep-ph/0311148].
- [144] M. Awramik, M. Czakon, and A. Freitas, *Electroweak two-loop corrections to the effective weak mixing angle*, *JHEP* **11** (2006) 048, [hep-ph/0608099].
- [145] R. Barbieri and L. Maiani, *Renormalization of the Electroweak ρ Parameter from Supersymmetric Particles*, *Nucl.Phys.* **B224** (1983) 32.
- [146] C. Lim, T. Inami, and N. Sakai, *The ρ Parameter in Supersymmetric Models*, *Phys.Rev.* **D29** (1984) 1488.
- [147] E. Eliasson, *Radiative Corrections to Electroweak Interactions in Supergravity GUTs*, *Phys.Lett.* **B147** (1984) 65.
- [148] Z. Hioki, *One Loop Effects of Heavy Scalar Quarks in Supersymmetric Electroweak Theory*, *Prog.Theor.Phys.* **73** (1985) 1283.
- [149] J. Grifols and J. Sola, *One Loop Renormalization of the Electroweak Parameters in $N = 1$ Supersymmetry*, *Nucl.Phys.* **B253** (1985) 47.
- [150] R. Barbieri, M. Frigeni, F. Giuliani, and H. Haber, *Precision Measurements in Electroweak Physics and Supersymmetry*, *Nucl.Phys.* **B341** (1990) 309–321.
- [151] M. Drees and K. Hagiwara, *Supersymmetric Contribution to the Electroweak ρ Parameter*, *Phys.Rev.* **D42** (1990) 1709–1725.
- [152] M. Drees, K. Hagiwara, and A. Yamada, *Process independent radiative corrections in the minimal supersymmetric standard model*, *Phys.Rev.* **D45** (1992) 1725–1743.
- [153] P. H. Chankowski, A. Dabelstein, W. Hollik, W. Mosle, S. Pokorski, and J. Rosiek, Δr in the MSSM, *Nucl.Phys.* **B417** (1994) 101.
- [154] D. Garcia and J. Sola, *Full one loop supersymmetric quantum effects on M_W* , *Mod.Phys.Lett.* **A9** (1994) 211–224.
- [155] D. M. Pierce, J. A. Bagger, K. T. Matchev, and R.-j. Zhang, *Precision corrections in the minimal supersymmetric standard model*, *Nucl.Phys.* **B491** (1997) 3–67, [hep-ph/9606211].
- [156] S. Heinemeyer, W. Hollik, D. Stöckinger, A. M. Weber, and G. Weiglein, *Precise prediction for M_W in the MSSM*, *JHEP* **08** (2006) 052, [hep-ph/0604147].
- [157] A. Djouadi, P. Gambino, S. Heinemeyer, W. Hollik, C. Junger, and G. Weiglein, *Supersymmetric contributions to electroweak precision observables: QCD corrections*, *Phys.Rev.Lett.* **78** (1997) 3626, [hep-ph/9612363].

-
- [158] A. Djouadi, P. Gambino, S. Heinemeyer, W. Hollik, C. Junger, and G. Weiglein, *Leading QCD corrections to scalar quark contributions to electroweak precision observables*, *Phys.Rev.* **D57** (1998) 4179, [[hep-ph/9710438](#)].
- [159] S. Heinemeyer and G. Weiglein, *Leading electroweak two loop corrections to precision observables in the MSSM*, *JHEP* **0210** (2002) 072, [[hep-ph/0209305](#)].
- [160] J. Haestier, S. Heinemeyer, D. Stöckinger, and G. Weiglein, *Electroweak precision observables: Two-loop Yukawa corrections of supersymmetric particles*, *JHEP* **0512** (2005) 027, [[hep-ph/0508139](#)].
- [161] S. Heinemeyer, W. Hollik, F. Merz, and S. Penaranda, *Electroweak precision observables in the MSSM with nonminimal flavor violation*, *Eur.Phys.J.* **C37** (2004) 481–493, [[hep-ph/0403228](#)].
- [162] S. K. Kang and J. D. Kim, *CP violating supersymmetric contributions to the electroweak ρ parameter*, *Phys.Rev.* **D62** (2000) 071901, [[hep-ph/0008073](#)].
- [163] F. Domingo and T. Lenz, *W mass and Leptonic Z-decays in the NMSSM*, *JHEP* **1107** (2011) 101, [[arXiv:1101.4758](#)].
- [164] S. Heinemeyer, W. Hollik, and G. Weiglein, *Electroweak precision observables in the minimal supersymmetric standard model*, *Phys.Rept.* **425** (2006) 265–368, [[hep-ph/0412214](#)].
- [165] **Particle Data Group**, J. Beringer, et al., *Review of Particle Physics (RPP)*, *Phys.Rev.* **D86** (2012) 010001. And 2013 partial update for the 2014 edition.
- [166] **MuLan** Collaboration, D. Webber et al., *Measurement of the Positive Muon Lifetime and Determination of the Fermi Constant to Part-per-Million Precision*, *Phys.Rev.Lett.* **106** (2011) 041803, [[arXiv:1010.0991](#)].
- [167] R. Behrends, R. Finkelstein, and A. Sirlin, *Radiative corrections to decay processes*, *Phys.Rev.* **101** (1956) 866–873.
- [168] T. Kinoshita and A. Sirlin, *Radiative corrections to Fermi interactions*, *Phys.Rev.* **113** (1959) 1652–1660.
- [169] T. van Ritbergen and R. G. Stuart, *On the precise determination of the Fermi coupling constant from the muon lifetime*, *Nucl.Phys.* **B564** (2000) 343–390, [[hep-ph/9904240](#)].
- [170] M. Steinhauser and T. Seidensticker, *Second order corrections to the muon lifetime and the semileptonic B decay*, *Phys.Lett.* **B467** (1999) 271–278, [[hep-ph/9909436](#)].
- [171] A. Pak and A. Czarnecki, *Mass effects in muon and semileptonic $b \rightarrow c$ decays*, *Phys.Rev.Lett.* **100** (2008) 241807, [[arXiv:0803.0960](#)].
- [172] M. Veltman, *Limit on Mass Differences in the Weinberg Model*, *Nucl.Phys.* **B123** (1977) 89.

- [173] N. Cabibbo and R. Gatto, *Electron Positron Colliding Beam Experiments*, *Phys.Rev.* **124** (1961) 1577–1595.
- [174] M. Steinhauser, *Leptonic contribution to the effective electromagnetic coupling constant up to three loops*, *Phys.Lett.* **B429** (1998) 158–161, [[hep-ph/9803313](#)].
- [175] L. Okun, *Leptons and quarks*, 1985.
- [176] D. Y. Bardin, A. Leike, T. Riemann, and M. Sachwitz, *Energy dependent width effects in e^+e^- annihilation near the Z pole*, *Phys. Lett.* **B206** (1988) 539.
- [177] F. Halzen, B. A. Kniehl, and M. L. Stong, *Two loop electroweak parameters*, *Z.Phys.* **C58** (1993) 119–132.
- [178] A. Stremplat, *Zwei-Schleifen-Beiträge zu leptonischen Präzisionsobservablen*, 1998. Diplomarbeit.
- [179] M. Consoli, W. Hollik, and F. Jegerlehner, *The Effect of the Top Quark on the $M_W - M_Z$ Interdependence and Possible Decoupling of Heavy Fermions from Low-Energy Physics*, *Phys.Lett.* **B227** (1989) 167.
- [180] R. Barbieri, M. Beccaria, P. Ciafaloni, G. Curci, and A. Vicere, *Two loop heavy top effects in the Standard Model*, *Nucl.Phys.* **B409** (1993) 105–127.
- [181] J. Fleischer, O. Tarasov, and F. Jegerlehner, *Two loop heavy top corrections to the ρ parameter: A Simple formula valid for arbitrary Higgs mass*, *Phys.Lett.* **B319** (1993) 249–256.
- [182] Wolfram Research, Inc., *Mathematica*, Version 8.0, Champaign, IL (2010).
- [183] J. Vermaseren, *New features of FORM*, [math-ph/0010025](#).
- [184] T. Hahn, S. Heinemeyer, W. Hollik, H. Rzehak, and G. Weiglein, *FeynHiggs: A program for the calculation of MSSM Higgs-boson observables - Version 2.6.5*, *Comput.Phys.Commun.* **180** (2009) 1426–1427.
- [185] G. Degrandi, S. Heinemeyer, W. Hollik, P. Slavich, and G. Weiglein, *Towards high precision predictions for the MSSM Higgs sector*, *Eur.Phys.J.* **C28** (2003) 133–143, [[hep-ph/0212020](#)].
- [186] S. Heinemeyer, W. Hollik, and G. Weiglein, *The Masses of the neutral CP even Higgs bosons in the MSSM: Accurate analysis at the two loop level*, *Eur.Phys.J.* **C9** (1999) 343–366, [[hep-ph/9812472](#)].
- [187] S. Heinemeyer, W. Hollik, and G. Weiglein, *FeynHiggs: A Program for the calculation of the masses of the neutral CP even Higgs bosons in the MSSM*, *Comput.Phys.Commun.* **124** (2000) 76–89, [[hep-ph/9812320](#)].
- [188] U. Ellwanger, J. F. Gunion, and C. Hugonie, *NMHDECAY: A Fortran code for the Higgs masses, couplings and decay widths in the NMSSM*, *JHEP* **0502** (2005) 066, [[hep-ph/0406215](#)].

- [189] U. Ellwanger and C. Hugonie, *NMHDECAY 2.0: An Updated program for sparticle masses, Higgs masses, couplings and decay widths in the NMSSM*, *Comput.Phys.Commun.* **175** (2006) 290–303, [[hep-ph/0508022](#)].
- [190] G. Belanger, F. Boudjema, C. Hugonie, A. Pukhov, and A. Semenov, *Relic density of dark matter in the NMSSM*, *JCAP* **0509** (2005) 001, [[hep-ph/0505142](#)].
- [191] U. Ellwanger and C. Hugonie, *NMSPEC: A Fortran code for the sparticle and Higgs masses in the NMSSM with GUT scale boundary conditions*, *Comput.Phys.Commun.* **177** (2007) 399–407, [[hep-ph/0612134](#)].
- [192] K. E. Williams, H. Rzehak, and G. Weiglein, *Higher order corrections to Higgs boson decays in the MSSM with complex parameters*, *Eur.Phys.J.* **C71** (2011) 1669, [[arXiv:1103.1335](#)].
- [193] See: <http://www.th.u-psud.fr/NMHDECAY/README>.
- [194] P. Bechtle, O. Brein, S. Heinemeyer, O. Stål, T. Stefaniak, et al., *Recent Developments in HiggsBounds and a Preview of HiggsSignals*, [arXiv:1301.2345](#).
- [195] P. Bechtle, O. Brein, S. Heinemeyer, G. Weiglein, and K. E. Williams, *HiggsBounds 2.0.0: Confronting Neutral and Charged Higgs Sector Predictions with Exclusion Bounds from LEP and the Tevatron*, *Comput.Phys.Commun.* **182** (2011) 2605–2631, [[arXiv:1102.1898](#)].
- [196] P. Bechtle, O. Brein, S. Heinemeyer, G. Weiglein, and K. E. Williams, *HiggsBounds: Confronting Arbitrary Higgs Sectors with Exclusion Bounds from LEP and the Tevatron*, *Comput.Phys.Commun.* **181** (2010) 138–167, [[arXiv:0811.4169](#)].
- [197] P. Bechtle, O. Brein, S. Heinemeyer, O. Stål, T. Stefaniak, et al., *HiggsBounds-4: Improved Tests of Extended Higgs Sectors against Exclusion Bounds from LEP, the Tevatron and the LHC*, [arXiv:1311.0055](#).
- [198] L. Covi and J. E. Kim, *Axinos as Dark Matter Particles*, *New J.Phys.* **11** (2009) 105003, [[arXiv:0902.0769](#)].
- [199] W. Buchmüller, L. Covi, K. Hamaguchi, A. Ibarra, and T. Yanagida, *Gravitino Dark Matter in R-Parity Breaking Vacua*, *JHEP* **0703** (2007) 037, [[hep-ph/0702184](#)].
- [200] U. Ellwanger, M. Rausch de Traubenberg, and C. A. Savoy, *Phenomenology of supersymmetric models with a singlet*, *Nucl.Phys.* **B492** (1997) 21–50, [[hep-ph/9611251](#)].
- [201] S. King and P. White, *Resolving the constrained minimal and next-to-minimal supersymmetric standard models*, *Phys.Rev.* **D52** (1995) 4183–4216, [[hep-ph/9505326](#)].
- [202] D. Miller, R. Nevzorov, and P. Zerwas, *The Higgs sector of the next-to-minimal supersymmetric standard model*, *Nucl.Phys.* **B681** (2004) 3–30, [[hep-ph/0304049](#)].
- [203] F. Staub, *SARAH*, [arXiv:0806.0538](#).

- [204] F. Staub, *From Superpotential to Model Files for FeynArts and CalcHep/CompHep*, *Comput.Phys.Commun.* **181** (2010) 1077–1086, [arXiv:0909.2863].
- [205] N. D. Christensen and C. Duhr, *FeynRules - Feynman rules made easy*, *Comput.Phys.Commun.* **180** (2009) 1614–1641, [arXiv:0806.4194].
- [206] D. Das, U. Ellwanger, and A. M. Teixeira, *NMSDECAY: A Fortran Code for Supersymmetric Particle Decays in the Next-to-Minimal Supersymmetric Standard Model*, *Comput.Phys.Commun.* **183** (2012) 774–779, [arXiv:1106.5633].
- [207] O. Stål and G. Weiglein, *Light NMSSM Higgs bosons in SUSY cascade decays at the LHC*, *JHEP* **1201** (2012) 071, [arXiv:1108.0595].
- [208] M. Carena, S. Gori, N. R. Shah, C. E. Wagner, and L.-T. Wang, *Light Stau Phenomenology and the Higgs $\gamma\gamma$ Rate*, *JHEP* **1207** (2012) 175, [arXiv:1205.5842].
- [209] M. Carena, S. Gori, N. R. Shah, and C. E. Wagner, *A 125 GeV SM-like Higgs in the MSSM and the $\gamma\gamma$ rate*, *JHEP* **1203** (2012) 014, [arXiv:1112.3336].
- [210] H. Baer, T. Barklow, K. Fujii, Y. Gao, A. Hoang, et al., *The International Linear Collider Technical Design Report - Volume 2: Physics*, arXiv:1306.6352.
- [211] V. Barger, P. Huang, M. Ishida, and W.-Y. Keung, *Scalar-Top Masses from SUSY Loops with 125 GeV m_h and Precise M_W* , *Phys.Lett.* **B718** (2013) 1024–1030, [arXiv:1206.1777].
- [212] S. King, M. Mühlleitner, and R. Nevzorov, *NMSSM Higgs Benchmarks Near 125 GeV*, *Nucl.Phys.* **B860** (2012) 207–244, [arXiv:1201.2671].
- [213] M. E. Peskin and T. Takeuchi, *A New constraint on a strongly interacting Higgs sector*, *Phys.Rev.Lett.* **65** (1990) 964–967.
- [214] W. J. Marciano and J. L. Rosner, *Atomic parity violation as a probe of new physics*, *Phys.Rev.Lett.* **65** (1990) 2963–2966. [Erratum-ibid. **68** (1992) 898].
- [215] CMS Collaboration, S. Chatrchyan et al., *Search for the standard model Higgs boson produced in association with a W or a Z boson and decaying to bottom quarks*, *Phys.Rev.* **D89** (2014) 012003, [arXiv:1310.3687].
- [216] ATLAS Collaboration. ATLAS-CONF-2013-079.
- [217] K. Ender, T. Graf, M. Mühlleitner, and H. Rzehak, *Analysis of the NMSSM Higgs Boson Masses at One-Loop Level*, *Phys.Rev.* **D85** (2012) 075024, [arXiv:1111.4952].
- [218] J. F. Gunion, D. Hooper, and B. McElrath, *Light neutralino dark matter in the NMSSM*, *Phys.Rev.* **D73** (2006) 015011, [hep-ph/0509024].
- [219] F. Domingo and U. Ellwanger, *Constraints from the Muon $g - 2$ on the Parameter Space of the NMSSM*, *JHEP* **0807** (2008) 079, [arXiv:0806.0733].

- [220] G. Degrossi and G. Giudice, *QED logarithms in the electroweak corrections to the muon anomalous magnetic moment*, *Phys.Rev.* **D58** (1998) 053007, [[hep-ph/9803384](#)].
- [221] S. Heinemeyer, D. Stöckinger, and G. Weiglein, *Two loop SUSY corrections to the anomalous magnetic moment of the muon*, *Nucl.Phys.* **B690** (2004) 62–80, [[hep-ph/0312264](#)].
- [222] S. Heinemeyer, D. Stöckinger, and G. Weiglein, *Electroweak and supersymmetric two-loop corrections to $(g - 2)_\mu$* , *Nucl.Phys.* **B699** (2004) 103–123, [[hep-ph/0405255](#)].
- [223] **Heavy Flavor Averaging Group**, Y. Amhis, et al., *Averages of B-Hadron, C-Hadron, and tau-lepton properties as of early 2012*, [arXiv:1207.1158](#). See: <http://www.slac.stanford.edu/xorg/hfag>.
- [224] G. Hiller, *B physics signals of the lightest CP odd Higgs in the NMSSM at large $\tan\beta$* , *Phys.Rev.* **D70** (2004) 034018, [[hep-ph/0404220](#)].
- [225] F. Domingo and U. Ellwanger, *Updated Constraints from B Physics on the MSSM and the NMSSM*, *JHEP* **0712** (2007) 090, [[arXiv:0710.3714](#)].
- [226] **Heavy Flavor Averaging Group**, E. Barberio, et al., *Averages of b-hadron properties at the end of 2005*, [hep-ex/0603003](#).
- [227] **CMS, LHCb Collaborations**. CMS-PAS-BPH-11-019, LHCb-CONF-2011-047.
- [228] **Heavy Flavor Averaging Group**, D. Asner, et al., *Averages of b-hadron, c-hadron, and τ -lepton properties*, [arXiv:1010.1589](#).
- [229] **CDF Collaboration**, A. Abulencia et al., *Observation of $B_s^0 - \bar{B} + s^0$ Oscillations*, *Phys.Rev.Lett.* **97** (2006) 242003, [[hep-ex/0609040](#)].
- [230] **ATLAS Collaboration**. ATLAS-CONF-2011-161.
- [231] **CMS Collaboration**. CMS-HIG-11-030.
- [232] S. Heinemeyer, W. Hollik, and G. Weiglein, *Decay widths of the neutral CP even MSSM Higgs bosons in the Feynman diagrammatic approach*, *Eur.Phys.J.* **C16** (2000) 139–153, [[hep-ph/0003022](#)].
- [233] L. J. Hall, R. Rattazzi, and U. Sarid, *The Top quark mass in supersymmetric $SO(10)$ unification*, *Phys.Rev.* **D50** (1994) 7048–7065, [[hep-ph/9306309](#)].
- [234] M. S. Carena, M. Olechowski, S. Pokorski, and C. Wagner, *Electroweak symmetry breaking and bottom - top Yukawa unification*, *Nucl.Phys.* **B426** (1994) 269–300, [[hep-ph/9402253](#)].
- [235] M. S. Carena, D. Garcia, U. Nierste, and C. E. Wagner, *Effective Lagrangian for the $\bar{t}bH^+$ interaction in the MSSM and charged Higgs phenomenology*, *Nucl.Phys.* **B577** (2000) 88–120, [[hep-ph/9912516](#)].

- [236] D. Noth and M. Spira, *Higgs Boson Couplings to Bottom Quarks: Two-Loop Supersymmetry-QCD Corrections*, *Phys.Rev.Lett.* **101** (2008) 181801, [[arXiv:0808.0087](#)].
- [237] D. Noth and M. Spira, *Supersymmetric Higgs Yukawa Couplings to Bottom Quarks at next-to-next-to-leading Order*, *JHEP* **1106** (2011) 084, [[arXiv:1001.1935](#)].
- [238] J. Cao, F. Ding, C. Han, J. M. Yang, and J. Zhu, *A light Higgs scalar in the NMSSM confronted with the latest LHC Higgs data*, *JHEP* **1311** (2013) 018, [[arXiv:1309.4939](#)].
- [239] U. Ellwanger, *Enhanced di-photon Higgs signal in the Next-to-Minimal Supersymmetric Standard Model*, *Phys.Lett.* **B698** (2011) 293–296, [[arXiv:1012.1201](#)].
- [240] J. Cao, Z. Heng, T. Liu, and J. M. Yang, *Di-photon Higgs signal at the LHC: A Comparative study for different supersymmetric models*, *Phys.Lett.* **B703** (2011) 462–468, [[arXiv:1103.0631](#)].
- [241] **ATLAS** Collaboration, G. Aad et al., *Search for the Higgs boson in the $H \rightarrow WW(*) \rightarrow \ell\nu\ell\nu$ decay channel in pp collisions at $\sqrt{s} = 7$ TeV with the ATLAS detector*, *Phys.Rev.Lett.* **108** (2012) 111802, [[arXiv:1112.2577](#)].
- [242] **CMS** Collaboration. CMS-HIG-11-024.
- [243] **ALEPH, DELPHI, L3, OPAL, LEP Working Group for Higgs Boson Searches**, S. Schael, et al., *Search for neutral MSSM Higgs bosons at LEP*, *Eur.Phys.J.* **C47** (2006) 547–587, [[hep-ex/0602042](#)].
- [244] **Tevatron New Phenomena and Higgs Working Group**, D. Benjamin, et al., *Combined CDF and DØ Upper Limits on MSSM Higgs Boson Production in tau-tau Final States with up to 2.2 fb^{-1}* , [arXiv:1003.3363](#).
- [245] **CDF, DØ** Collaborations, T. Aaltonen, et al., *Search for Neutral Higgs Bosons in Events with Multiple Bottom Quarks at the Tevatron*, *Phys.Rev.* **D86** (2012) 091101, [[arXiv:1207.2757](#)].
- [246] **ATLAS** Collaboration. ATLAS-CONF-2012-094.
- [247] **ATLAS** Collaboration. ATLAS-CONF-2012-011.
- [248] **CMS** Collaboration. CMS-PAS-HIG-13-021.
- [249] **CMS** Collaboration, S. Chatrchyan et al., *Search for Neutral MSSM Higgs Bosons Decaying to Tau Pairs in pp Collisions at $\sqrt{s} = 7$ TeV*, *Phys.Rev.Lett.* **106** (2011) 231801, [[arXiv:1104.1619](#)].
- [250] **CMS** Collaboration, S. Chatrchyan et al., *Search for a light charged Higgs boson in top quark decays in pp collisions at $\sqrt{s} = 7$ TeV*, *JHEP* **1207** (2012) 143, [[arXiv:1205.5736](#)].

- [251] **CMS** Collaboration, S. Chatrchyan et al., *Search for a Higgs boson decaying into a b -quark pair and produced in association with b quarks in proton-proton collisions at 7 TeV*, *Phys.Lett.* **B722** (2013) 207–232, [[arXiv:1302.2892](#)].
- [252] M. S. Carena, S. Heinemeyer, C. Wagner, and G. Weiglein, *Suggestions for improved benchmark scenarios for Higgs boson searches at LEP-2*, [hep-ph/9912223](#).
- [253] M. S. Carena, S. Heinemeyer, C. Wagner, and G. Weiglein, *Suggestions for benchmark scenarios for MSSM Higgs boson searches at hadron colliders*, *Eur.Phys.J.* **C26** (2003) 601–607, [[hep-ph/0202167](#)].
- [254] M. S. Carena, S. Heinemeyer, C. Wagner, and G. Weiglein, *MSSM Higgs boson searches at the Tevatron and the LHC: Impact of different benchmark scenarios*, *Eur.Phys.J.* **C45** (2006) 797–814, [[hep-ph/0511023](#)].
- [255] S. AbdusSalam, B. Allanach, H. Dreiner, J. Ellis, U. Ellwanger, et al., *Benchmark Models, Planes, Lines and Points for Future SUSY Searches at the LHC*, *Eur.Phys.J.* **C71** (2011) 1835, [[arXiv:1109.3859](#)].
- [256] A. Arbey, M. Battaglia, and F. Mahmoudi, *Light Neutralino Dark Matter in the p MSSM: Implications of LEP, LHC and Dark Matter Searches on SUSY Particle Spectra*, *Eur.Phys.J.* **C72** (2012) 2169, [[arXiv:1205.2557](#)].
- [257] P. Bechtle, S. Heinemeyer, O. Stål, T. Stefaniak, and G. Weiglein, *HiggsSignals: Confronting arbitrary Higgs sectors with measurements at the Tevatron and the LHC*, [arXiv:1305.1933](#).
- [258] J. Espinosa, C. Grojean, M. Mühlleitner, and M. Trott, *First Glimpses at Higgs' face*, *JHEP* **1212** (2012) 045, [[arXiv:1207.1717](#)].
- [259] **LHC Higgs Cross Section Working Group**, S. Dittmaier, et al., *Handbook of LHC Higgs Cross Sections: 1. Inclusive Observables*, [arXiv:1101.0593](#).
- [260] S. Dittmaier, S. Dittmaier, C. Mariotti, G. Passarino, R. Tanaka, et al., *Handbook of LHC Higgs Cross Sections: 2. Differential Distributions*, [arXiv:1201.3084](#).
- [261] See: <https://twiki.cern.ch/twiki/bin/view/LHCPhysics/CrossSections>.
- [262] D. de Florian and M. Grazzini, *Higgs production through gluon fusion: Updated cross sections at the Tevatron and the LHC*, *Phys.Lett.* **B674** (2009) 291–294, [[arXiv:0901.2427](#)]. See: <http://theory.fi.infn.it/grazzini/hcalculators.html>.
- [263] T. Hahn, S. Heinemeyer, F. Maltoni, G. Weiglein, and S. Willenbrock, *SM and MSSM Higgs boson production cross-sections at the Tevatron and the LHC*, [hep-ph/0607308](#).
- [264] T. Hahn, S. Heinemeyer, W. Hollik, H. Rzehak, and G. Weiglein, *FeynHiggs 2.7*, *Nucl.Phys.Proc.Suppl.* **205-206** (2010) 152–157, [[arXiv:1007.0956](#)].
- [265] R. Bonciani, G. Degrossi, and A. Vicini, *Scalar particle contribution to Higgs production via gluon fusion at NLO*, *JHEP* **0711** (2007) 095, [[arXiv:0709.4227](#)].

- [266] U. Aglietti, R. Bonciani, G. Degrassi, and A. Vicini, *Analytic Results for Virtual QCD Corrections to Higgs Production and Decay*, *JHEP* **0701** (2007) 021, [[hep-ph/0611266](#)].
- [267] A. Dedes and P. Slavich, *Two loop corrections to radiative electroweak symmetry breaking in the MSSM*, *Nucl.Phys.* **B657** (2003) 333–354, [[hep-ph/0212132](#)].
- [268] A. Dedes, G. Degrassi, and P. Slavich, *On the two loop Yukawa corrections to the MSSM Higgs boson masses at large tan beta*, *Nucl.Phys.* **B672** (2003) 144–162, [[hep-ph/0305127](#)].
- [269] S. Heinemeyer, W. Hollik, and G. Weiglein, *Decay widths of the neutral CP even MSSM Higgs bosons in the Feynman diagrammatic approach*, *Eur.Phys.J.* **C16** (2000) 139–153, [[hep-ph/0003022](#)].
- [270] **Belle** Collaboration, I. Adachi et al., *Measurement of $B^- \rightarrow \tau^- \bar{\nu}_\tau$ with a Hadronic Tagging Method Using the Full Data Sample of Belle*, *Phys.Rev.Lett.* **110** (2013) 131801, [[arXiv:1208.4678](#)].
- [271] **BaBar** Collaboration, J. Lees et al., *Evidence for an excess of $\bar{B} \rightarrow D^{(*)} \tau^- \bar{\nu}_\tau$ decays*, *Phys.Rev.Lett.* **109** (2012) 101802, [[arXiv:1205.5442](#)].
- [272] F. Mahmoudi, *SuperIso: A Program for calculating the isospin asymmetry of $B \rightarrow K^* \gamma$ in the MSSM*, *Comput.Phys.Commun.* **178** (2008) 745–754, [[arXiv:0710.2067](#)].
- [273] F. Mahmoudi, *SuperIso v2.3: A Program for calculating flavor physics observables in Supersymmetry*, *Comput.Phys.Commun.* **180** (2009) 1579–1613, [[arXiv:0808.3144](#)].
- [274] F. Mahmoudi, *SuperIso v3.0, flavor physics observables calculations: Extension to NMSSM*, *Comput.Phys.Commun.* **180** (2009) 1718–1719.
- [275] M. Misiak and M. Steinhauser, *NNLO QCD corrections to the $\bar{B} \rightarrow X_s \gamma$ matrix elements using interpolation in m_c* , *Nucl.Phys.* **B764** (2007) 62–82, [[hep-ph/0609241](#)].
- [276] **LHCb**, **CMS**, **ATLAS** Collaborations. LHCb-CONF-2012-017, CMS-PAS-BPH-12-009, ATLAS-CONF-2012-061.
- [277] **Muon $g - 2$** Collaboration, G. Bennett et al., *Measurement of the negative muon anomalous magnetic moment to 0.7 ppm*, *Phys.Rev.Lett.* **92** (2004) 161802, [[hep-ex/0401008](#)].
- [278] P. Bechtle, S. Heinemeyer, O. Stål, T. Stefaniak, and G. Weiglein, *Probing the Standard Model with Higgs signal rates from the Tevatron, the LHC and a future ILC*, [arXiv:1403.1582](#).
- [279] **Heavy Flavor Averaging Group**. See: www.slac.stanford.edu/xorg/hfag/rare/2013/rad11/OUTPUT/HTML/rad11_table7.html.
- [280] U. Haisch and F. Mahmoudi, *MSSM: Cornered and Correlated*, *JHEP* **1301** (2013) 061, [[arXiv:1210.7806](#)].
- [281] **CMS** Collaboration. CMS-PAS-HIG-11-029.

-
- [282] J. Frere, D. Jones, and S. Raby, *Fermion Masses and Induction of the Weak Scale by Supergravity*, *Nucl.Phys.* **B222** (1983) 11.
- [283] M. Claudson, L. J. Hall, and I. Hinchliffe, *Low-Energy Supergravity: False Vacua and Vacuum Predictions*, *Nucl.Phys.* **B228** (1983) 501.
- [284] C. Kounnas, A. Lahanas, D. V. Nanopoulos, and M. Quiros, *Low-Energy Behavior of Realistic Locally Supersymmetric Grand Unified Theories*, *Nucl.Phys.* **B236** (1984) 438.
- [285] J. Gunion, H. Haber, and M. Sher, *Charge / Color Breaking Minima and a -Parameter Bounds in Supersymmetric Models*, *Nucl.Phys.* **B306** (1988) 1.
- [286] J. Casas, A. Lleyda, and C. Munoz, *Strong constraints on the parameter space of the MSSM from charge and color breaking minima*, *Nucl.Phys.* **B471** (1996) 3–58, [[hep-ph/9507294](#)].
- [287] P. Langacker and N. Polonsky, *Implications of Yukawa unification for the Higgs sector in supersymmetric grand unified models*, *Phys.Rev.* **D50** (1994) 2199–2217, [[hep-ph/9403306](#)].
- [288] A. Strumia, *Charge and color breaking minima and constraints on the MSSM parameters*, *Nucl.Phys.* **B482** (1996) 24–38, [[hep-ph/9604417](#)].
- [289] R. Hempfling, *Yukawa coupling unification with supersymmetric threshold corrections*, *Phys.Rev.* **D49** (1994) 6168–6172.
- [290] D. Noth and M. Spira, *Higgs Boson Couplings to Bottom Quarks: Two-Loop Supersymmetry-QCD Corrections*, *Phys.Rev.Lett.* **101** (2008) 181801, [[arXiv:0808.0087](#)].
- [291] M. Papucci, K. Sakurai, A. Weiler, and L. Zeune, *Fastlim: a fast LHC limit calculator*, [arXiv:1402.0492](#).
- [292] J. Alwall, M. Herquet, F. Maltoni, O. Mattelaer, and T. Stelzer, *MadGraph 5 : Going Beyond*, *JHEP* **1106** (2011) 128, [[arXiv:1106.0522](#)].
- [293] S. Sekmen, S. Kraml, J. Lykken, F. Moortgat, S. Padhi, et al., *Interpreting LHC SUSY searches in the phenomenological MSSM*, *JHEP* **1202** (2012) 075, [[arXiv:1109.5119](#)].
- [294] M. Cahill-Rowley, J. Hewett, A. Ismail, and T. Rizzo, *p MSSM Studies at the 7, 8 and 14 TeV LHC*, [arXiv:1307.8444](#).
- [295] A. Arbey, M. Battaglia, and F. Mahmoudi, *Supersymmetry with Light Dark Matter confronting the recent CDMS and LHC Results*, *Phys.Rev.* **D88** (2013) 095001, [[arXiv:1308.2153](#)].
- [296] J. Reuter, M. Tonini, and M. de Vries, *Littlest Higgs with T -parity: Status and Prospects*, [arXiv:1310.2918](#).
- [297] C. Gutschow and Z. Marshall, *Setting limits on supersymmetry using simplified models*, [arXiv:1202.2662](#).

- [298] N. Arkani-Hamed, P. Schuster, N. Toro, J. Thaler, L.-T. Wang, et al., *MARMOSET: The Path from LHC Data to the New Standard Model via On-Shell Effective Theories*, hep-ph/0703088.
- [299] P. Z. Skands, B. Allanach, H. Baer, C. Balazs, G. Belanger, et al., *SUSY Les Houches accord: Interfacing SUSY spectrum calculators, decay packages, and event generators*, *JHEP* **0407** (2004) 036, [hep-ph/0311123].
- [300] W. Beenakker, R. Hopker, and M. Spira, *PROSPINO: A Program for the production of supersymmetric particles in next-to-leading order QCD*, hep-ph/9611232.
- [301] W. Beenakker, S. Brensing, M. Krämer, A. Kulesza, E. Laenen, et al., *Squark and Gluino Hadroproduction*, *Int.J.Mod.Phys.* **A26** (2011) 2637–2664, [arXiv:1105.1110].
- [302] W. Beenakker, S. Brensing, M. Krämer, A. Kulesza, E. Laenen, et al., *Soft-gluon resummation for squark and gluino hadroproduction*, *JHEP* **0912** (2009) 041, [arXiv:0909.4418].
- [303] A. Kulesza and L. Motyka, *Soft gluon resummation for the production of gluino-gluino and squark-antisquark pairs at the LHC*, *Phys.Rev.* **D80** (2009) 095004, [arXiv:0905.4749].
- [304] A. Kulesza and L. Motyka, *Threshold resummation for squark-antisquark and gluino-pair production at the LHC*, *Phys.Rev.Lett.* **102** (2009) 111802, [arXiv:0807.2405].
- [305] W. Beenakker, R. Hopker, M. Spira, and P. Zerwas, *Squark and gluino production at hadron colliders*, *Nucl.Phys.* **B492** (1997) 51–103, [hep-ph/9610490].
- [306] S. Oryn, X. Rouby, and V. Lemaitre, *DELPHES, a framework for fast simulation of a generic collider experiment*, arXiv:0903.2225.
- [307] J. Conway and et al.
www.physics.ucdavis.edu/~conway/research/software/pgs/pgs4-general.htm.
- [308] I.-W. Kim, M. Papucci, K. Sakurai, and A. Weiler. ATOM: Automated Tests of Models, in preparation.
- [309] M. Drees, H. Dreiner, D. Schmeier, J. Tattersall, and J. S. Kim, *CheckMATE: Confronting your Favourite New Physics Model with LHC Data*, arXiv:1312.2591.
- [310] A. Buckley, *PySLHA: a Pythonic interface to SUSY Les Houches Accord data*, arXiv:1305.4194.
- [311] A. L. Read, *Presentation of search results: The $CL(s)$ technique*, *J.Phys.* **G28** (2002) 2693–2704.
- [312] M. Krämer, A. Kulesza, R. van der Leeuw, M. Mangano, S. Padhi, et al., *Supersymmetry production cross sections in pp collisions at $\sqrt{s} = 7$ TeV*, arXiv:1206.2892.

-
- [313] See: <https://twiki.cern.ch/twiki/bin/view/LHCPhysics/SUSYCrossSections>.
- [314] See: <http://fastlim.web.cern.ch/fastlim/>.
- [315] M. L. Mangano, M. Moretti, F. Piccinini, and M. Treccani, *Matching matrix elements and shower evolution for top-quark production in hadronic collisions*, *JHEP* **0701** (2007) 013, [[hep-ph/0611129](https://arxiv.org/abs/hep-ph/0611129)].
- [316] M. Papucci, J. T. Ruderman, and A. Weiler, *Natural SUSY Endures*, *JHEP* **1209** (2012) 035, [[arXiv:1110.6926](https://arxiv.org/abs/1110.6926)].
- [317] C. Brust, A. Katz, S. Lawrence, and R. Sundrum, *SUSY, the Third Generation and the LHC*, *JHEP* **1203** (2012) 103, [[arXiv:1110.6670](https://arxiv.org/abs/1110.6670)].
- [318] B. Allanach and B. Gripaios, *Hide and Seek With Natural Supersymmetry at the LHC*, *JHEP* **1205** (2012) 062, [[arXiv:1202.6616](https://arxiv.org/abs/1202.6616)].
- [319] K. Kowalska and E. M. Sessolo, *Natural MSSM after the LHC 8 TeV run*, *Phys.Rev.* **D88** (2013) 075001, [[arXiv:1307.5790](https://arxiv.org/abs/1307.5790)].
- [320] H. Baer, V. Barger, P. Huang, and X. Tata, *Natural Supersymmetry: LHC, dark matter and ILC searches*, *JHEP* **1205** (2012) 109, [[arXiv:1203.5539](https://arxiv.org/abs/1203.5539)].
- [321] J. Berger, J. Hubisz, and M. Perelstein, *A Fermionic Top Partner: Naturalness and the LHC*, *JHEP* **1207** (2012) 016, [[arXiv:1205.0013](https://arxiv.org/abs/1205.0013)].
- [322] H. Baer, V. Barger, P. Huang, A. Mustafayev, and X. Tata, *Radiative natural SUSY with a 125 GeV Higgs boson*, *Phys.Rev.Lett.* **109** (2012) 161802, [[arXiv:1207.3343](https://arxiv.org/abs/1207.3343)].
- [323] O. Buchmueller and J. Marrouche, *Universal mass limits on gluino and third-generation squarks in the context of Natural-like SUSY spectra*, [arXiv:1304.2185](https://arxiv.org/abs/1304.2185).
- [324] J. A. Evans, Y. Kats, D. Shih, and M. J. Strassler, *Toward Full LHC Coverage of Natural Supersymmetry*, [arXiv:1310.5758](https://arxiv.org/abs/1310.5758).
- [325] A. Djouadi, M. Mühlleitner, and M. Spira, *Decays of supersymmetric particles: The Program SUSY-HIT (SUspect-SdecaY-Hdecay-InTerface)*, *Acta Phys.Polon.* **B38** (2007) 635–644, [[hep-ph/0609292](https://arxiv.org/abs/hep-ph/0609292)].
- [326] **ATLAS** Collaboration. ATLAS-CONF-2013-024.
- [327] H. Baer, V. Barger, P. Huang, D. Mickelson, A. Mustafayev, et al., *Radiative natural supersymmetry: Reconciling electroweak fine-tuning and the Higgs boson mass*, *Phys.Rev.* **D87** (2013), no. 11 115028, [[arXiv:1212.2655](https://arxiv.org/abs/1212.2655)].
- [328] For this coordinating effort, see:
<https://indico.cern.ch/conferenceDisplay.py?confId=272303>.